Characterising the stress-life response of mechanical and laser formed titanium components

By

Herman Fidder

Submitted in fulfilment of the requirements for the degree of Magister Technologiae: Engineering: Mechanical at the Nelson Mandela Metropolitan University

December 2012

Supervisor : Prof. P J M^{c}Grath

Copyright © 2012 Nelson Mandela Metropolitan University
All rights reserved

Declaration

I, *Herman Fidder* hereby declare that the *dissertation* for *Magister Technologiae: Engineering: Mechanical* is my own work and that it has not previously been submitted for assessment or completion of any postgraduate qualification to another university or for another qualification.

……...
H. Fidder

Abstract

Characterising the stress-life response of mechanical and laser formed titanium components

H. Fidder

Faculty of Engineering, the Built Environment and Information Technology,

Nelson Mandela Metropolitan University

PO BOX 77000, Port Elizabeth, South Africa

Thesis: Magister Technologiae: Engineering: Mechanical

2012

This dissertation involves the experimental investigation of commercially pure titanium (CP Ti) which was subjected to laser forming and mechanical forming processes. Commercially pure titanium grade 2 was formed to a radius of curvature of approximately 120 mm using three forming procedures, i.e. i) laser forming; ii) mechanical forming (stretched forming) and iii) a combined forming process (laser-mechanical forming). Fatigue testing revealed, for all the forming processes, that samples produced by laser forming performed the best at high load settings. However, mechanically formed specimens performed the best at low load settings, whereas the laser-mechanical process resulted in midway performance between laser and mechanical processing. Considering microstructure vs fatigue; impact vs fatigue; and residual stress vs fatigue; at high load settings it is evident that the microstructure is the dominant contributor to crack initiation and growth. Crack morphology of fatigue samples revealed that secondary cracks (parallel to main crack front) followed the grain boundaries of the Widmanstätten microstructure, whereas irregular secondary cracks grew parallel and through the twinning planes and along the grain boundaries of the equiaxed microstructure.

Laser forming resulted in microstructural changes from equiaxed grains to a Widmanstätten structure due to fast cooling rates. Excessive twinning is developed within the equiaxed microstructure after the mechanical forming procedure. This is due to cold working / strain hardening. The combined process shows a combination of equiaxed grains and Widmanstätten microstructure. Residual stress relieved for all forming processes revealed an increase in the magnitude of the residual stress compared to the parent plate and that the maximum values were obtained at the inner radius of curvature (i.e. 118.4 mm). Laser forming revealed the highest values in residual stress whereas the other two processes i.e. mechanical and laser-mechanical forming exhibited an increase midway between the parent plate and laser forming. The second most influential factor with regards to fatigue was the magnitude of the residual stress, especially at medium to low load settings. When considering theoretical models to predict fatigue life it was found that the Goodman model showed the closest relation to the actual fatigue data when considering the entire theoretical curve. Vickers microhardness profiling was applied to the thickness of the samples for the parent plate and all forming processes. No significant hardening occurred due to the forming processes and differences in hardness were considered negligible. Charpy impact testing revealed that the laser formed specimens exhibited the most brittle behaviour when compared to the parent plate results. Mechanical formed specimens showed a slight increase in brittleness compared to parent plate whereas the combined process yielded results midway between the laser and mechanically formed specimens. Mathematical equations are formulated and presented for predicting the fatigue life of CP Ti grade 2 for the parent plate and the three forming processes. This study proved that the laser forming process can be successfully used as a production stage in the forming of CP Ti grade 2.

Table of Contents

Copyright statement……..……i

Declaration……..……ii

Abstract……..iii

Table of Contents…….……..…….v

List of Figures…….……x

List of Tables…….……..xvii

Glossary of Terms…….…….xix

Acknowledgements……..xxvii

CHAPTER 1 - INTRODUCTION 1

1.1 Introduction 1

1.2 Problem statement 2

1.3 Aims & objectives 2

1.4 Hypothesis 4

1.5 Assumption 4

1.6 Delimitations 4

1.7 Significance of research 5

1.8 Research methodology 5

1.9 Project flow diagram 10

1.10 Layout of Dissertation 11

CHAPTER 2 - LITERATURE STUDY 12

2.1 Introduction – fatigue 12

2.2 Factors influencing fatigue life 13

2.3 Fatigue approaches to total life 14

2.4 Stress life approach 17

2.5 Strain life approach 17

2.6 Fatigue models 18

2.6.1 Gerber model 19

2.6.2 Goodman model 19

2.6.3 Morrow model 19

2.6.4 Soderberg model 20

2.7 Direct factors influencing CP Ti fatigue life 21

2.7.1 Influence of microstructure on fatigue life 23

2.8 Mechanical hot and cold forming 24

2.8.1 Deep drawing 26

2.8.2 Press brake forming 27

2.8.3 Three roll forming 29

2.8.4 Stretch forming 30

2.9 Laser applications 31

2.10 Laser forming techniques 31

2.11 Laser forming of Titanium 35

2.12 Microstructure associated with CP Ti grade 2 38

2.13 Production of CP Ti grade 2 41

2.14 Residual stress introduction 43

2.14.1 Non destructive method, X-Ray 43

2.14.2 Destructive method 43

2.15 Summary 47

CHAPTER 3 - EXPERIMENTAL SETUP 48

3.1 Introduction 48

3.2 Forming Processes 48

3.2.1 Mechanical Forming 48

3.2.2 Laser Forming 51

3.2.3 Laser-mechanical forming 54

3.3 Charpy impact testing 54

3.4 Hardness 56

3.5 Tensile testing 57

3.6 Typical chemical composition 59

3.7 Residual Stress 59

3.8 Fatigue 61

3.8.1 Fatigue specimen preparation for ASTM standard E466-96 61

3.8.2 Alignment of fatigue machine 62

3.8.3 Amplitude settings 64

3.9 Summary 66

CHAPTER 4 - RESULTS AND DISCUSSION 67

4.1 Introduction 67

4.2 Microstructure 67

4.2.1 Parent plate 67

4.2.2 Laser formed 68

4.2.3 Mechanically formed 69

4.2.4 Laser-mechanically formed 71

4.3 Microhardness 73

4.3.1 Parent plate 73

4.3.2 Formed specimens 74

4.4 Charpy impact testing 76

4.5 Residual stress data 81

4.5.1 Parent plate 81

4.5.2 Laser formed 83

4.5.3 Mechanically formed 85

4.5.4 Laser-mechanically formed 87

4.5.5 Combined residual stress graphs 89

4.6 Fatigue testing 92

4.6.1 Life prediction method according to Juvinall and Marshek 92

4.6.2 Parent plate 94

4.6.3 Laser formed 96
4.6.4 Mechanically formed 98
4.6.5 Laser-mechanically formed 100
4.6.6 Combined Graphs 101
4.6.7 Theoretical models to predict fatigue life 105
4.7 Crack morphology 108
4.7.1 Typical fracture surface appearance 108
4.7.2 Crack initiation position in relation to the bottom surface of the sample 110
4.7.3 Secondary cracks in region of fatigue fracture surface 111
4.8 Correlation between results 116
4.8.1 Microstructure vs. fatigue 116
4.8.2 Impact vs. fatigue 117
4.8.3 Residual stress vs. fatigue 118
4.8.4 Theoretical (predicted) vs. actual fatigue data 120
4.9 Prototype prediction fatigue curve for the fatigue life of CP Ti grade 2 127
4.9.1 Parent plate 128
4.9.2 Laser 130
4.9.3 Mechanical 133
4.9.4 Laser-mechanical 135
4.10 Summary 137

CHAPTER 5 - FINAL CONCLUSIONS 139

5.1 Introduction..... 139

5.2 Final conclusions..... 139

Future work..... 146

Bibliography 147

List of Figures

Figure 1.1 : Cyclic curve representing a fully reversed-strain cycle with sinusoidal wave form 7

Figure 1.2 : Illustration of a patent plate and bent sample 8

Figure 1.3 : Curvature dimensions of formed specimens in millimeters 8

Figure 2.1 : A typical S-N Curve, also known as a Wöhler curve, illustrating the fatigue life of aluminium. 13

Figure 2.2 : Classification of stress parameters affecting fatigue life 15

Figure 2.3 : Haigh diagram 16

Figure 2.4 : Master diagram for AISI 4340 steel..... 16

Figure 2.5 : Comparison of mean stress equation of Soderberg, Goodman, Morrow …18

Figure 2.6 : Generalized S-N curve for steel 22

Figure 2.7 : Illustrating the relationship between the surface factor and tensile strength 22

Figure 2.8 : S-N curve of CP Ti..... 23

Figure 2.9 : Graphical depiction of the three types of fatigue scenarios 23

Figure 2.10 : Grain size vs cycles to failure 24

Figure 2.11 : Springback effect (R_i = Radius initially, R_f = Radius final, θ_i = Angle initially, θ_f = Angle final)..... 25
Figure 2.12 : Illustration of a deep drawing sequence 27
Figure 2.13 : Illustration of deep drawing..... 27
Figure 2.14 : Air bending (forming) and bottoming forming 28
Figure 2.15 : Illustration of press brake 28
Figure 2.16 : Illustration of the three roll forming process 29
Figure 2.17 : Illustration of stretch forming with tensile forces 30
Figure 2.18 : Flow chart of a laser forming process 32
Figure 2.19 : Temperature gradient mechanism..... 32
Figure 2.20 : A doughnut laser beam distribution 33
Figure 2.21 : Laser distribution on material and laser path..... 34
Figure 2.22 : Temperature distribution caused by a laser on a material..... 34
Figure 2.23 : Effect of the beam power on the bending angle..... 36
Figure 2.24 : Bending angle isochors as a function of laser beam properties..... 36
Figure 2.25 : Material thickening as a function of number of scans 37
Figure 2.26 : CP Ti temperature phase diagram..... 39
Figure 2.27: Relatively pure titanium, x150 39
Figure 2.28 : Ti-03 wt% O alloy obtained after annealing in the beta region then cooled to 25ºC, x150 39
Figure 2.29 : Ti-0.3 wt% N alloy, x150 [2] 40
Figure 2.30 : Annealing at 1000ºC and quenched, x100[2] 40
Figure 2.31 : Annealing at 800ºC and quenched , x100 [2]..... 40
Figure 2.32 : Annealing at 1000ºC and furnace cooled (20h) to 25ºC, x100[2] 40
Figure 2.33 : Production cycle for ingot products..... 42

Figure 2.34 : Production cycle for mill products.....42

Figure 2.35 : Residual strain gauge and residual stress force distribution during drilling. 46

Figure 3.1 : Gosmeta EP-25 mechanical press ……..….49

Figure 3.2 : Parent plate sample clamped in fixture. 50

Figure 3.3 : Mechanically bent specimen 50

Figure 3.4 : Trumpf laser cell used at the National Laser Centre (CSIR). 51

Figure 3.5 : Doughnut Laser beam distribution 52

Figure 3.6 : Scanning pattern used to laser form CP Ti Grade 2.....53

Figure 3.7 : CP Ti Grade 2 specimens which was irradiated in an open mold fixture.....53

Figure 3.8 : Location of samples removed from specimens 55

Figure 3.9 : PSW type 30/15 Charpy V-Notch impact tester 55

Figure 3.10 : Future Tech FM 700 Vickers micro-hardness system.....56

Figure 3.11 : Hardness profile through the thickness of CP Ti grade 2 57

Figure 3.12: Tensile specimen undergoing deformation before failure 57

Figure 3.13 : Behavior of CP Ti grade 2 during tensile testing 58

Figure 3.14 : Strain gauge positioned on top of the apex 60

Figure 3.15 : Strain gauge positioned at the bottom of the apex 60

Figure 3.16 : Automatic centre drilling system.....61

Figure 3.17 : Fatigue dimentions of specimens (ASTM E466-96).....62

Figure 3.18 : Parent plate (top), Formed sample (middle), Final fatigued specimen (bottom) 62

Figure 3.19 : Fatigue specimen with fatigue alignment shims fitted 63

Figure 3.20 : Side view of specimen aligned with loading axis 63

Figure 3.21 : Front view of specimen aligned through rotating axis 64

Figure 3.22 : Master fatigue specimen 65

Figure 3.23 : Calibration of master sample.....65
Figure 3.24 : Fatigue specimen installed and coupled to machine.....66
Figure 4.1 : Original microstructure of CP Ti grade 2 (x100, electrolytically polished, polarized light)……..68
Figure 4.2 : Microstructure of laser formed CP Ti grade 2 (x50, electrolytically polished, polarized light, colour image).....69
Figure 4.3 : Microstructure of mechanically formed CP Ti grade 2(x100, electrolytically polished, polarized light), inner radius.....70
Figure 4.4 : Microstructure of mechanical formed CP Ti grade 2(x100, electrolytically polished, polarized light), outer radius.....70
Figure 4.5 :Microstructure of laser-mechanically formed CP Ti grade 2(x50, electrolytically polished, polarized light), inner radius 71
Figure 4.6 : Microstructure of laser-mechanically formed CP Ti grade 2(x50, electrolytically polished, polarized light), outer radius.....72
Figure 4.7 : Indication of position where the hardness through the thickness of the material was measured 73
Figure 4.8 : Micro-hardness profile measured through the thickness of the parent plate 74
Figure 4.9 : Illustrating the hardness profile (measure through the thickness) of all three bending processes 75
Figure 4.10 : Hardness profile of laser-mechanically formed specimen within the laser and twinning region (HV0.3) (x100, electrolytically polished, polarized light, inner radius).....75
Figure 4.11 : Illustration of the relationship between energy absorbed and temperature (in specific room temperature and -40ºC) 78
Figure 4.12 : Charpy impact surface of the parent plate specimen 79

Figure 4.13 : Charpy impact surface of laser formed specimen 79
Figure 4.14 : Charpy impact surface of mechanically formed specimen 80
Figure 4.15 : Charpy impact surface of laser-mechanically formed specimen 80
Figure 4.16 : Strain relaxation curve as a function of drilling depth – Parent plate specimen 82
Figure 4.17 : Plot of relieved residual stress versus hole depth – Parent plate specimen 82
Figure 4.18 : Relieved residual stress versus hole depth – inner radius, laser formed 83
Figure 4.19 : Plot of relieved residual stress versus hole depth – outer radius, laser formed 84
Figure 4.20 : Relieved residual stress versus hole depth – inner radius, mechanically formed 85
Figure 4.21 : Relieved residual stress versus hole depth – outer radius, mechanically formed 86
Figure 4.22 : Relieved residual stress versus hole depth – inner radius, laser-mechanically formed 87
Figure 4.23 : Relieved residual stress versus hole depth – outer radius, laser-mechanically formed 88
Figure 4.24 : Combined outer (top) relieved residual stress of parent plate and formed samples 89
Figure 4.25 : Combined inner (bottom) relieved residual stress of parent plate and formed samples 90
Figure 4.26 : Estimated S-N curve for CP titanium grade 2 93
Figure 4.27 : S-N curve (plotted with average results) for the parent plate specimen 95
Figure 4.28 : S-N curve (plotted with average results) for the laser formed specimen 97

Figure 4.29 : S-N curve (plotted with average results) for the mechanically formed specimen.....99
Figure 4.30 : S-N curve (plotted with average results) for the laser-mechanically formed specimen.....101
Figure 4.31 : S-N curves plotted (with average results) of all three forming processes and the parent plate.....102
Figure 4.32 : Percentage cycles to failure relative to the parent plate specimen.....104
Figure 4.33 : Indication of fatigue failure of parent plate specimen.....108
Figure 4.34 : Indication of fatigue failure of mechanically formed specimen.....109
Figure 4.35 : Indication of fatigue failure of laser-mechanically formed specimen.....109
Figure 4.36 : Indication of fatigue failure of laser formed specimen.....109
Figure 4.37 : Crack initiation position relative to the bottom surface.....110
Figure 4.38 : Secondary crack observation location.....111
Figure 4.39 : Microstructure of parent plate CP Ti grade 2 (x200, electrolytically polished, colour polarized light),.....112
Figure 4.40 : SEM image of parent plate CP Ti grade 2 showing the jagged nature of secondary cracks.....112
Figure 4.41 : Microstructure of laser formed CP Ti grade 2 (x500, electrolytically polished, colour polarized light),.....113
Figure 4.42 : SEM image of laser formed CP Ti grade 2 showing the nature of secondary cracks.....113
Figure 4.43 : Microstructure of mechanically formed CP Ti grade 2 (x50, electrolytically polished, colour polarized light).....114
Figure 4.44 : SEM image of mechanically formed CP Ti grade 2 showing the nature of secondary cracks.....114

Figure 4.45 : Microstructure of laser-mechanically formed CP Ti grade 2 (x500, electrolytically polished, colour polarized light) 115
Figure 4.46 : SEM image of laser-mechanically formed CP Ti grade 2 showing the nature of secondary cracks..... 115
Figure 4.47 : Impact (room temperature) vs. fatigue life at different load settings (expressed as a percentage relative to the parent plate) 118
Figure 4.48 : Residual stress vs. fatigue life at different load settings (expressed as a percentage relative to the parent plate) 120
Figure 4.49 : Correlation between actual fatigue data and the theoretical predicted number of cycles (parent plate)..... 121
Figure 4.50 : Correlation between actual fatigue data and the theoretical predicted number of cycles (Mechanically formed) 123
Figure 4.51 : Correlation between actual fatigue data and the theoretical predicted number of cycles (Laser-Mechanically formed)..... 124
Figure 4.52 : Correlation between actual fatigue data and the theoretical predicted number of cycles (Laser formed) 122
Figure 4.53 : Example of the Manson-Coffin-Basquin curve 126
Figure 4.54 : Prototype prediction curve for parent plate 130
Figure 4.55 : Prototype prediction curve for mechanical forming..... 132
Figure 4.56 : Prototype prediction curve for laser-mechanical forming 134
Figure 4.57 : Prototype prediction curve for laser forming 136

List of Tables

Table 1.1: Laser settings 6

Table 1.2: Test matrix 9

Table 2.1 : Bending angles at various powers and diameters for Ti-6Al-2Sn-4Zr-2Mo ... 36

Table 3.1 : Tensile properties of CP Ti grade 2 58

Table 3.2 : Chemical analyses supplied by foundry (percentage by weight) 59

Table 4.1 : Amount of energy absorbed by specimens at different temperatures (sub – standard) 77

Table 4.2 : Maximum stress values for each forming process at each specific depth for inner curvatures 91

Table 4.3 : Fatigue data of parent plate specimens 94

Table 4.4 : Fatigue data of laser formed specimens 96

Table 4.5 : Fatigue data of mechanically formed specimens 98

Table 4.6 : Fatigue data of laser-mechanically formed specimens 100

Table 4.7 : Average number of cycles to failure at the various load settings 102

Table 4.8 : Percentage decrease in life cycles compared to the parent plate specimens 103

Table 4.9 : Fatigue life (N_f) prediction according to the Gerber, Soderberg and Goodman models 107

Table 4.10 : Crack initiation position relative to the bottom surface 111

Table 4.11 : Relationship between microstructure and fatigue life until fracture 116

Table 4.12 : Relationship between Charpy impact and fatigue life until fracture at a single temperature. i.e. room temperature 117
Table 4.13 : Relationship between residual stress and fatigue life 119
Table 4.14 : Actual fatigue data and predicted fatigue models at different load settings 125
Table 4.15 : Percentage difference in fatigue life at different load settings 133
Table 4.16 : Percentage difference in fatigue life at different load settings 136

Table 5.1 : Combined data high load setting 144
Table 5.2 : Combined data low load setting 144
Table 5.3 : Proposed prototype prediction equations for CP Ti grade 2 145

Glossary of Terms

A

Annealing – heating to and maintaining at a suitable temperature.

Apex – refers to the top-most position of a bend.

As manufactured – pertains to sheet metal plate in its manufactured form.

B

BCC – Body-Centred Cubic system that has one lattice point in the centre of the unit cell in addition to the eight corner points. It has a net total of 2 lattice points per unit cell.

C

Catastrophic failure – is when the sample breaks due to fatigue.

D

Dislocation – a linear imperfection in a crystalline array of atoms.

E

Etchant – a chemical solution used to etch a metal to reveal structural details.

F

Fatigue – a phenomenon which results in the sudden fracture of a component after a period of cyclic loading in the elastic regime.

Fatigue life – is the number of load cycles a component can withstand prior to failure.

Fatigue limit – refers to the fatigue testing of non-ferrous materials which do not show finite life conditions.

Fatigue performance – refer to fatigue life.

Fatigue strength – the maximum stress that can be sustained for a specified number of cycles without failure.

Forming – refers to a manufacturing process whereby a sheet metal plate is shaped by means of a stamping press.

Fracture – is the loss of structural integrity through crack propagation.

Fracture stress – is the stress magnitude at fracture of a component.

Full stress relief – is the maximum relieved stress obtained, usually associated with residual stress assessment conditions.

G

Grain – an individual crystal in a polycrystalline metal or alloy, including twinned regions or sub-grains (if present).

Grain boundary – an interface separating two grains at which the orientation of the lattice changes from that of one grain to that of another. When the change in orientation is very small, the boundary is sometimes referred to as a sub-boundary structure.

Grain growth – an increase in the grain size of a metal usually as a result of heating at an elevated temperature.

Grain size – a measure of the areas or volumes of grains in a polycrystalline metal or alloy, usually expressed as an average when the individual sizes are fairly uniform. Grain size is reported in terms of the number of grains per unit area or volume, average diameter or as a number derived from area measurements.

H

Hardness – is a term used for describing the resistance of a material to plastic deformation under the action of an indenter.

Hardenability – the relative ability of a ferrous alloy to harden under cold working conditions.

Hardening – increasing hardness by suitable treatment, usually cold working.

HCP – Hexagonal close pack, i.e. a hexagonal crystal system consisting of 7 point groups such that all their space groups have the hexagonal lattice as underlying lattice. The hexagonal crystal family consists of 12 point groups such that at least one of their space groups has the hexagonal lattice as underlying lattice, and is the union of the hexagonal crystal system.

Homogeneous – a chemical composition and physical state of any physical small portion are the same as those of any other portion.

I

Impurities – undesirable elements or compounds in a material.

Isotropic continuum – having similar mechanical and microstructural properties in all directions.

L

LASER – Light Amplification by Stimulated Emission of Radiation.

M

Macrostructure – the structure of metals as revealed by macroscopic examination of the etched surface of a polished specimen.

Magnification – ratio of the length of a line in the image plane to the length of a line on the imaged material.

Mean stress – refers to a pre-strained loading condition.

Mechanical properties – the properties of a material that reveal its elastic and inelastic behaviour where force is applied, thereby indicating its suitability for mechanical applications.

Microcrack – a crack of microscopic proportions.

Microstructure – the structure of a prepared surface of a metal as revealed by a microscope at a magnification exceeding 25x.

P

Parent material – material as received from the manufacturer.

Polished surface – a surface that reflects a large proportion of the incident light in a spectacular manner.

Principal strains – the maximum and minimum direct strains in a material, subjected to complex stress. These strains act in the directions of the principal stresses.

Principal stresses – at any point within a stressed material there exist three mutually perpendicular planes on each of which the resultant stress is a normal stress (i.e. no shear stresses act on these planes). These mutually perpendicular planes are called principal planes, and the resultant normal stresses are principal stresses.

Pure bending conditions – the bending of a material under unconstrained conditions.

R

Recrystallisation – stage in the annealing process of cold worked metals above 0.4-0.5 Tm, in which deformed crystals are replaced by a new generation of crystals, which begin to grow at certain points in the deformed metal and eventually absorb the deformed crystals. The new crystals have more equal axes and contain far fewer dislocations than the deformed ones.

Relieved – allowing for freedom of movement or relaxation.

Residual stress – are stresses inherent in a component prior to service loading conditions or the stresses present in a body that are free of external forces or thermal gradients.

S

Sheet metal forming – *refer to forming*.

Slip – plastic deformation by the irreversible shear displacement of one part of a crystal relative to another in a definite crystallographic direction and usually on a specific crystallographic plane.

Slip band – a group of parallel slip lines so closely spaced that they appear as a single line when observed under an optical microscope.

Spacers – are shim stock or plates of specific sizes manufactured to raise a component or member to a specific height.

Springback – is the elastic recovery after a component has undergone plastic deformation.

Springback load – is the load required to return the material to its original pre-strained condition.

σ_f - true fracture stress.

Springback angle – is the angle between the springback position and the original pre-strained position in a pure bent plate component.

Strain – is a measure of the deformation of a body acted upon by external forces and can be expressed as a change in dimension per unit of original dimension or in the case of shear as a change in angle between two initially perpendicular planes.

Strain amplifier – the ratio of the voltage supplied to the voltage delivered by the Wheatstone Bridge as a result of the imbalance caused by a change in strain gauge resistance. It is equivalent to the strain and is amplified into a suitable voltage or current which can be fed into an analogue, digital indicator or graphic recorder.

Strain rosettes – a combination of three strain gauges set along three axes with respect to each other, usually at 45º or 60º. They are used to determine strain at a point of a surface when the strain directions are unknown.

Stress – is the load applied to a piece of material which tends to cause deformation and is resisted by internal forces created within the material. The intensity of the stress is estimated as the force acting on a unit cross-section area, namely as Newton's per square meter or Pascal's.

Stress amplitude – refers to a stress loading magnitude above and/or below a particular mean stress level.

Stress ratio – is the ratio of minimum to maximum stress levels usually associated with fatigue testing conditions.

Stress raisers – changes in contour or discontinuities in the structure that cause local increases in stress.

Stress relieving – heating to a suitable temperature, holding long enough to reduce residual stresses, then cooling slowly enough to minimise the development of new residual stresses.

S_e – endurance limit.

S_y – yield strength.

S_u – ultimate strength.

U

UTS – is the ultimate tensile strength of the material.

V

Vickers hardness test – a common method of determining the hardness of metals by indenting them with a diamond pyramid under a specified load and measuring the size of the impressions produced.

W

Widmanstätten structure – a mesh-like distribution of a precipitating phase in a solid state transformation which occurs along preferred crystal planes. Usually produced by rapid cooling and when the transforming phase has a large grain size.

Work hardening – the increase in strength and hardness produced by plastic deformation of metals at temperatures below about 0.5 Tm that results from increasing numbers of dislocations and their entanglement and is accompanied by reduction in ductility.

Y

Yield point – the stress at which a substantial amount of plastic deformation takes place under constant or reduced load. This sudden yielding is a characteristic of iron and annealed steels.

Yield stress – the stress at the onset of plastic deformation determined from the yield point or from a defined amount of plastic strain, called the proof stress.

Young's Modulus – is the ratio (E) of the tensile stress (σ) to the tensile strain (e) in a linear elastic material at loads less than the elastic limit of the material.

Z

Zero mean stress – pertains to the fatigue testing of a component under zero pre-strain conditions.

Acknowledgements

I would like to express my sincere gratitude towards the following people. Without their support and understanding this study would not have been possible.

Dr. Sonia Woudberg and family, for their support and encouragement. Their advice and knowledge are truly appreciated.

Prof. Narisscia Botha, Anna Kotzé and Andre du Toit for their support and friendship.

The staff of the mechanical engineering department at NMMU and fellow post-graduate, for guidance and insight into complex problems. A special thanks to the staff of the metallurgy and workshop laboratories for their assistance and time.

The eNtsa staff and researchers for their opinions and guidance.

Magda and Clive Moore for their support and understanding.

Prof. Patrick M^{c}Grath who granted me the opportunity to do this research.

Dr. Annelize Botes, a special thanks for her involvement during my studies as my co-supervisor and for financial support, especially during this study.

I thank you all!

CHAPTER 1 - INTRODUCTION

1.1 Introduction

Laser bending is currently a relatively new application in manufacturing industries about which little is known [1]. Therefore, an opportunity exists to compare laser bending to conventional mechanical-bending processes which will aid the industry in making a more informed choice when confronted with various available manufacturing processes. The aim of this research is to increase the fatigue life of commercially pure titanium (CP Ti) grade 2 in general applications. Initial investigations into the fatigue behaviour of laser-formed components indicate an increase in fatigue life compared to parent material for High Strength Low Alloy (HSLA) sheet metal [1]. Thus, if laser forming or the combination of laser and mechanical forming contributes to the fatigue life of HSLA sheet metal [1], it could mean that a thinner gauge material can be used while still meeting safety requirements. It could also mean that a material of the same size may withstand more cyclic-loading conditions [1].

Generally, when a material is subjected to cyclic loading, progressive and localised damage occurs to the specific material. These loadings, measured in stress values, are less than that of the ultimate tensile strength and could be below the tensile yield strength. In common practice, cyclic loading can be described as repeated loading and unloading of a specific material that could lead to microscopic cracks at the surface. When these cracks develop to a critical size on the surface, sudden failure of a structure can occur. A significant effect on fatigue life is the shape of the related structure which can amplify concentrated stress levels [2, 3].

1.2 Problem statement

Laser forming is considered a relatively new process of forming sheet metal by means of thermal expansion and contraction. Although little is known about the fatigue behaviour of components produced by a laser forming process, it could improve the mechanical behaviour of such components.

This research aims to characterise the fatigue behaviour of formed specimens processed from commercially pure titanium grade 2 sheets.

1.3 Aims & objectives

Aim

The aim of this study is to characterise and compare the fatigue behaviour of laser, mechanically and laser-mechanically formed components (CP Ti grade 2) to that of commercially pure titanium grade 2 sheet parent plate specimens.

Objectives

The objectives of this study are the following:

Objective 1

To ascertain the actual mechanical properties of the parent material, namely the yield strength, ultimate tensile strength and hardness.

Objective 2

To manufacture specimens according to the following three applications (i) mechanical bending (ii) combined laser-mechanical bending and (iii) pure laser bending from parent material. These conditions ensure that each sample is bent

under the same conditions and has approximately the same mean radii of curvature (i.e. 120 mm).

Objective 3

To conduct fatigue testing of parent plate samples as well as those subjected to the three bending applications mentioned in Objective 3 above. Three stress amplitudes will be considered to produce stress-life curves for the above samples under reverse-bending fatigue conditions.

Objective 4

To evaluate and study the fatigue data of all three bending conditions and compare it to the parent material in terms of stress-life behaviour.

Objective 5

To conduct residual stress analysis on the three bending conditions after the bending application. The residual stress analysis of the parent material will also be conducted.

Objective 6

To verify the results against the four standard fatigue models, i.e. Gerber, Soderberg, Morrow and Goodman [9], by incorporating the residual stress values into the models. When a suitable fatigue model is identified, actual fatigue data are to be used to validate the model.

Objective 7

To produce a prototype prediction fatigue curve for all the forming processes.

1.4 Hypothesis

The hypothesis for this research is that the fatigue behaviour of CP Ti grade 2 specimens which have undergone laser forming will show an enhanced fatigue life compared to that of purely mechanically formed specimens.

1.5 Assumptions

The material used is a homogenous, continuous, isotropic continuum that is free from any defects and flaws.

1.6 Delimitations

The only laser used for this investigation is a 5kW CW CO_2 Trumpf laser. American Society for Testing and Materials (ASTM) standards will be used as guidelines for all testing done in this study. The Gosmeta mechanical press Type 25 at Nelson Mandela Metropolitan University (NMMU), Port Elizabeth, will be used to form the mechanically bent samples. Fatigue specimens will be fatigued in an Avery type 3057 fatigue testing machine at a fixed frequency of 24 Hz at NMMU. Only three stress levels will be considered for producing S-N curves due to limited resources.

1.7 Significance of research

This study will add value to NMMU's current research scope on laser forming of titanium and develops a better understanding in the field of fatigue assessment. Knowledge is gained on the behaviour of the material after laser forming which include residual stress analysis, fatigue behaviour, macro analysis, micro analysis, micro hardness and Charpy impact behaviour. Generating a prototype prediction fatigue curve will aid as a tool for the material's fatigue life under this new forming process.

1.8 Research methodology

All three bending methods will shape the parent plate specimens to an approximate radius of 120 mm, as illustrated in Figure 1.2 and Figure 1.3 (p 8) . For the mechanical bending application a tool and die method will be used while the peripheral edges of the specimens will be clamped (45 mm on both sides of the 200 mm specimens) (see Figure 1.2) to simulate stretch bending. Stretch bending is a typical application used in the industry when forming objects or products. The full laser bending method will utilize a 5 kW CO_2 Continuous Wave Trumpf laser to bend the two-dimensional titanium grade 2 plates. For the laser-mechanical combination method the 5 kW CO_2 CW Trumpf laser will curve the titanium grade 2 material to an approximate radius of 240 mm. The final bend will be established by means of the mechanical press to a radius of about 120 mm. This laser-mechanical method will be used to obtain a midpoint between laser and mechanically forming specimens. This combined process may lead to cost reduction and an increase in life-cycles.

The laser parameters which were chosen from the literature, includes: (i) Laser beam diameter (ii) Number of scans per location (iii) Laser power (iv) Interval spacing and (v) Scanning velocity [1].

Table 1.1 below gives the parameter settings used in the laser process.

Table 1.1: Laser settings [1]

Laser power	Beam diameter	Interval spacing	Scanning velocity	Number of scan/location
1.5 kW	12 mm	6 mm	1.2 m/min	6

Fatigue testing will be conducted according to ASTM E468-82 specifications. A minimum of five specimens are required to be fatigue tested at a single stress level. S-N (A plot of stress, S, against the number of cycles to failure, N) curves will be produced to provide information about the behaviour of these specimens. The specimens will be fatigued on a "fully-reversed" based strain-cycle scenario, namely for which R = -1, as illustrated in Figure 1.1 (p 7). The construction of these S-N curves will contribute to the understanding of the manufactured components' fatigue behaviour. The increase or decrease in fatigue life will be recorded and plotted on a S-N curve for each of the forming processes namely:

(i) Purely mechanical (tool & die method)

(ii) Combination of laser and mechanical

(iii) Pure laser

(iv) Parent material specimens (CP Ti grade 2 sheet plate)

These S-N curves will be related to the Gerber, Soderberg, Morrow and Goodman [4] fatigue models to characterise the fatigue behaviour of the material and to identify if any of the fatigue models can be used as a prediction model for this type of material. The fatigue specimens, which will be subjected to full-reverse-bending conditions, will be tested to failure to establish an S-N curve or until a maximum established limit has been reached. Figure 1.1 illustrates the strain amplitude of a fully reversed scenario in one cycle.

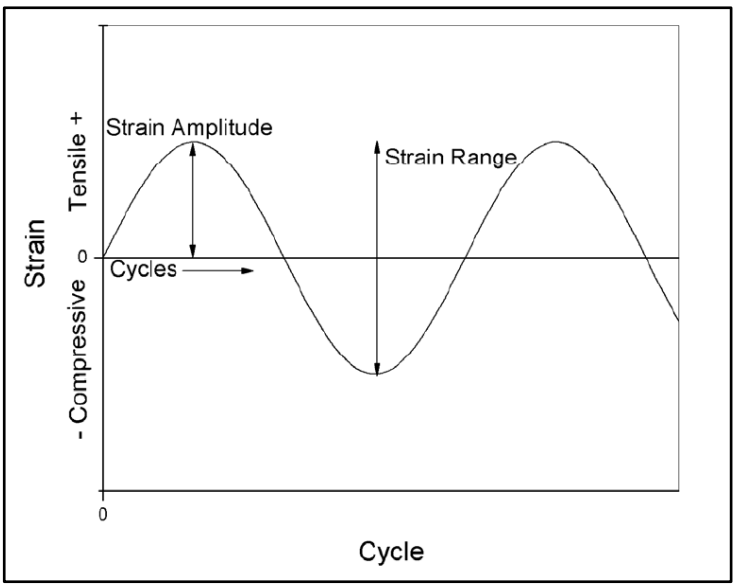

Figure 1.1 : Cyclic curve representing a fully reversed-strain cycle with sinusoidal wave form [35]

Figure 1.2 and Figure 1.3 (p 8) illustrates the parent material sample and the end product which is bent to a radius of curvature of approximately 120 mm.

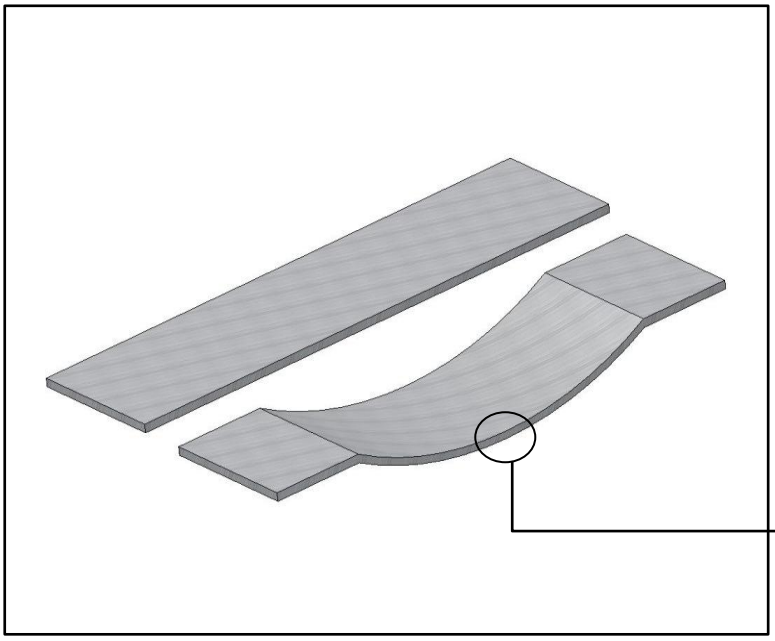

Figure 1.2 : Illustration of a patent plate and bent sample

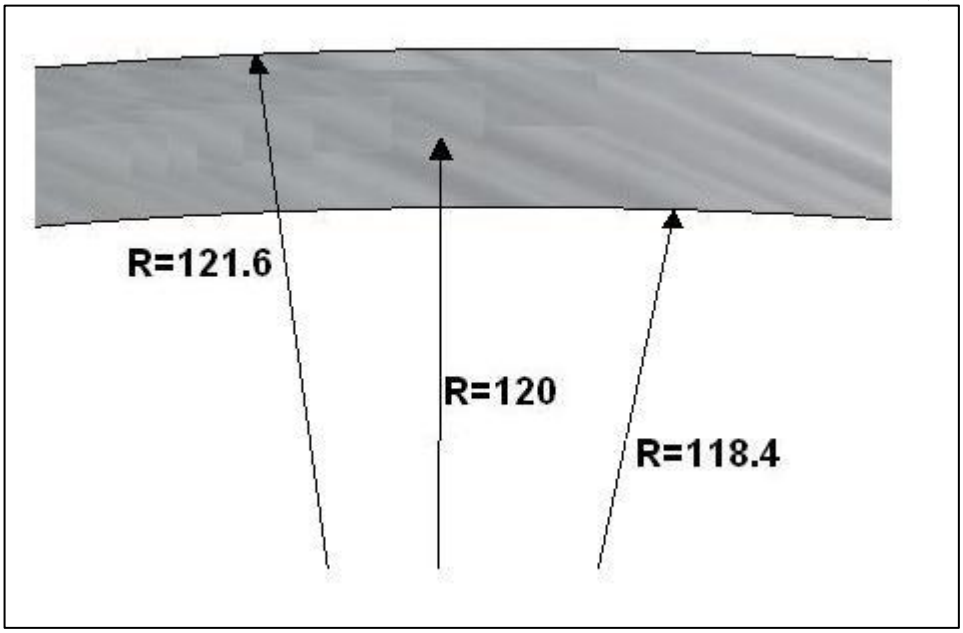

Figure 1.3 : Curvature dimensions of formed specimens (in millimeters)

Tensile testing will be conducted on the parent plate material to verify the supplier's specifications according to ASTM standard, E8M-01. ASTM E18-02 standards will be used for the micro-Vickers hardness tests. The parent plate material as well as the three bent method samples will be micro-hardness tested using a 300 g force. For the residual stress analysis, the ASTM E837-01 standard will be used. Therefore, all microstructures will be analysed with an optical microscope (OM) and scanning electron microscope (SEM) for the parent plate and three bending-method samples. Attention will be given to the samples that will undergo the laser formed method to identify if any structural changes have developed within the material. Table 1.2 illustrates the amount of test specimens needed for the different bending methods.

Table 1.2: Test matrix*

RESIDUAL STRESS				
	Parent plate 3 Samples	Mechanical 3 Samples	Laser-Mech. 3 Samples	Laser 3 Samples
FATIGUE TESTING				
	Parent plate	Mechanical	Laser-Mech.	Laser
Load 1	8 Samples	8 Samples	8 Samples	8 Samples
Load 2	8 Samples	8 Samples	8 Samples	8 Samples
Load 3	8 Samples	8 Samples	8 Samples	8 Samples
MACRO/MICRO ANALYSIS				
	Parent plate 1 Sample	Mechanical 1 Sample	Laser-Mech. 1 Sample	Laser 1 Sample
MICRO HARDNESS				
	Parent plate 1 Sample	Mechanically 1 Sample	Laser-Mech. 1 Sample	Laser 1 Sample

* Position of measurement will be discussed in detail in Chapter 3, dealing with the experimental setup

1.9 Project flow diagram

This project flow diagram presented below provides an overall layout of the present study in order to aid in the understanding of the research approach followed.

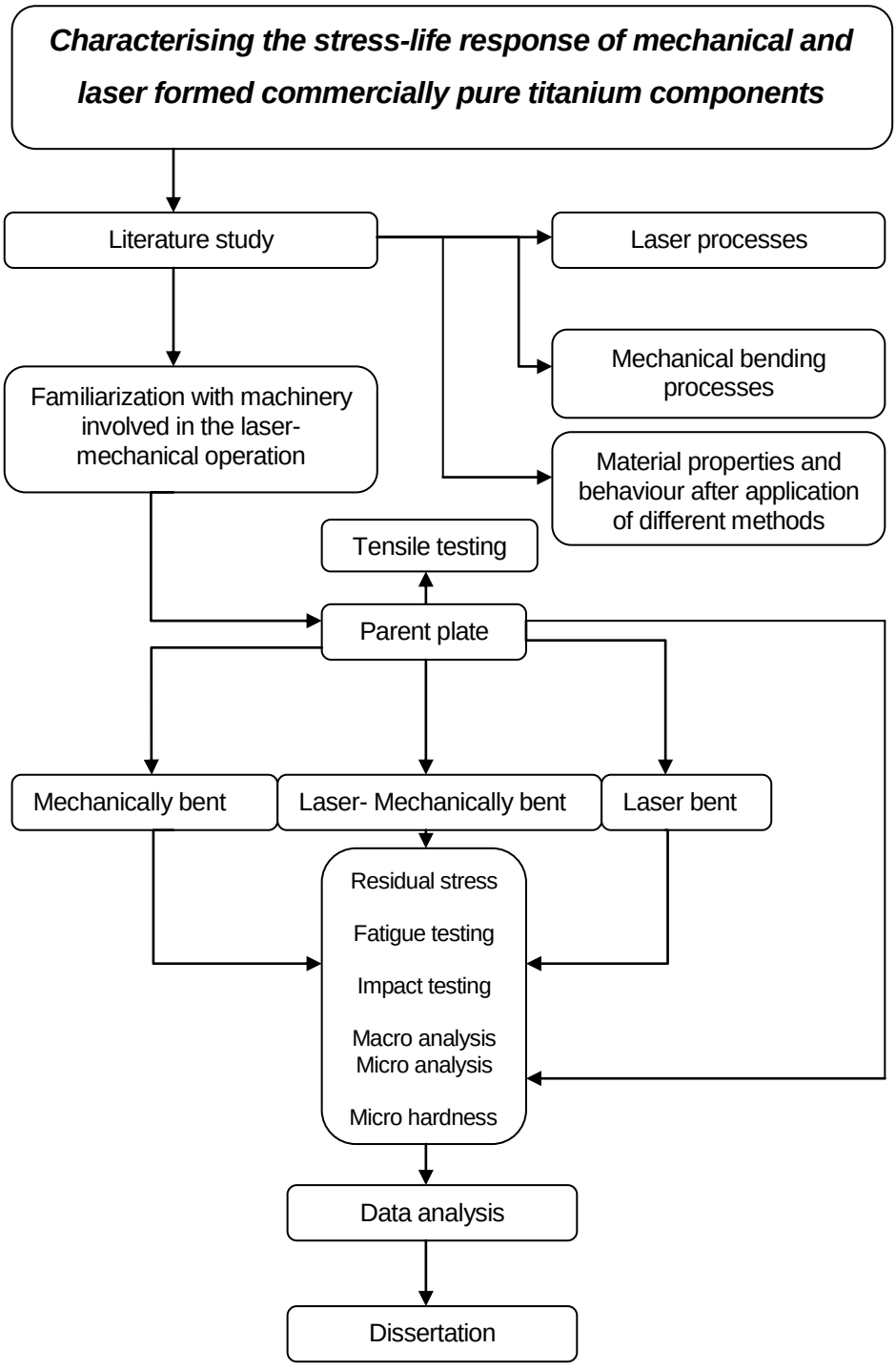

In the next section the layout of the thesis is presented in paragraph from with respect to the content of each chapter.

1.10 Layout of Dissertation

In this chapter the introduction, objectives and research methodology were discussed to understand the impact and approach of this study. Chapter 2 contains a literature study of the material and all the forming processes as well as the fatigue model dealing with fatigue life. In Chapter 3 the experimental setup of all the forming processes and testing methods are discussed. In Chapter 4 a detailed analysis is presented of the microstructure, microharness, Charpy impact testing, residual stress, fatigue testing and crack morphology of CP Ti grade 2 subjected to laser bending, mechanical bending and laser-mechanical bending as well as for the parent plate. Theoretical models for predicting fatigue life (i.e. the Gerber, Soderberg, Goodman and Morrow models) are discussed and utilized to produce a prototype prediction for the fatigue life of CP Ti grade 2 over a wide range of cycles to failure. Chapter 5 contains a summary of the main conclusions drawn from this study. Three tables are also presented which summarizes the results obtained in Chapter 4, followed by suggestions for future work.

CHAPTER 2 – LITERATURE STUDY

2.1 Introduction – fatigue

Fatigue was first documented in the early 1800s when several investigations in Europe reported cracking when components were subjected to repeated loading in the building and railway industry [5]. As time progressed and machinery became more widely used, an increase in the expansion of metal usage resulted in an increase in the failure of components subjected to repeated loading. In the mid 1800s August Wöhler [5] proposed a method to mitigate, and in some cases eliminate, failure of components which were subjected to repeated loading. This proposed method resulted in the stress-life graph shown in Figure 2.1 (p 13) and the test model approach to fatigue design. The graph represents the magnitude of the cyclic stress in MPa against the logarthmic scale of cycles to failure. This design method was undertaken in the mid-to late 1800s and is still used today [5]. Since the 1900s, not a great deal was known about the physical behaviour of materials as a result of fatigue, nevertheless, an increase in understanding of this phenomenon is still underway which aids in developing engineering materials and leads to improvement in design.

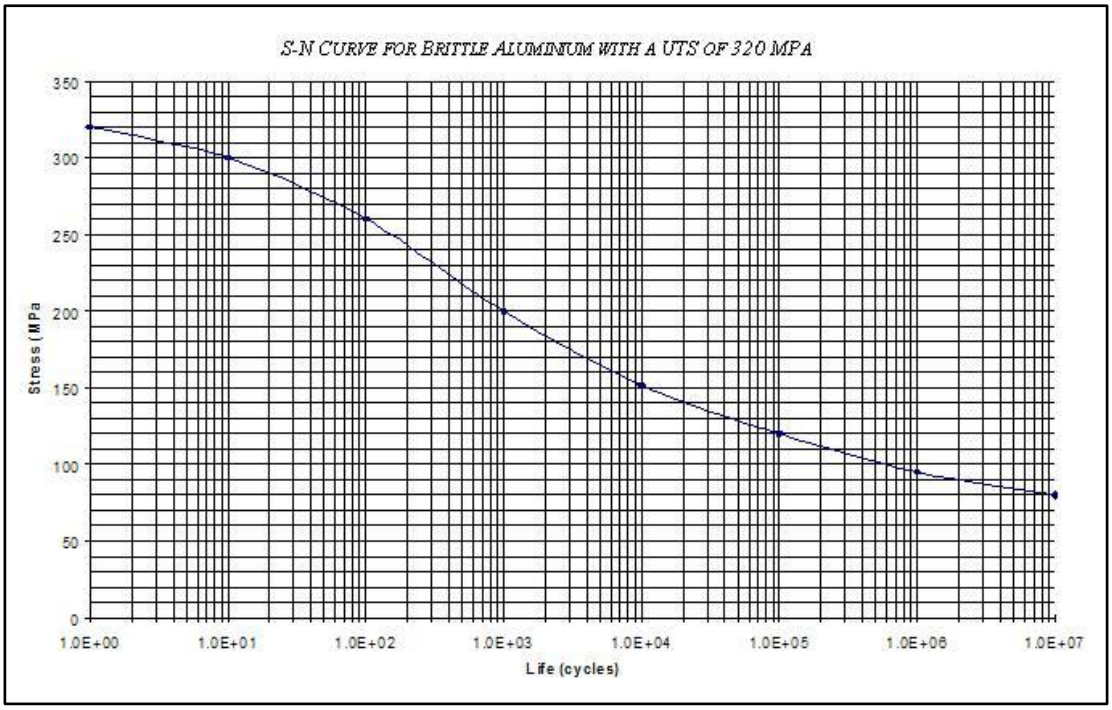

Figure 2.1 : A typical S-N curve, also known as a Wöhler curve, illustrating the fatigue life of aluminium [36]

2.2 Factors influencing fatigue life

Fatigue damage can be classified in several different stages in engineering components. Defects may nucleate until finally catastrophic fracture occurs. This fatigue damage can be classified as follows [6] :

- Sub-structural and microstructural changes which cause nucleation which, as a result, could cause permanent damage.
- Formation of microscopic cracks.
- Growth and coalescence of microscopic flaws to form 'dominant' cracks, which may eventually lead to catastrophic failure. (There is differentiated between crack initiation and crack propagation.)
- Stable propagation of the dominant macro-crack.
- Structural instability or complete failure.

Strong influences such as mechanical, microstructural, residual stress and environmental factors contribute an important role to the nucleation of micro defects and the rate at which principal fatigue cracks advances. Design criteria often reflect on the crack initiation and crack propagation stages leading to fatigue failure [6].

2.3 Fatigue approaches to total life

Characterization of total fatigue life is a classical approach to fatigue design in terms of the cyclic stress loading, strain loading, mean stress and environment. This method accounts for the controlled amplitudes of cyclic stresses or strains which are recorded by means of the number of stress or strain cycles necessary to induce fatigue failure [6]. Therefore it can be seen that the total fatigue life approach incorporates the number of cycles that will initiate a dominant crack and to propagate until catastrophic failure occurs. Factors or adjusted values are available to account for the effects of mean stress, stress concentration, environments, multi-axial stresses and variable amplitude stress variation in the prediction of total fatigue life. Crack initiation contributes a major role to the fatigue life when classical methods like stress-based and strain-based methods are used, and as a result, the component will be designed to resist fatigue crack initiation [6]. During high cycle fatigue (stress based approach) or low stress fatigue conditions, the material is likely to deform elastically. However, stresses associated with low cycle fatigue (strain based approach) or high stress fatigue are high enough to cause considerable plastic deformation until catastrophic failure occurs [6]. Figure 2.2 (p 15) illustrates the terminology associated with

constant amplitude cycling. Furthermore, [4] indicate that the dividing line between low and high cycle fatigue depends on the material and grain structure, but falls in the range 10^3 to 10^4 cycles [6].

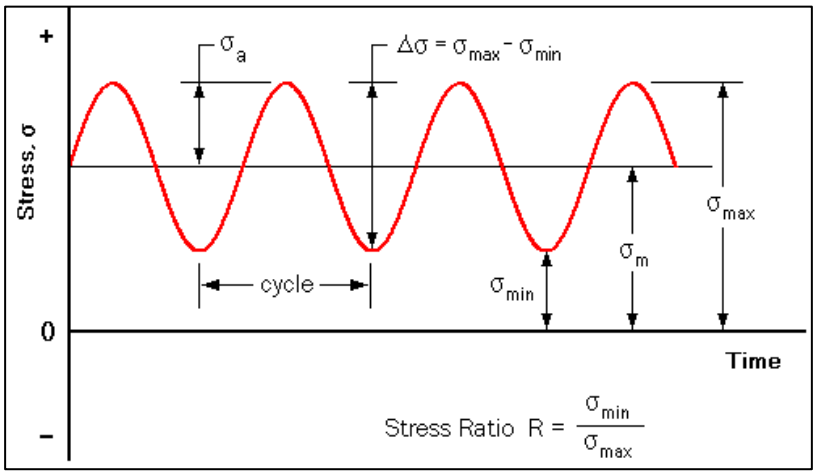

Figure 2.2 : Classification of stress parameters affecting fatigue life [7]

The following terms and relationships are generally used when discussing mean and alternating stress:

Stress range: $\Delta\sigma = \sigma_{max} - \sigma_{min}$ (2. 1)

Stress amplitude: $\sigma_a = \frac{\sigma_{max} - \sigma_{min}}{2}$ (2. 2)

Mean stress: $\sigma_m = \frac{\sigma_{max} + \sigma_{min}}{2}$ (2. 3)

Stress ratio: $R = \frac{\sigma_{min}}{\sigma_{max}}$ (2. 4)

Amplitude ratio: $A = \frac{\sigma_a}{\sigma_m}$ (2. 5)

The R and A values corresponding to several common loading conditions are as follows:

Fully reversed: R= -1 ; A=∞ (2. 6)

Zero to maximum: R=0 ; A=1 (2. 7)

Zero to minimum: R=∞ ; A= -1 (2. 8)

In order to generate a Haigh diagram (Figure 2.3) or master diagram (Figure 2.4) for an existing material, can become costly and time consuming. Therefore numerous empirical relationships have been developed to generate the line defining the infinite life design region [5].

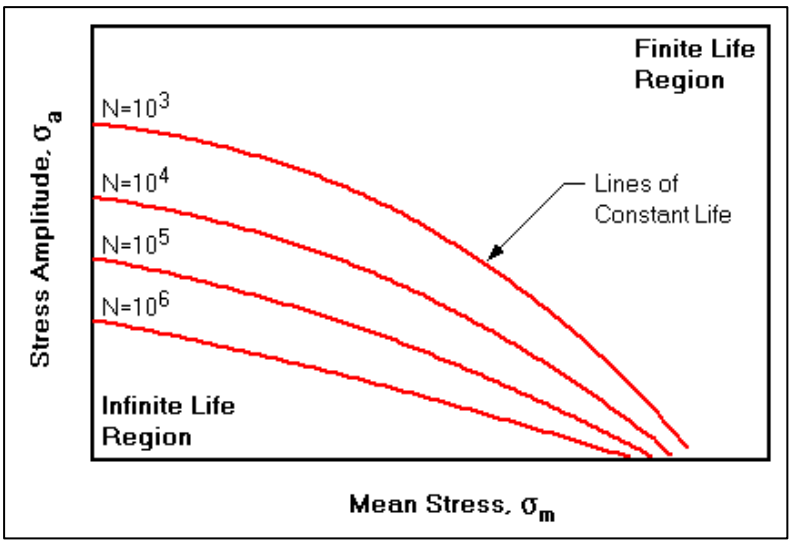

Figure 2.3 : Haigh diagram [7]

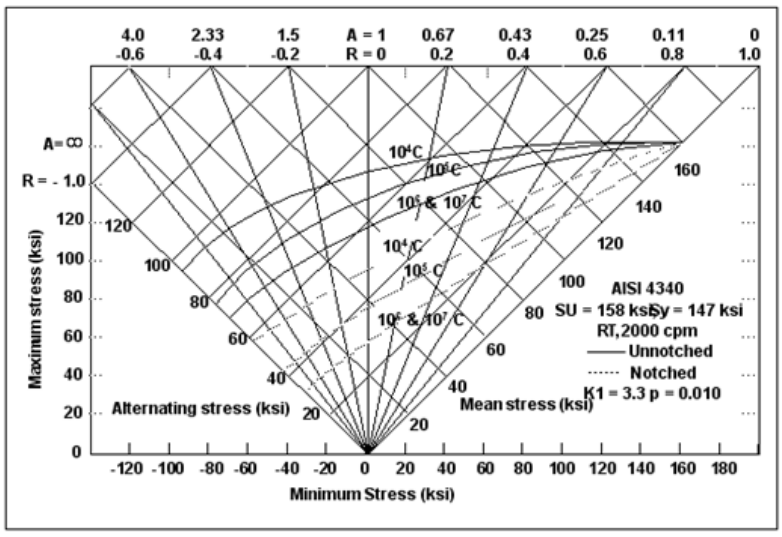

Figure 2.4 : Master diagram for AISI 4340 steel [8]

2.4 Stress life approach

The stress life approach employs a smooth test specimen which is typically machined or cut out to provide a disposable cylindrical or hour-glass specimen that will be fatigued in plane bending, rotating bending, uniaxail compression-tension or tension-tension cyclic loading. For fully reversed bending the stress amplitude should be constant and is plotted against the number of fatigue cycles to catastrophic failure. In addition, for this method to be efficient, the fatigue test must be primarily in the elastic region. Mild steel and other materials which strengthen by strain hardening, exhibits a plateau in the stress life curve, characteristically at about 10^6 fatigue cycles. Amplitudes below this curve of 10^6 cycles is known as the fatigue limit or endurance limit [6]. Titanium and its alloys behave like steel which exhibits a true endurance limit in the range of 10^6 to 10^7 cycles with the endurance limit ranging between 0.45 to 0.65 times the ultimate tensile strength. For mild steel the endurance limit is between 0.35 and 0.5 of the ultimate tensile strength [4]. Materials which do not undergo strain hardening, an endurance limit may be determined or calculated for the desired cycles to failure. In general, specimens to be subjected to fatigue are designed to support fatigue cycles of up to 10^7 cycles [6].

2.5 Strain life approach

Characterizing the fatigue life, when using the strain life approach, requires the material to be deformed predominantly plastically i.e. above the yield point. It is in this regime that the ductility controls the fatigue life of the material. This approach can be implemented in industry where rotating machinery are subjected to alternating stresses, pressure vessels are subjected to periodic

loading and unloading or in aircraft fuselage which is subjected to pressurization and depressurization. The experimental approach was derived and proposed by Coffin and Manson (1954) [6] when they obtained a linear relationship resulted (when plotting the plastic strain amplitude to the logarithm of cycles to failure when fully reversed bending is employed). Furthermore, the approach was derived in such a manner that it is based on the sum of the elastic and plastic components when subjected to strain loading. In addition, the literature indicates that tensile mean stress affects fatigue life negatively [6].

2.6 Fatigue models

These methods or models make use of a range of curves to connect the endurance limit (S_e) on the alternating stress (σ_a) axis, to either the yield strength (S_y), the ultimate strength (S_u) or true fracture stress (σ_f) on the mean stress axis [4]. Therefore these curves or models define the boundary of combined mean amplitude for anticipated safe line response. The Goodman, Morrow, and Soderberg relations are linear and the Gerber model is parabolic. These relationships are frequently used and are shown in Figure 2.5.

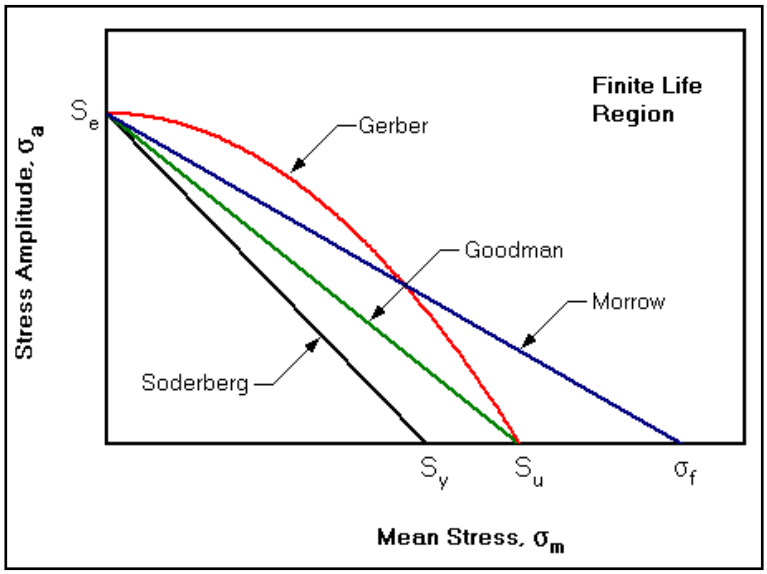

Figure 2.5 : Comparison of mean stress equation of Soderberg, Goodman, Morrow and Gerber [7]

2.6.1 Gerber model

The Gerber model [4] treats negative and positive mean stresses the same and does not involve any correction for negative mean stresses. The Gerber theory is normally a good choice for ductile materials. The predictive equation of the Gerber model is given by,

$$\frac{\sigma_a}{S_n} + \left(\frac{\sigma_m}{S_u}\right)^2 = 1 \quad . \qquad (2.9)$$

2.6.2 Goodman model

The Goodman model [4] does also not involve any correction for negative mean stresses. This is because a compressive mean stress can retard fatigue-crack growth. The Goodman model is normally a good choice for ductile to brittle materials and is given by [4] ,

$$\frac{\sigma_a}{S_n} + \frac{\sigma_m}{S_u} = 1 \quad . \qquad (2.10)$$

2.6.3 Morrow model

The Morrow model [4] exhibits less sensitivity to mean stress when the fracture stress is close to or greater than the ultimate strength. The Morrow model is given by,

$$\frac{\sigma_a}{S_n} + \frac{\sigma_m}{\sigma_f} = 1 \quad . \qquad (2.11)$$

2.6.4 Soderberg model

The Soderberg model [4] does also not involve any correction for negative stresses. The reason is that although a compressive mean stress can slow down fatigue-crack growth, ignoring the negative mean stress is usually a more conservative means of calculation. The predictive equation of the Soderberg model is given by,

$$\frac{\sigma_a}{S_n} + \frac{\sigma_m}{S_y} = 1 \quad . \qquad (2.12)$$

2.7 Direct factors influencing CP Ti fatigue life

Juvinall , Marshek, Boyer and Radonovich [9 -11] indicate that titanium exhibits an endurance limit in the range of 10^6 to 10^7 cycles at loadings between 0.45 and 0.65 times the tensile strength. However, literature also indicates (e.g Juvinall [9]) that bending is the most detrimental process for fatigue whereas torsion is the least detrimental and this can be demonstrated by Figure 2.6 (p 22). Surface finishing also plays an important role when considering fatigue and this can be seen in Figure 2.7 (p 22) which illustrates the relationship between the surface factor (C_s) and tensile strength when subjected to different finishing affects. According to literature (e.g. Boyer [10]), when subjecting CP Ti grade 2 (annealed condition) to torsion fatigue it will achieve 10^4 cycles when a load of approximately the same value as the yield strength (352 MPa) is applied. When the load is decreased to approximately 280 MPa, 10^7 cycles is plausible. However, upon examining Figure 2.8 (p 23) it is evident that the S-N curve for CP Ti exhibits a distinctive flattening at approximately 10^5 cycles. Therefore a steeper decrease in fatigue life is observed between 10^4 and 10^5 cycles as opposed to the range 10^5 to 10^7 cycles. Radonovich [11] also encountered this phenomena, whereby the transition from high cycle fatigue (HCF) to low cycle fatigue (LCF) differ in gradient, as shown in Figure 2.10 (p 24). The method of Juvinall [9] will be used to determine the approximate load settings for this study. However, this method for determining the fatigue limit is an estimation model which deals with a broad spectrum of conditions as mentioned above. Secondly this method can be adopted for a broad variety of materials such as aluminium, steels, titanium, etc. despite its microstructure or residual stress conditions.

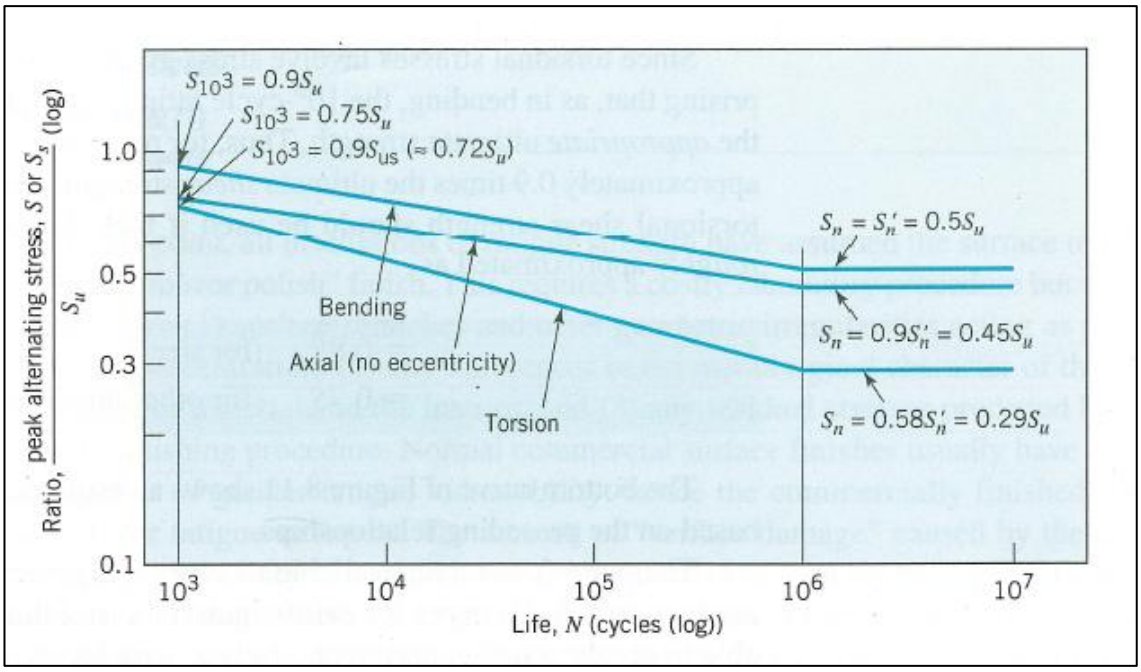

Figure 2.6 : Generalized S-N curve for steel [9]

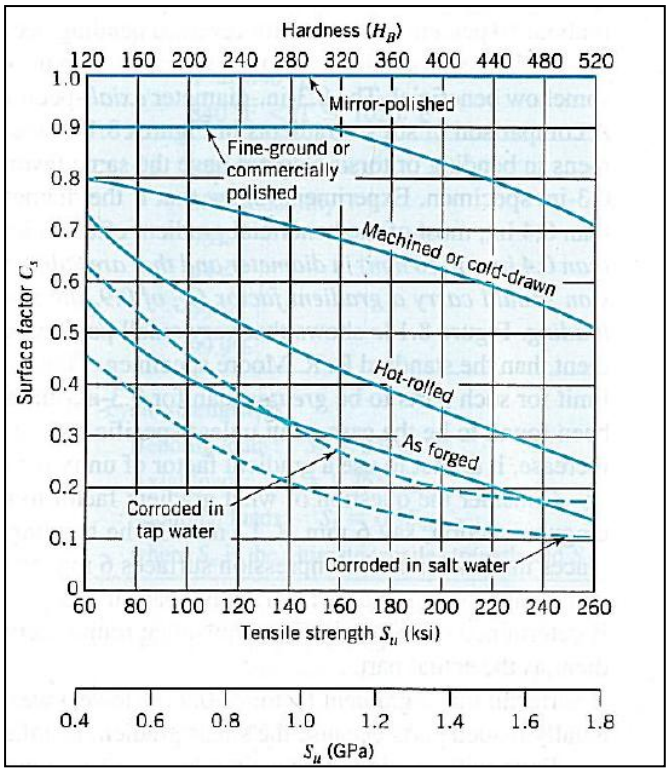

Figure 2.7 : Illustrating the relationship between the surface factor and tensile strength [9]

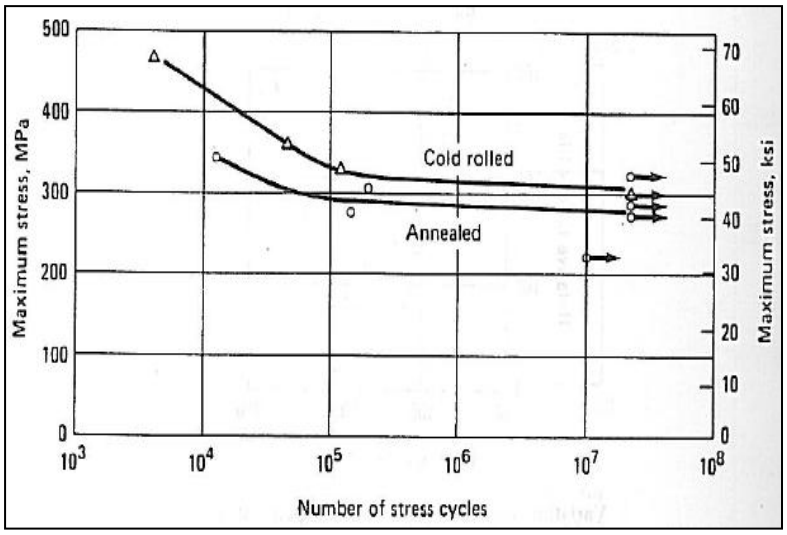

Figure 2.8 : S-N curve of CP Ti [10]

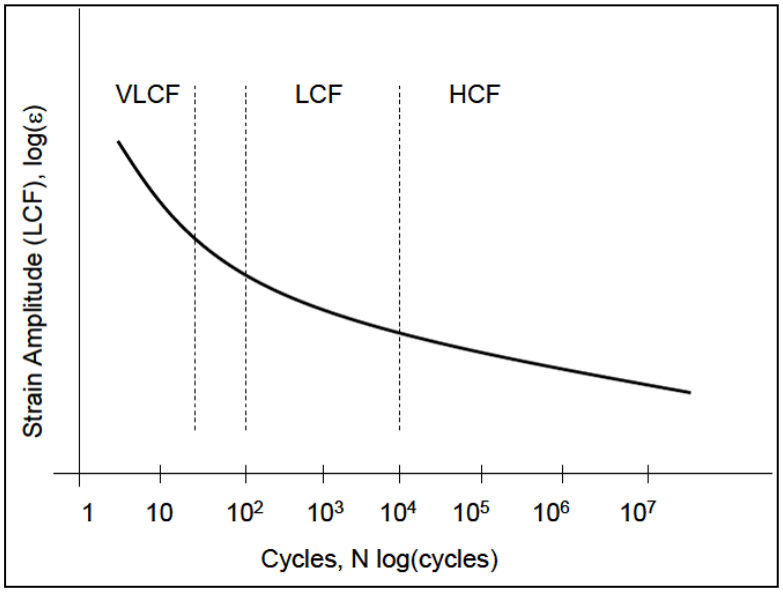

Figure 2.9 : Graphical depiction of the three types of fatigue scenarios [11]

2.7.1 Influence of microstructure on fatigue life

Grain size plays a dominant role in unalloyed titanium. This can be seen in Figure 2.10 (p 24) where a grain size of 110 µm is defined as very coarse and a fine grain is defined as 6 µm. When the grain size is reduced from 110 µm to 6 µm an improvement of 30% is seen in the 10^7 range. Therefore, high cycle

fatigue depends on the interstitial content in addition to the tensile yield strength and the ultimate tensile strength.

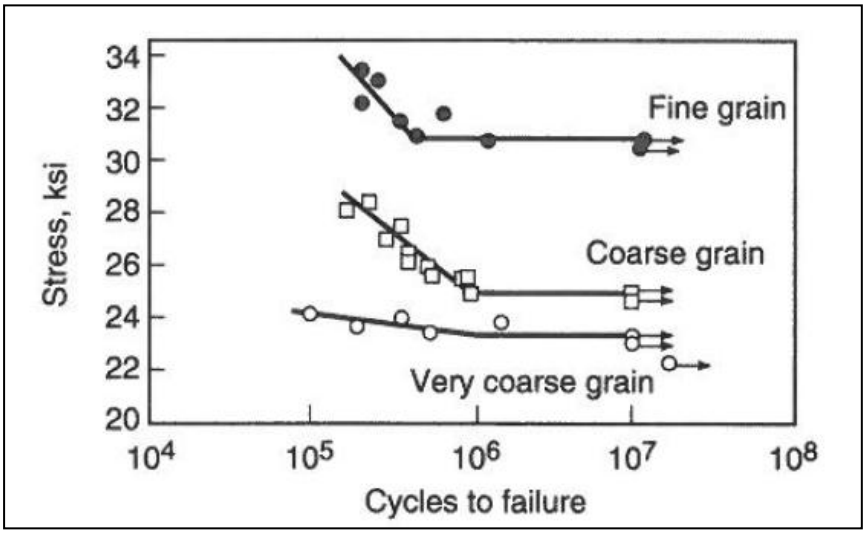

Figure 2.10 : Grain size vs cycles to failure [12]

2.8 Mechanical hot and cold forming

The process of forming titanium is more complicated than that of ordinary steels and aluminium due to its less predictable forming characteristics, however, certain limitations are recognized within industry. An established guideline for hot and cold forming is available to successfully shape complex parts (three dimensional forming) [12]. Titanium and stainless steel exhibit similar characteristics during forming processes due to their high degree of springback and strain rate sensitivity. Therefore titanium must be extensively over formed or, as is done more frequently in industry, hot sized after being cold formed. However, when the springback effect needs to be reduced, to gain the advantage of increased ductility, the parts are commonly hot formed or cold pre-formed and then hot sizing is applied [12]. Figure 2.11 (p 25) illustrates graphically the effect of springback. Other characteristics adversely affecting the formability of titanium alloys include:

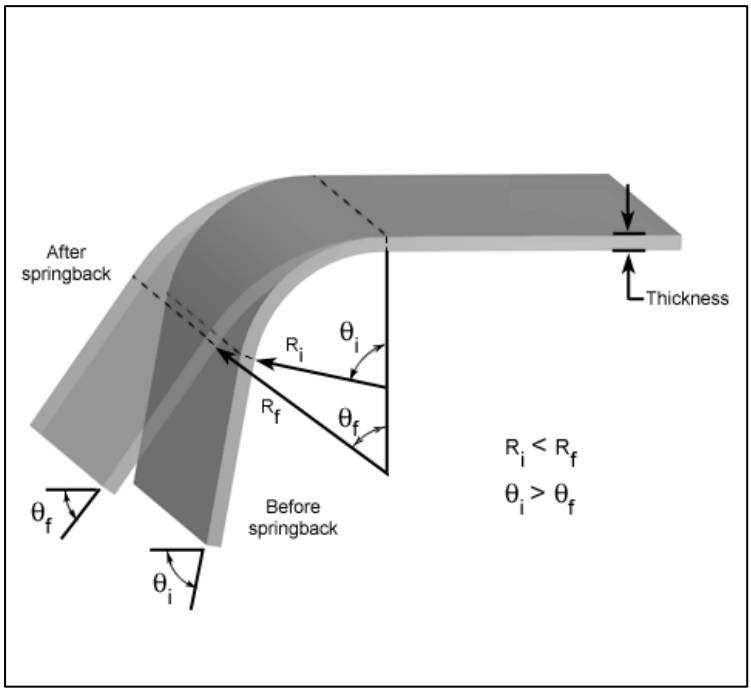

Figure 2.11 : Springback effect [13] (R_i = Radius initially, R_f = Radius final, θ_i = Angle initially, θ_f = Angle final)

- Notch sensitivity, which may cause cracking and tearing, especially in cold forming
- Galling (which is more severe with titanium than with stainless steel)
- Relatively poor ability to shrink
- Potential embrittlement from overheating and from absorption of gasses (mainly oxygen)
- Limited workability
- Tendency towards non-uniformity in sheets

Titanium sheets and plates undergo strain hardening when cold formed, although cold forming introduces a higher yield strength, but causes a slight drop in ductility, whereas hot forming has a minor influence on the latter properties. Hot forming temperatures for CP Ti grade 2 range between 480ºC and 595ºC.

When exposed to the atmosphere, titanium tends to absorb oxygen and nitrogen which forms an interstitial layer called “alpha case”. “Alpha case” is detrimental because of the brittle nature of the oxygen enriched alpha structure. All pure titanium and titanium alloys are susceptible to the Bauschinger effect [12]. This occurs when the compressive yield strength drops in one loading direction but increases in tensile strength in another direction due to strain hardening. The Bauschinger effect is mostly observed at room temperature when plastic deformation (1 - 5% tensile elongation) introduces a substantial loss in compressive yield strength despite the initial heat treatment. On the other hand, full thermal stress relieving completely relieves the Bauschinger effect [2] [12].

2.8.1 Deep drawing

General guidelines for titanium, when applied to deep drawing, are: 1) lubrication and size of tool, 2) use of a dedicated - double action draw press, 3) draw radii depends on thickness of material and should not be less than five times the thickness, 4) the work piece should be clean and the edges must be smooth and 5) an overlay can be used to prevent wrinkles. The drawing must be completed at elevated temperatures, but should not exceed 675ºC. However, high temperature deep drawing of titanium alloys has been largely replaced by the superplastic forming process [2].

Figure 2.12 and Figure 2.13 (p 27) show graphically the principles of deep drawing.

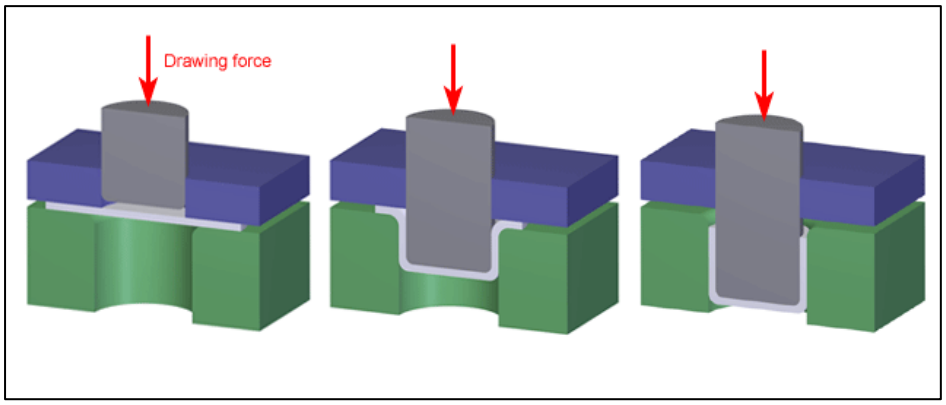

Figure 2.12 : Illustration of a deep drawing sequence [7]

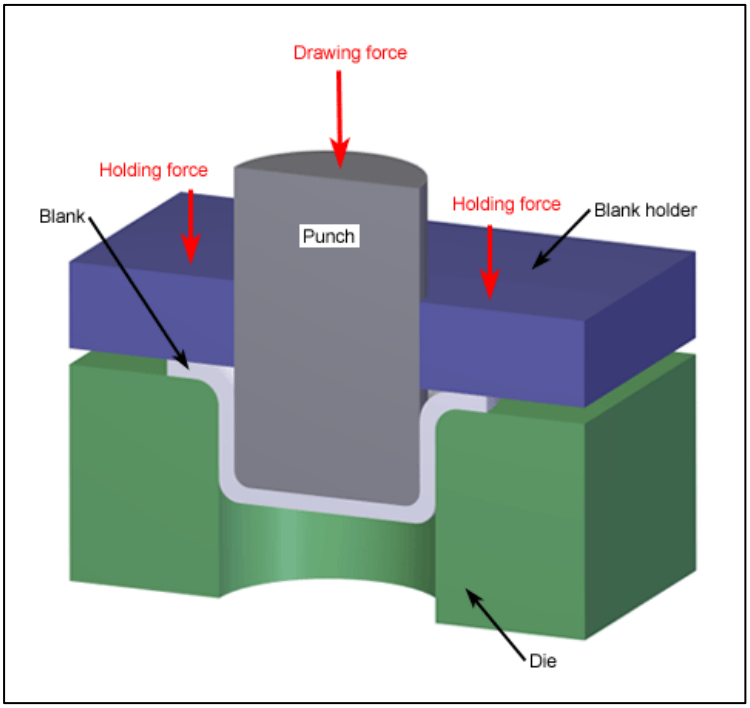

Figure 2.13 : Illustration of deep drawing [7]

2.8.2 Press brake forming

Titanium and titanium alloys can be cold formed by press braking if the bend radii are large enough. However, when the radius is significantly small it can lead to cracking. Air bending is relatively straightforward due to the ram stroke that determines the bend angle, as shown in Figure 2.14 (p 28). The effect of tool adjustment is minimal; only the tool width and the die span can have a significant

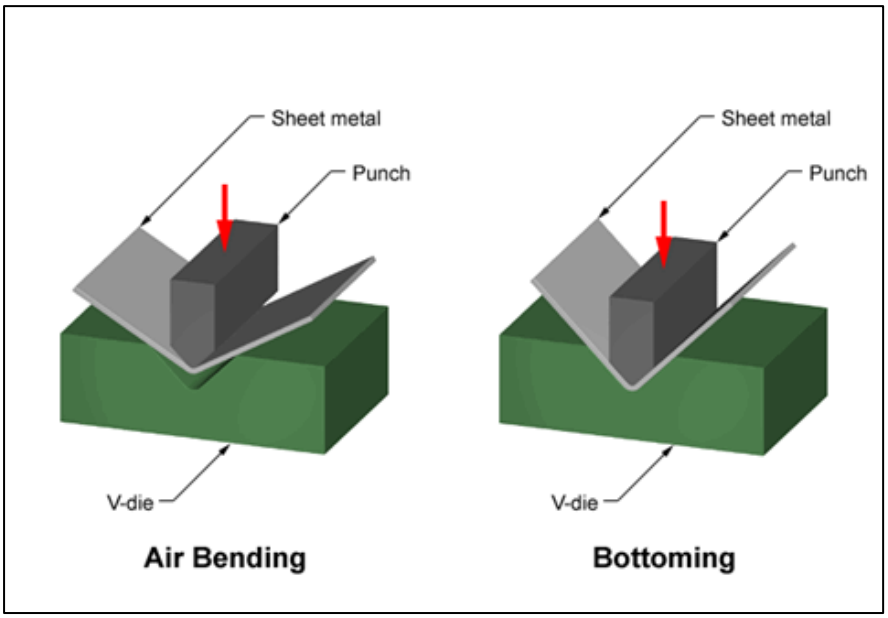

Figure 2.14 : Air bending (forming) and bottoming forming [7]

influence, although the latter two parameters affect the formability of bent specimens and is determined by the tool radius and metal thickness. Springback is somewhat elevated in press brake forming although it depends on the ratio of tool radius to stock thickness and forming temperature. Figure 2.15 shows the components of the press brake machine [2].

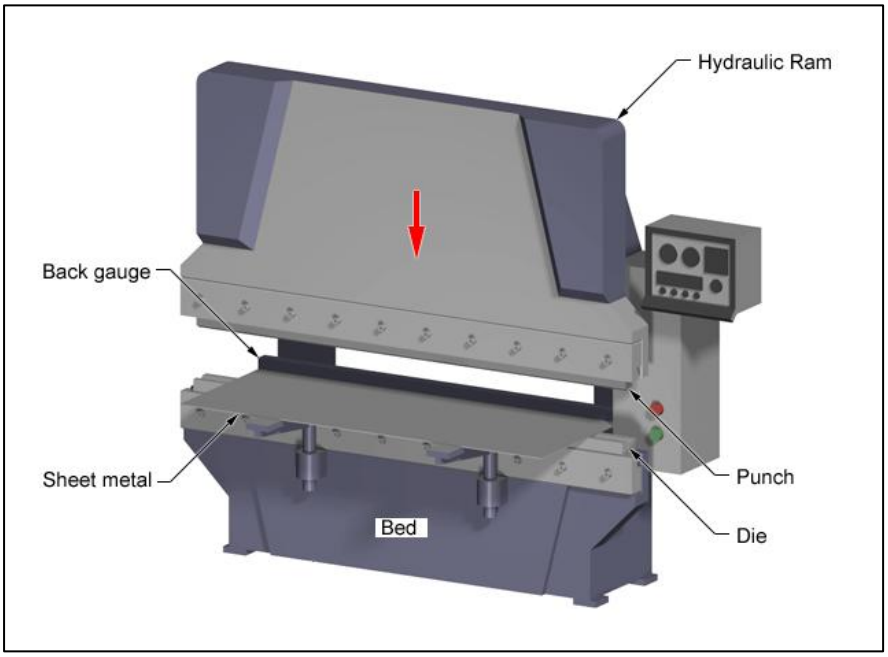

Figure 2.15 : Illustration of press brake [7]

2.8.3 Three roll forming

Three roll forming is an economical method to form titanium and titanium alloys with sheet flatness not exceeding 0.15 mm for every 50 mm in length. Common industrial applications for three roll forming are aircraft skins, cylinders, parts of cylinders etc. The upper roller can be adjusted vertically to control the radius of the bend, but premature failure can occur when the radius is reduced rapidly. The material is subjected to work hardening with each pass through the rollers. Figure 2.16 demonstrates the three roll forming process [2].

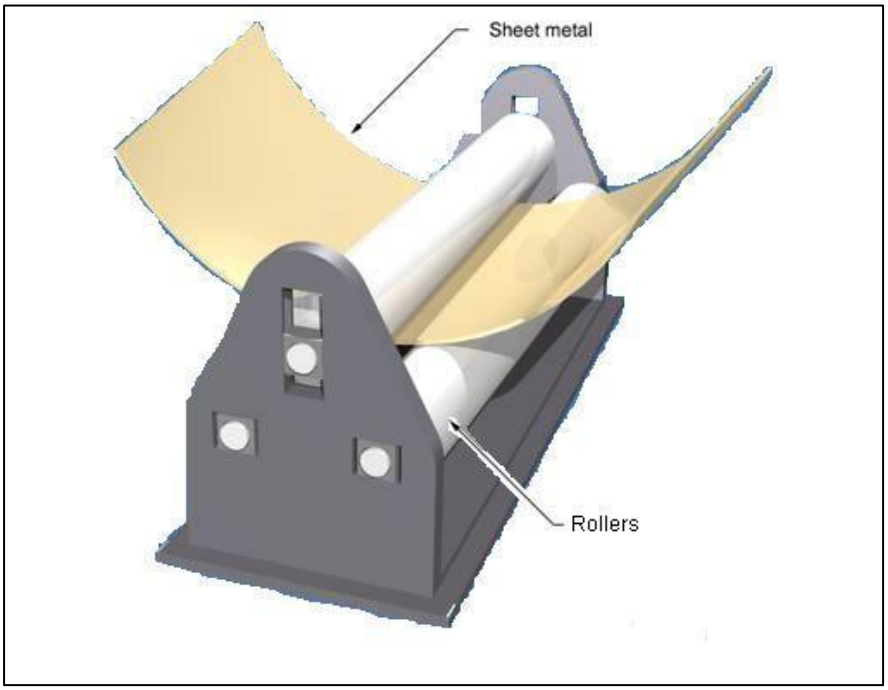

Figure 2.16 : Illustration of the three roll forming process [7]

2.8.4 Stretch forming

Tooling is subjected to high clamping forces when titanium and titanium alloys are stretch formed. This is caused by eliminating slipping and tearing of the parent plate when the drawing force is applied. Forming should be done at slow increments (200 mm/min) because titanium exhibits irregular incremental stretching when under tension loading. Deformation mainly occurs through bending at the fulcrum point of the die surface. Therefore compression buckling is avoided by implementing a sufficient amount of tensile load to produce about 1% elongation in the inner fibres, although it can be expected that the outer fibres will elongate more, depending on the curvature. However, it should be noted that over forming should be limited to the amount that it can effectively remove by hot sizing. Figure 2.17 shows the stretch forming process [2].

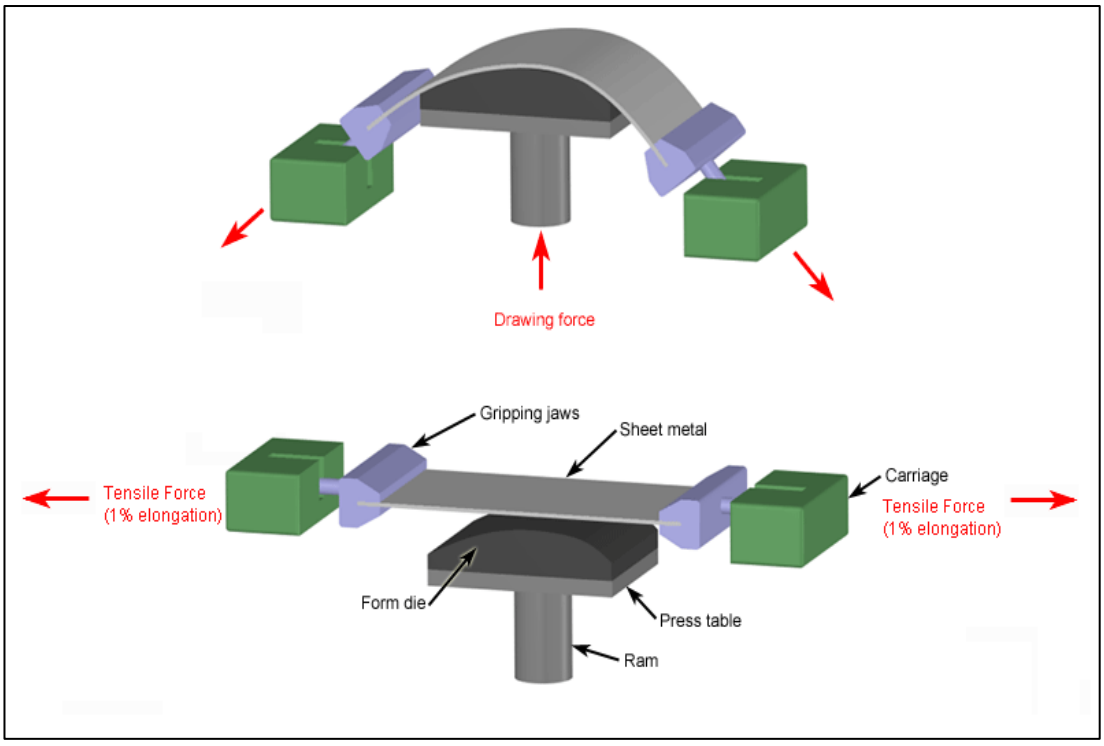

Figure 2.17 : Illustration of stretch forming with tensile forces [7]

2.9 Laser applications

Materials processed by lasers cover basic operations such as cutting, drilling, welding, scribing, trimming, annealing and hardening. Several types of lasers can be used when processing materials and the most common industrial lasers are: the ruby laser, Nd-YAG laser, Nd-glass laser, CO_2 laser, fibre laser and the argon laser. For the majority of processing work, lasers serve as a source of intense thermal energy. For the energy to be transferred effectively close compatibility between the material and laser beam must exist. This compatibility property depends mainly on the wavelength of the laser beam [14]. A Nd-YAG laser with a wavelength of 1.064 µm, corresponds to a CO_2 laser with a wavelength of 1/10 (10.64 µm). As the beam's wavelength decreases, the absorptivity of the metal surface increases [15].

2.10 Laser forming technique

Lasers have the ability to accurately focus their energy on a specific area on the material to produce characteristic thermal compressive strain or tensile stresses. These thermal stresses are due to the irradiation of the laser beam that causes the material to bend or buckle. The stresses are greater than the yield strength but less than the fracture strength of the material. To understand this forming process, one has to examine the process as displayed graphically in Figure 2.18 and Figure 2.19 (p 32).

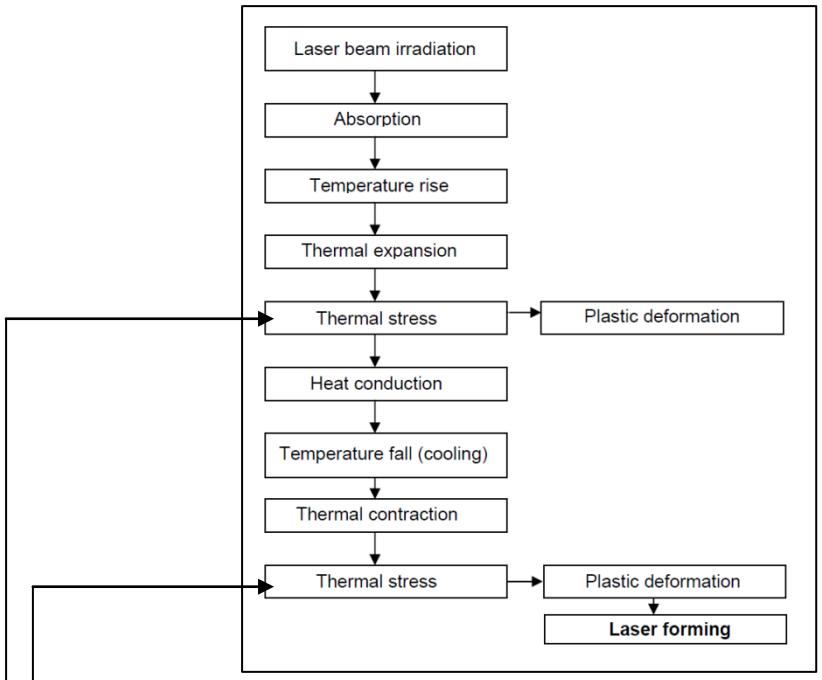

Figure 2.18 : Flow chart of a laser forming process [16]

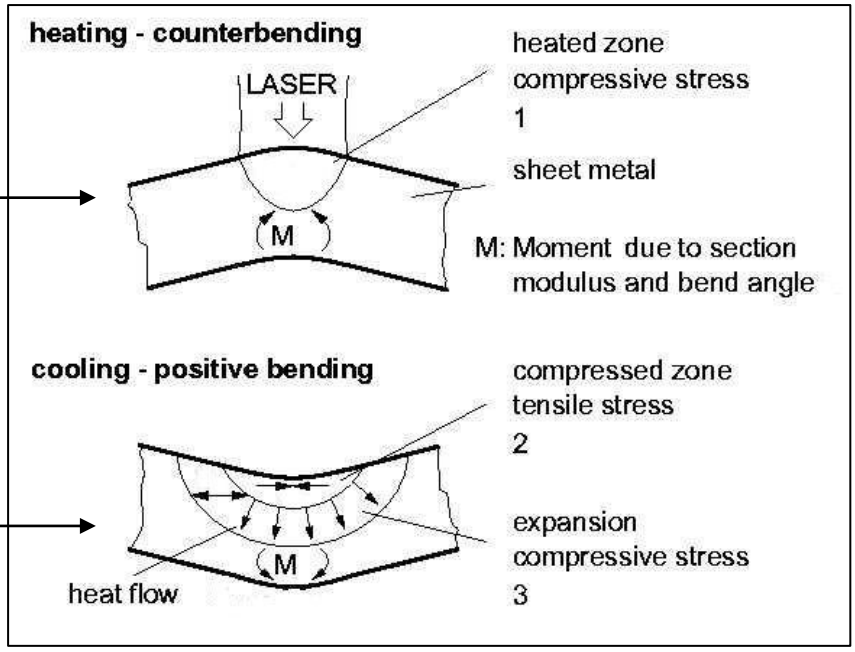

Figure 2.19 : Temperature gradient mechanism [17]

Material being irradiated by a laser with a normal power density (Figure 2.20) (p 33) as shown in Figure 2.21 (p 34), absorbs some of the laser energy on the surface. The thermal energy is conducted into the material and a temperature

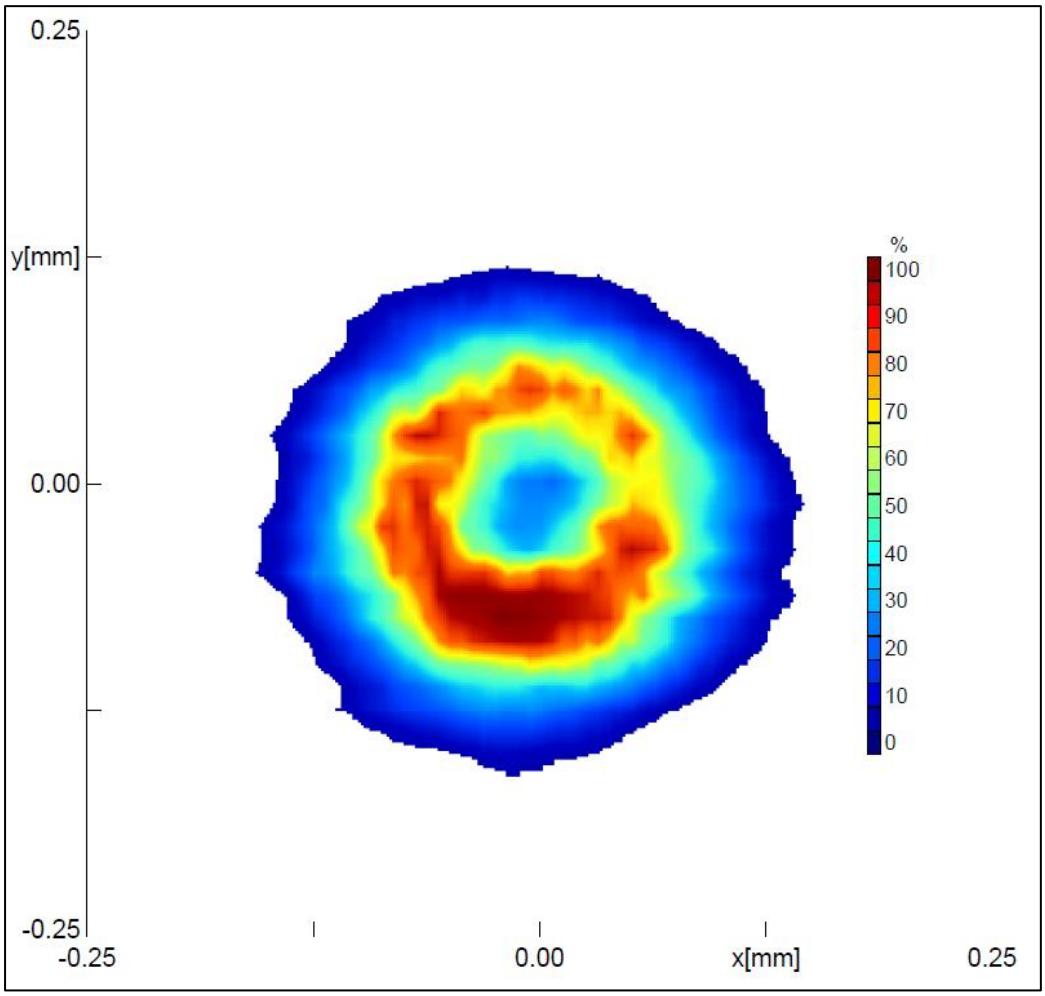

Figure 2.20 : A doughnut laser beam distribution [18]

distribution is generated inside the material as shown by isothermal lines in Figure 2.22 (p 34). The material expands where the temperature rises and hence the material bends to form a convex shape i.e. the bending occurs away from the beam. High stresses form due to the steep temperature gradient at the heated zone. These stresses lead to a drop in the material's yield strength whereas ductility of the material increases with temperature. For that reason the material yields during the heating process.

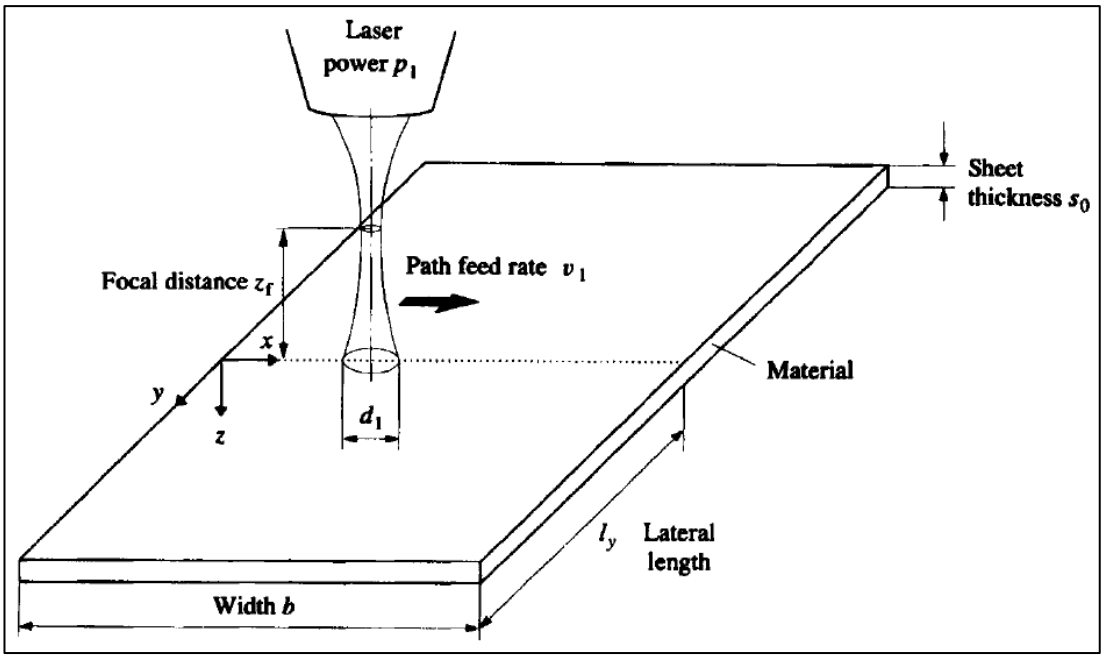

Figure 2.21 : Laser distribution on material and laser path [17]

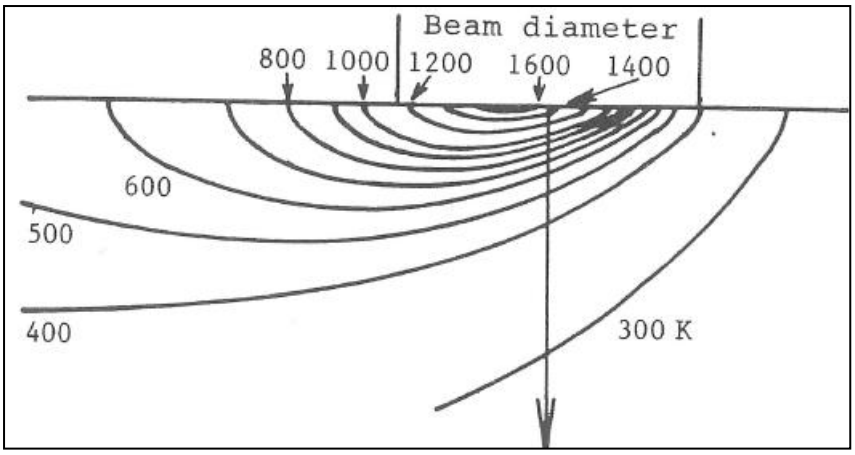

Figure 2.22 : Temperature distribution caused by a laser on a material [16]

Subsequently to the laser scan, the heated zone rapidly cools down via thermal conduction into the material creating uniform contractions. These contractions generate higher thermal stresses which are high enough to break brittle materials [16][17]. Materials can be plastically deformed to relax the higher stresses and bent into a concave shape without the use of any external force. This mechanism renders lasers useful for the process of forming [19].

2.11 Laser forming of Titanium

Marya and Edwards [20] indicate that titanium (Ti-6Al-2Sn-4Zr-2Mo) exhibits a maximum bending angle which is independent of the number of scans. When lower beam power is utilized (e.g. 150 W), the behaviour of the material at the bending angles is limited. Increasing the beam power to such an extent that melting of the surface occurs does not necessarily correspond to a maximum bending angle. A narrow range of intermediate power produced maximum bending angles [20]. This can be seen in Figure 2.23 and Figure 2.24 (p 36). Marya and Edwards [20] state that the beam spot diameter plays a major role when laser forming titanium, since the thickness of the plate is proportional to the beam diameter due to the thermal expansion of the upper and lower layers of the material, as illustrated in Table 2.1 (p 36) (dimension of material: 0.6 mm thick and 26 mm wide). Again, a narrow range of beam diameters lead to the maximum bending angle. The effect of multiple scans on the same area resulted in bigger bending angels although the rate at which the bending angle changed, gradually decreased with the number of scans. This occurrence may be due to the thickening of the material at the scanned area, as seen in Figure 2.25 (p 37). Marya and Edwards [21] indicate that heat flow plays a major role in laser forming of titanium. The top surface or the laser side of the specimen indicated that the largest bending angle was produced at temperatures between 800˚C and 1100˚C, although the bottom surface temperature or riverside temperature ranges between 350˚C and 500˚C. Marya and Edwards [21] furthermore indicate that the threshold top surface temperature is approximately 600˚C and that the yield temperature should not exceed 600˚C.

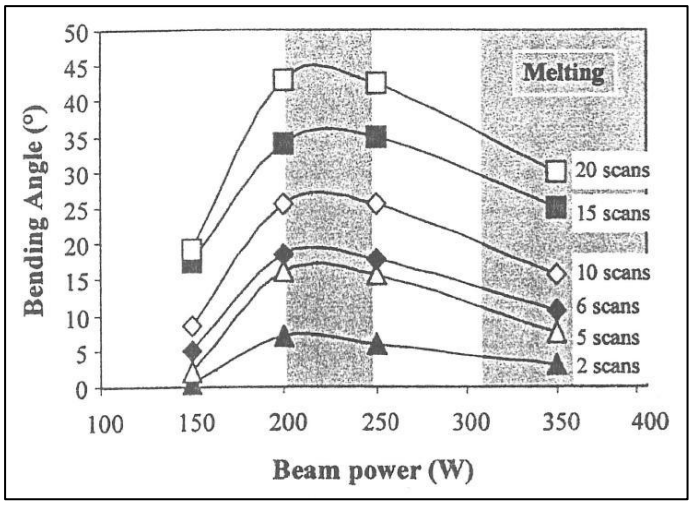

Figure 2.23 : Effect of the beam power on the bending angle [21]

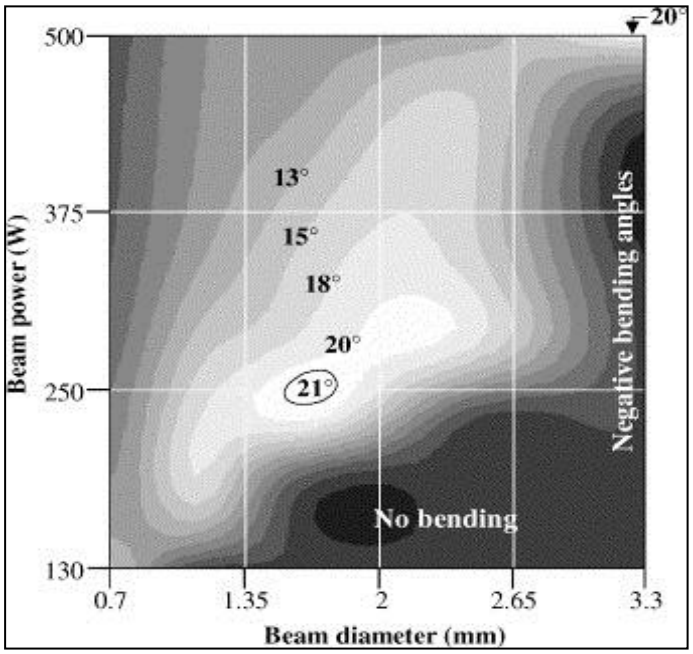

Figure 2.24 : Bending angle isochors as a function of laser beam properties [21]

Table 2.1 : Bending angles at various powers and diameters for Ti-6Al-2Sn-4Zr-2Mo [21]

Beam diameter (mm)	Beam power (W)									Optimized powers (W)
	130	160	200	230	280	330	420	500	600	
0.70	14.0	10.0	8.0	6.5	4.5	3.5	2.5	2	–	≈100
1.15	0	12.0	18.5	15.5	15.0	11.0	9.0	8.0	–	190
1.40	0	6.0	12.0	19.0	17.0	14.0	10.5	8.5	–	220
1.60	0	0	6.0	20.0	19.0	16.0	12.0	9.0	–	240
2.45	0	0	0	0	17.5	17.5	16.0	11.5	–	330–390
3.30	0	0	0	0	0	−1.0	−3.5	20	19.0	480–570

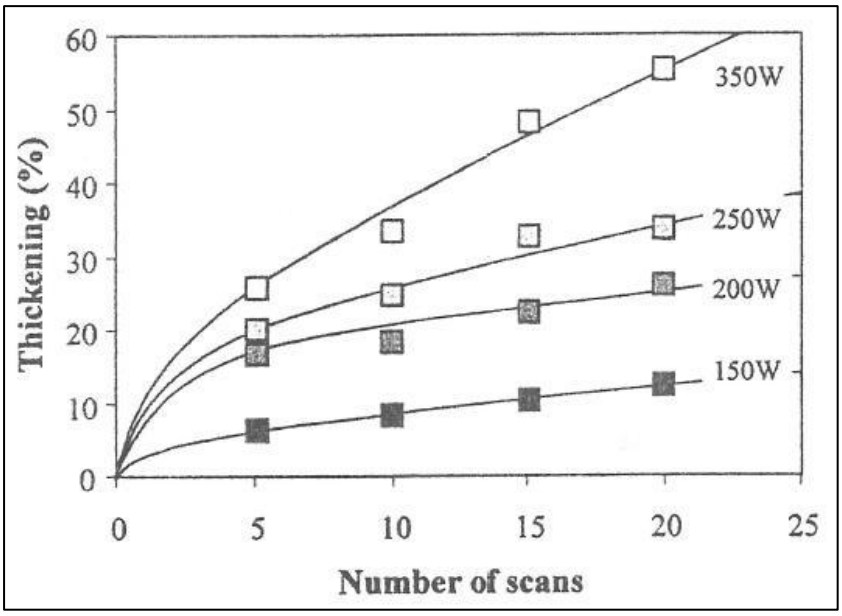

Figure 2.25 : Material thickening as a function of number of scans [21]

2.12 Microstructure associated with CP Ti grade 2

The microstructure of commercially pure titanium is typically 100% alpha phase (i.e. a Hexagonal close packed structure) (Figure 2.26, p 39) at room temperature. The typical unit cell parameters for an alpha crystal structure at 25ºC are, a = 0.2950 nm & c = 0.4683 nm (a = length of the basal plane of the hexagon, c = height of the hexagonal prism) although impurities like oxygen and nitrogen influence the unit cell dimensions. However, oxygen and nitrogen can be difficult to exclude from CP Ti due to the high solubility of the interstitial elements. At elevated temperatures hydrides form as hydrogen diffuses into the material during exposure with either gaseous or cathodic hydrogen. Hydrides cause loss in ductility and reduce the intensity threshold for crack propagation. However, due to the presence of oxygen and nitrogen, the alpha formed from beta has a much more distinctive Widmanstätten structure than does titanium essentially free of these elements as seen in Figure 2.27 and Figure 2.28 (p 39) and Figure 2.29 (p 40) [12]. At temperatures ranging between 883ºC and 910ºC, which is typically below the annealing temperature, the microstructure transforms to a beta crystal structure (body centred cubic), as shown in Figure 2.26 (p 39). The equiaxed microstructure of titanium after annealing at 800ºC in the alpha region is shown in Figure 2.31 (p 40). Annealing in the beta region at 1000ºC followed by rapid cooling to 25ºC, by means of water, produces a structure as shown in Figure 2.30 (p 40). Rapid cooling does not suppress the beta to alpha transformation. This structure is stronger than the equiaxed structure developed by annealing only in the alpha region. Cooling slowly from 1000ºC to 25ºC over a period of 20 hours produces the structure in Figure 2.32 (p 40) [12].

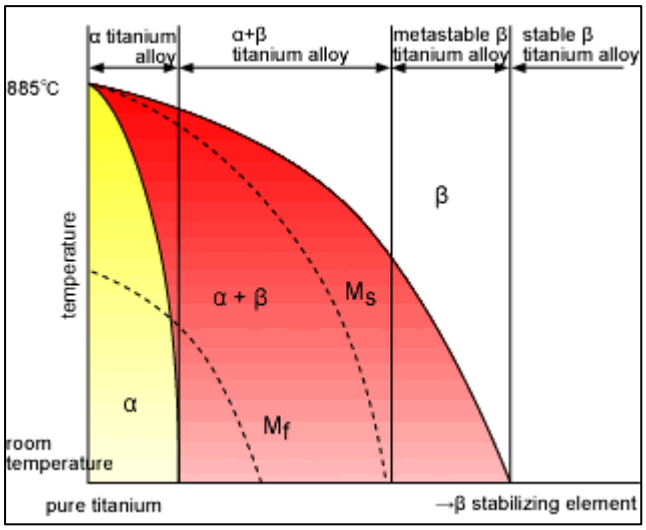

Figure 2.26 : CP Ti temperature phase diagram [22]

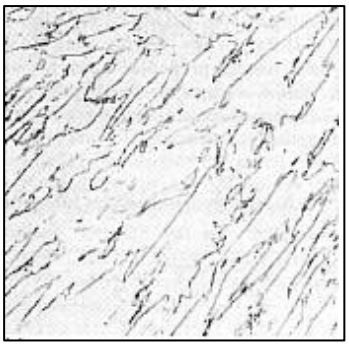

Figure 2.27: Relatively pure titanium, x150 [2]

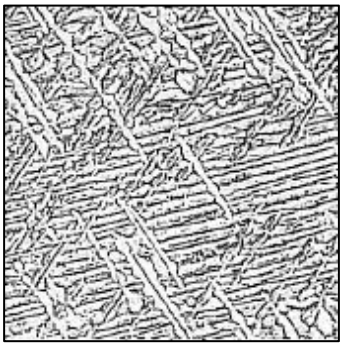

Figure 2.28 : Ti-03 wt% O alloy obtained after annealing in the beta region then cooled to 25ºC, x150 [2]

Figure 2.29 : Ti-0.3 wt% N alloy, x150 [2]

Figure 2.30 : Annealing at 1000ºC and quenched, x100 [2]

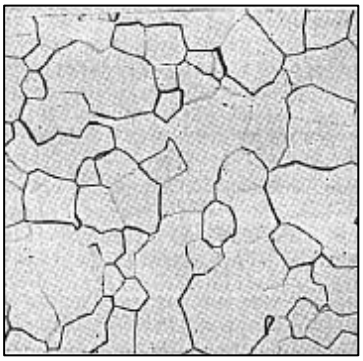

Figure 2.31 : Annealing at 800ºC and quenched, x100 [2]

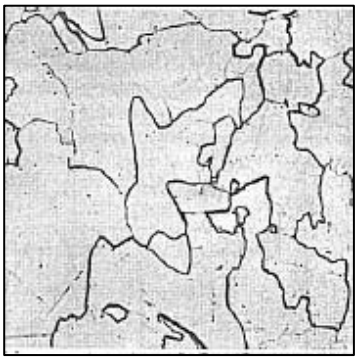

Figure 2.32 : Annealing at 1000ºC and furnace cooled (20h) to 25ºC, x100 [2]

2.13 Production of CP Ti grade 2

Titanium is the ninth most abundant element on planet earth and the fourth most abundant structural metal. Mineral sources of titanium are rutile, ilmenite and leucoxene, a deviation of ilmenite. World producers of ilmenite and titanium slag made from ilmenite are Australia, Canada, Norway, South Africa, USA and Russia. Titanium sponge is mostly produced by Russia, Kazakhstan, USA, Japan, United Kingdom and China. The main process for creating raw titanium is the Kroll process [12] in which magnesium is used to react with titanium tetrachloride. The resultant element produced is then leached free of the magnesium chloride compound leaving a spongy residue behind called “sponge titanium” [12]. Matthew Hunter [12] was the first to develop a process to produce fundamental titanium with the use of sodium to react with the titanium tetrachloride composite. The Hunter process was used initially but the Kroll process eventually became dominant. Vacuum arc remelting has been the principal method for the production of titanium ingots. This process is used to control the melting and solidification of environmentally responsive alloys. Figure 2.33 (p 42) is a schematic illustration of the production cycle for ingot products.

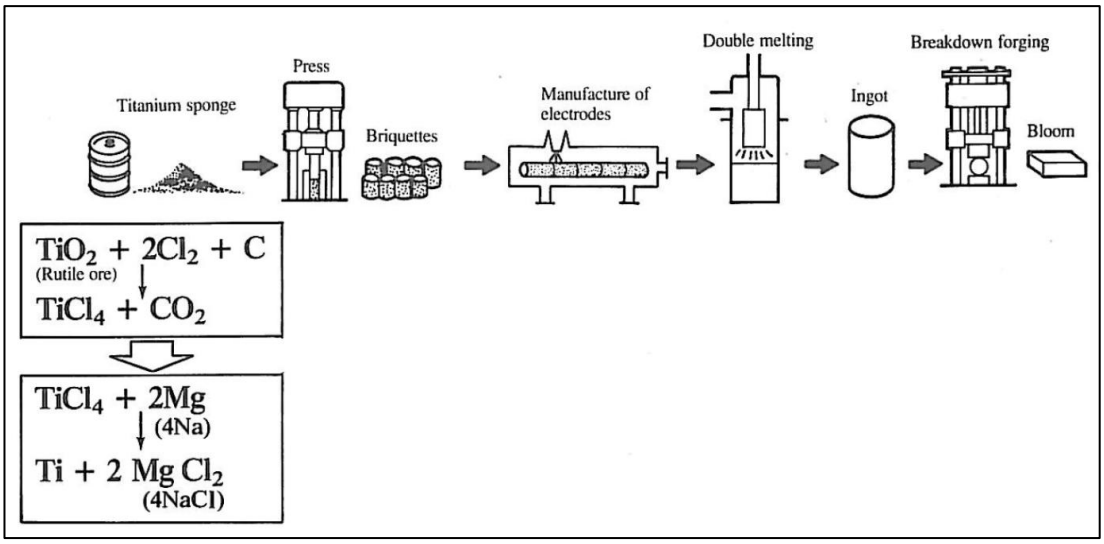

Figure 2.33 : Production cycle for ingot products [12]

Processing of the ingot is generally done by press cogging or roll cogging in the beta temperature range. On the other hand, working in the alpha range below the beta transus is essential to produce billets or slabs with a refined structure [12]. Billet reduction processes are normally carried out high in the alpha region to allow greater reduction or forming capabilities which improve grain refinement with a minimum amount of surface rupturing. If fracture toughness is essential, beta range processing is generally preferred [12]. Figure 2.34 illustrates the production cycle for mill products from slabs, followed by tandem hot rolling, annealing and pickling to the final hot rolled product [12].

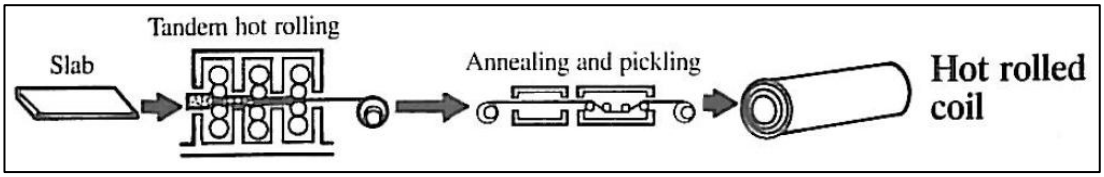

Figure 2.34 : Production cycle for mill products [12]

2.14 Residual stress introduction

Stresses that are induced in metal components by the application of external loads can be classified as either destructive or non-destructive methods. The hole drilling and strain gauge method require removal of part of the specimen and is thereby termed destructive or semi-destructive. In this method, stresses are relieved by drilling small shallow holes or by removing small disks from the surface by means of a tool called a trepan or, alternately, by progressively removing thin layers of the specimen by machining. The X-ray method does not damage the specimen and hence the term non-destructive is used [23]. This method will be discussed shortly below.

2.14.1 Non destructive method, X-Ray

This method measures residual stresses, or more precisely, strains due to residual stresses. This technique is, however, only valid for stress measurement in materials which are elastic, homogeneous and isotropic. Polycrystalline metals satisfy this requirement to a reasonable degree of certainty in selected crystals with stresses in the elastic range. A limitation of X-ray methods is that strain can only be measured at the surface of the element.

2.14.2 Destructive method

The hole-drilling method for measuring residual stresses involves the drilling of a shallow hole in the test specimen to a depth approximately equal to the hole diameter. Typical hole diameters range from 0.8 to 5.0 mm. The creation of the hole redistributes the stresses in the material surrounding the hole. A specially designed three-element strain-gauge rosette measures the associated partial

strain relief. The in-plane residual stresses that originally existed at the hole location can then be calculated from the measured strain reliefs using the method described in ASTM E 837, “Measurements of Residual Stresses by Hole-Drilling Strain-Gauge Method.” The ASTM standard also gives details of practical drilling procedures [23]. The residual stress calculation will be explained in Section 2.14.2.1.

2.14.2.1 Residual stress calculations for the hole drilling method

Three combinations of gauges are used to calculate the strains as illustrated by the force distribution shown schematically in Figure 2.35 (p 46). The gauges are designated P, Q, and T in conjunction with three combined strains p, q, and t. The following dimensionless formulas are used:

$$\boldsymbol{P = -E(\Sigma \bar{a}.p)/\bar{a}^{2}/(1+v)} \quad , \tag{2.13}$$

$$\boldsymbol{Q = -E(\Sigma \bar{b}.q)/(\Sigma \bar{b}^{2})} \quad , \tag{2.14}$$

$$\boldsymbol{T = -E(\Sigma \bar{b}.t)/(\Sigma \bar{b}^{2})} \quad , \tag{2.15}$$

$$\boldsymbol{p = (\varepsilon_3 + \varepsilon_1)/2} \quad , \tag{2.16}$$

$$\boldsymbol{q = (\varepsilon_3 - \varepsilon_1)/2} \quad , \tag{2.17}$$

$$\boldsymbol{t = (\varepsilon_3 + \varepsilon_1 - 2\varepsilon_2)/2} \quad . \tag{2.18}$$

$\bar{a}$ and $\bar{b}$ are provided in a table supplied by the manufactures or calculated with the following formulas:

$$\bar{a} = -\frac{\bar{A}(2E)}{(1+\nu)} \quad , \tag{2.19}$$

$$\bar{b} = -\bar{B}(2E) \quad . \tag{2.20}$$

To calculate the relieved stresses on the surface of the material the following equation is derived from the minimum and maximum principal strains:

$$\varepsilon_r = (\bar{A} + \bar{B}\cos 2\beta)\sigma_{max} + (\bar{A} + \bar{B}\cos 2\beta)\sigma_{max} \quad , \tag{2.21}$$

with the principal stresses given by:

$$\sigma_{max}, \sigma_{min} = P \pm \sqrt{Q^2 + T^2} \quad . \tag{2.22}$$

Nomenclature:

ε_r = Relieved strain measured by a radially aligned strain gauge at P

A, B = Calibration constants

σ_{max} = Maximum (most tensile) principal stress present at hole location before drilling

σ_{min} = Minimum (most compressive) principal stress present at hole location before drilling

β = Angle measured clockwise from the direction of gauge 1 to the direction of σ_{max}

D = Diameter of gauge circle (see Figure 2.35)

D_o = Diameter of the drilled hole (see Figure 2.35)

E = Modulus of Elasticity

ν = Poisson's ratio

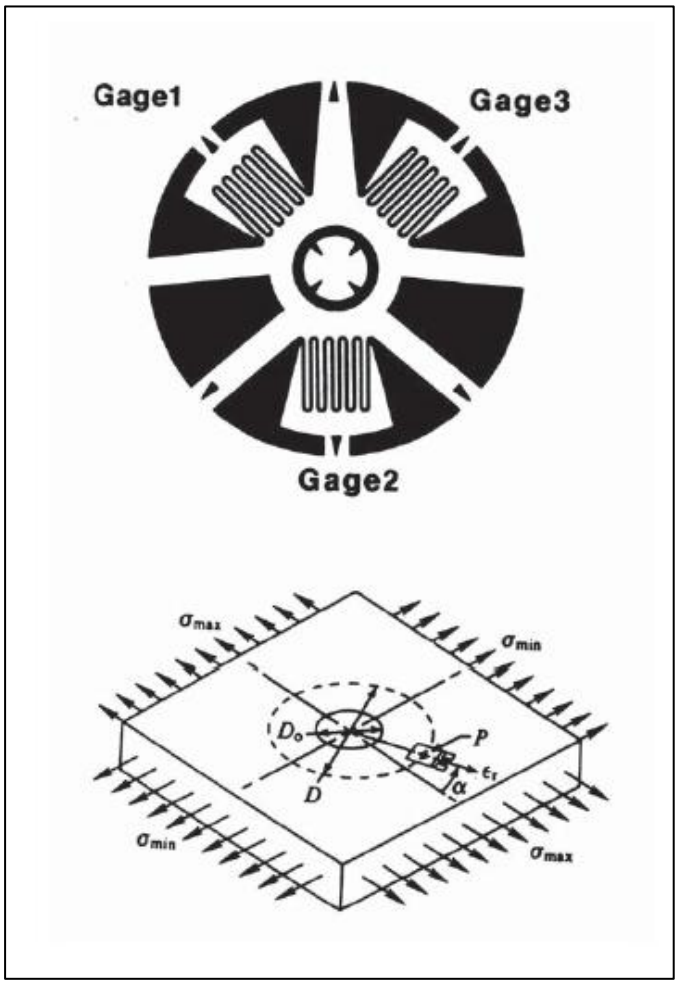

Figure 2.35 : Residual strain gauge and residual stress force distribution during drilling [24]

2.15 Summary

From the literature it is evident that laser forming is a fairly new technology for bending sheet metal. Although sheet metal has been laser formed and studied, it is clear that information regarding mechanical properties is extremely rare and incomplete. Factors such as fatigue, toughness, microstructure etc. are scarce and as a result, industry is reluctant to implement this new forming process. Lasers are widely used in industry regarding applications such as welding and cutting. Therefore adaptation towards this new process should be relatively straightforward. The literature also indicates that laser forming can be beneficial to fatigue properties. This may lead to the use of thinner metals or thinner gauge sheet material in certain fields of application in industry.

CHAPTER 3 – EXPERIMENTAL SETUP

3.1 Introduction

The method of producing curved specimens to a radius of curvature of approximately 120 mm will be discussed in this chapter as well as the relevant test methods used. The experimental setup for the following procedures will furthermore be discussed: Mechanical forming, Laser forming, Laser-mechanical forming, Charpy impact testing, Hardness testing, Residual stress measurement and fatigue testing.

3.2 Forming Processes

The forming processes will itself consist of three processes in order to form the samples to a radius of curvature of approximately 120 mm. The radius of curvature recorded, was measured in the middle of the specimen i.e. the approximate outside curvature of the specimens is 121.6 mm and the approximate inside curvature is 118.4 mm. The predetermined sample sizes were cut to dimensions of 50 mm in width and 200 mm in length (3.2 mm material thickness) to accommodate the mechanical press and fatigue specimens.

3.2.1 Mechanical Forming

Mechanical forming was performed on a Rejva\Gosmeta mechanical bending press capable of a maximum force of 25 tons, as shown in Figure 3.1 (p 49). The complete procedure of the setup of the mechanical press is described in

Appendix A (p 150). The tool radius fitted to the mechanical press was 121.6 mm and that of the die radius was 118.4 mm.

After setup of the mechanical press, the parent plate sample was inserted as displayed in Figure 3.2 (p 50). Four fasteners were used to clamp the plate at each end to the fixture which is torqued to a predetermined value of approximately 120 N.m [25]. After the mechanical press deformed the parent plate to a radius of approximately 120 mm, as shown in Figure 3.3 (p 50), the specimen was removed and inspected for any anomalies.

Figure 3.1 : Gosmeta EP-25 mechanical press

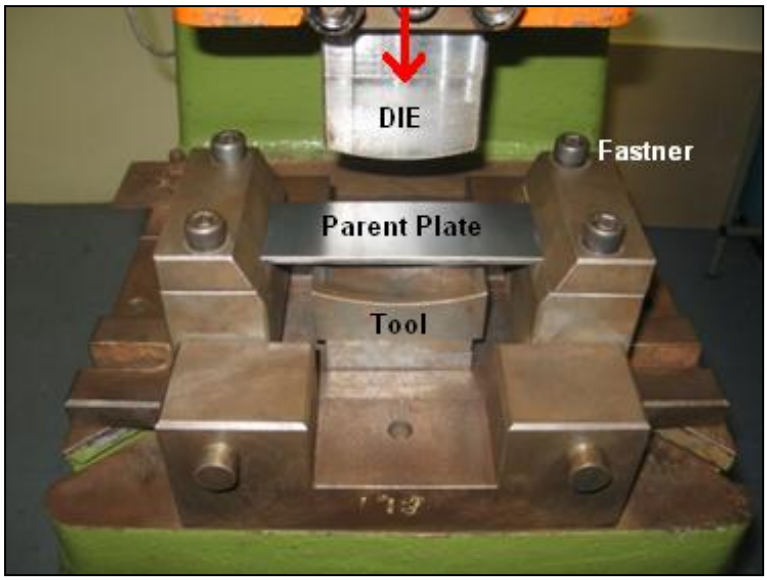

Figure 3.2 : Parent plate sample clamped in fixture

Figure 3.3 : Mechanically bent specimen

3.2.2 Laser Forming

Predetermined laser power, scanning velocities and beam diameters [26] were used to irradiate the CP Ti grade 2 specimens. The Trumpf laser system (shown in Figure 3.4) has a maximum set power of 5 kW (continuous wave CO_2) in conjunction with a doughnut shaped laser beam. The laser system is classified as a Class 1 laser system. Distribution of the laser beam was kept constant during all scanning procedures. An actual beam distribution is shown in Figure 3.5 (p 52). No shielding gas was used when the specimens were formed by the laser system.

Figure 3.4 : Trumpf laser cell used at the National Laser Centre (CSIR)

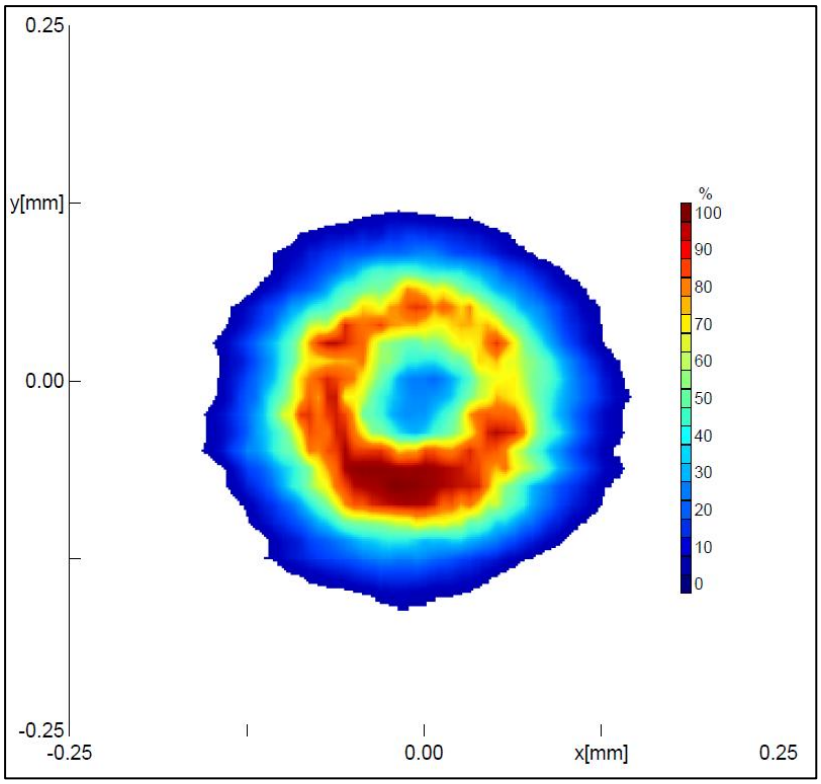

Figure 3.5 : Doughnut laser beam distribution [18]

The laser parameters used were the following: Power of 1500 W; a beam spot diameter of 12 mm; an interval spacing between laser lines of 6 mm, a scanning velocity of 1.2 m/min, the number of scans used per location was 6 and a total of 24 scans were used per specimen. The resulting pattern is shown in Figure 3.6 (p 53), where the specimen was first scanned at the left hand side (six times) and designated as 1st scan. Thereafter the specimen was scanned at the right hand side (six times) and designated as 2nd scan. A total of 24 scans were performed, finishing in the middle of the specimen. Moving inwards, the 3rd scan was performed 6 mm inwards from the 1st scan, creating a 50% overlap between the first and third scans.

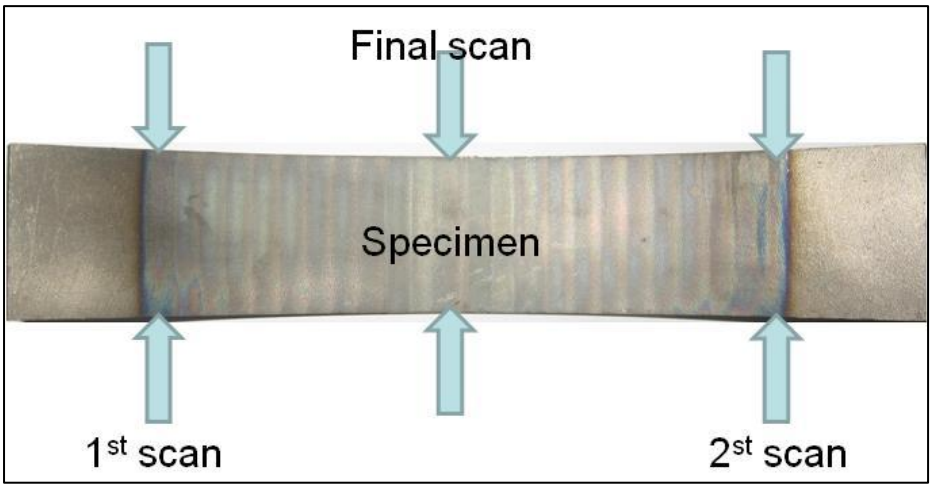

Figure 3.6 : Scanning pattern used to laser form CP Ti Grade 2

The final bent specimens, shown in Figure 3.7, have been irradiated individually. As can be seen in Figure 3.7 a constant radius of curvature has been maintained for the specimens.

Figure 3.7 : CP Ti Grade 2 specimens which were irradiated in an open mold fixture

3.2.3 Laser-mechanical forming

The laser-mechanical forming process (or combined process) utilizes first the laser bending method and secondly the mechanical bending method. The laser forming process used is the same as described in Section 3.2.2 (p 51) except that the number of scans per location was reduced to 3. After the laser forming procedure was executed the average radius of the specimens was approximately 240 mm. Thereafter the mechanical forming procedure was used as described in Section 3.2.1 (p 48). The final radius of the mechanical laser formed specimens was approximately 120 mm.

3.3 Charpy impact testing

Charpy impact testing was performed on samples taken from each bending application as well as from the parent plate. Figure 3.8 (p 55) shows where the samples were removed from the specimens. Substandard Charpy specimens of dimensions 50 x 10 x 3.2 mm were machined and tested according to ASTM E23-02 [27] standards. As seen in Figure 3.8 (p 55), four samples were removed from each specimen (for the purpose of direct comparison between the original specimen and the three forming processes considering, i.e. Parent plate, Mechanical bending, Laser bending and Laser-mechanical bending). As a result, a total of sixteen samples were tested. Two temperature settings were used, i.e. -40ºC and room temperature (21ºC). Figure 3.9 (p 55) shows the PSW type 30/15 Charpy V-Notch impact tester used for this purpose.

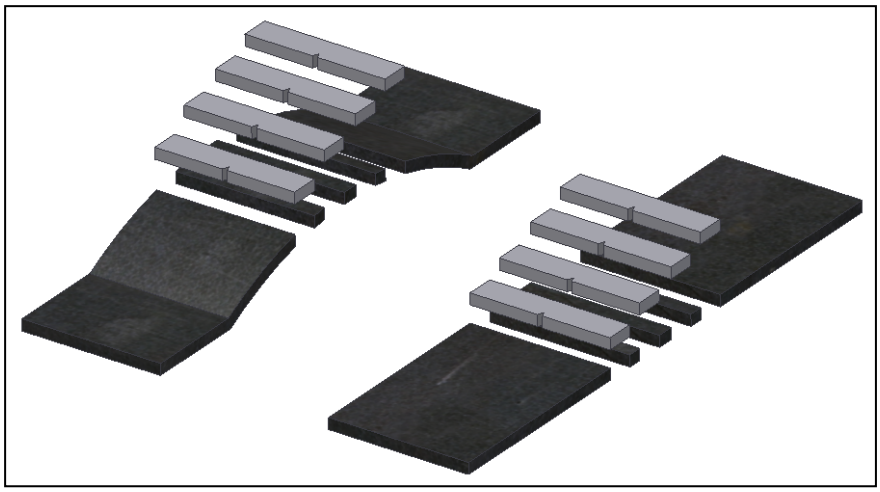

Figure 3.8 : Location of samples removed from specimens

Figure 3.9 : PSW type 30/15 Charpy V-Notch impact tester

3.4 Hardness

Vickers micro-hardness assessment was performed on samples from all three forming processes and from the parent plate. ASTM E384-99 [28] and ASTM E92-82 [29] standards were used for this procedure. A Future Tech FM 700 computerized Vickers micro-hardness system was used, as shown in Figure 3.10.

The hardness profile through the thickness of the specimen was utilized starting at a distance of 0.14 mm from the surface and using 0.2 mm space intervals, as shown in Figure 3.11 (p 57). The indenter load was set to 300 g and a dwell-time of 15 seconds was used. For all three forming processes and the parent plate, the average hardness was calculated.

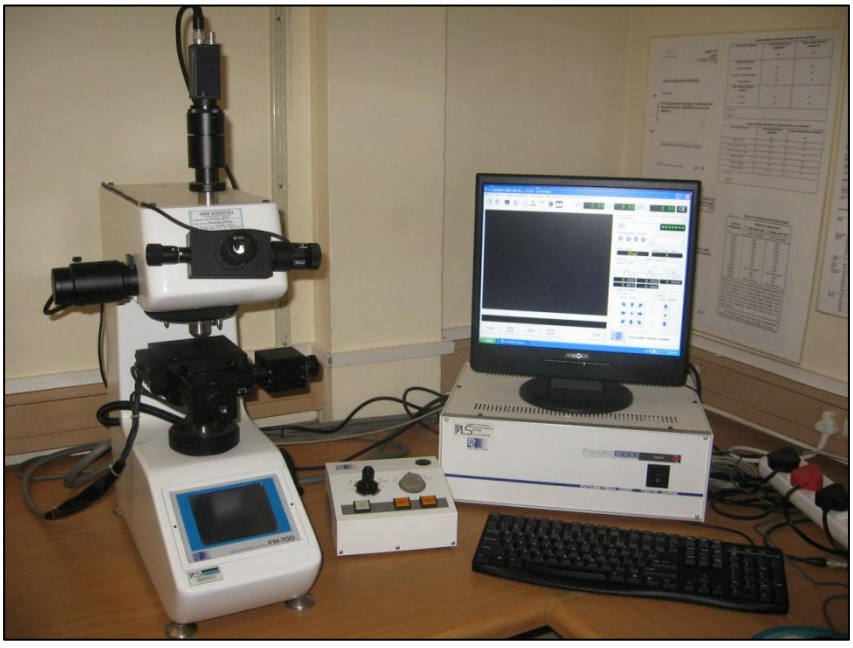

Figure 3.10 : Future Tech FM 700 Vickers micro-hardness system

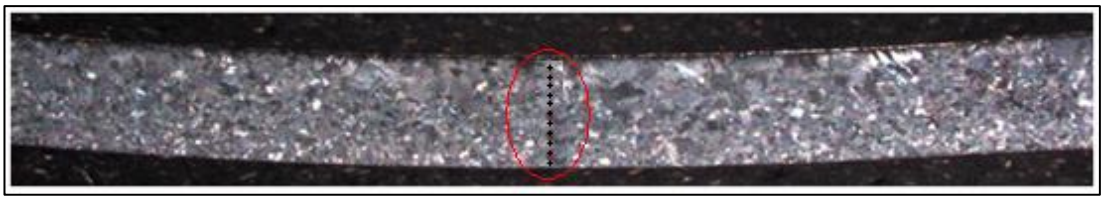

Figure 3.11 : Hardness profile through the thickness of CP Ti grade 2

3.5 Tensile testing

Tensile testing was done to determine the yield strength of the material to verify the supplier data given. A substandard specimen was used to determine the tensile properties (dimensions shown in Appendix C, p 154). Testing was performed according to ASTM E8M-01[30] standards. Figure 3.12 illustrates the typical necking of a typical CP Ti grade2 under tensile testing.

Figure 3.12: Tensile specimen undergoing deformation before failure

Figure 3.13 shows the tensile graph of CP Ti grade 2 during testing and Table 3.1 displays the tensile properties of CP Ti grade 2.

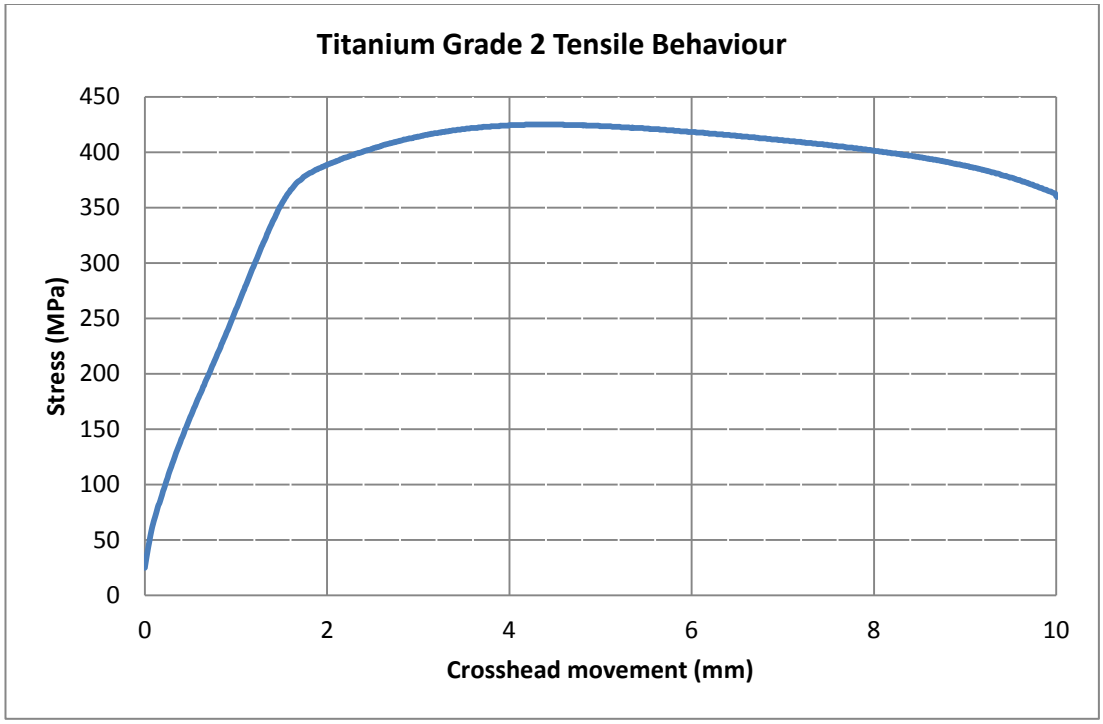

Figure 3.13 : Behaviour of CP Ti grade 2 during tensile testing

Table 3.1 : Tensile properties of CP Ti grade 2

0.2% Proof stress	≈ 353.75 MPa
Tensile stress	≈ 425.00 MPa
% Elongation	≈ 26.00 %

3.6 Typical chemical composition

The chemical compositions as displayed in Table 3.2 were supplied by the manufacturer. There are no deliberate elements in CP Ti grade 2, however, oxygen and hydrogen determine the CP grade. The test report is included in Appendix B (p 153).

Table 3.2 : Chemical analyses supplied by foundry (percentage by weight)

%N	%C	%H	%Fe	%O	%Ti
0.009	0.005	0.003	0.04	0.155	BAL

3.7 Residual Stress

Residual stress measurements were performed using the hole drilling method. The following predetermined parameters were used [1]:

- Drilling depth: 2 mm
- Evaluation method: linear
- Number of incremental drilling steps: 20
- Drilling feed rate: 0.2 mm/min
- Delay time: 10 s

A strain gauge was applied to the apex of the outer bent surface and in the centre of the inner curved surface as shown in Figure 3.14 and Figure 3.15 (p 60). An EA-06-062RE-120 type strain gauge was used for this study and mounted according to the manufacturer's standard. The three grids were

connected to the MGC amplifier (Figure 3.16, p 61) and then the drilling head was aligned and levelled to the drilling location. The predetermined parameters were entered into the software after which the gauges were calibrated and drilling commenced. After drilling, the eccentricity of the hole was measured. The principal stresses were calculated using ASTM E837-01 standards [31].

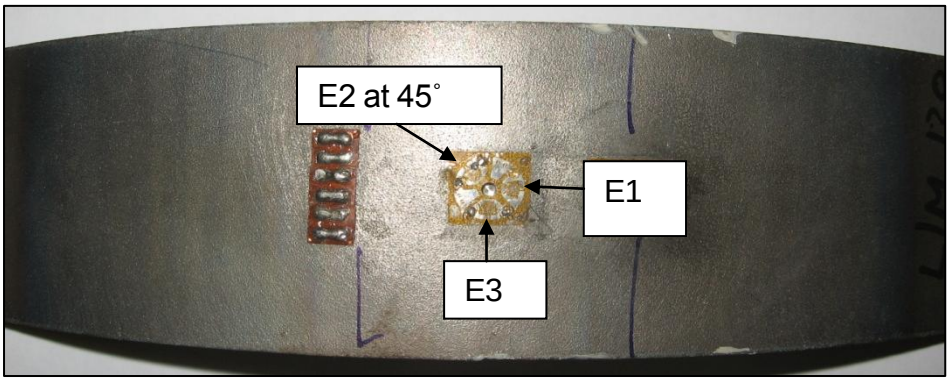

Figure 3.14 : Strain gauge positioned on top of the apex

Figure 3.15 : Strain gauge positioned at the bottom of the apex

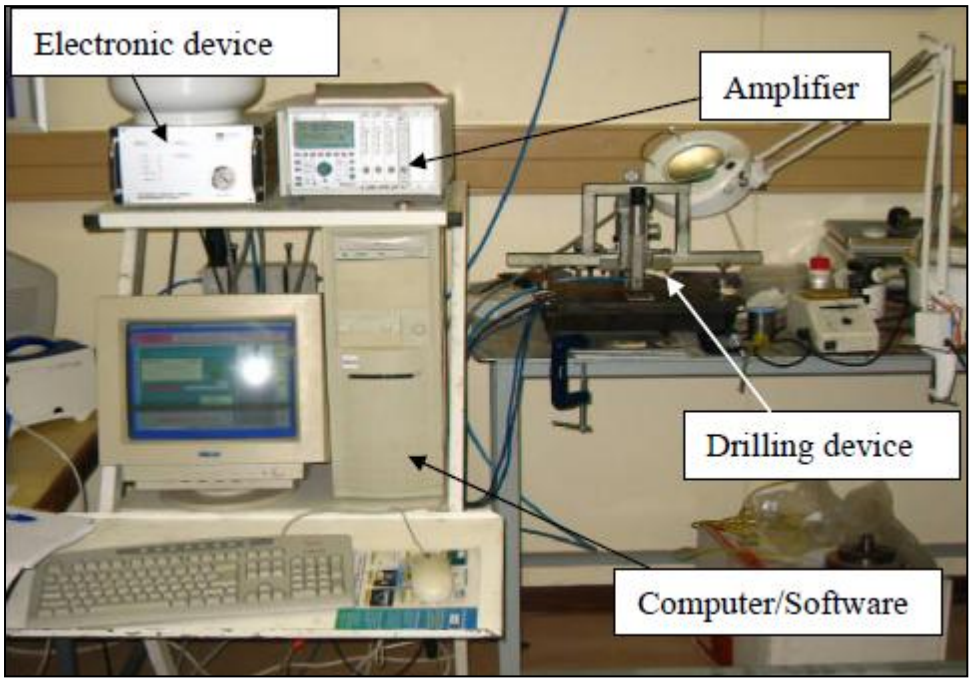

Figure 3.16 : Automatic centre drilling system

3.8 Fatigue

The fatigue procedure will be discussed below:

3.8.1 Fatigue specimen preparation for ASTM standard E466-96

Fatigue specimens from all three bending methods and the parent plate were machined according to ASTM E466 - 96 [32] dimensions, as shown in Figure 3.17 (p 62). The width of the specimen in the middle was measured to be 19 mm. The parent plate and mechanically bent samples were water jet cut (to ensure minimal microstructure damage / change) and machined down to specification. Laser-mechanical and laser formed specimens were laser cut to the dimensions as shown in Figure 3.18 (p 62). All the samples were cleaned around the edges with a deburring tool. After cleaning each specimen with acetone, the specimens were coated with a non-conductive primer as shown in Figure 3.18.

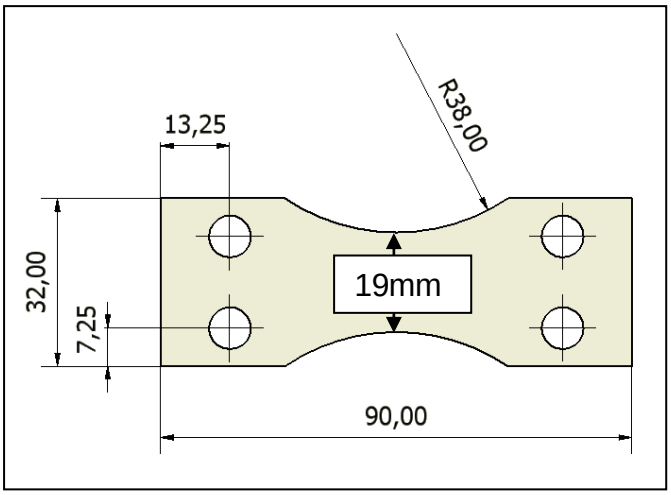

Figure 3.17 : Fatigue dimensions of specimens (ASTM E466-96)

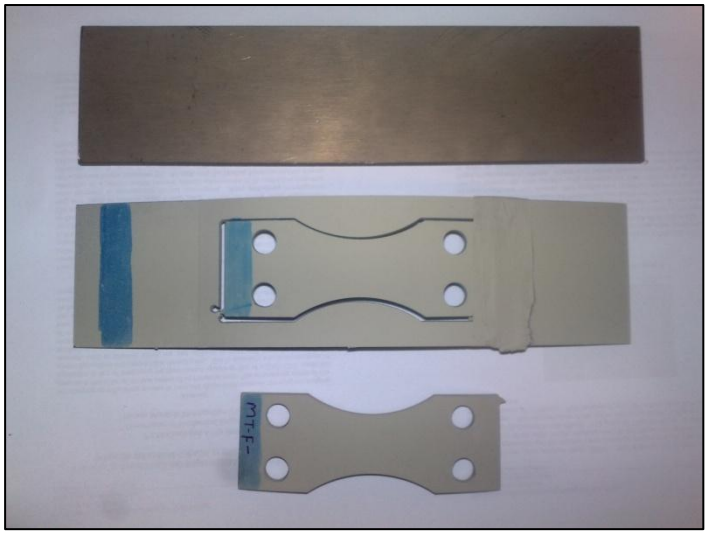

Figure 3.18 : Parent plate (top), Formed sample (middle), Final fatigued specimen (bottom)

3.8.2 Alignment of fatigue machine

The most important consideration for specimen alignment is the fatigue alignment shims. This ensures constant alignment from specimen to specimen and ensures minimal misalignment, as illustrated in Figure 3.19 (p 63). To minimize bending stresses, specimens should be aligned in such a way that the major axis of the specimen closely coincides with the load axis throughout each

cycle, as displayed in Figure 3.20 and Figure 3.21 (p 64). Detailed drawings are included in Appendix D (p 155). The main fatigue components and electronic mechanisms were selected, designed and built by the author of this thesis (Appendix D).

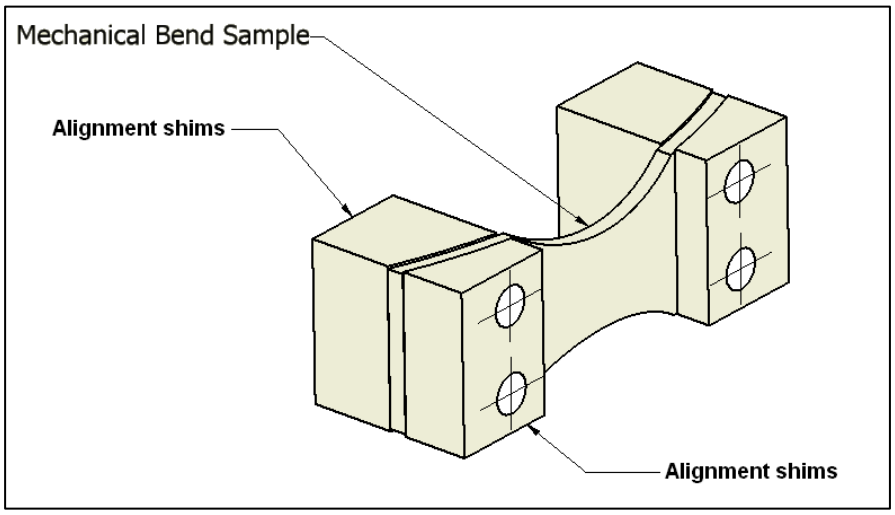

Figure 3.19 : Fatigue specimen with fatigue alignment shims fitted

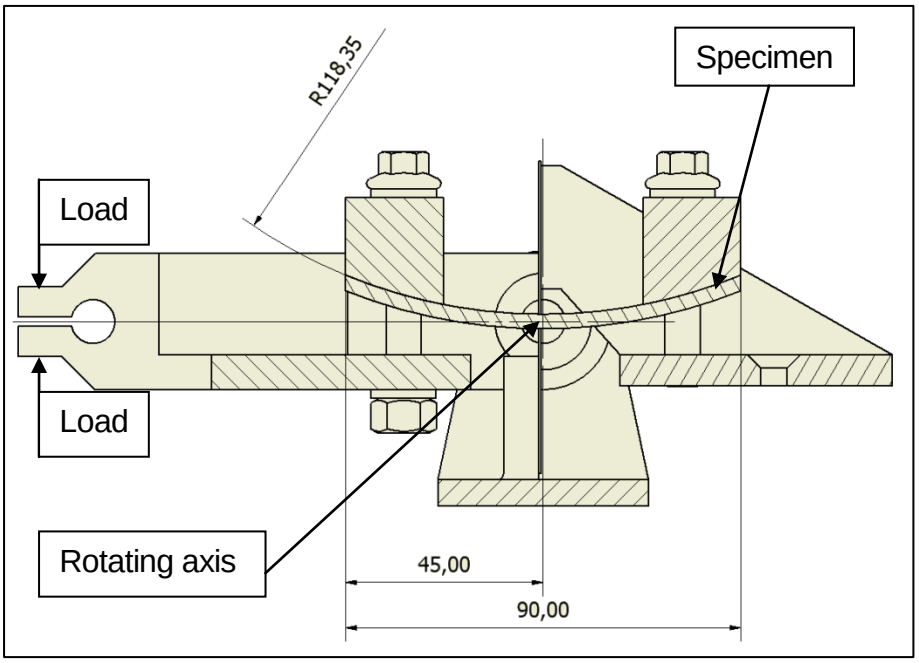

Figure 3.20 : Side view of specimen aligned through loading axis

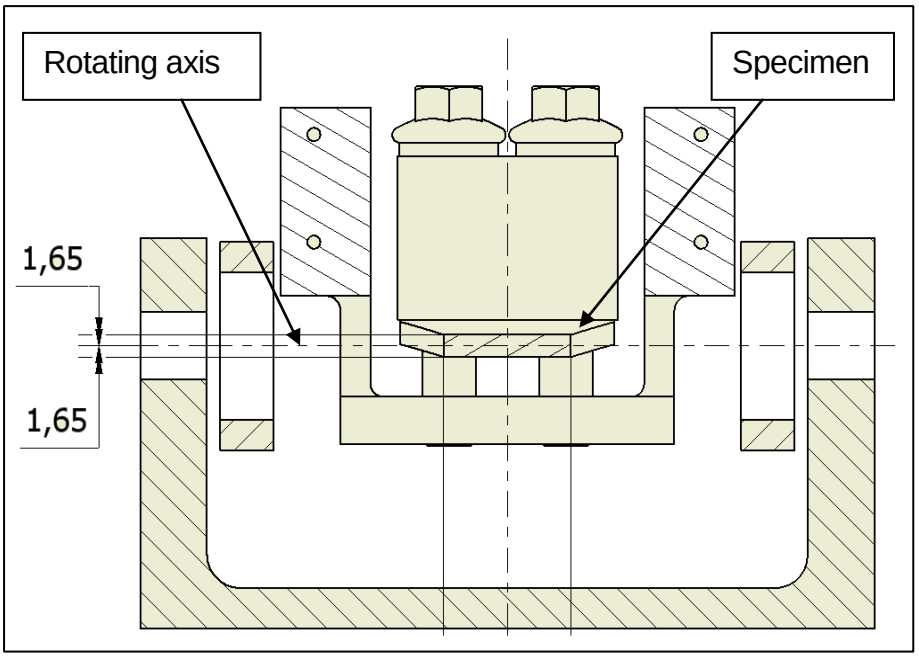

Figure 3.21 : Section view of specimen aligned through rotating axis

3.8.3 Amplitude settings

A master sample was produced to ensure a repeatable setup and loading condition. This master sample consists of two strain gauges placed in the middle of the specimen for each process i.e. four master specimens were fabricated in total. A strain gauge was placed at the top and bottom of the master sample i.e. above and below the loading axis, as seen in Figure 3.22 (p 65). This configuration ensures equal bending for top and bottom surfaces. Strain gauge fitment was performed according to the manufacturer's standards. Calibration of the master specimen was carried out to ensure linear repeatability and loading. This was achieved by loading the specimen to 60%, 70% and 80% of its yield stress and repeating the process three times in the fatigue machine with a special manufactured load hanger bracket (Figure 3.23, p 65). Additionally, when loading the specimen to 99% of the yield stress, the master specimen always

returned to zero microstrain when it was removed from the fatigue machine, therefore linearity was always achieved at the high load setting.

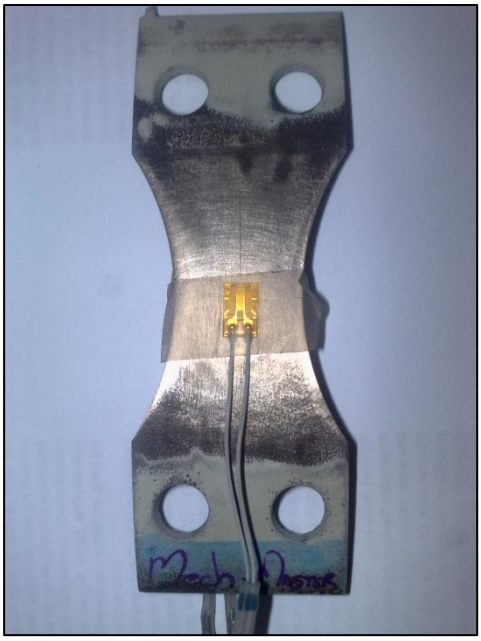

Figure 3.22 : Master fatigue specimen

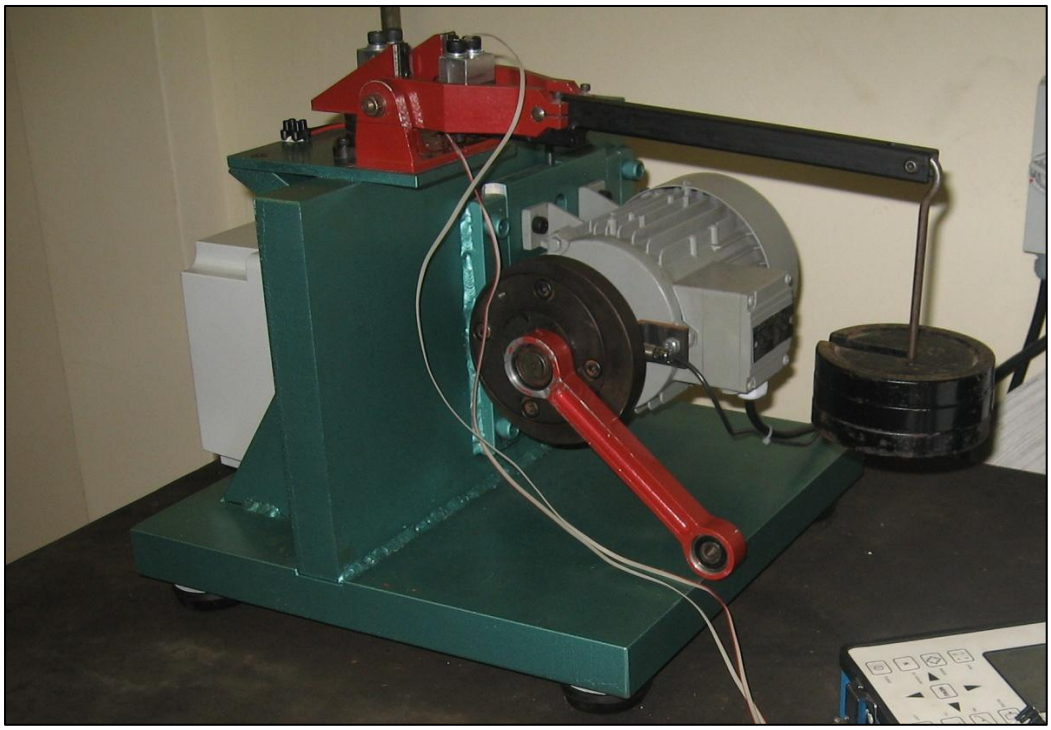

Figure 3.23 : Calibration of master sample

The procedure to follow for installing a specimen in the fatigue machine is described in Appendix E (p 158).

Before placing the fatigue specimens in the fatigue machine, a conductive paint was used to replicate a circuit on the specimen, as shown in Figure 3.24. This ensures that the machine switches off once crack initiation commences.

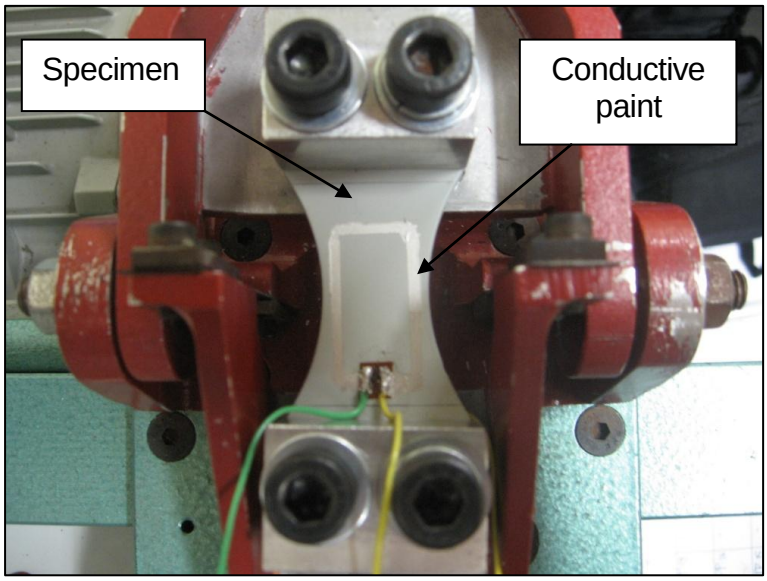

Figure 3.24 : Fatigue specimen installed and coupled to machine

3.9 Summary

An experimental setup is of utmost importance for repeatability and to obtain reliable results. The results that will be discussed in the next chapter should be reproducible when performing mechanical forming, laser forming, impact, hardness, tensile, residual stress and fatigue testing (as described and documented in this chapter) to ensure that repeatable results are obtained from the experimental setup. All testing done was according to acceptable ASTM and manufacturing standards.

CHAPTER 4 - RESULTS AND DISCUSSION

4.1 Introduction

In this chapter the results obtained from the various mechanical tests on CP Ti grade 2 and the microscopy of the parent plate, laser-, mechanically- and laser-mechanically formed specimens (combined process) will be evaluated. The following properties of CP Ti grade 2 were also analysed: the mechanical characterization of the microstructure, the hardness, toughness, residual stress, fatigue and fatigue crack morphology. Various relationships between the properties will also be determined.

4.2 Microstructure

The microstructure of the parent plate and all the bending processes will be discussed below.

4.2.1 Parent plate

The original microstructure of the CP Ti grade 2 specimen is shown in Figure 4.1 (p 68). The microstructure consists of equiaxed grains. A typical characteristic of the equiaxed grain structure is that the grain dimensions are approximately the same in all directions. The average grain size was determined according to the ASTM E112-96 standard and found to be in the range of numbers 3 - 6. The average grain diameter was determined to be 89.8 µm throughout the specimen. The material was supplied in the hot rolled and pickled condition.

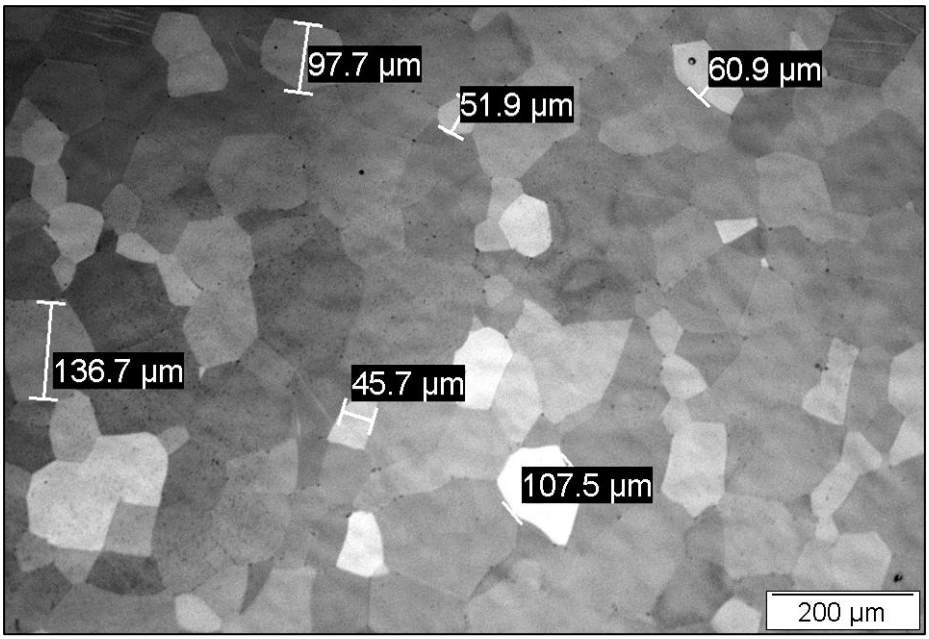

Figure 4.1 : Original microstructure of CP Ti grade 2 (x100, electrolytically polished, polarized light)

4.2.2 Laser formed

From the laser formed specimens, a Widmanstätten-like microstructure can be observed in the heated region of the sample, as shown in Figure 4.2 (p 69). This microstructure is typically associated with a material subjected to fast cooling rates, i.e. fast cooling rates typically ranging from 800˚C to 25˚C via quenching.

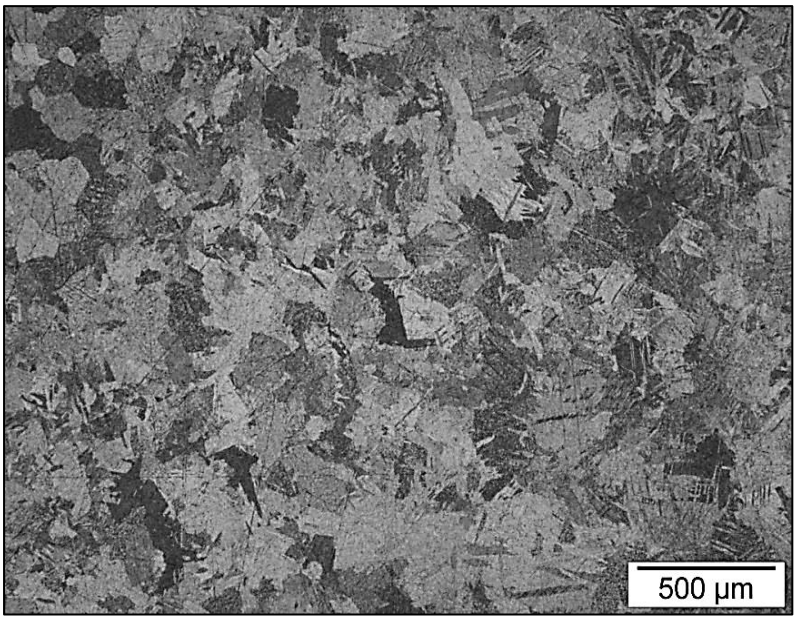

Figure 4.2 : Microstructure of laser formed CP Ti grade 2 (x50, electrolytically polished, polarized light, colour image)

4.2.3 Mechanically formed

The microstructure of the mechanically formed specimens is similar to that of the parent plate specimens although twinning of the microstructure is observed near the inner and outer edges of the specimens. The average depth of twinning from the inner radius (i.e. 118.4 mm) inwards was found to be approximately 502 µm, as shown in Figure 4.3 (p 70). The average depth of twinning from the outer radius (i.e. 121.6 mm) inwards was approximately 257 µm, as shown in Figure 4.4 (p 70). Twinning is a deformation mechanism of several metals. This is a common appearance for these metals when they were subjected to forming processes and/or high temperatures. Twinning is also recognised as a strengthening mechanism within the material [3].

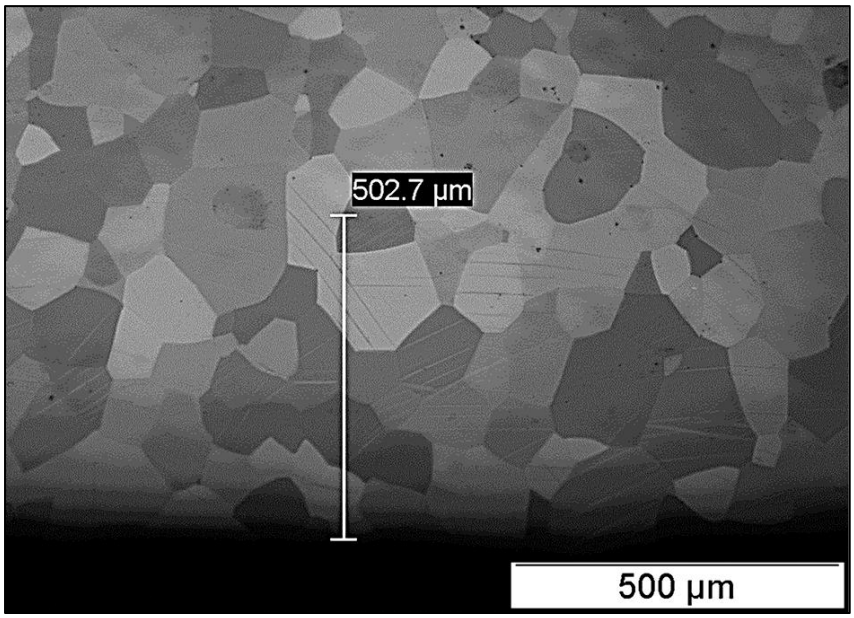

Figure 4.3 : Microstructure of mechanically formed CP Ti grade 2 (x100, electrolytically polished, polarized light), inner radius

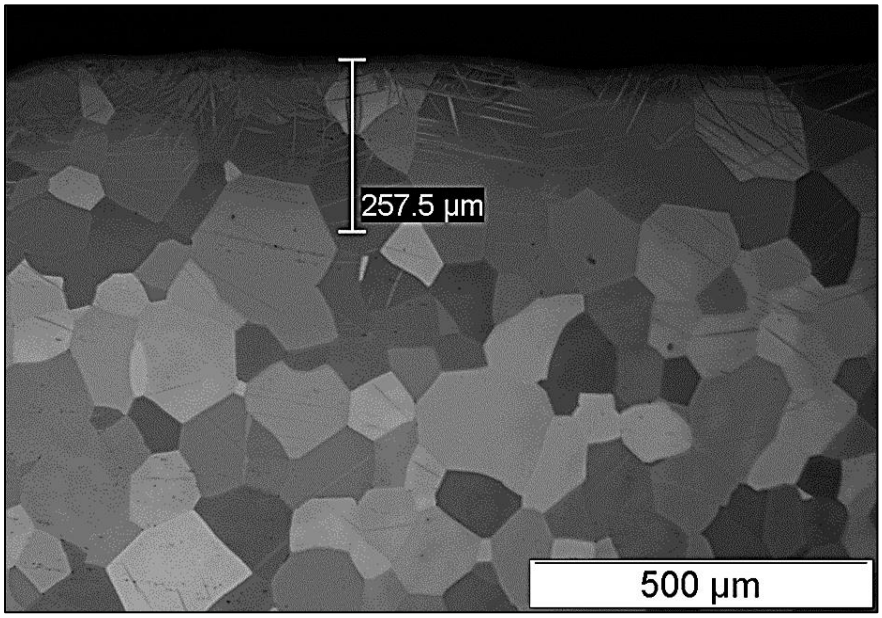

Figure 4.4 : Microstructure of mechanically formed CP Ti grade 2 (x100, electrolytically polished, polarized light), outer radius

4.2.4 Laser-mechanically formed

From the inner radius of the laser-mechanically formed specimens, a Widmanstätten-like structure can be seen to a depth of approximately 312.5 µm, as shown in Figure 4.5. This is due to the irradiation of the laser beam resulting in fast cooling rates up to that specific depth. The remaining microstructure is found to be equiaxed and twinning can be seen to a depth of approximately 557 µm below the Widmanstätten structure. This is due to mechanical forming which follows the laser forming procedure.

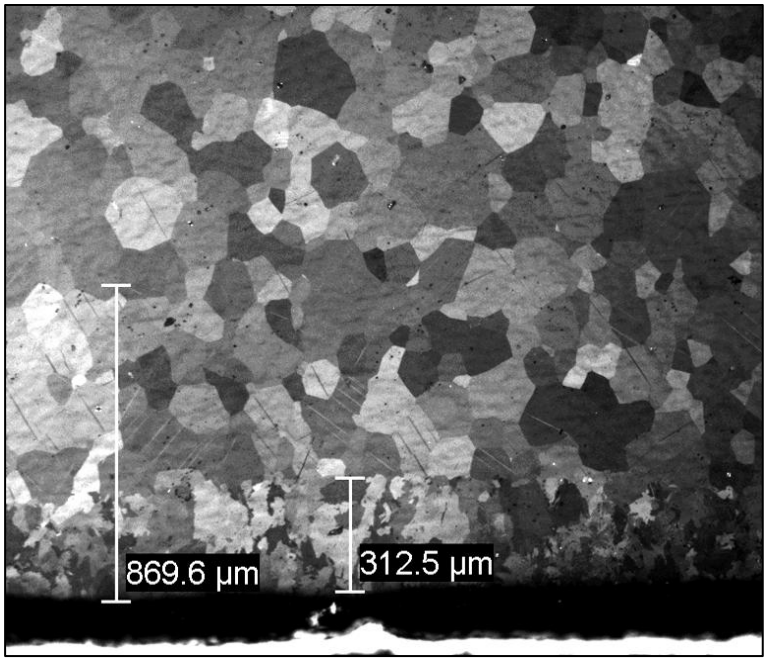

Figure 4.5 : Microstructure of laser-mechanically formed CP Ti grade 2 (x50, electrolytically polished, polarized light), inner radius

From Figure 4.6 (p 72) it is evident that twinning appeared at the outside radius of the laser-mechanical process. It was measured inwards to be approximately 261 µm below the outside surface.

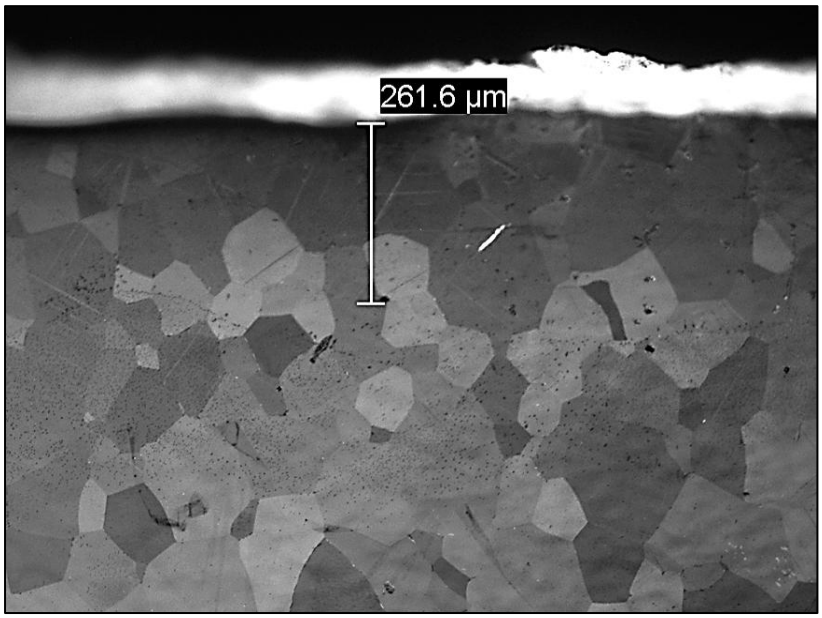

Figure 4.6 : Microstructure of laser-mechanically formed CP Ti grade 2 (x50, electrolytically polished, polarized light), outer radius

4.3 Microhardness

The microhardness of the parent plate and all the bending processes will be discussed below.

4.3.1 Parent plate

Vickers microhardness profiling was performed through the thickness of the parent plate (middle / apex of specimen) at the position shown in Figure 4.7. The measured average hardness value is 176HV0.3. A maximum value of 188HV0.3 was recorded together with a minimum value of 164HV0.3. Figure 4.8 (p 74) illustrates the hardness profile of the parent plate.

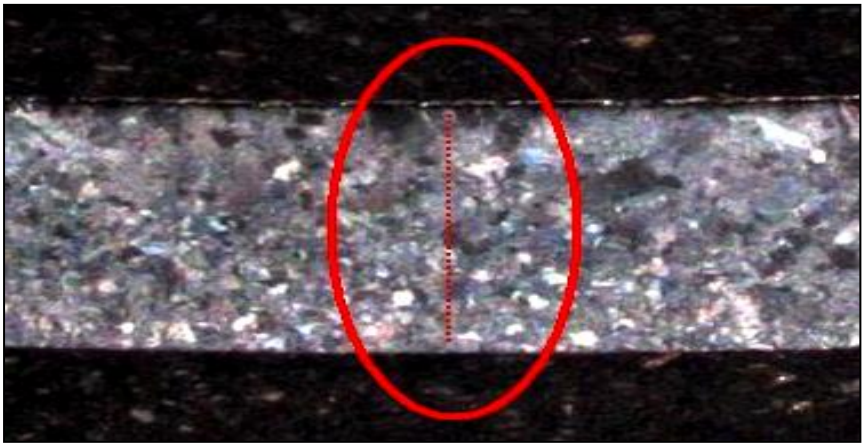

Figure 4.7 : Indication of position where the hardness through the thickness of the material was measured

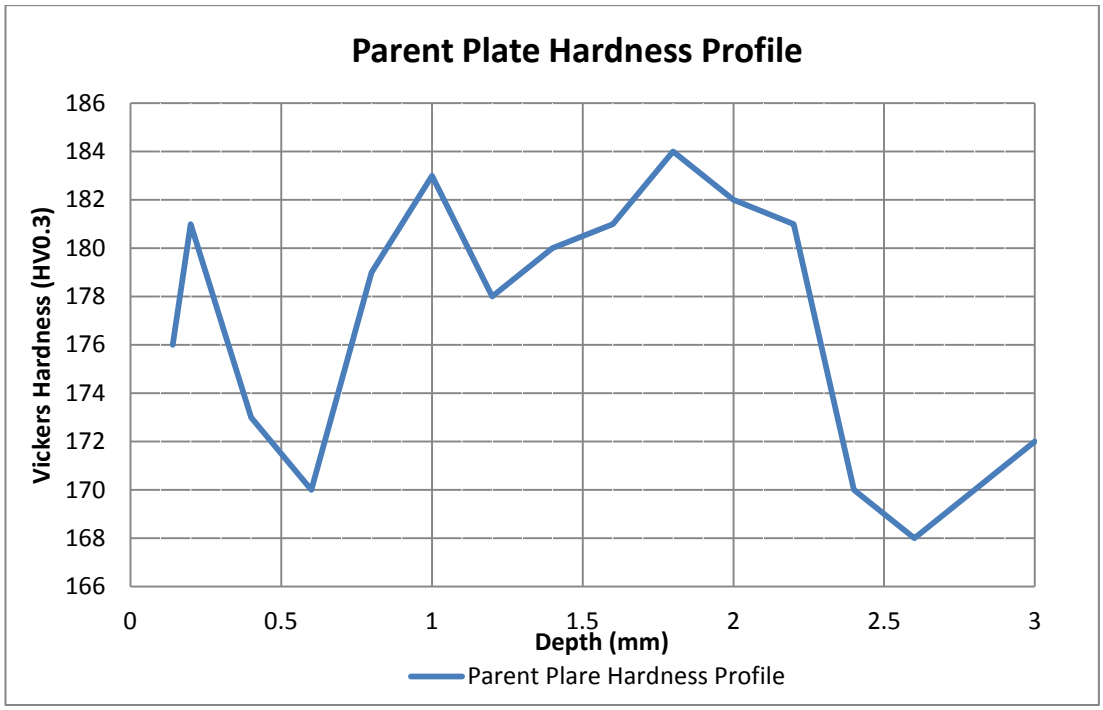

Figure 4.8 : Microhardness profile measured through the thickness of the parent plate

4.3.2 Formed specimens

Vickers microhardness profiles were measured for all three bending methods through the thickness of the sample, as seen in Figure 4.9 (p 75). The laser bent samples displayed an average hardness of 173HV0.3, whereas the average laser-mechanical hardness obtained was 169HV0.3. The highest average hardness value was recorded for the mechanically formed samples, i.e. 177HV0.3. It can be noted that the maximum average difference between the forming processes is 8HV units.

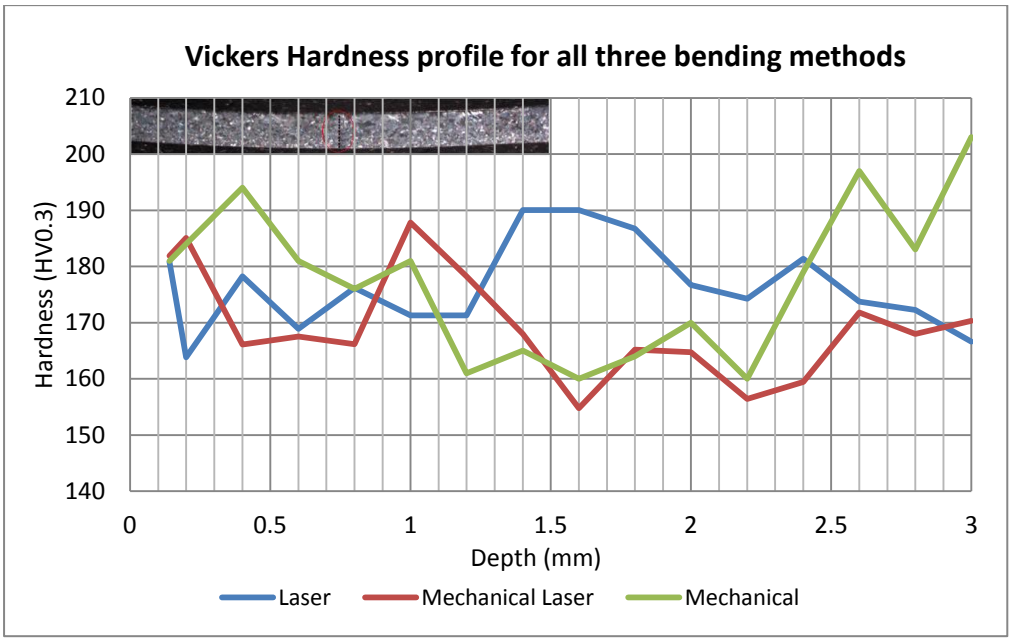

Figure 4.9 : Illustrating the hardness profile (measure through the thickness) of all three bending processes

Figure 4.10 illustrates the hardness profile of the laser-mechanically formed specimens in the two different microstructural regions. This was done to verify that the hardness value is constant throughout the specimens i.e. in regions where recrystallization occurred vs. regions of equiaxed grains.

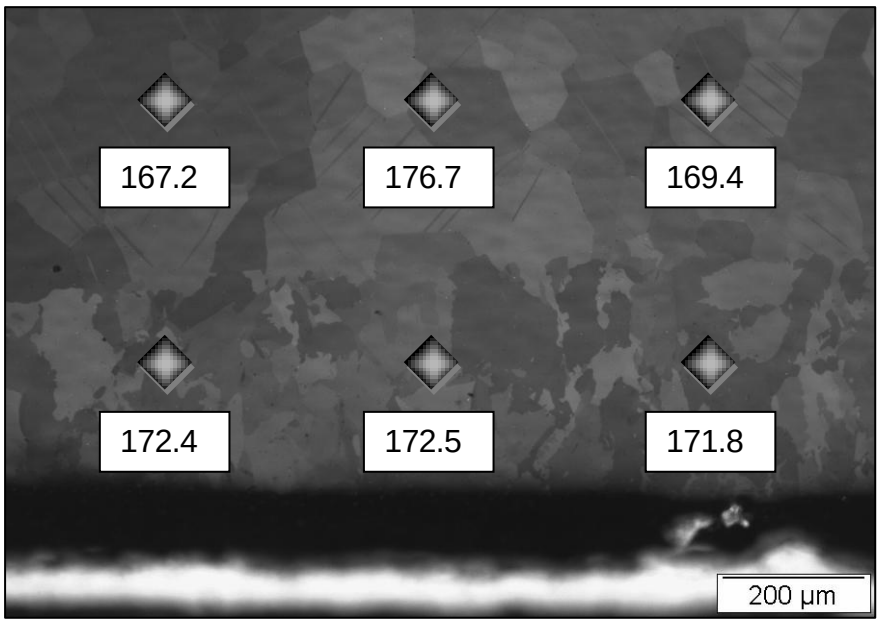

Figure 4.10 : Hardness profile of laser-mechanically formed specimen within the laser and twinning region (HV0.3) (x100, electrolytically polished, polarized light, inner radius)

When considering a maximum difference of 8HV0.3 units between the forming processes and a value of only 4.9HV0.3 between the recrystallization regions of the laser-mechanically formed specimens, the difference in hardness can be considered negligible i.e. no significant hardening occurred due to the forming processes.

4.4 Charpy impact testing

Charpy impact testing was performed on the parent plate as well as on the three bending processes (i.e. mechanically, laser-mechanically and laser formed). The tests were conducted at room temperature (i.e. at approximately 21.4ºC) and at approximately -40ºC. The results of the Charpy V-notch testing are given in Table 4.1 (p 77) and shown graphically in Figure 4.11 (p 78). Charpy impact testing was performed to compare the effect of the forming processes with each other in terms of fracture toughness. Due to the HCP lattice properties [3], titanium does not exhibit a ductile to brittle transition temperature zone (as commonly observed for steel). It is evident from Figure 4.11 that the parent plate has more promising impact properties (i.e. 27.2 J or 1.0625 J/mm^2) than the other forming processes. The behaviour of the slightly less ductile mechanically formed specimens (i.e. 24.8 J or 0.9688 J/mm^2) could be attributed to the twinning within the microstructure. Laser (13.85 J or 0.541 J/mm^2) and laser-mechanically (15.95 J or 0.623 J/mm^2) formed specimens exhibit the worst impact properties and this may be attributed to hydrogen and oxygen contamination during the high temperature forming process i.e. with the aid of laser forming. Hydrogen and oxygen contamination occurred because no gas shielding was used during laser forming [12]. Since the amount of contamination

was not quantified for this study, further investigation is required. As reported in [3], a fine Widmanstätten structure exhibits low ductility and toughness. They indicate that CP Ti grade 2 exhibits upper and lower limits of 1 J/mm^2 to 1.875 J/mm^2 at room temperature (i.e. at approximately 20˚C).

Table 4.1 : Amount of energy absorbed by specimens at different temperatures (sub – standard)

ID	Description	Temp. (˚C)	Energy absorbed (J)	Avg Energy absorbed (J)	Avg Joules / mm^2
1	Parent Plate	21.4	24.20	27.20	1.063
2	Parent Plate	21.4	30.20		
3	Laser Bent	21.4	13.85	13.85	0.541
4	Laser Bent	21.4	13.85		
5	Laser Mechanical Bent	21.4	14.10	15.95	0.623
6	Laser Mechanical Bent	21.4	17.80		
7	Mechanical Bent	21.4	25.80	24.80	0.969
8	Mechanical Bent	21.4	23.80		
9	Parent Plate	-39.8	20.00	20.00	0.781
10	Parent Plate	-38.7	20.00		
11	Laser Bent	-39.8	11.20	11.60	0.453
12	Laser Bent	-39.0	12.00		
13	Laser-Mechanical Bent	-38.8	10.80	11.40	0.445
14	Laser-Mechanical Bent	-39.9	12.00		
15	Mechanical Bent	-39.2	16.00	18.90	0.738
16	Mechanical Bent	-38.4	21.80		

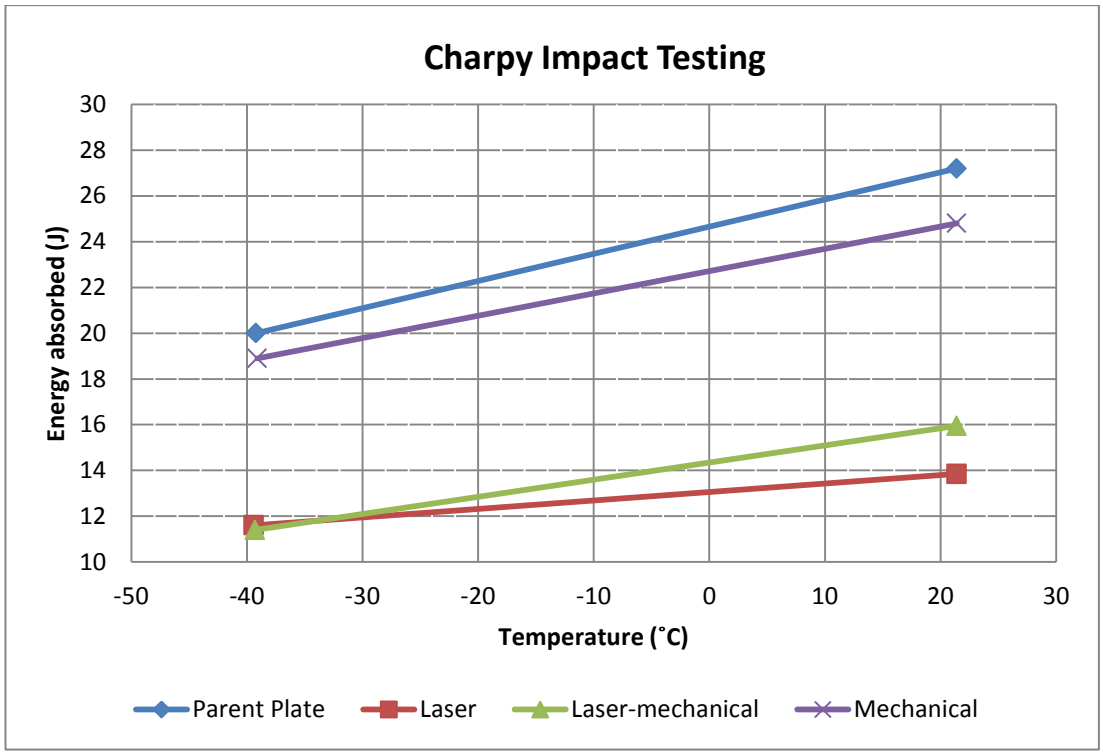

Figure 4.11 : Illustrating of the relationship between energy absorbed and temperature (in specific room temperature and -40ºC)

Figure 4.12 to Figure 4.15 (pp 79 - 80) show the typical fracture surface appearance after impact testing at room temperature. As shown for the parent plate and all three bending processes, the nature of the specimen surfaces is mainly ductile (cup and cone/tearing). No major brittle (cleavage) fracture regions could be detected on the surfaces evaluated.

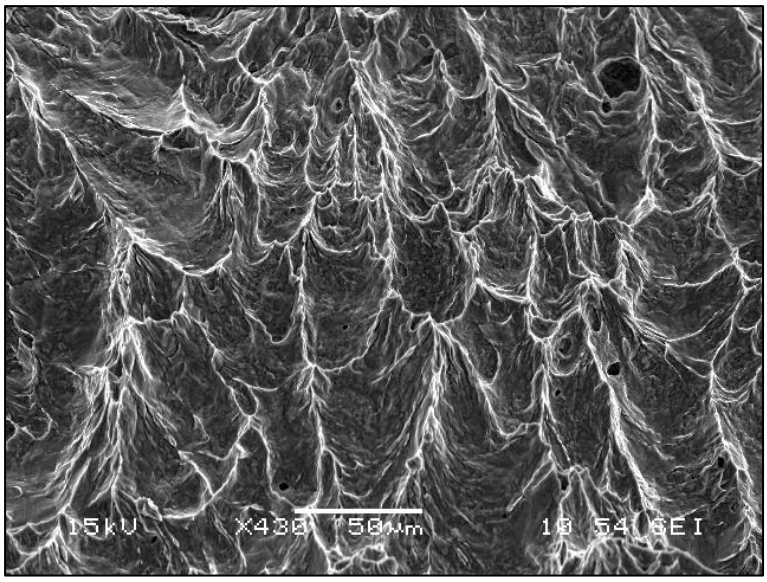

Figure 4.12 : Charpy impact surface of the parent plate specimen

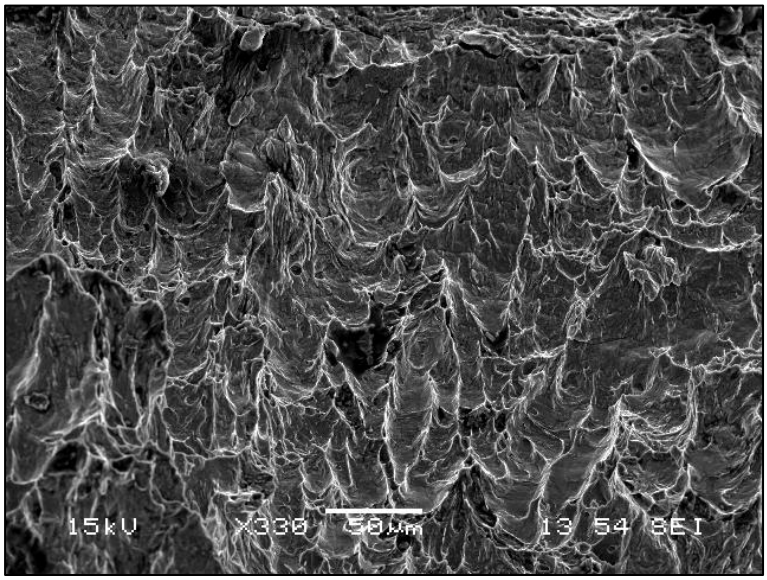

Figure 4.13 : Charpy impact surface of the laser formed specimen

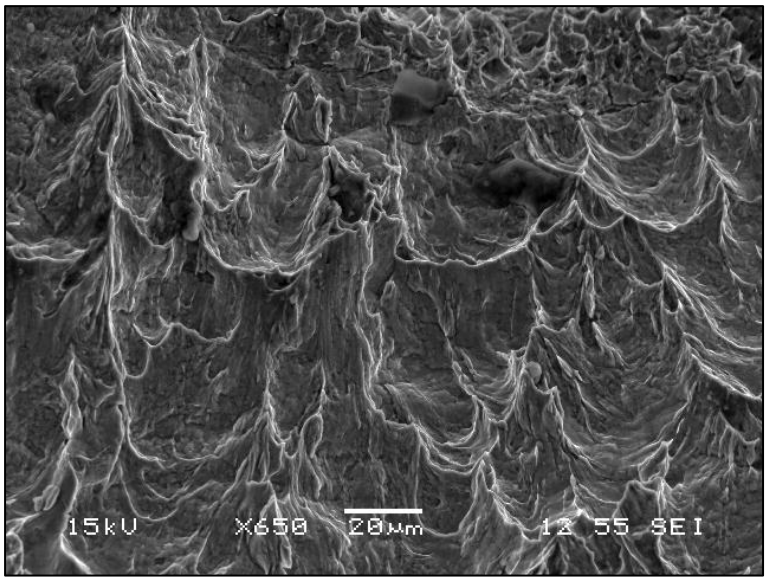

Figure 4.14 : Charpy impact surface of mechanically formed specimen

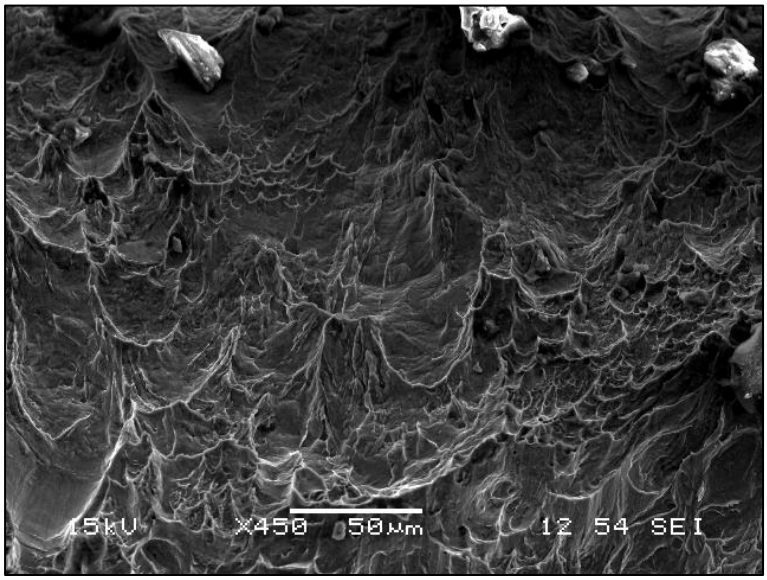

Figure 4.15 : Charpy impact surface of laser-mechanically formed specimen

4.5 Residual stress data

Following the ASTM E837-01-standards [31], the residual stress was recorded for the parent plate specimens and for all three forming methods. For the forming processes residual stress measurements were performed on the inner radius (i.e. with a 118.4 mm radius of curvature) and outer radius (i.e. with a 121.6 mm radius of curvature) of the specimens. Furthermore, the Uniform Stress Method [33] was used to compare the results obtained from the various samples. The actual results obtained regarding the magnitude and directions of the principal relieved stresses as calculated according to ASTM E837-01-standards are tabulated in Appendix F (p 161).

4.5.1 Parent plate

Figure 4.16 (p 82) shows the strain relaxation curves of the parent plate specimen that was recorded at all three strain gauges during the hole drilling method. Gauge 1 and 2 evened out at a depth of approximately 1.5 mm whereas gauge 3 continued to decrease in value until a depth of approximately 1.8 mm.

Figure 4.17 (p 82) illustrates the maximum and minimum principal stresses (according to ASTM E837-01-standards) versus hole depth drilled. The maximum stress measured at a depth of approximately 2 mm, is 60.51 MPa. The maximum and minimum principal stresses are tensile stresses throughout the specimen.

From here on only the principal stress data will be shown. All the strain data is included in Appendix F.

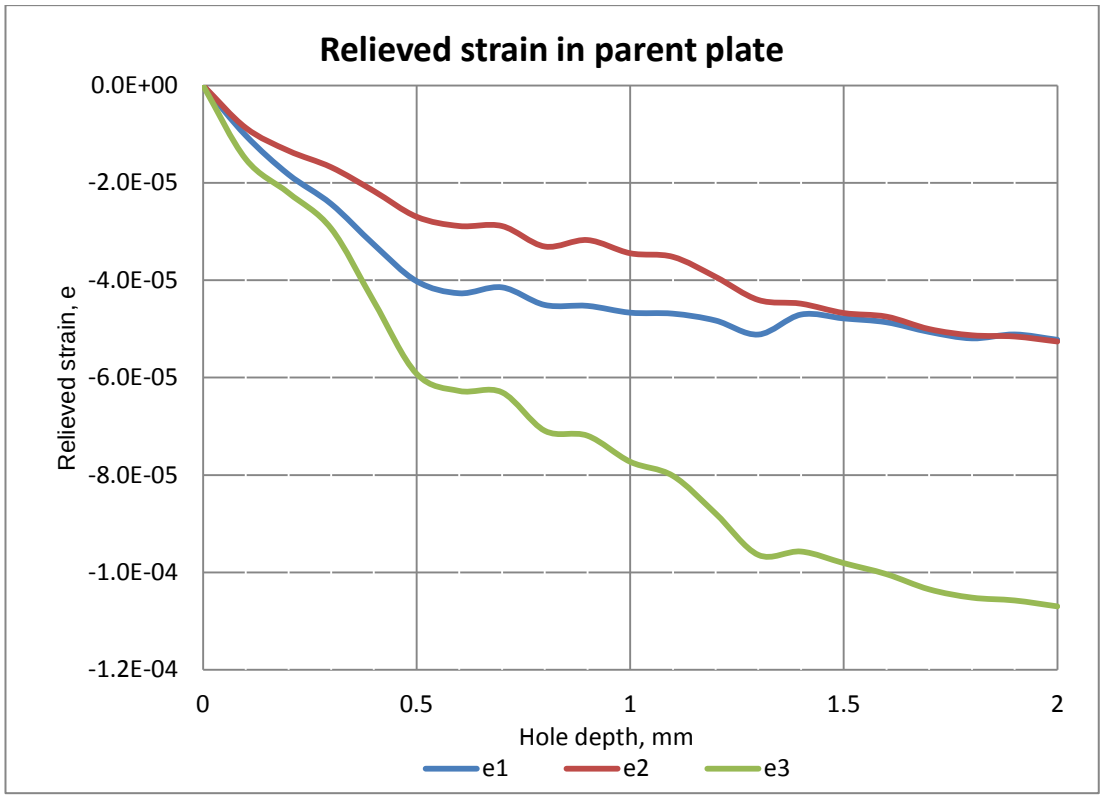

Figure 4.16 : Strain relaxation curve as a function of drilling depth of the parent plate specimen

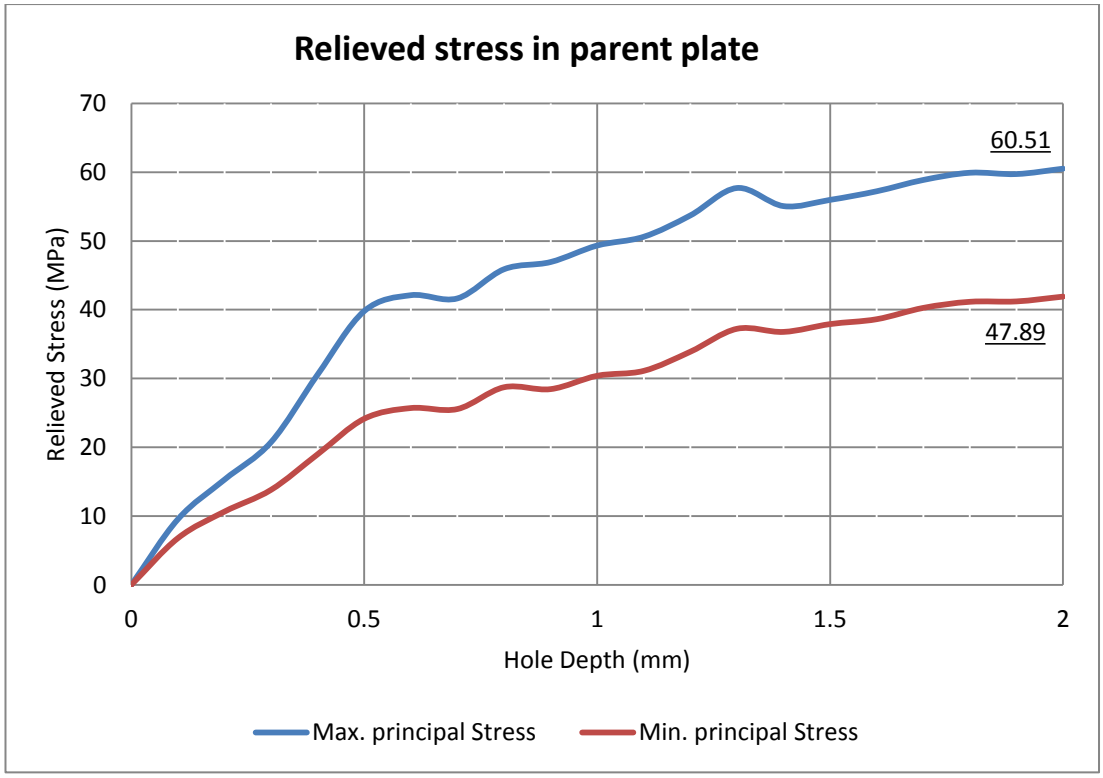

Figure 4.17 : Plot of relieved residual stress versus hole depth of the parent plate specimen

4.5.2 Laser formed

For comparative purposes, this section will be divided into two sections, namely inner radius and outer radius.

4.5.2.1 Inner radius

Figure 4.18 shows the stress relaxation as a function of hole depth for the laser formed specimen. The highest residual stress recorded was 109.34 MPa at a depth of approximately 1.3 mm. Both maximum and minimum principal stresses stabilized at a depth of approximately 1 mm.

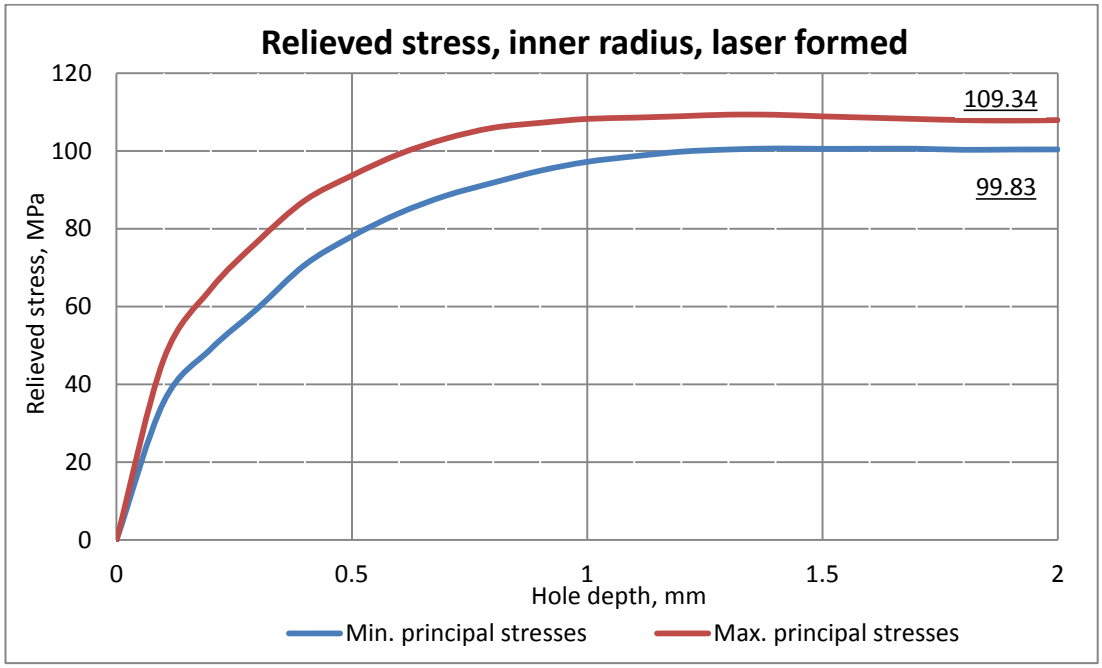

Figure 4.18 : Relieved residual stress versus hole depth – inner radius, laser formed specimen

4.5.2.2 Outer radius

Figure 4.19 shows the stress relaxation as a function of hole depth for the laser formed specimen. The maximum residual stress recorded was 53.94 MPa at a depth of approximately 1.3 mm. Both maximum and minimum principal stresses are tensile and stabilized at a depth of approximately 1.3 mm.

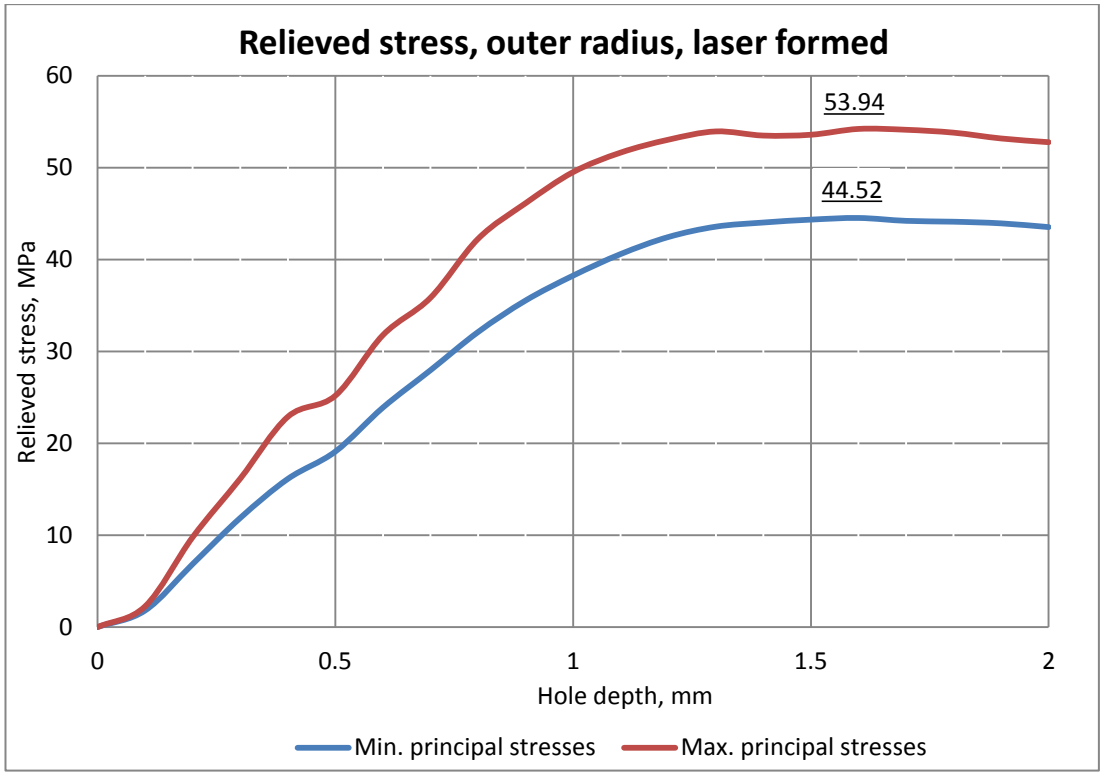

Figure 4.19 : Plot of relieved residual stress versus hole depth – outer radius, laser formed specimen

4.5.3 Mechanically formed

As in the previous section, this section will be divided into two sections, namely inner radius and outer radius.

4.5.3.1 Inner radius

Figure 4.20 illustrates the relaxation of residual stress at the inner radius of the mechanically formed specimen. The measurement was performed at the apex of the formed specimens for both the inner radius and outer radius. The data recorded indicates that all the residual stresses are tensile stresses. The maximum principal stress was observed at a depth of 1.9 mm (87.44 MPa) whereas the minimum principal stresses stabilized at a depth of approximately 1 mm.

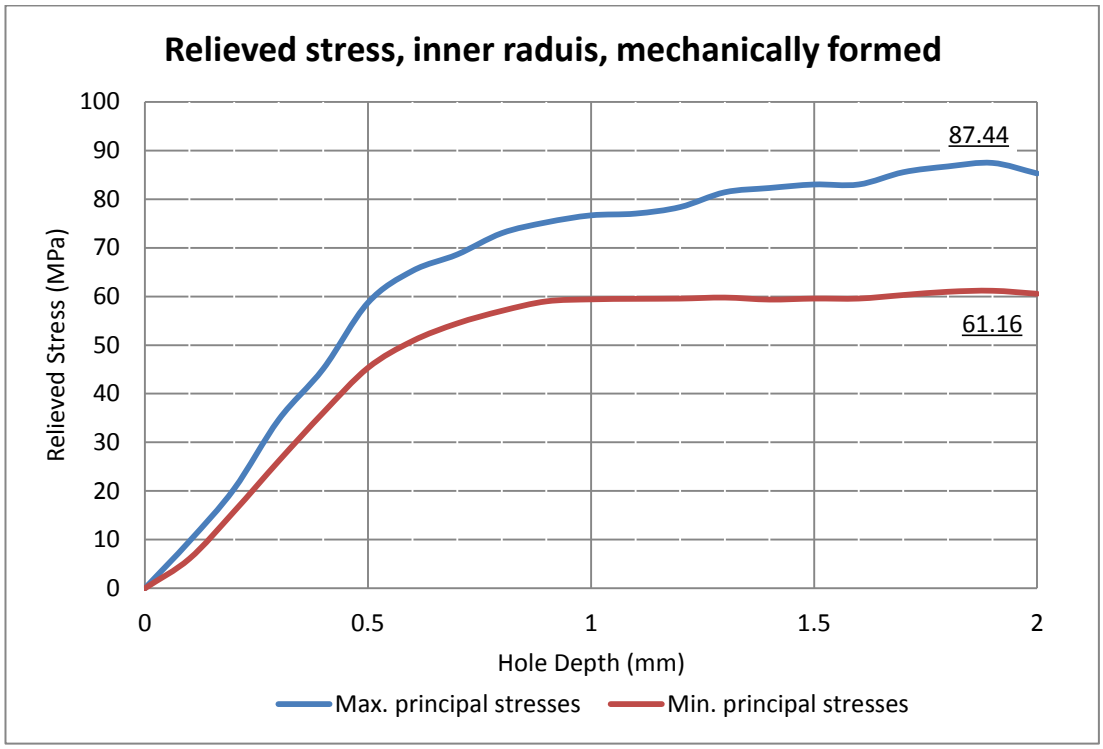

Figure 4.20 : Relieved residual stress versus hole depth – inner radius, mechanically formed specimen

4.5.3.2 Outer radius

Figure 4.21 shows the stress relaxation as a function of hole depth for the mechanically formed specimen. The outer radius was recorded at the apex. The maximum principal stress behaves somewhat erratic but this can be attributed to the forming process (stretch forming - press brake forming method (tool & die)). The maximum stress was recorded as 9.47 MPa, whereas the minimum principal stress reached a maximum at a depth of approximately 0.3 mm.

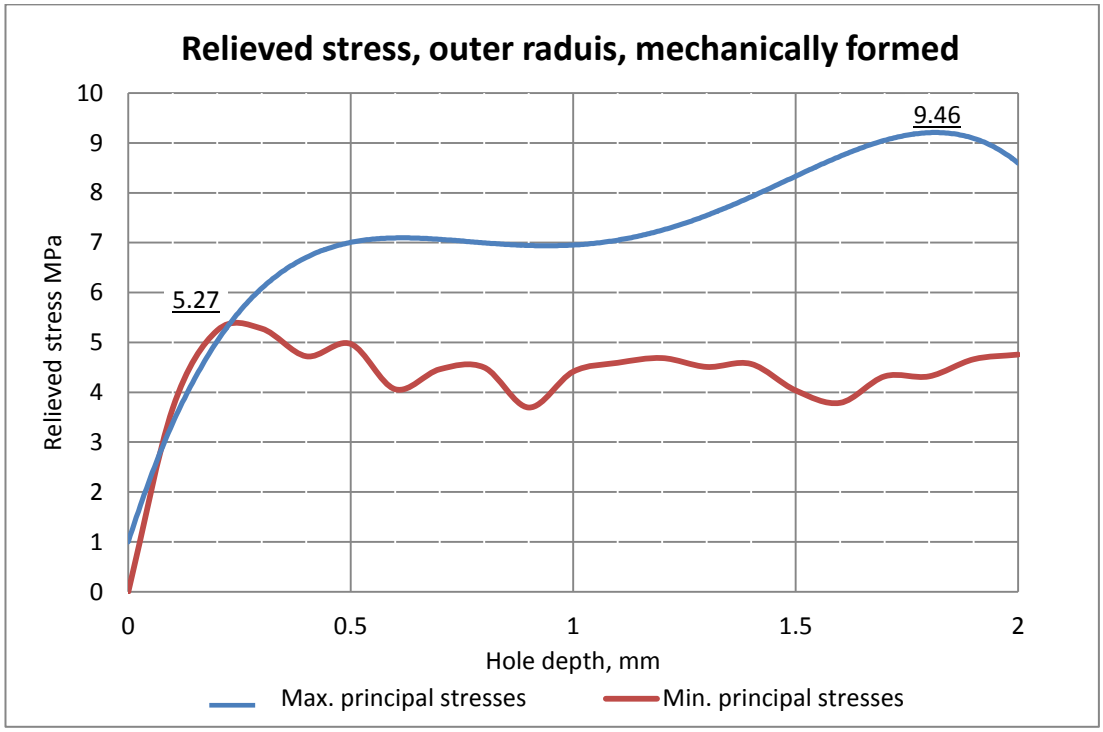

Figure 4.21 : Relieved residual stress versus hole depth – outer radius, mechanically formed specimen

4.5.4 Laser-mechanically formed

Once again, for comparative purposes this section will be divided into two sections, namely inner radius and outer radius.

4.5.4.1 Inner radius

Figure 4.22 illustrates the stress relaxation as a function of hole depth for the laser-mechanically formed specimen. The maximum recorded stress was found to be approximately 87.76 MPa. Both maximum and minimum principal stresses stabilized at a depth of approximately 1.1 mm. When comparing laser-mechanically formed specimen stresses to that of mechanically formed specimens, the maximum stress value is virtually identical. However, the gradient of the laser-mechanically formed specimens is much greater at a depth of zero to 1.1 mm. Both principal stresses were found to be tensile stresses.

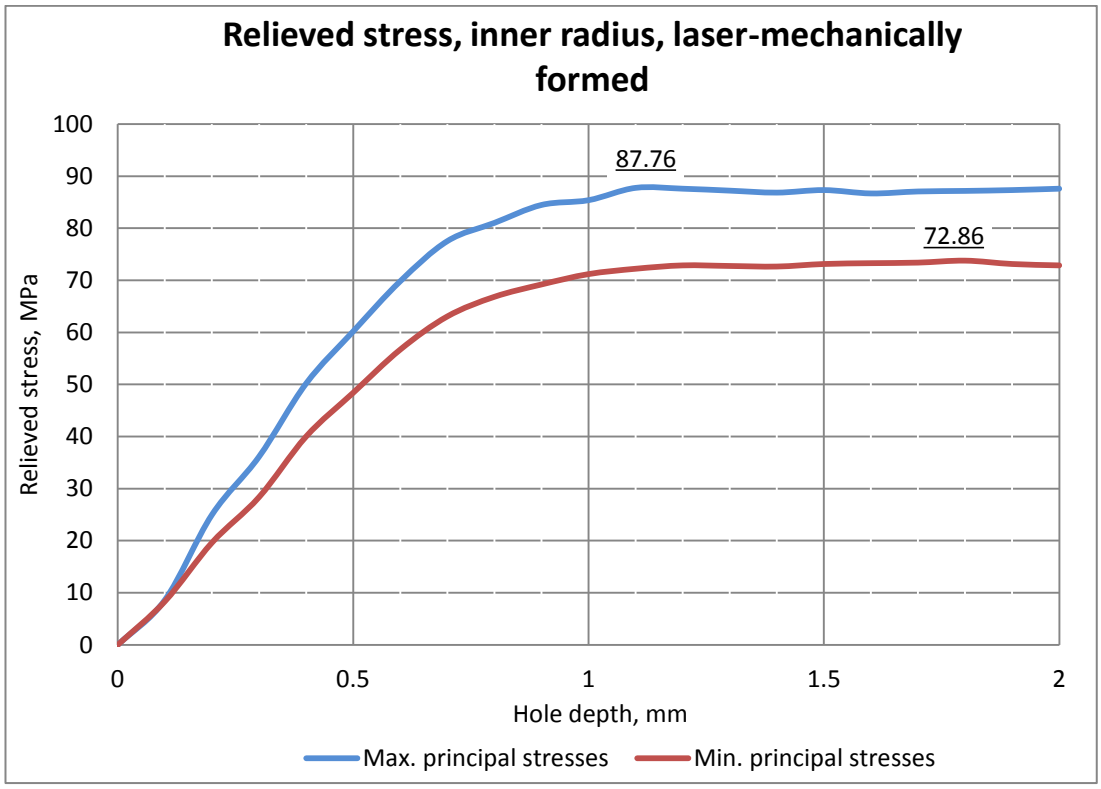

Figure 4.22 : Relieved residual stress versus hole depth – inner radius, laser-mechanically formed specimen

4.5.4.2 Outer radius

Figure 4.23 shows the stress relaxation as a function of hole depth for the laser-mechanically formed specimen. Similarly, but to a lesser degree than the mechanically formed outer surface, the residual stress appear to be erratic. Again this can be attributed to the forming process (stretch forming - press brake forming method (tool & die)). The maximum stress relieved was recorded to be 23.99 MPa at a depth of approximately 2 mm. Furthermore, Figure 4.23 also shows that the residual stresses are in compression from a depth of approximately 0 mm to a depth of approximately 0.8 mm after which they become both tensile stresses.

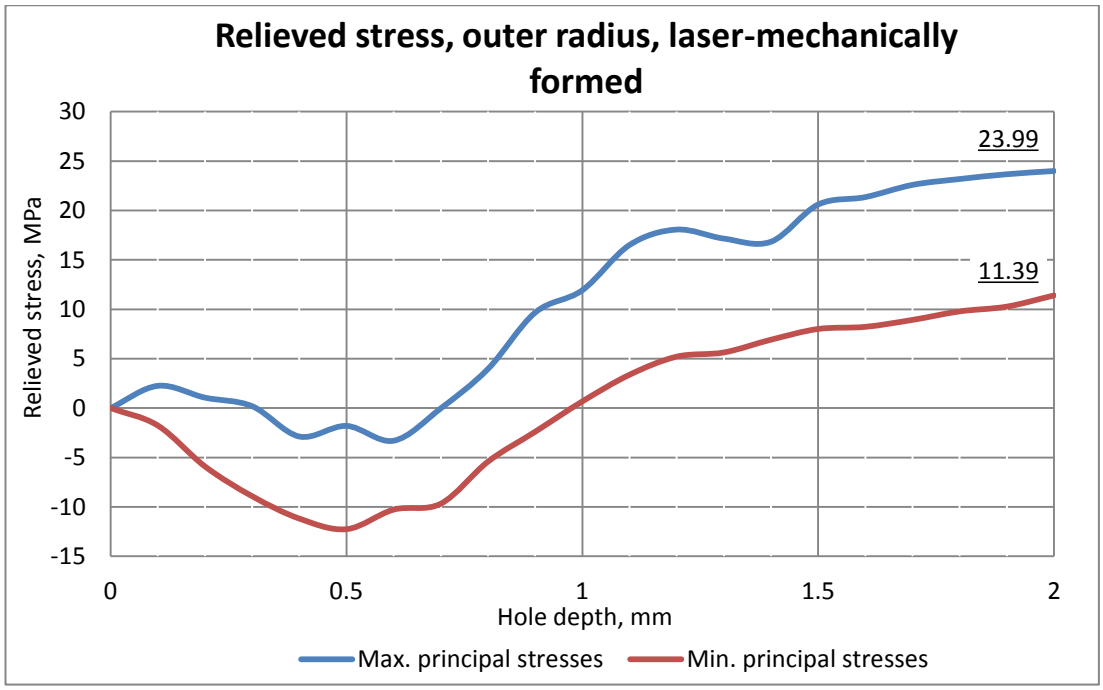

Figure 4.23 : Relieved residual stress versus hole depth – outer radius, laser-mechanically formed specimen

4.5.5 Combined residual stress graphs

Figure 4.24 shows the stress relaxation as a function of hole depth drilled for the parent plate and all formed specimens at the top surface or outer radius of curvature (i.e.121.6 mm). Using the parent plate as reference, it is evident that the laser formed specimen reached a similar stress relaxation. Noting that the laser formed specimen was irradiated on the opposite side of the specimen (i.e. on the inner radius) and that it did not experience the same heat input, it reached a relative average residual stress. The laser-mechanically and laser formed specimens, in turn, reached similar values. It may be considered that the stretch forming - press brake forming method (tool & die) induced compressive stresses on the top and/or bottom surface. However, the laser-mechanically formed specimen achieved slightly higher values due to the lower forming curvature it experiences (240 to 120 mm).

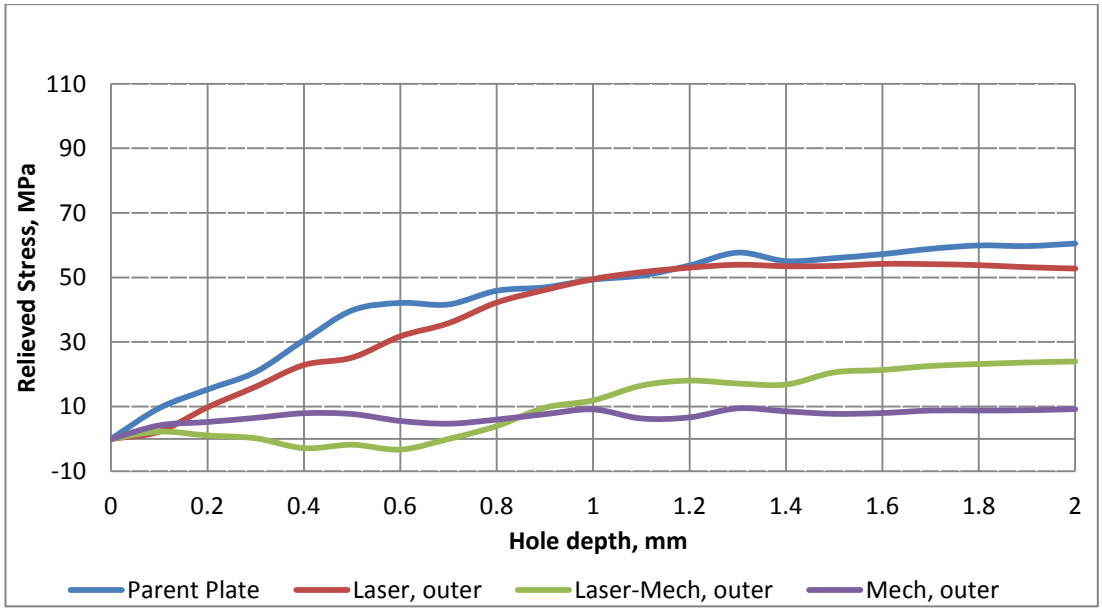

Figure 4.24 : Combined outer (top) relieved residual stress of parent plate and formed samples

Figure 4.25 shows that the stress relaxation as a function of hole depth drilled for the parent plate and all formed specimens at the bottom surface or inner radius of curvature (i.e. 118.4 mm). Also in this case, when considering the parent plate as reference, it can be observed that the laser formed specimen gives the highest residual stress value of all the forming processes. Considering the forming process of laser forming (i.e. with the aid of thermal stresses) a higher residual stress value than average stresses is expected.

When considering the mechanically and laser-mechanically formed specimens, similar stress values are once again reached when compared to one another. However, opposite to the top surface, the stretch forming - press brake forming method (tool & die) induced tensile stresses into the bottom (inner) surface, although the laser-mechanically formed specimen attained a slightly higher stress relaxation which may be attributed to the laser forming process inducing higher stresses.

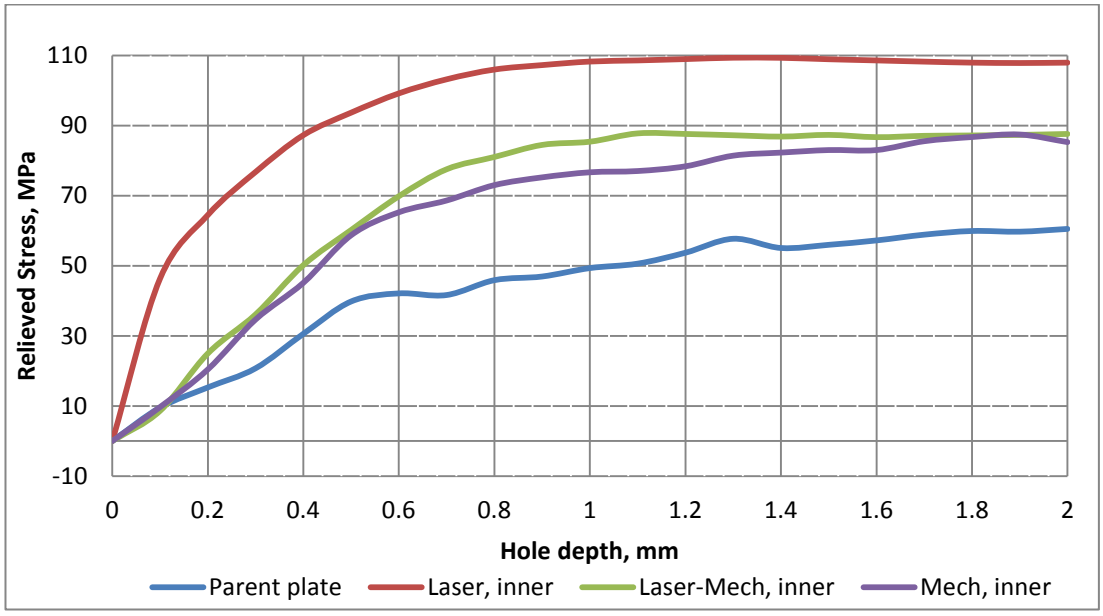

Figure 4.25 : Combined inner (bottom) relieved residual stress of parent plate and formed samples

Table 4.2 gives the maximum stress relaxation of each forming process at each specific depth drilled considering the inner curvatures.

Table 4.2 : Maximum stress values for each forming process at each specific depth for inner curvatures

Forming Process	Maximum stress (MPa)	Depth at which maximum stress is recorded (mm)
Parent Plate	60.514	2.0
Laser	109.34	1.3
Mechanical	87.44	1.9
Laser-Mechanical	87.76	1.1

4.6 Fatigue testing

Life prediction, fatigue results, fatigue models of the parent plate and all three bending processes will be investigated below.

4.6.1 Life prediction method according to Juvinall and Marshek

The Juvinall and Marshek method [9] was used to determine an estimated theoretical fatigue life of the CP Ti grade 2 specimen (ductile material). For this life prediction model a set of two data points is needed. An load setting is calculated (vertical axis) which corresponds with 1000 cycles (horizontal axis) on the graph (Figure 4.26, p93). A second applied loading was calculated which corresponds with approximately 5 x 10^6 cycles (as stated in Section 2.4 (p 17). Titanium exhibits a true endurance limit between 10^6 and 10^7 cycles, hence, a midpoint was selected). A straight line is then drawn between the two data points indicating a theoretical S-N curve for CP Ti grade 2.

The fatigue load was determined as follows:

For 1000 cycles:

$$S_{1000} = 0.9 \times S_{uts}$$

$$S_{1000} = 0.9 \times 452 \times 10^6 = \mathbf{406.8\ MPa}$$

For 5x10^6 cycles:

$$S_{5\times10^6} = 0.5 \times S_{uts} \times Surface\ factor$$

$$S_{5\times10^6} = 0.5 \times 452 \times 10^6 \times 0.7 = \mathbf{158.2\ MPa}$$

Plotting the calculated points on a normal-log scale resulted in the curve shown in Figure 4.26 (p 93). Life prediction can now be determined by using the following logarithmic function obtained for the straight line in Figure 4.26 for 1000 to 5x10^6 cycles:

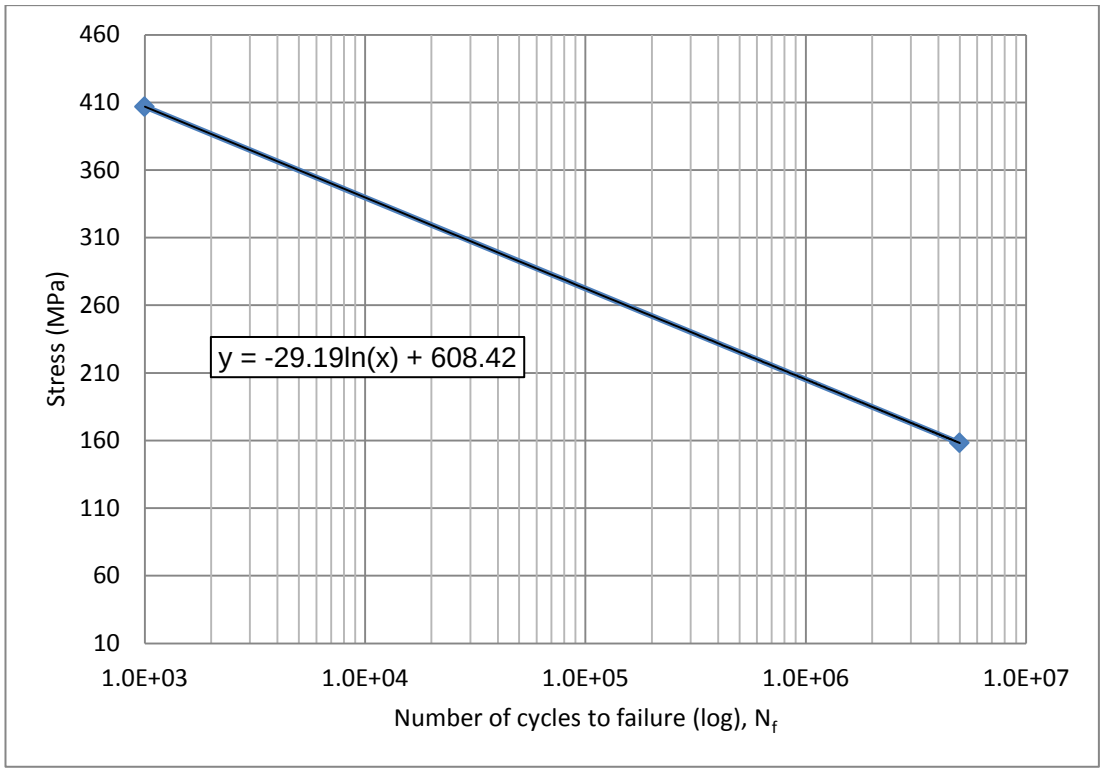

Figure 4.26 : Estimated S-N curve for CP Ti grade 2

$$S_n = -29.19 \ln(N_f) + 608.42 \quad . \qquad (4.1)$$

When comparing the estimated S-N curve (Figure 4.26) with literature ((Figure 2.8 (p 23)) it is evident that titanium has a unique fatigue curve behaviour, especially at 10^5 cycles. Therefore, one would expect an increased difference between the estimated and actual S-N fatigue curve, especially at high cycles. Therefore, the stress amplitude were selected (from Figure 4.26 which is similar to Figure 2.8) so that the number of cycles to failure will not be less than 10^4 cycles (i.e. the stress life approach). Interest is drawn to approximate 10^5 cycles to failure due to the unique fatigue curve at that point. Therefore, stress amplitudes were determined via trial and error, but the estimated S-N curve was used to determine a preliminary point as a Figure 2.8 was for a higher grade CP Ti. The reason is that after 10^5 cycles the behaviour of the curve flattens out which gives the impression that the endurance limited has been reached.

4.6.2 Parent plate

The following results were obtained by fatigue testing of the parent, mechanically, laser-mechanically and laser bent specimens subjected to the criteria of R= -1 (or as close as possible) or conditions close to zero mean stress i.e. A=∞.

The fatigue samples were tested at a minimum of three different loads in order to obtain a representative fatigue curve. The results obtained for the parent plate are shown in Table 4.3 and Figure 4.27 (p 95). The stress amplitude (indicated as percentage yield) and ultimate tensile strength (also indicated as a percentage) are shown in the first column of Table 4.3.

Table 4.3 : Fatigue data of parent plate specimens

Stress amplitude (MPa)	Number of cycles (N_f)	Standard deviation (N_f)	Average number of cycles to failure (N_f)
350.0 (99.4% of yield / 77.9% of UTS)	55158 44945 55471 50043 37313	16723.53	45420
241.5 (68.6% of yield / 53.4% of UTS)	45442 75469 60122 90831 60423	17273	66457
231.0 (65.5% of yield / 51% of UTS)	104780 95000 81587 75633 78164	14688	88115

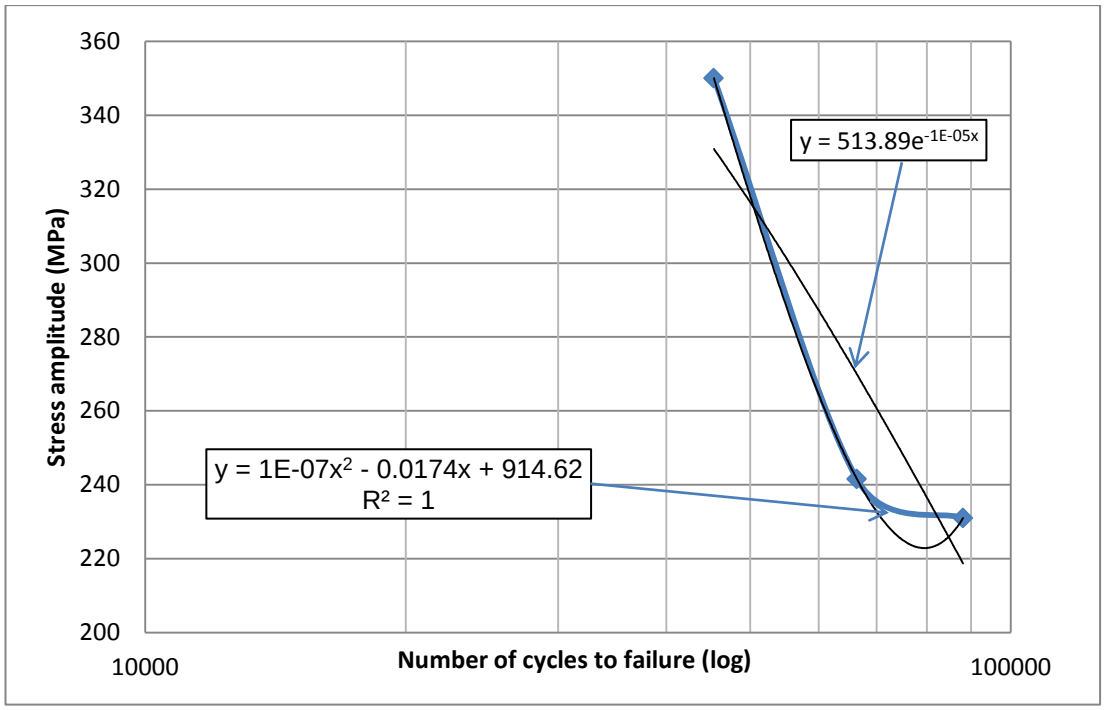

Figure 4.27 : S-N curve (plotted with average results) for the parent plate specimen

The applied loading was chosen so that the sample reaches approximately 100 000 cycles to failure (low load, i.e. at approximately 231 MPa). As can be observed from Figure 4.27, the first portion of the fatigue life decrease drastically and follows more or less a straight line between the first two loads. Thereafter the decrease in life is less drastic. This trend was also observed by Boyer [10] (Figure 2.8, p 28) where CP titanium shows a drastic change in slope beyond 10^5 cycles i.e. the slope levels off. Due to the significant change in slope at the lower loads, the small change in magnitude between load 2 and load 3 will result in a relatively large difference in fatigue life i.e. in the value of N_f.

The trendline equation for the second order polynomial indicated in Figure 4.27 follows closely the trend of the actual data at the higher load settings, whereas, the trendline tends to under-predict the actual curve at lower load settings. This trendline was the best fit obtained for the actual data. The trendline shown in Figure 4.27 for the exponential curve will be explained in subsequent section.

4.6.3 Laser formed

All the laser formed specimens were curved to an approximate radius of 120 mm although curvatures varied from 118 to 126 mm. Table 4.4 and Figure 4.28 (p 97) show the actual fatigue data obtained from fatigue tested laser formed specimens. The loading was approximately identical to that of the parent plate. Also in Figure 4.28 two trendlines are shown. Although the logarithmic curve appears to be less accurate, its R^2-value is closer to unity than that of the exponential curve. The latter curve will be used for further trend analysis in a subsequent section.

Table 4.4 : Fatigue data of laser formed specimens

Stress amplitude (MPa)	Number of cycles (N_f)	Standard deviation (N_f)	Average number of cycles to failure (N_f)
350.0 (99.4% of yield / 77.9% of UTS)	13596 13605 13816 14007 14457	2923	14242
241.5 (68.6% of yield / 53.4% of UTS)	30355 37714 39035 35717 30842	7645	36526
231.0 (65.5% of yield / 51% of UTS)	41111 38657 34713 35316 42735	6437.9	40801

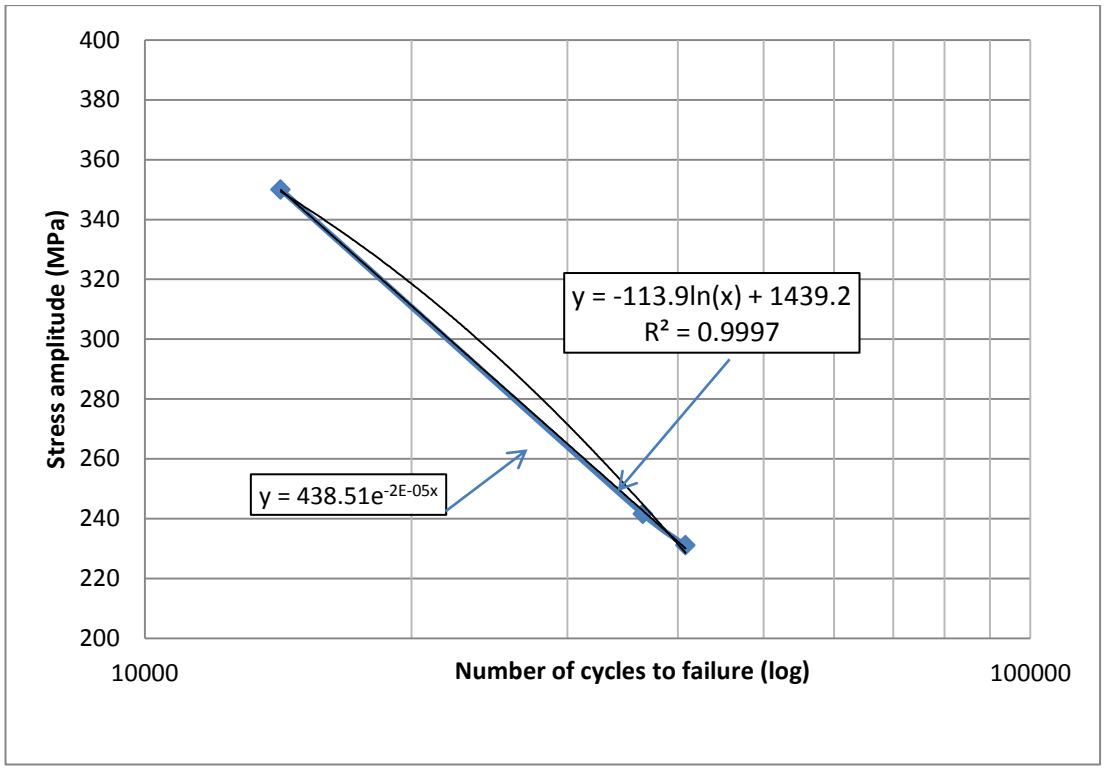

Figure 4.28 : S-N curve (plotted with average results) for the laser formed specimen

Considering all the forming processes, the laser formed specimens performed superior at the highest load setting although it performed the weakest at the middle and lowest load setting when considering fatigue testing. This could be due to the fact that no twinning was observed after forming, therefore crack initiation was slower to develop. When considering the lower load setting, it can be observed that crack propagation develops quickly within the Widmanstätten structure. This phenomenon was also encountered by Matthew and Donachie [12] where the equiaxed microstructure achieved more cycles before failure than that of the lamellar microstructure.

4.6.4 Mechanically formed

The mechanically formed specimens was formed to a radius of approximately 120 mm, and tested to approximately identical load settings as that of the parent plate. The results of the fatigue data is displayed in Table 4.5 and in Figure 4.29 (p 99). Also in this case two trendlines are shown. The logarithmic curve in Figure 4.29 provides the best fit for the experimental data obtained. The exponential curve will again be addressed in a subsequent section.

Table 4.5 : Fatigue data of mechanically formed specimens

Stress amplitude (MPa)	Number of cycles (N_f)	Standard deviation (N_f)	Average number of cycles to failure (N_f)
350.0 (99.4% of yield / 77.9% of UTS)	9856 11258 13707 10994 12471	1610	11281
241.5 (68.6% of yield / 53.4% of UTS)	49831 47907 43997 52763 49363	5935	46649
231.0 (65.5% of yield / 51% of UTS)	62023 60128 67050 68396 59573	4469	64504

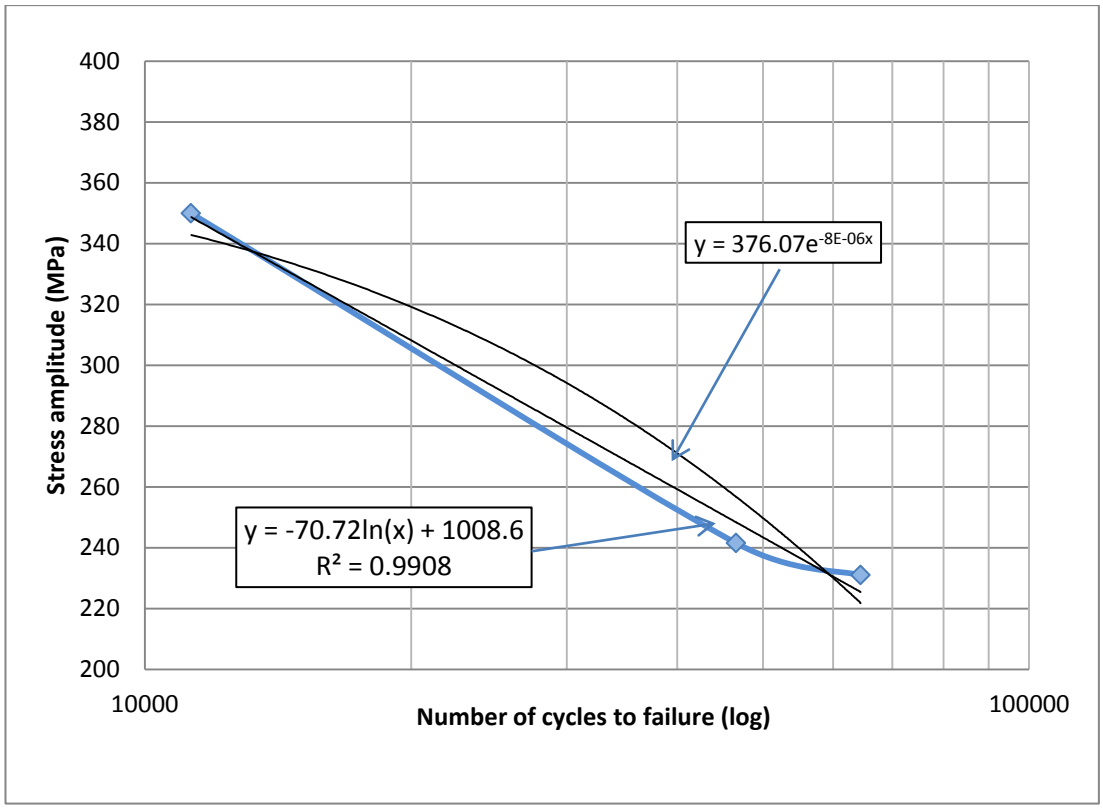

Figure 4.29 : S-N curve (plotted with average results) for the mechanically formed specimen

Compared to the original parent plate specimens, the mechanically formed specimens show a decrease in fatigue life with respect to the number of cycles to failure. The decrease in fatigue life for the same load setting could be attributed to the microstructure that exhibits twinning induced by the forming process. The excessive twinning may lead to earlier crack initiation combined with fast crack growth due to the high load applied.

4.6.5 Laser-mechanically formed

Specimens were deformed using a CO_2 laser to an approximate radius of 240 mm, after which it was mechanically formed to an approximate radius of curvature of 120 mm. Table 4.6 and Figure 4.30 (p 101) show the actual fatigue data obtained by fatigue testing the laser-mechanically formed specimens to approximately identical load settings to that of the parent plate specimens. Once again, the logarithmic curve in Figure 4.30 provides the best fit to the experimental data obtained. The exponential curve will be discussed in a subsequent section.

Table 4.6 : Fatigue data of laser-mechanically formed specimens*

Stress amplitude (MPa)	Number of cycles (N_f)	Standard deviation (N_f)	Average number of cycles to failure (N_f)
350.0 (99.4% of yield / 77.9% of UTS)	19133 13575 11105 9714	4153	13382
241.5 (68.6% of yield / 53.4% of UTS)	46691 36971 42424 44315	4139	42600
231.0 (65.5% of yield / 51% of UTS)	60541 48237 65383 49832	8306	55998

*** Only 4 specimens were tested due to a limited number of formed samples for the laser-mechanically formed process.**

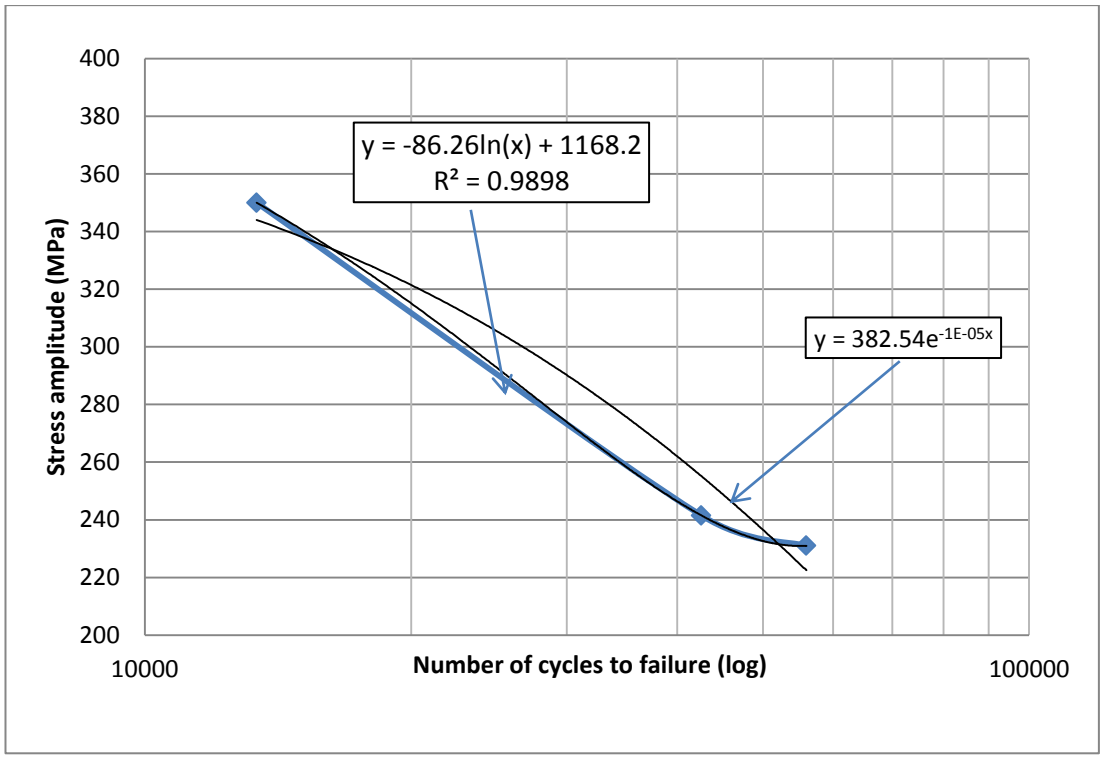

Figure 4.30 : S-N curve (plotted with average results) for the laser-mechanically formed specimen

4.6.6 Combined Graphs

In order to compare the fatigue life of the parent plate and formed specimens, all the S-N curves presented in Figure 4.27 to Figure 4.30 are shown on the same plot in Figure 4.31 (p 102). This gives a better visual comparison of the fatigue behaviour in terms of the functional dependence of the various forming processes on the number of cycles to failure.

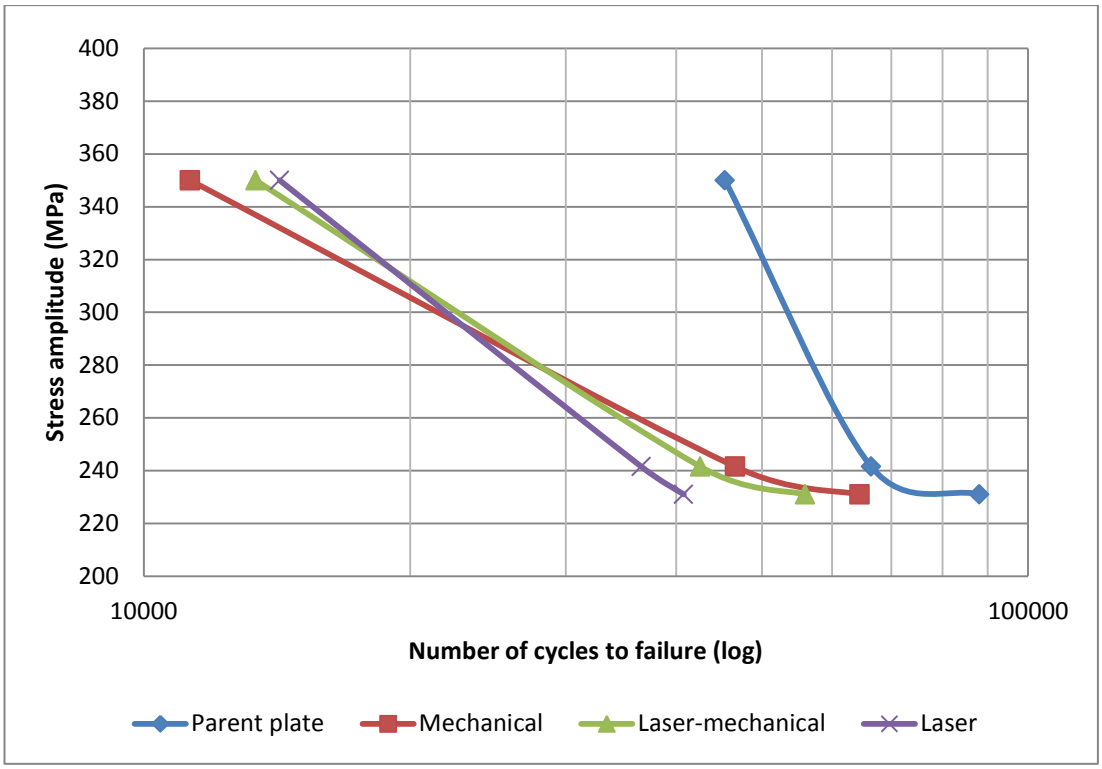

Figure 4.31 : S-N curves plotted (with average results) of all three forming processes and the parent plate specimens

Table 4.7 gives a quantitative comparison of all three forming processes and the parent plate and represents the average number of cycles to failure at the various load settings.

Table 4.7 : Average number of cycles to failure at the various load settings

Load (percentage yield)	Parent plate	Laser formed	Mechanically formed	Laser-mechanically formed
Load 1 (99.4%)	45420	14242	11281	13382
Load 2 (68.6%)	66457	36526	46649	42600
Load 3 (65.5%)	88115	40801	64504	55998

Table 4.8 illustrates the percentage decrease of cycles to failure compared to the parent plate as reference i.e. 100%. The largest percentage decrease (i.e. regarded as the worst) can be seen at load 1 (i.e. the highest load) where the mechanically formed specimens achieved 74.3% less cycles to failure than that of the parent plate. The smallest difference (i.e. regarded as the best) of 28% (load 3, i.e. the lowest) is achieved for the mechanically formed specimens in comparison to that of the parent plate. At the lowest load setting the mechanically formed specimens achieved 63434 cycles which is 28% less than that of the parent plate.

Table 4.8 : Percentage decrease in life cycles compared to the parent plate specimens

Load (percentage yield)	Parent plate	Laser formed	Mechanically formed	Laser-mechanically formed
Load 1 (99.4%)	100%	69.4%	74.3%	70.5%
Load 2 (68.6%)	100%	45%	26.6%	35.9%
Load 3 (65.5%)	100%	56.3%	28%	36.4%

The laser-mechanically formed specimens performed slightly better than that of the mechanically formed specimens at the highest load setting (13382 vs. 11657). However, a reduction of 70.5% is observed in cycles compared to that of the parent plate at the highest load. The laser-mechanically formed specimens produced 11.7% less cycles to failure at the lowest load setting compared to that

of the mechanically formed specimens. On the other hand, the laser-mechanically formed specimens produced 36.4% less cycles to failure than that of the parent plate specimens at the lowest load setting. The fact that it performed superior to that of the mechanically formed specimens, could be attributed to the fact that the twinning of the specimens were of a lesser degree, due to the half mechanical process. In addition, no twinning was observed in the Widmanstätten structure at the inner radius.

Figure 4.32 illustrates graphically the percentage cycles until failure compared to that of the parent plate. For example, at load 1 (i.e. the highest load) the mechanically formed specimens only achieved 25.7% cycles compared to that of the parent plate (100%) (i.e. 11657 vs. 45420).

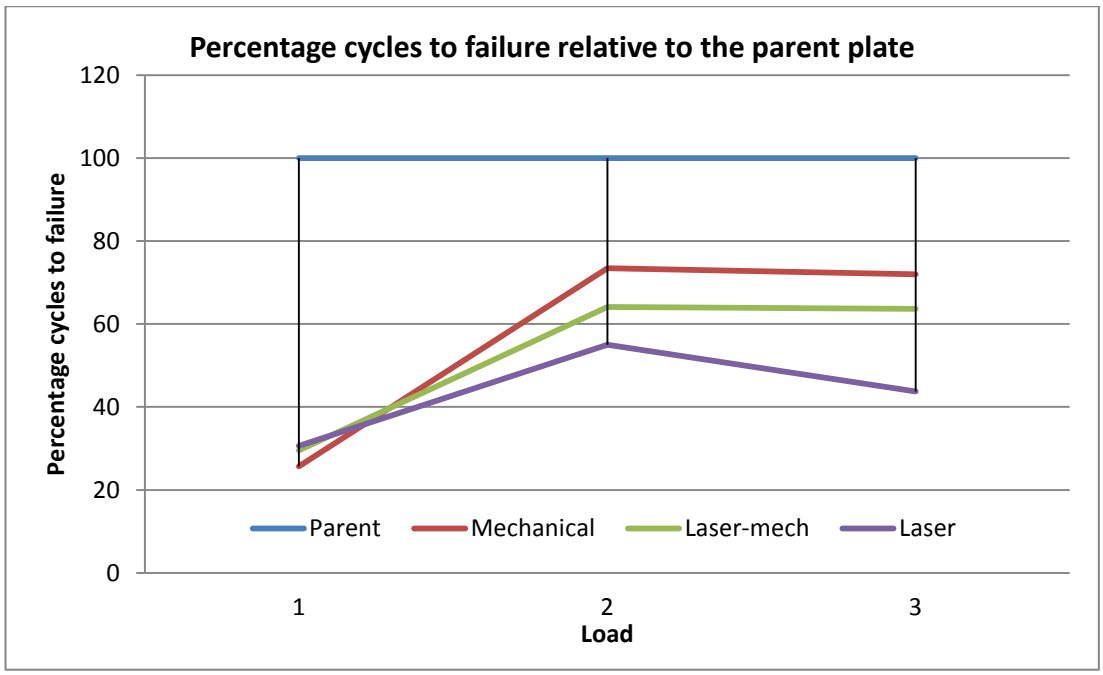

Figure 4.32 : Percentage cycles to failure relative to the parent plate specimen

4.6.7 Theoretical models to predict fatigue life

Theoretical fatigue models were used to determine whether the experimental data generated for fatigue life has the same dependence on the number of cycles to failure than that predicted by the models. These models are: The Gerber, Soderberg, Goodman and Morrow models [4].

Using the equations as defined in Sections 2.3 and 2.6 (pp 14 and 18, respectively), the mean stress and alternating stress for each loading condition will be determined. The effective mean stress ($S_{eff\ mean}$) will include residual stress. The residual stress that will be used in the effective mean stress calculations for the models is extracted from Section 4.5 (p 81). It has been found that all the maximum residual stress values were measured at the inner radius of all formed samples. The following calculations were performed with the parent plate values in order to calculate the theoretical model behaviour:

The mechanical properties of CP Ti grade 2 required are the ultimate tensile strength, S_u = 452 MPa and yield strength, S_y = 352 MPa.

The alternating stress at 99.4% of the yield strength for the parent plate is given by:

$$\sigma_a = \frac{\sigma_{max} - \sigma_{min}}{2}$$

$$= \frac{350.385 - (-350)}{2}$$

$$= 350.193\ \text{MPa} \quad . \qquad (4.2)$$

σ_{max} and σ_{min} respectively denote the higher and lower values recorded on the master sample as describe in Section 3.8.3 (p 64) and Appendix E (p 158).

The mean stress at 99.4% of the yield strength for the parent plate leads to

$$\sigma_{\text{mean}} = \frac{\sigma_{\max} + \sigma_{\min}}{2}$$

$$= \frac{350.385 + (-350)}{2}$$

$$= \mathbf{0.193\ MPa} \quad . \tag{4.3}$$

The effective mean stress at 99.4% of the yield strength for the parent plate is given by

$$\sigma_{eff\ mean} = \frac{\sigma_{max} + \sigma_{min}}{2} + \sigma_{residual\ stress\ max}$$

$$= \frac{350.385 + (-350)}{2} + 69.16$$

$$= \mathbf{69.352\ MPa} \quad . \tag{4.4}$$

A typical sample calculation for the fatigue models is given below. According to the Gerber model, the effective average stress at the endurance limit at an applied stress of approximately 350 MPa (which includes the residual stress) is given by:

$$S_{n_{eff\ mean}} = \frac{\sigma_a}{1 - \left[\frac{\sigma_{eff\ mean}}{S_u}\right]^2}$$

$$= \frac{350.193}{1 - \left[\frac{69.352}{452}\right]^2}$$

$$= \mathbf{358.636\ MPa} \quad . \tag{4.5}$$

These calculations were used to predict the fatigue life results according to the Gerber, Soderberg and Goodman models of which the results are displayed in Table 4.9. However, Bannantine, Comer and Handrock [4] indicate that the Soderberg model is very conservative and seldomly used and that the Morrow model is used when the ultimate tensile strength is approaching the true fracture stress of the material. Therefore, the Morrow model was not considered since the ultimate tensile strength is far below the true fracture strength [4]. Using the equation obtained from the estimated fatigue curve i.e. equation (4.1), the following life prediction can be made:

Using equation (4.1) for the life prediction, i.e.

$$S_{n_{eff\,mean}} = -29.19\ln(N_f) + 608.42\ , \qquad (4.6)$$

the value of $S_{n_{eff\,mean}} = 358.636$ obtained from the Gerber model (i.e. equation (4.5)) can be substituted, yielding

$$358.636 = -29.19\ln(N_f) + 608.42\ . \qquad (4.7)$$

Solving for N_f from equation (4.7) leads to $N_f = 5197$.

Table 4.9 : Fatigue life (N_f) prediction according to the Gerber, Soderberg and Goodman models

Load	Process	Gerber	Soderberg	Goodman
99.4% Of Yield	Parent	5197	366	786
	Laser	3266	32	152
	Mechanical	4469	134	397
	Laser-Mechanical	4325	120	366
68.6% Of yield	Parent	233505	36469	62342
	Laser	151041	5928	17575
	Mechanical	201251	17669	37492
	Laser-Mechanical	196045	17082	36332
65.5% Of yield	Parent	337223	58359	96700
	Laser	216637	9816	27691
	Mechanical	262437	24831	51483

	Laser-Mechanical	277758	26571	54929

4.7 Crack morphology

In this section the crack initiation position and crack growth pattern(s) will be investigated for the parent plate and all three bending processes.

4.7.1 Typical fracture surface appearance

Typical fracture surfaces of the parent plate of the three forming processes are shown in Figure 4.33 to Figure 4.36 (pp 108 – 109). It was observed that at high loading conditions (i.e. 99.4% of yield strength) the fracture surface is irregular and noticeable fatigue cavities (or fissures) are present. At lower loads (i.e. 65% of yield strength) fatigue cavities are less and the fracture surface is less irregular i.e. smoother. All surfaces showed evidence of ratchet markings, indicated by white arrows in the figures, and represent multiple crack initiation.

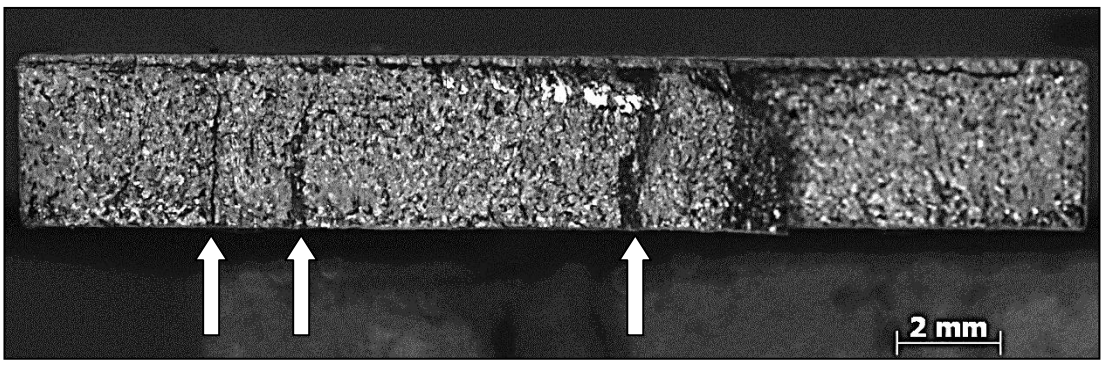

Figure 4.33 : Indication of fatigue failure of parent plate specimen

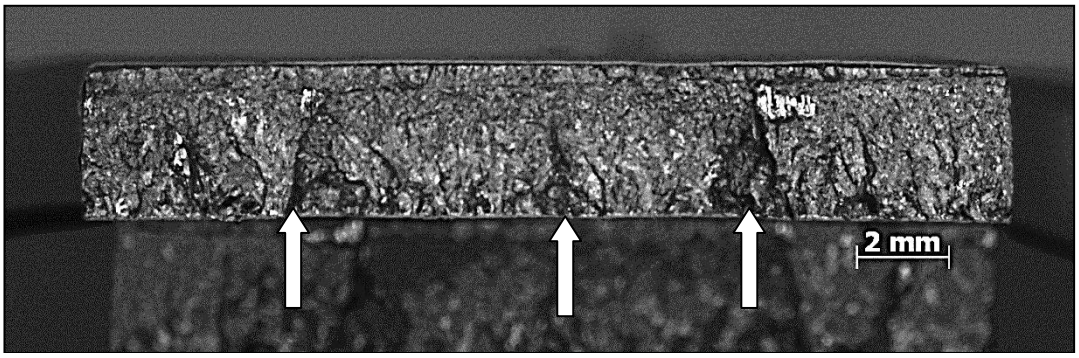

Figure 4.34 : Indication of fatigue failure of laser formed specimen

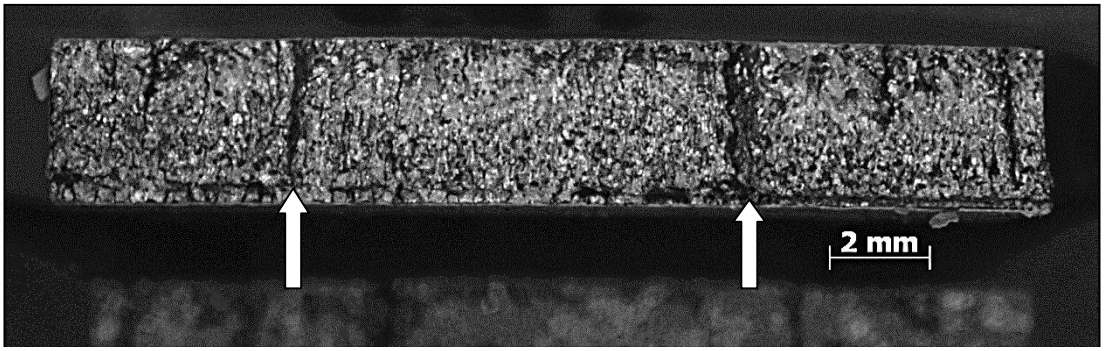

Figure 4.35 : Indication of fatigue failure of mechanically formed specimen

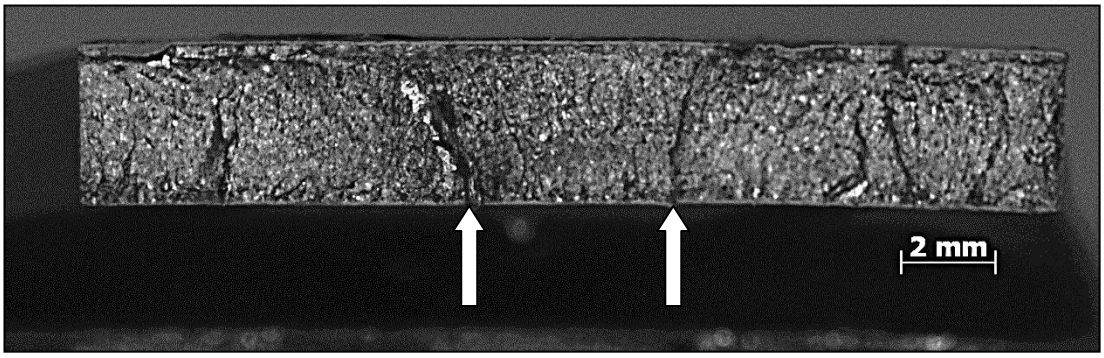

Figure 4.36 : Indication of fatigue failure of laser-mechanically formed specimen

4.7.2 Crack initiation position in relation to the bottom surface of the sample

Figure 4.37 shows the crack initiation position as a percentage relative to the bottom surface. Considering the parent plate at the lowest setting, 66.7% of all specimens tested failed from the top surface, i.e. from the outer radius (121.6 mm). When considering the laser specimens at the same load setting (i.e. the low load) all the specimens failed at the inner radius (118.4 mm).

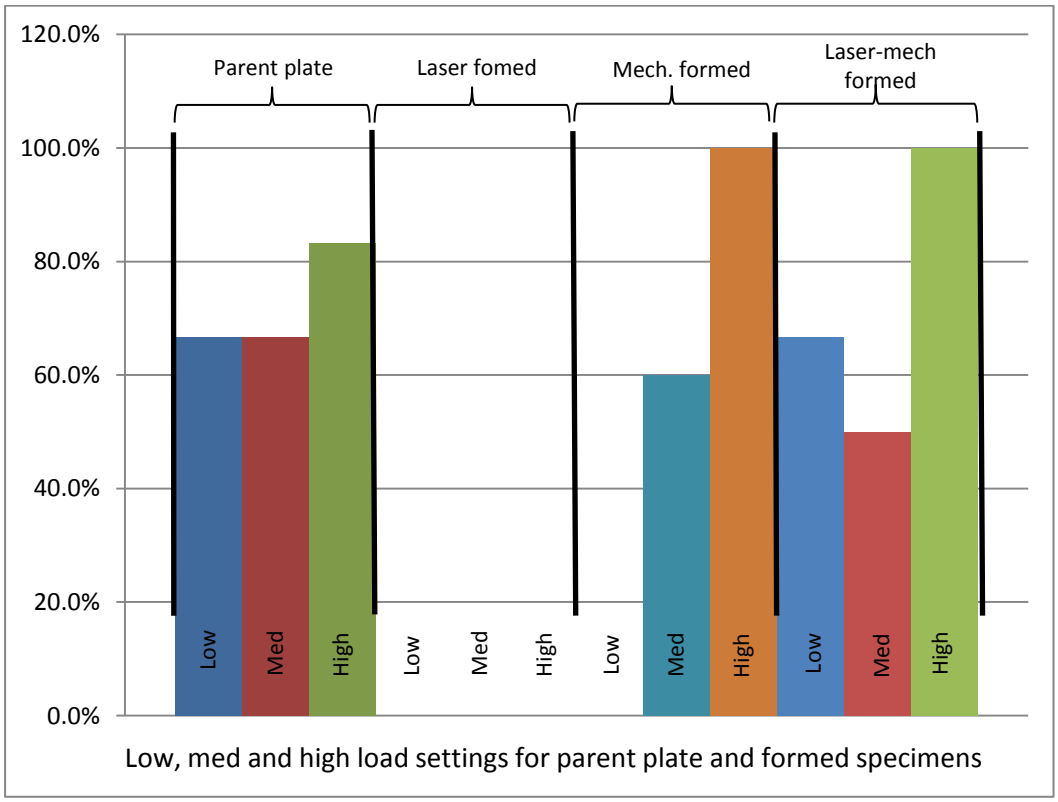

Figure 4.37 : Crack initiation position relative to the bottom surface

Table 4.10 (p111) shows the percentages of the crack initiation position relative to the bottom surface as indicated graphically in Figure 4.37.

Table 4.10 : Crack initiation position relative to the bottom surface*

Crack initiation position					
Parent Plate			Mechanically Formed		
Low Load	Med Load	High Load	Low Load	Med Load	High Load
66.7%	66.7%	83.3%	0.0%	60.0%	100.0%
Laser formed			Laser-mech formed		
Low Load	Med Load	High Load	Low Load	Med Load	High Load
0.0%	0.0%	0.0%	66.7%	50.0%	100.0%

***Top = Outer radius of formed specimen; Bottom = Inner radius of formed specimens**

4.7.3 Secondary cracks in region of fatigue fracture surface

Figure 4.38 shows the relative area observed in which secondary cracks were found with an optical microscope. The area is just behind the primary crack (approximately 0 to 10 mm from the fracture surface) and can be at the top (outer curve) or bottom (inner curve) surface.

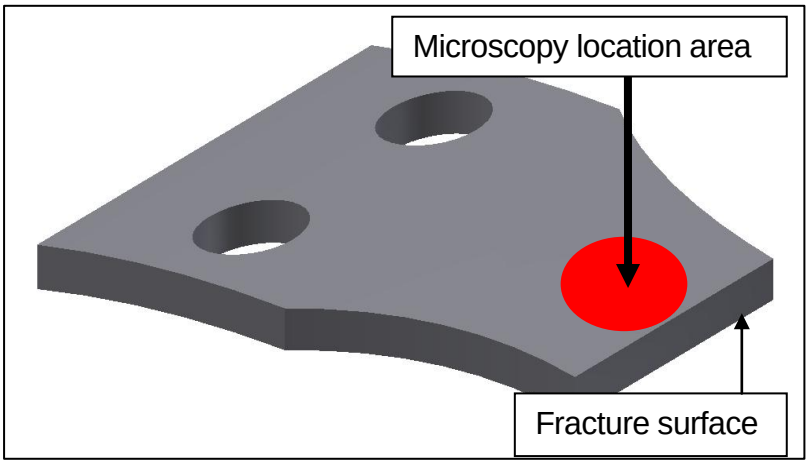

Figure 4.38 : Secondary crack observation location

Microscopy was performed for the parent plate and on specimens subjected to all formed processes (laser, mechanically and laser-mechanically) and will be discussed in the following subsections.

4.7.3.1 Parent plate

Secondary cracks within the microstructure of the parent plate were observed as shown in Figure 4.39 and Figure 4.40. Microscopy revealed that the cracks seem to follow an irregular path through the microstructure. Cracks grew parallel to the twinning boundaries in certain instances but in other instances the crack grew through the twin boundaries.

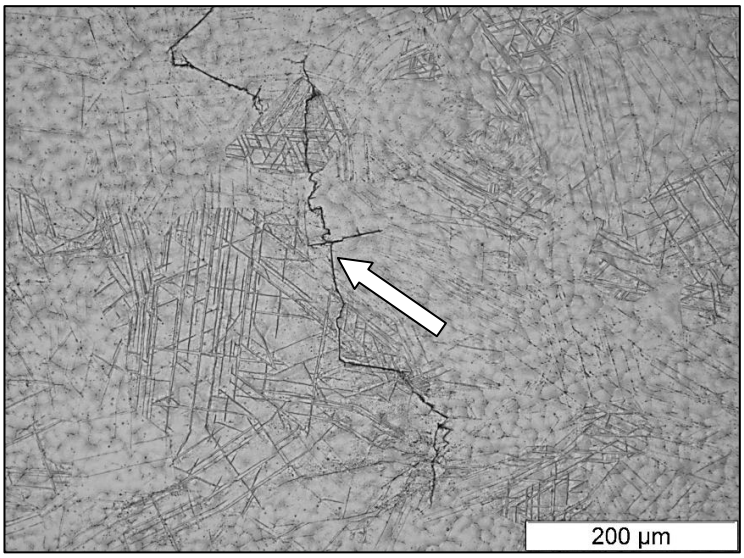

Figure 4.39 : Microstructure of parent plate CP Ti grade 2 (x200, electrolytically polished, colour polarized light),

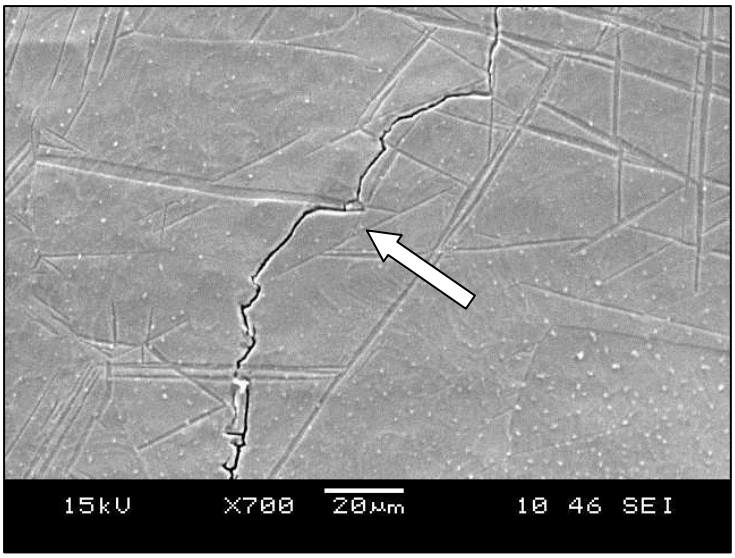

Figure 4.40 : SEM image of parent plate CP Ti grade 2 showing the jagged nature of secondary cracks

4.7.3.2 Laser formed

Figure 4.41 and Figure 4.42 show the nature of the secondary cracks in the microstructure of the laser formed specimens. The amount of secondary cracks developed on the surface is of a much higher density compared to that of the parent plate. Microscopy showed that the secondary cracks followed the boundaries of the microstructure in some instances and in other instances the cracks also exhibited a jagged-like behaviour.

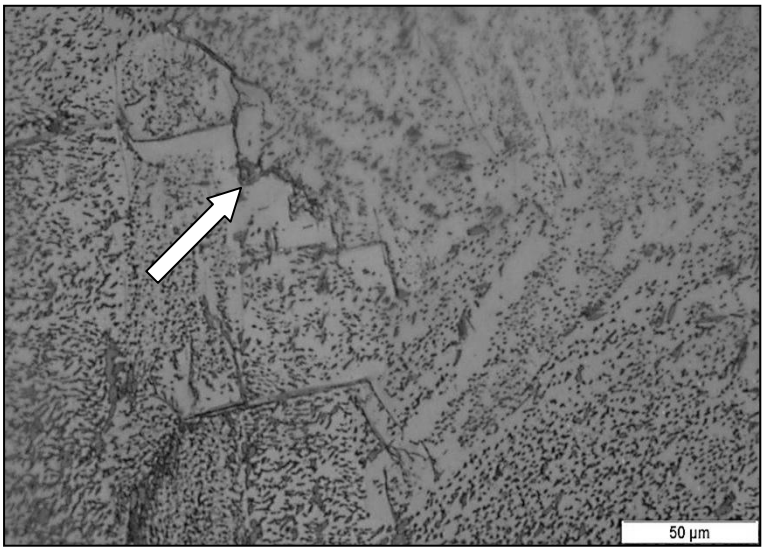

Figure 4.41 : Microstructure of laser formed CP Ti grade 2 (x500, electrolytically polished, colour polarized light),

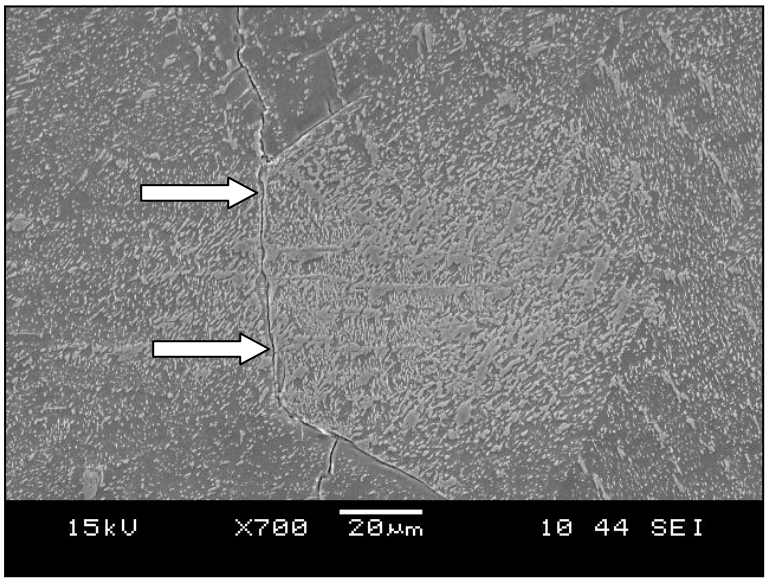

Figure 4.42 : SEM image of laser formed CP Ti grade 2 showing the nature of secondary cracks

4.7.3.3 Mechanically formed

Figure 4.43 and Figure 4.44 show the amount of twinning and jagged-like crack patterns within the microstructure after fracturing of the mechanically formed specimen. The secondary crack behaviour and density are similar to that of the parent plate. In some instances the crack follows twin boundaries and in other instances it grows across the twin boundaries.

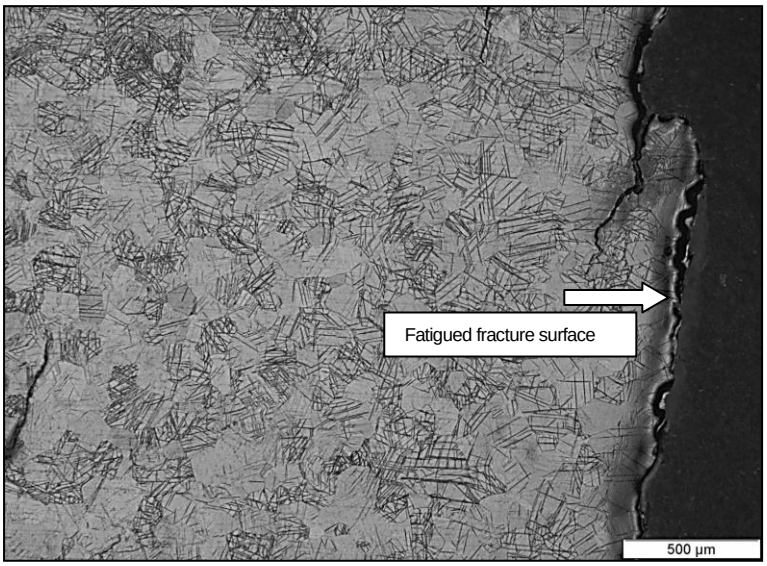

Figure 4.43 : Microstructure of mechanically formed CP Ti grade 2 (x50, electrolytically polished, colour polarized light)

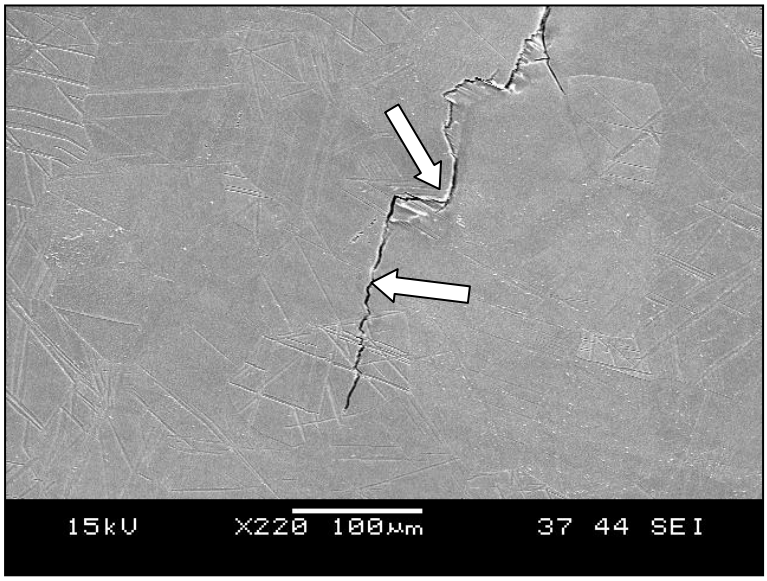

Figure 4.44 : SEM image of mechanically formed CP Ti grade 2 showing the nature of secondary cracks

4.7.3.4 Laser-mechanically formed

Figure 4.45 and Figure 4.46 show the secondary cracks within the microstructure of the laser-mechanically formed specimens. Similar to that of the parent plate, the cracks show an irregular behaviour and grow with and through the twin boundaries. The secondary crack density was slightly higher than that of the parent plate but not as significant as in the case of the laser formed specimen.

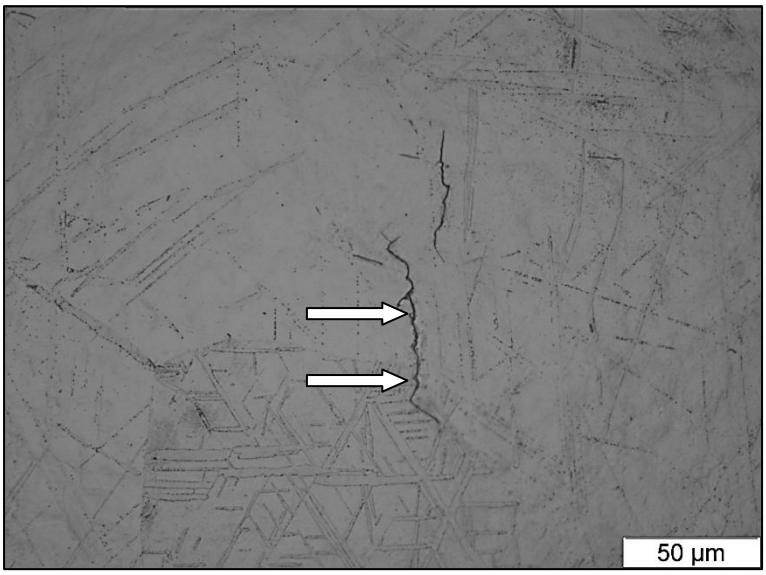

Figure 4.45 : Microstructure of laser-mechanically formed CP Ti grade 2 (x500, electrolytically polished, colour polarized light)

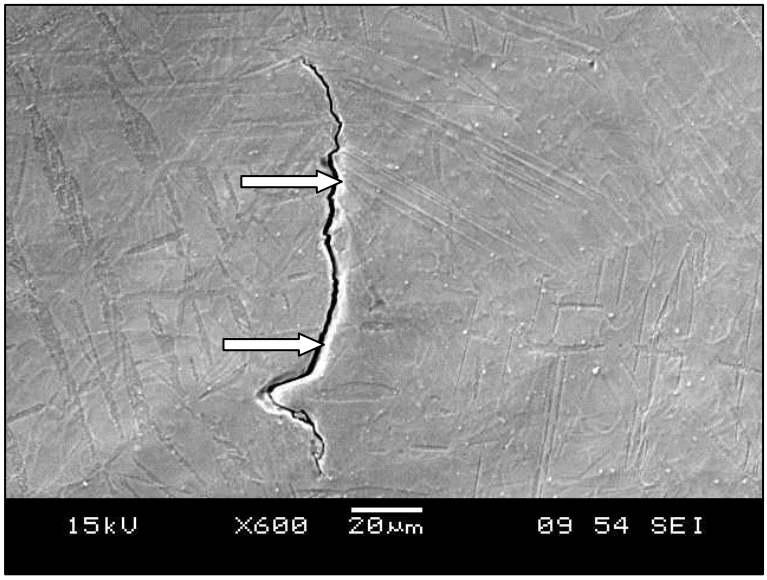

Figure 4.46 : SEM image of laser-mechanically formed CP Ti grade 2 showing the nature of secondary cracks

4.8 Correlation between results

In the next sections the measured properties (fatigue life etc.) will be compared to the parent plate as reference. Considering fatigue conditions of the parent plate as 100%, the formed specimens will be expressed as percentages relative to the parent plate i.e. 45420 vs. 11657 leads to 100% vs. 25.70%.

4.8.1 Microstructure vs. fatigue

Table 4.11 shows the relationship between the microstructure and the fatigue life (until fracture) at different load settings. The table is divided into two sections, vertically demonstrating the load setting during fatigue testing and horizontally the formed process, condition of microstructures and fatigue life as a percentage, relative to the parent plate. When considering the mechanically formed specimens at a high load setting, the fatigue life only reaches 25.70% of that of the parent plate, whereas the laser formed specimens reach a higher fatigue life at the same condition. Therefore it can be concluded that the Widmanstätten microstructure is beneficial for increasing fatigue life at high load settings as indicated in Section 2.7.1 (p 23). However, at low load settings the Widmanstätten microstructure is not dominantly beneficial for the fatigue life.

Table 4.11 : Relationship between microstructure and fatigue life until fracture

Load (percentage yield)	Parent plate	Laser formed	Mechanically formed	Laser-mechanically formed
Micro-structure	Equiaxed	Widmanstätten	Equiaxed	Equiaxed-Widmanstätten
Load high (99.4%)	100.00%	30.60%	25.70%	29.50%
Load low (65.5%)	100.00%	43.70%	72.00%	63.60%

4.8.2 Impact vs. fatigue

Table 4.12 shows the relationship between the Charpy impact energy absorbed and fatigue life until fracture at different load settings. Considering both load settings, a decrease in toughness and fatigue life is observed in all formed specimens. Therefore, a relationship can be obtained, when a decrease in toughness is observed and a reduction in fatigue life is expected.

Table 4.12 : Relationship between Charpy impact and fatigue life until fracture at a single temperature. i.e. room temperature

Load (percentage yield)	Parent Plate		Laser formed		Laser-mechanically formed		Mechanically formed	
	Impact	Fatigue	Impact	Fatigue	Impact	Fatigue	Impact	Fatigue
Load high (99.4%)	100.00%	100.00%	50.92%	30.60%	58.64%	29.50%	91.18%	25.70%
Load low (65.5%)	100.00%	100.00%	50.92%	43.70%	58.64%	63.60%	91.18%	72.00%

Figure 4.47 (p 118) is a graphical illustration of Table 4.12 (Impact (room temperature) vs. fatigue life (N_f) as a percentage relative to the parent plate). Figure 4.47 also illustrates the impact slope (at room temperature.). A direct comparison reveals that the fatigue slope at low load settings tends to be negative whereas the fatigue slope at high load settings tends to be positive.

Therefore this relationship indicates, as previously stated, that the interstitial content of the microstructure is a dominant contributor to the behaviour of the fatigue curve for CP Ti grade 2.

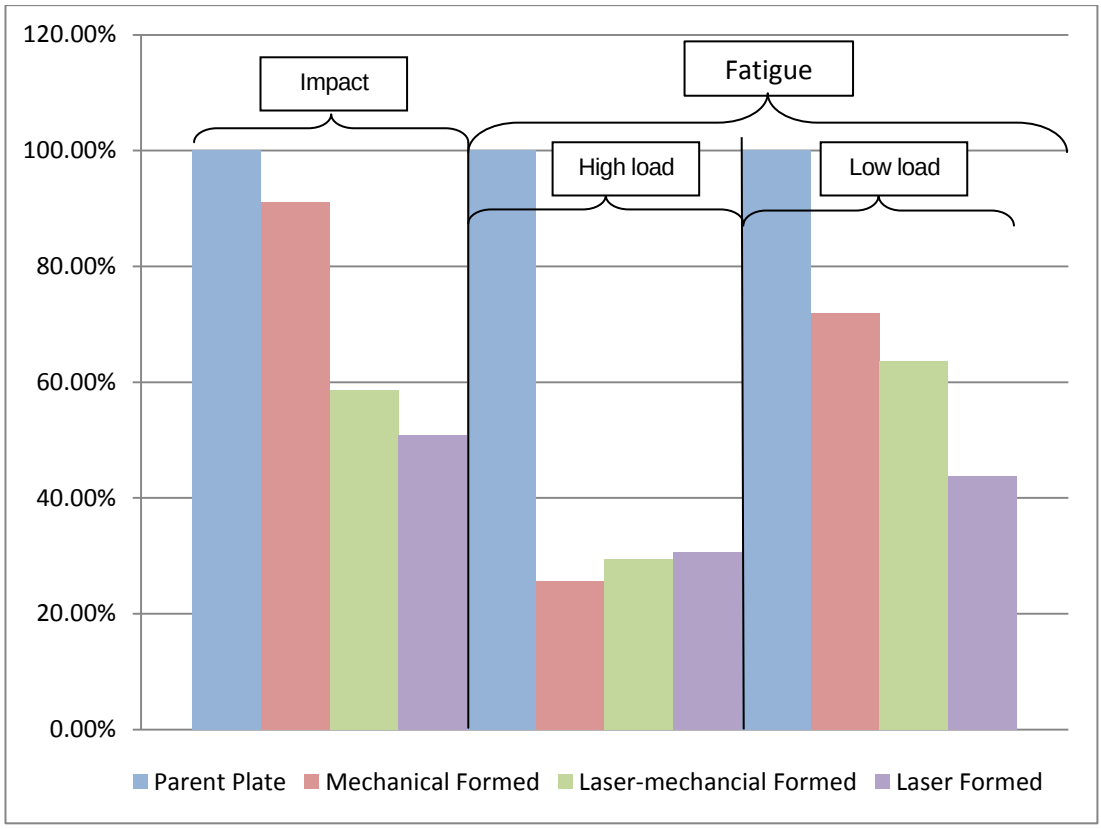

Figure 4.47 : Impact (room temperature) vs. fatigue life at different load settings (expressed as a percentage relative to the parent plate)

4.8.3 Residual stress vs. fatigue

Table 4.13 (p 119) shows the relationship between the residual stresses relieved and the number of cycles to failure at different load settings. Considering the high load, the residual stress does not influence the fatigue life negatively due to the fact that the laser formed specimens achieved the second highest cycles until failure relative to the parent plate (which has the highest relieved stress). However, at low load conditions, the residual stress does affect the fatigue life at higher number of cycles to failure. Therefore it can be concluded that, at high load settings and low number of cycles to failure, residual stress does not influence fatigue negatively. On the other hand, at low load settings, residual stress influences the fatigue life significantly when comparing the mechanically

formed fatigue life to the laser formed fatigue life. A difference of 28.30% is observed.

Table 4.13 : Relationship between residual stress and fatigue life

Load (percentage yield)	Parent plate		Laser formed		Laser-mechanically formed		Mechanically formed	
	Residual	Fatigue	Residual	Fatigue	Residual	Fatigue	Residual	Fatigue
Load high	100.00%	100.00%	156.50%	30.60%	126.00%	29.50%	116.00%	25.70%
Load low	100.00%	100.00%	156.50%	43.70%	126.00%	63.60%	116.00%	72.00%

Figure 4.48 (p120) is a graphical representation of Table 4.13. It shows an opposite slope to that of the Charpy impact. The residual stress slope and high load fatigue slope tend to be positive whereas the low load fatigue slope tends to be negative. This is due to the fact that the finer microstructure supports fatigue life and that residual stress is not a dominant factor at high load settings. However, at low load settings residual stress plays a significant role when considering fatigue.

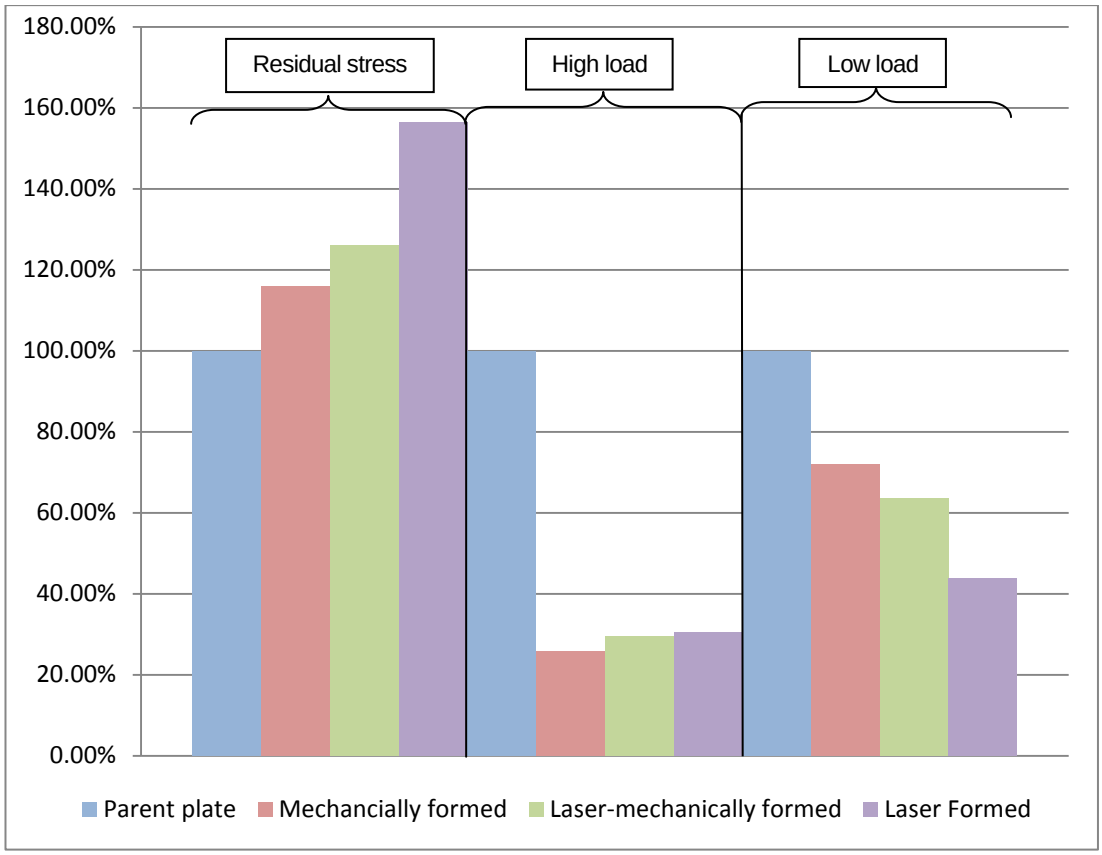

Figure 4.48 : Residual stress vs. fatigue life at different load settings (expressed as a percentage relative to the parent plate)

4.8.4 Theoretical (predicted) vs. actual fatigue data

Considering all the predicted fatigue equations given in Section 2.6 (p 18), only the Goodman model yields a relatively close prediction to the experimental data when considering the entire curve. However, the Gerber model was more accurate at the high load settings. Figure 4.49 (p 121) shows the correlation between the regression curve representing the actual fatigue data and the theoretical fatigue curves (i.e. Goodman and Gerber) for the parent plate. At high loads (i.e. at 350 MPa) the theoretical model prediction of Goodman tends to under-predict the number of cycles to failure, however, at intermediate load to low load conditions (i.e. ranging between 241 and 230 MPa), the Goodman model corresponds well with the experimental curve. Initially the Gerber model

tends to be more accurate at the high load (i.e. at 350 MPa), however, at loads below approximately 330 MPa the Gerber model over-predicts the experimental data. Furthermore, Figure 4.49 to Figure 4.52 (pp 121-124) are not presented on a LOG scale due to the small variations in fatigue life prediction versus the actual data.

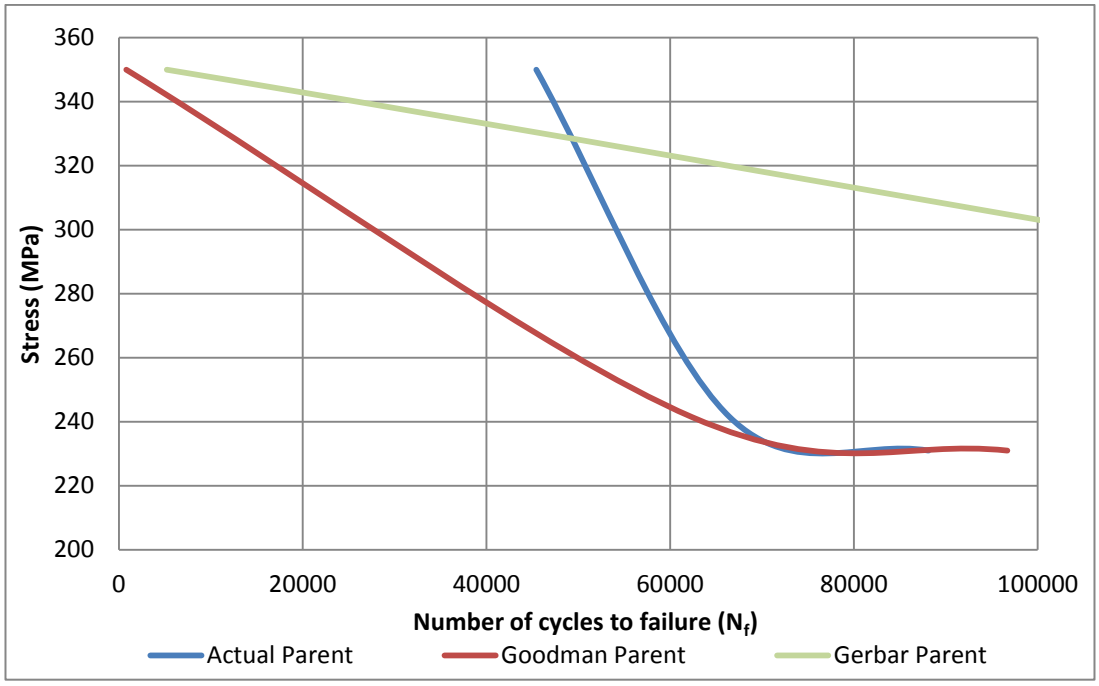

Figure 4.49 : Correlation between actual and predicted number of cycles (parent plate)

Figure 4.50 (p 122) shows a comparison between the Goodman and Gerber models and the regression curve representing the actual fatigue data for the laser formed specimens. Similar to that of the mechanically formed fatigue data, the Goodman model under-predict throughout the entire range of the fatigue curve with approximately 14090 cycles. The Gerber model is to a degree more accurate at high loads ranging from 340 to 350 MPa, but starts over-predicting and increases to over-predict at loads below 340 MPa.

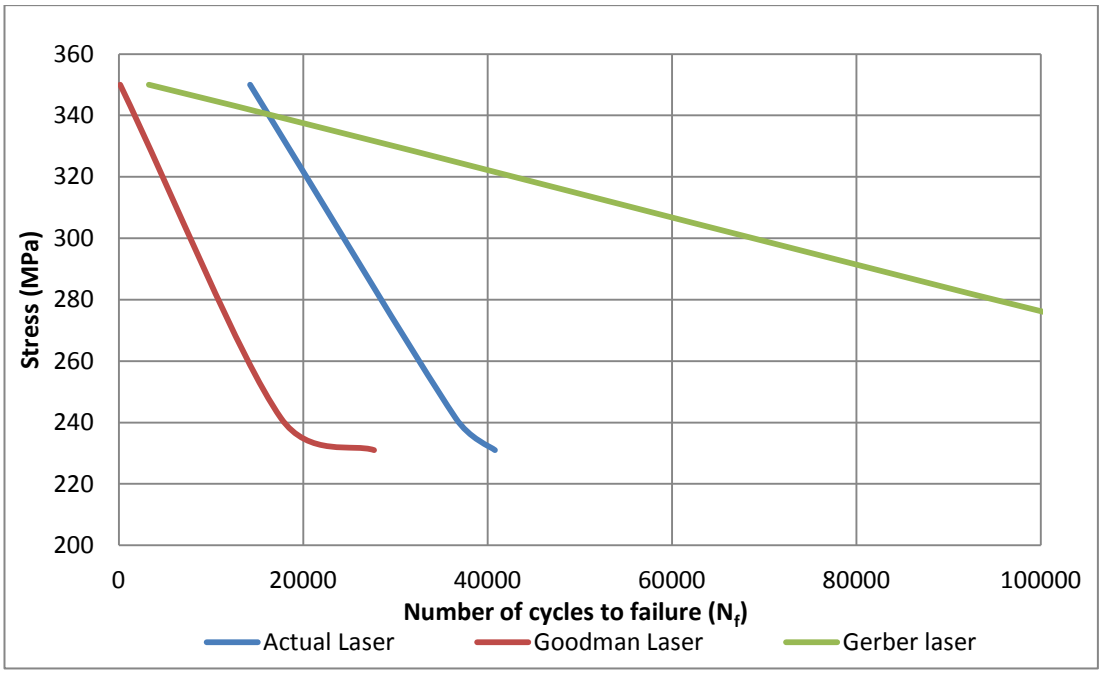

Figure 4.50 : Correlation between actual and predicted number of cycles (laser formed)

Considering the curves in Figure 4.51 (p123), the Goodman model under-predicts the experimental data of the mechanically formed specimens with approximately 10880 cycles over the entire range of cycles to failure tested. Therefore, the Goodman model may be used for life prediction while keeping in mind that the model is somewhat conservative. The Gerber model tends to be more accurate at the high load setting (i.e. at 350 MPa), however, at loads below 340 MPa the Gerber model yields an over-prediction which increases as the load decreases.

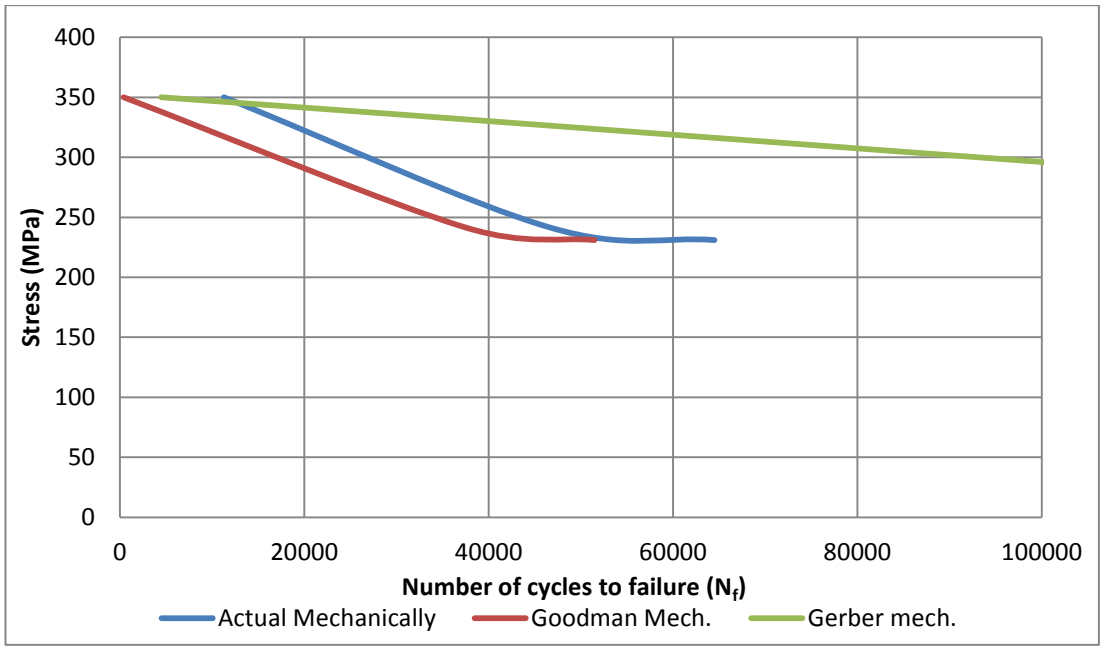

Figure 4.51 : Correlation between actual fatigue data and the theoretically predicted number of cycles (mechanically formed)

Considering Figure 4.52 (p 124) for the laser-mechanically formed specimens, the regression curve representing the actual fatigue data and the Goodman model behave similarly to that of the parent plate (compare Figure 4.49 (p 121) and Figure 4.52). The Goodman model tends to under-predict the experimental curve at high load settings (i.e. at 350MPa) but shows close correlation with the experimental curve at intermediate to low load settings. Again, the Gerber model tends to be more accurate than the Goodman modal at the high loads, ranging from 345 – 350 MPa, but yields an over-prediction at loads below 345MPa.

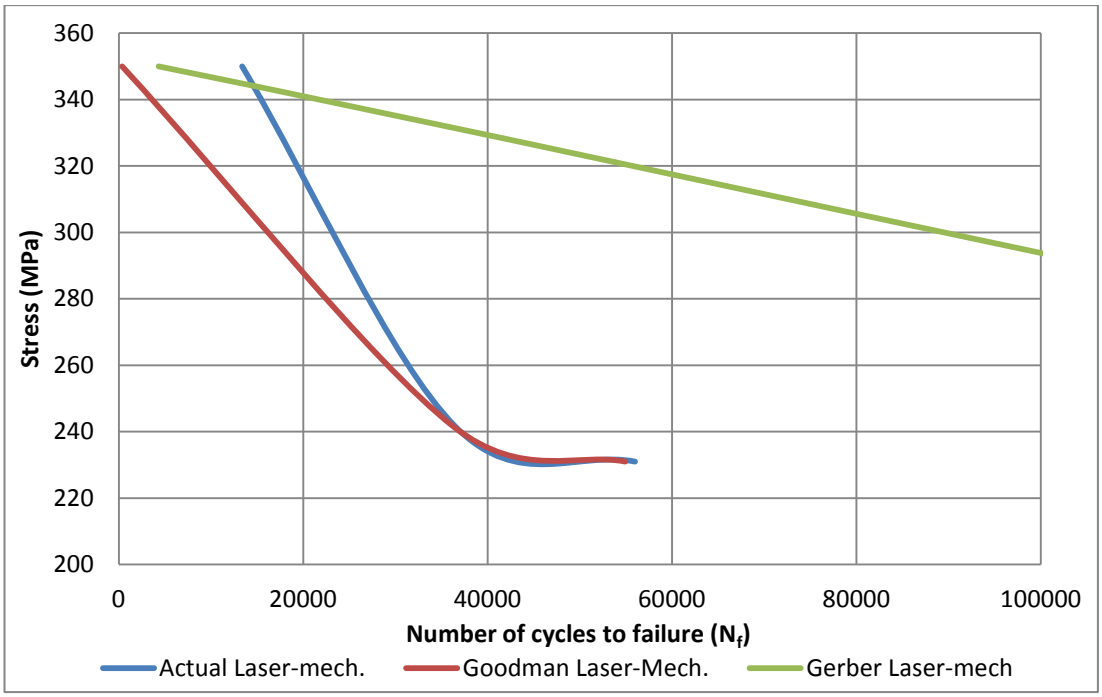

Figure 4.52 : Correlation between actual and predicted number of cycles (laser-mechanically formed)

Table 4.14 (p 125) shows the actual number of cycles to failure compared to the theoretical model predictions of Goodman and Gerber. As indicated above, the Goodman model prediction is somewhat conservative at high load conditions but prediction at medium to low load conditions are more reliable when compared to the actual data. The Gerber model tends to be more reliable at high loads but begins to increasingly over-predict at decreasing loads starting at approximately 340MPa.

Table 4.14 : Actual fatigue data and predicted fatigue models at different load settings

Load	Process	Actual	Goodman	Gerber
99.4% Yield	Parent	45420	786	5197
	Laser	13896	152	3266
	Mechanically	11657	397	4468
	Laser-Mechanically	13382	366	4324
68.6% yield	Parent	66457	62342	233504
	Laser	34732	17575	151041
	Mechanically	48772	37492	201251
	Laser-Mechanically	36526	36332	196044
65.5% yield	Parent	88115	96700	337222
	Laser	40801	27691	216637
	Mechanically	64504	51483	262437
	Laser-Mechanically	55998	54929	277758

The large discrepancy between the actual fatigue data and the predicted fatigue models at high load settings may be attributed to the specimens possibly being deformed plastically under fatigue testing conditions. Therefore, the proposed prediction curve by Manson, Coffin and Basquin [34] (as shown in Figure 4.53, p 126) was selected since the equation incorporates the elastic and plastic domains during fatigue testing. The equation is given by,

$$\varepsilon_{total} = \varepsilon_{a,e} + \varepsilon_{a,p} = \frac{\sigma_f'}{E}\left(2N_f\right)^b + \varepsilon_f'\left(2N_f\right)^c \ , \qquad (4.8)$$

where $\varepsilon_{a,e}$ represents the elastic region and $\varepsilon_{a,p}$ represents the plastic region.

However, the highest load setting was below the yield strength of the material and therefore it was considered that the maximum amount of plastic deformation that can occur during the high load fatigue testing was not greater than 5% over the yield tensile strength in order for this equation to be valid (plastic) and to verify if an improvement will be seen between the actual and theoretical data. Therefore, a strain value of approximately 167.613×10^{-6} was used for the plastic region to see if the percentage error will degrease between the predicted and actual fatigue data.

The average shifting exponents used for the exponents *b* and *c* in equation (4.8) was -0.085 and -0.6, respectively (as indicated by Manson, Coffin and Basquin [34] to be an average). The calculations, however, revealed (with the aid of MATLAB) that the number of cycles to failure (N_f) was less than that of all the previous model predictions. Therefore, considering that there would be a plastic region was rendered not viable.

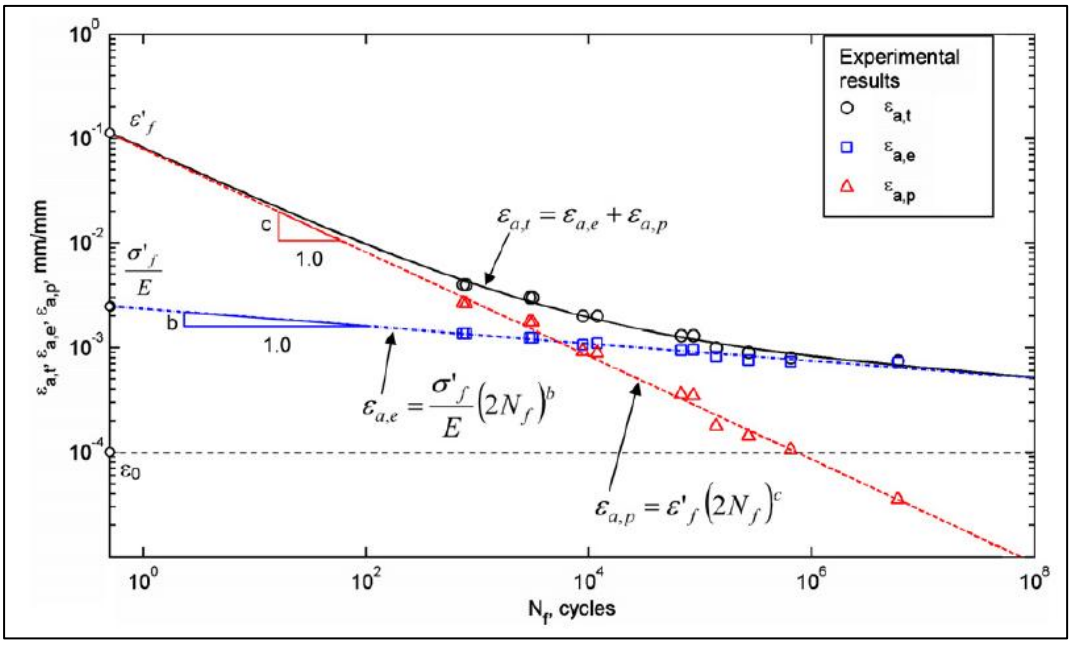

Figure 4.53 : Example of the Manson-Coffin-Basquin curve [34]

4.9 Prototype prediction fatigue curve for the fatigue life of CP Ti grade 2

The objective here was to obtain a prototype mathematical model to predict the dependence of the fatigue life on the number of cycles to failure, as obtained experimentally for CP Ti grade 2. In order to achieve this, the power addition technique of Churchill and Usagi is applied [35]. Given two different functions f_1 and f_2 as limits, e.g. for the fatigue life, each of which dominates in a given region of the independent variable (in this case the number of cycles to failure) a unified function can be obtained that approaches the two limits in their region of dominance by application of the following formula:

$$f = [(f_1)^s + (f_2)^s]^{1/s} , \quad (4.9)$$

where f_1 and f_2 are functions describing the fatigue life and s is a shifting exponent. The Manson, Coffin and Basquin equation (equation (4.8)) may be obtained in a similar manner by application of the power addition technique with a shifting exponent of unity. The shifting exponent determines the rate at which the cross-over takes place between the two asymptotic limits. The higher the value of s, the closer the resulting curve approaches the point over intersection of the two limits.

4.9.1 Parent plate

For the parent plate, the model prediction resembling the experimental data was obtained as follows by application of the power addition technique:

From Excel an equation was obtained to represent the actual data. This equation was however inaccurate (as is evident in Figure 4.27 ($y = 513.89e^{-1\times10^{-5}x}$), p 95) and therefore curve fitting was applied and the coefficients were adjusted but the form of the equation was conserved to obtain the best fit. The resulting equation used is given by

$$y_{actual} = 900e^{-2\times10^{-5}x} \quad . \tag{4.10}$$

Equation (4.10) represents the fatigue life of the parent plate as a function of the number of cycles to failure and is only applicable for the range measured, i.e. for $45420 \leq N_f \leq 88115$. In order to extend the range of applicability, the models of Goodman and Gerber are used as asymptotic limits in the power addition technique – Gerber as an upper limit and Goodman as a lower limit. In order to obtain the limiting equation of Gerber, Excel is used to obtain a linear equation through the two experimental data points corresponding to the highest loadings (i.e. 350 and 241.5 MPa). This equation is given by

$$y_{Gerber} = -0.0005x + 352.47\ , \tag{4.11}$$

and serves as the upper limit. Similarly for Goodman a linear equation is obtained, but in this case the two experimental data points corresponding to the lower loadings (i.e. 241.5 and 231 MPa) are used as this forms the lower limit.

This equation is given by

$$y_{Goodman} = -0.00045x + 270.55 \quad . \tag{4.12}$$

Application of the power addition technique first to the limit represented by Gerber and the actual data curve, leads to (Y_{int} = where the line intercepts the actual data)

$$y_{Int} = [(\, y_{Gerber}\,)^{s} + (\, y_{actual})^{s}]^{1/s} \ , \tag{4.13}$$

and secondly to the latter equation and the lower asymptote provided by $y_{Goodman}$ leads to

$$y = [(\, y_{int}\,)^{-t} + (\, y_{Goodman})^{-t}]^{-1/t} \ . \tag{4.14}$$

In the latter equation the exponent is negative since y is bounded from above and there is a decreasing dependence upon the independent variable between y_{int} and $y_{Goodman}$. Equation (4.14) represents a model prediction for the fatigue life of the parent plate as an implicit function of the number of cycles to failure. Matlab was used to produce a graphical representation of equation (4.14) which is shown in Figure 4.54 (by the black curve). It is evident that the model prediction follows the Gerber model at the higher loadings, the trend of the experimental data at intermediate loadings and the model of Goodman at the lower loadings.

The higher the value of the shifting exponent the closer the model prediction approaches the point of intersection between two limits. The value of *s* and *t* was chosen to be 50 as it provides the most accurate model prediction in the cross over regions between the individual models (i.e. the Gerber and Goodman models as well as the curve representing the actual data).

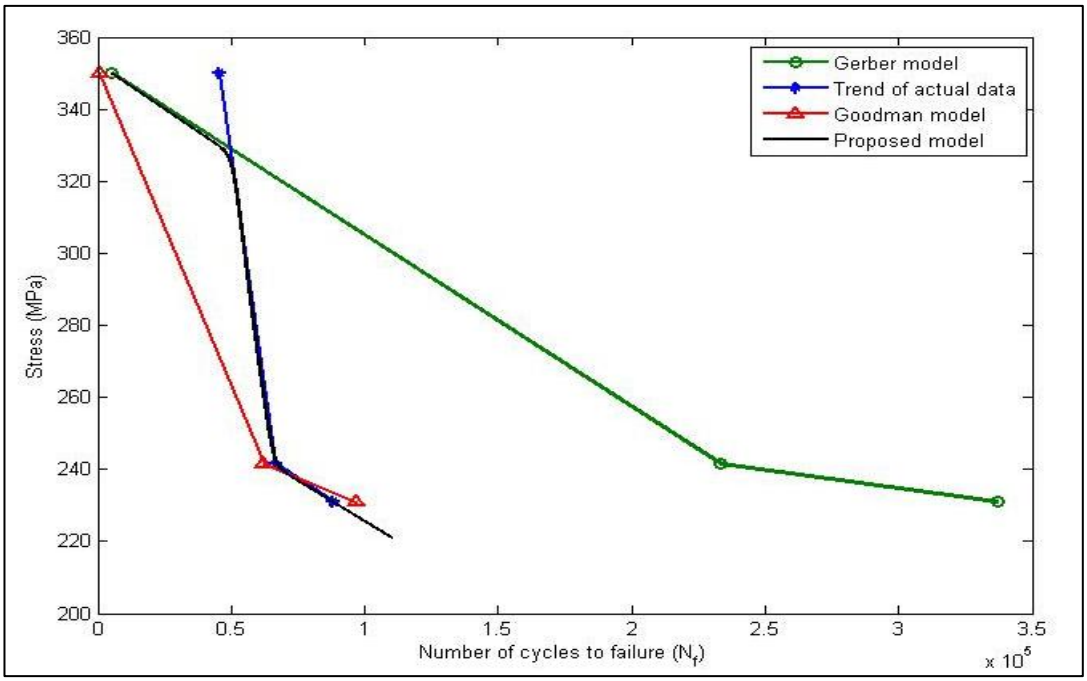

Figure 4.54 : Prototype prediction curve for parent plate

4.9.2 Mechanical

For the mechanically bent specimen, the model prediction resembling the experimental data was obtained by following the same trend analysis as for the parent plate:

The equation obtained from Excel to represent the actual data was again inaccurate (as is evident in Figure 4.29 (for $y = 376.07e^{-8\times10^{-6}x}$), p 99) and

therefore the coefficients were adjusted but the form of the equation was conserved. The resulting equation used is given by

$$y_{actual} = 395e^{-1.03\times10^{-5}x}. \quad (4.15)$$

Equation (4.15) is only applicable for the range measured, i.e. for $11281 \leq N_f \leq 64504$. The equation obtained for the Gerber model is given by

$$y_{Gerber} = -0.0005x + 349.59, \quad (4.16)$$

and serves as the upper limit. For Goodman the following linear equation is obtained for the two experimental data points corresponding to the lowest loadings (i.e. 241.5 and 231 MPa) and serves as the lower limit. This equation is given by

$$y_{Goodman} = -0.0007x + 269.64. \quad (4.17)$$

Application of the power addition technique, first to the limit represented by y_{Gerber} and y_{actual} and secondly to the latter equation and $y_{Goodman}$, which leads to

$$y = \left[\left([(y_{Gerber})^s + (y_{actual})^s]^{1/s}\right)^{-t} + (y_{Goodman})^{-t}\right]^{-1/t}. \quad (4.18)$$

Equation (4.18) represents a model prediction for the fatigue life of the mechanically bent CP Ti grade 2 specimen as an implicit function of the number

of cycles to failure. A graphical representation of equation (4.16) with $s = t = 50$ is shown in Figure 4.55 (i.e. the black curve).

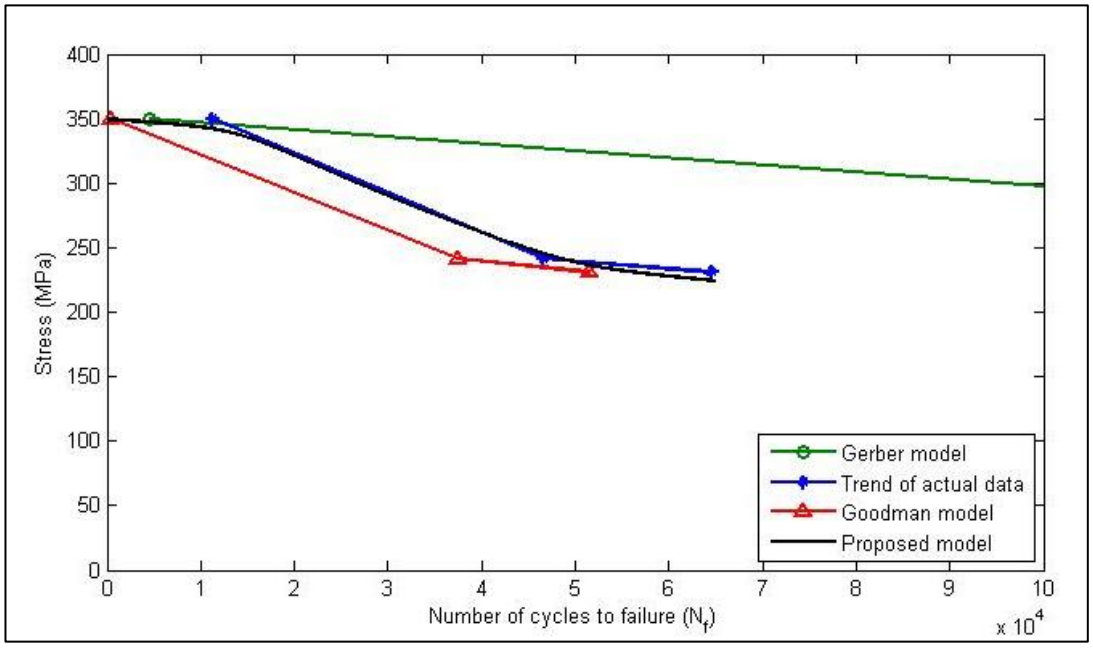

Figure 4.55 : Prototype prediction curve for mechanical forming

From Figure 4.51 it seems as if there is a constant relative percentage difference between the curve representing the actual data and that of the Goodman model. The calculated relative percentage difference, as shown in Table 4.15 (p 133), and calculated as

$$\text{Relative percentage difference} = 100 \times \frac{N_{f(\text{Actual})} - N_{f(\text{Goodman})}}{N_{f(\text{Actual})}} \quad , \qquad (4.19)$$

is significantly larger at the higher loading. The reason for this is that the Goodman model under-predicted the actual fatigue data with a constant value of approximately 10880 cycles to failure throughout the curve, hence the large difference at low cycles to failure. Additionally, the large difference could also be attributed to the slope of the high load setting (Figure 4.26, p 93), considering

that the transition between the slope of the strain life and that of the stress life is approximately 10^4 cycles.

Table 4.15 : Percentage difference in fatigue life at different load settings

Load	Relative percentage difference in fatigue life for mechanically formed specimens
350	96%
241.5	20%
231	20%

4.9.3 Laser-Mechanical

The exact same modelling procedure is followed for the laser-mechanical bending as for the mechanical bending, to predict the fatigue life. The coefficients of the equation obtained from Excel to represent the actual data (as is evident in Figure 4.30 (for $y = 382.54e^{-1\times10^{-5}x}$), p 101) were again adjusted due to inaccuracy but the form of the equation conserved. The resulting equation used is

$$y_{actual} = 436e^{-1.55\times10^{-5}x}. \quad (4.20)$$

Equation (4.20) is only applicable in the range $13382 \leq N_f \leq 55998$.

The equation obtained for the Gerber model is given by

$$y_{Gerber} = -0.00055x + 352.25, \quad (4.21)$$

and for Goodman the following linear equation is obtained

$$y_{Goodman} = -0.00057x + 262.01. \quad (4.22)$$

Application of the power addition technique leads to

$$y = \left[\left([(y_{Gerber})^s + (y_{actual})^s]^{1/s} \right)^{-t} + (y_{Goodman})^{-t} \right]^{-1/t},$$

which is the same general equation as equation (4.18).

Figure 4.56 shows that the resulting prediction for s = t = 50 representing the fatigue life of CP Ti grade 2 subjected to laser-mechanical bending corresponds to the Gerber model at high loads, to the actual data curve at intermediate loads and to the Goodman model at low loads.

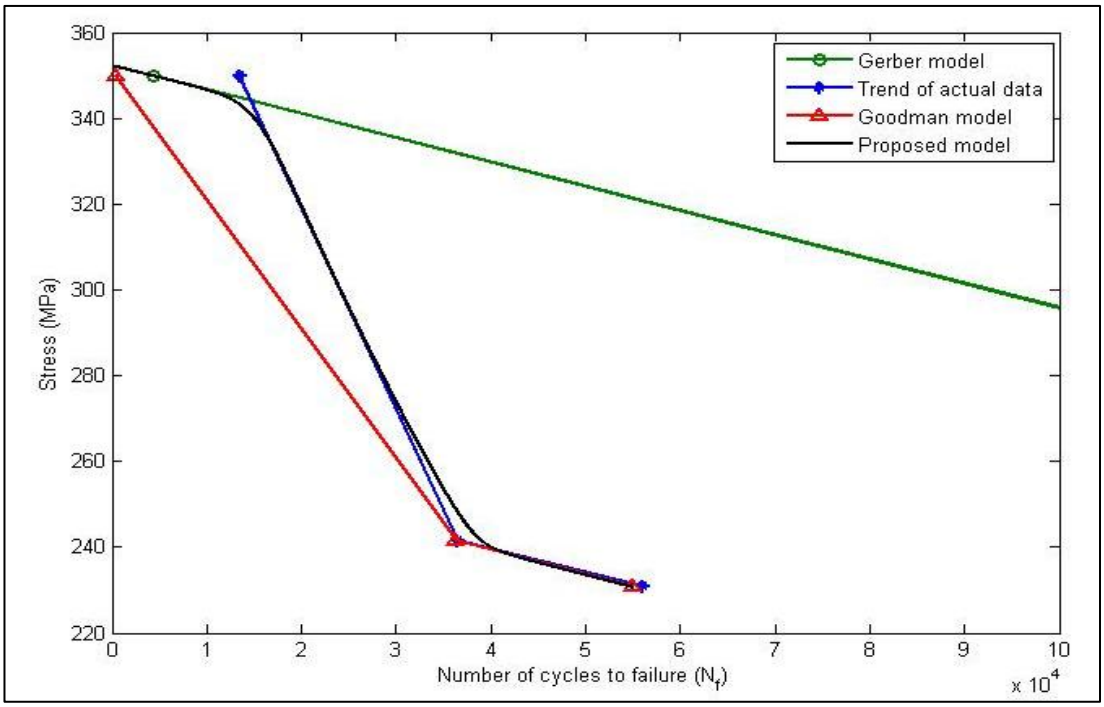

Figure 4.56 : Prototype prediction curve for laser-mechanical forming

4.9.4 Laser

Also in this case this same modelling procedure is used as for the mechanical bending. The equation obtained from Excel to represent the actual data was again inaccurate (as is evident in Figure 4.28 (for $y = 438.51e^{-2\times10^{-5}x}$), p 97). The equation of improved accuracy used is given by

$$y_{actual} = 440e^{-1.6\times10^{-5}x} \quad . \tag{4.23}$$

Equation (4.23) is only applicable in the range $14242 \leq N_f \leq 40801$.

The equation obtained for the Gerber model is given by

$$y_{Gerber} = -0.00075x + 352 \quad , \tag{4.24}$$

and for the Goodman model the following linear equation is obtained

$$y_{Goodman} = -0.0009x + 259.74 \quad . \tag{4.25}$$

Application of the power addition technique once again leads to

$$y = \left[\left([(y_{Gerber})^s + (y_{actual})^s]^{1/s}\right)^{-t} + (y_{Goodman})^{-t}\right]^{-1/t} ,$$

which is also the same as equation (4.18).

The resulting prediction for the fatigue life of CP Ti grade 2 subjected to laser forming is shown in Figure 4.57 for *s* = *t* = 50.

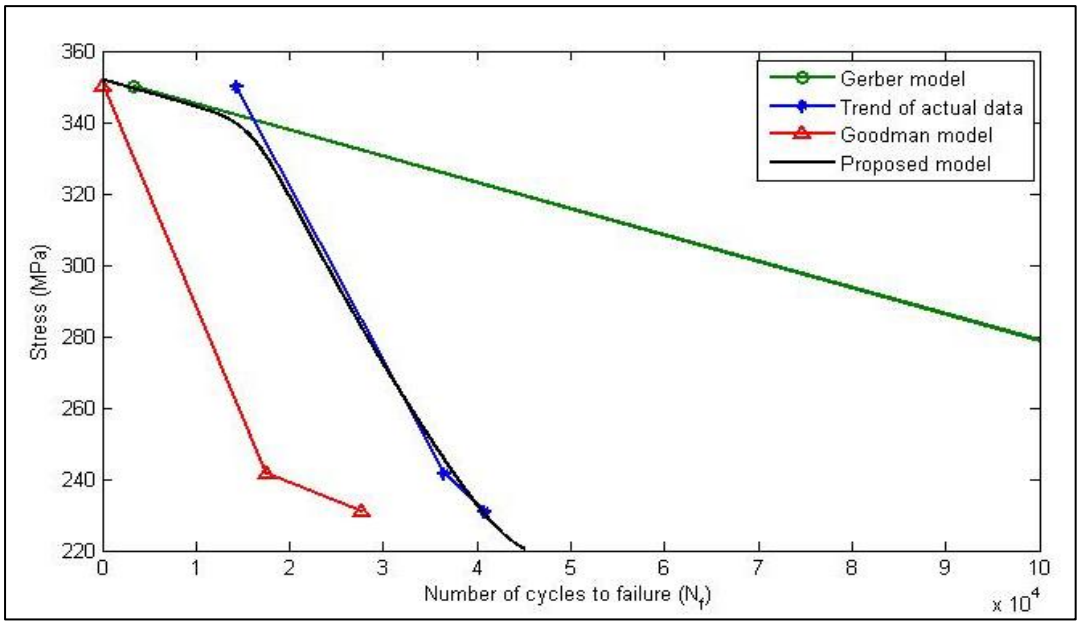

Figure 4.57 : Prototype prediction curve for laser forming

Similarly to that of the mechanically bent specimens, it seems from Figure 4.50 (p 124) as if there is a constant relative percentage difference between the curve representing the actual data and that of the Goodman model. The calculated relative percentage difference, as shown in Table 4.16 is significantly larger at the higher loading. The reason for this is that the Goodman model under-predicted the actual fatigue data with a constant value of approximately 14090 cycles to failure throughout the curve, hence the large difference at low cycles to failure. Once again, it could also be attributed to the slope of the high load setting when considering the transition between the slope of the strain life and that of the stress life at 10^4 cycles.

Table 4.16 : Percentage difference in fatigue life at different load settings

Load	Relative percentage difference in fatigue life for mechanically formed specimens
350	99%
241.5	52%
231	32%

4.10 Summary

From the results obtained it is clear that laser forming on commercially pure titanium grade 2 is feasible for industrial use. Fatigue is an important parameter (at high load conditions) when it is compared to the conventional mechanically formed process. A change in microstructure is observed after laser forming (equiaxed to Widmanstätten). However, the Widmanstätten microstructure promotes low ductility and toughness as measured by impact testing. The average hardness measured through the thickness of the specimen was not affected after the laser forming process when compared to the parent plate. An increase in the average residual stress is observed after laser forming, but it does not affect the fatigue life at the high load condition. At the low load condition, however, the residual stress affects the fatigue conditions significantly.

The mechanically formed process showed the most promising results during fatigue testing at the low load condition when compared to the other forming processes (laser and laser-mechanical). However, the opposite occurred at high load conditions. The microstructure was unaffected (equiaxed), however, twinning was observed throughout the specimen after mechanical bending and in the microstructure of the final fractured fatigue specimens. The maximum residual stress recorded for the mechanically formed specimens is the lowest when compared to the other forming processes.

When considering fatigue, residual stress and Charpy impact results, the laser-mechanical forming process showed results midway between those obtained for the other forming processes. The microstructure for the laser-mechanical forming process consisted of a combination of the equiaxed and Widmanstätten structures. Although twinning of the microstructure was observed, the amount of twinning was less than that of the mechanically formed process.

For the theoretical (predicted) fatigue models, the Goodman model achieved the closest relation to that of the actual fatigue data when considering the entire curve. However, for the parent plate and laser-mechanically formed process the model tends to under-predict at high load settings, but good correspondence is obtained at medium to low load settings. For the mechanical and laser forming process the Goodman model under predicts throughout the fatigue curve with approximately 10880 and 14090 cycles difference to that of the actual data.

Regarding the correlation between the microstructure and fatigue; impact and fatigue; and residual stress and fatigue it is evident that the microstructure has the most significant influence when considering fatigue. This is mainly due to the twinning and Widmanstätten microstructure that lowers the toughness. The second most dominant factor is the residual stress, especially at low load conditions. However, at high load conditions the residual stress did not influence the fatigue data significantly.

A prototype prediction fatigue curve for all the forming processes and parent plate was successfully generated and can be used for future work.

CHAPTER 5 - FINAL CONCLUSIONS

5.1 Introduction

The aim of this investigation was to characterise the effect of various forming processes on the structural integrity of CP Ti grade 2. The various forming processes investigated were laser forming, mechanical forming (stretch forming) and a combined laser-mechanical forming process. This chapter summarizes the final conclusions that can be drawn from the results of this study.

5.2 Final conclusions

The final conclusions of this study can be summarized as follows:

- Literature studies regarding materials that have been subjected to laser forming are limited and not commonly available in industry. Therefore, the need to investigate the material properties and structural integrity after laser forming was essential in order for this process to be considered in future production processes.

- Literature regarding CP Ti grade 2 that has been subjected to mechanical deformation is limited.

- The microstructure of CP Ti grade 2 (the parent plate) was found to be equiaxed. However, after mechanical forming, excessive twinning was observed. A Widmanstätten microstructure was observed after laser

forming. However, for the laser-mechanical process, only a small portion changed from an equiaxed to a Widmanstätten microstructure. This was observed at the irradiation side of the sample. The laser-mechanically formed process also exhibited a small amount of twinning in the equiaxed region.

- The hardness profiles were found to be relatively constant throughout the material thickness and after the forming processes were completed.

- The Charpy impact testing indicated slight embrittlement of the specimens after the forming processes. The mechanically formed specimens indicated the least amount of embrittlement in comparison with the laser formed specimens.

- The residual stress for the parent plate exhibited a tensile nature.

- An increase in the residual stress for all the formed processes was observed at the inner curve of the specimens whereas at the outer curve, the residual stresses were less (lower in magnitude) than that of the parent plate.

- Comparing residual stresses between the forming processes, the laser formed process achieved the highest value (108MPa), whereas the mechanical forming process produced the lowest value (87MPa) when compared to the parent plate (69MPa).

- Considering fatigue, the parent plate achieved similar results as indicated by Matthew and Donachie [12]. At high load settings the Goodman and Gerber model tends to under-predict the number of cycles to failure.

- The parent plate produced the most promising fatigue result when compared to the forming processes when considering the fatigue models.

- Comparing the fatigue data of the forming processes, it is clear that the laser formed process produced the most fatigue cycles at high loads (i.e. at low cycles (13896)). However, at low loads (i.e. at high cycles (63434)) the mechanical forming process provided the most promising results.

- Considering the theoretical models for predict fatigue life, the Goodman model provided overall the best correlation with the actual data. At high load settings, the Gerber model produced a slightly better correlation, although the deviations are still significant. At medium to low load settings the Goodman model prediction is more acceptable than the Gerber model. Due to the large deviations of the theoretical curves with respect to the actual data, none of the models can be used to predict the entire range of the fatigue life of CP Ti grade 2. Therefore, a prototype prediction fatigue curve was proposed for predicting the fatigue life of the parent plate and all the forming processes (i.e.

mechanically, laser-mechanically and laser formed) which can be considered more accurate.

- Fatigue crack morphology indicated that for the parent plate, mechanically formed (equiaxed) and laser-mechanically formed specimens (equiaxed plus twinning), cracks developed through and parallel to that of the twinning boundaries. On the other hand, considering the laser and laser-mechanically formed specimens (Widmanstätten), secondary cracks followed the microstructural grain boundaries.

- Considering Table 5.1 and Table 5.2 (p143) this research revealed that the microstructure is the dominant contributor to crack initiation and growth when considering fatigue. The second most influential factor was residual stress, especially at the medium to lower load settings.

- Laser forming can be used successfully on commercially pure titanium grade 2. Due to microstructural changes, the material's toughness is affected as well as the fatigue life at low load conditions.

- The most desired forming process for specific property requirements can be summarised as shown in the table below:

Desired property	Recommended forming process
High load condition (low cycles)	Laser forming
Low load condition (high cycles)	Mechanical forming
High toughness	Mechanical forming
Low toughness	Laser forming
High residual stress	Laser forming
Low residual stress	Mechanical forming

Table 5.1 : Combined data high load setting

Forming Process	Fatigue equations	Fatigue life (High load) (N_f)	Residual stress (MPa)	Impact (Joule)	Goodman prediction (N_f)	Gerber prediction (N_f)	Microstructure
Parent	y = 1E-07x2 - 0.0174x + 914.62	45420	69.15	27.20	786	5197	equiaxed
Laser	y = -113.9ln(x) + 1439.2	14242	108.25	13.85	152	3266	Widmanstätten
Mechanical	y = -70.72ln(x) + 1008.6	11281	87.44	24.80	397	4468	equiaxed + twinning
Laser-Mechanical	y = -86.26ln(x) + 1168.2	13382	87.76	15.95	366	4324	equiaxed – Widmanstätten + twinning

Table 5.2 : Combined data low load setting

Forming Process	Fatigue equations	Fatigue life (low load) (N_f)	Residual stress (MPa)	Impact (Joule)	Goodman prediction (N_f)	Gerber prediction (N_f)	Microstructure
Parent	y = 1E-07x^2 - 0.0174x + 914.62	88115	69.15	27.20	96700	337222	equiaxed
Laser	y = -113.9ln(x) + 1439.2	40801	108.25	13.85	27691	216637	Widmanstätten
Mechanical	y = -70.72ln(x) + 1008.6	64504	87.44	24.80	51483	262437	equiaxed + twinning
Laser-Mechanical	y = -86.26ln(x) + 1168.2	55998	87.76	15.95	54929	277758	equiaxed – Widmanstätten + twinning

Table 5.3 shows the prototype predictive equations for CP Ti grade 2. These predictions are obtained by substituting the respective fatigue equations for y_{Gerber} , y_{int} and $y_{Goodman}$ into the general unified equation (4.18).

Table 5.3 : Proposed prototype prediction equations for CP Ti grade 2

Prototype prediction fatigue curve equations for CP Ti grade 2	
Parent plate	$y = \left[\left(\left[(-0.0005x + 352.47)^{50} + \left(900e^{-2\times10^{-5}x}\right)^{50}\right]^{1/50}\right)^{-50} + (-0.00045x + 270.55)^{-50}\right]^{-1/50}$
Laser	$y = \left[\left(\left[(-0.00075x + 352)^{50} + \left(440e^{-1.6\times10^{-5}x}\right)^{50}\right]^{1/50}\right)^{-50} + (-0.0009x + 259.74)^{-50}\right]^{-1/50}$
Mechanical	$y = \left[\left(\left[(-0.0005x + 349.59)^{50} + \left(395e^{-1.03\times10^{-5}x}\right)^{50}\right]^{1/50}\right)^{-50} + (-0.0007x + 269.64)^{-50}\right]^{-1/50}$
Laser-mechanical	$y = \left[\left(\left[(-0.00055x + 352.25)^{50} + \left(436e^{-1.55\times10^{-5}x}\right)^{50}\right]^{1/50}\right)^{-50} + (-0.00057x + 262.01)^{-50}\right]^{-1/50}$

Future work

This research confirms that laser forming can be utilized in industry as a reliable, feasible forming process. Considering specific final results concerning critical components, it is of utmost importance to know the material's behaviour and microstructure before and after any forming process. Therefore, the following future work will improve further understanding and development of laser forming as a tool to be used in industry:

- The use of gas shielding during laser forming
- The production of more fatigue samples to generate a wider scatter when testing
- The use of a more refined fatigue setup i.e. measuring each sample individually when fatigue testing
- The use of a Nd:YAG laser system for better efficiency
- The development of laser forming parameters to produce the same radius of curvature with less heat input
- Laser forming of titanium grade 5 (Ti-6Al-4V)
- Laser forming of stainless steel
- Laser forming of aluminium
- Three dimensional shapes should be considered
- Develop laser parameters to produce three dimensional shapes
- The use of laser forming processes for industry i.e. aviation industry

Lastly, it is suggested that laser forming and further development thereof should be considered as tool in a wide variety of industries, such as the automotive and aeronautical industries, rapid prototyping, ship building etc.

Bibliography

1. Els-Botes A. *Material characterisation of laser formed dual phase steel components.* D-Tech Thesis, Nelson Mandela Metropolitan University, Port Elizabeth, South Africa, 2005.
2. ASM International. Boyer R, Welsch G. and Collings, E. W., editors. *Materials Properties Handbook: Titanium Alloys.* ASM International, Materials Park, Ohio, 1994.
3. ASM International. *Titanium - A Technical Guide.* (2nd Ed.) ASM International, Materials Park, Ohio, 2000.
4. Bannantine J. A., Comer J. J. and Handrock J. L. *Fundamentals of metal fatigue analysis.* Prentice-Hall, New Jersey, 1990.
5. ASM International. *Fatigue properties in engineering.* ASM metals handbook, Fatigue and Fracture, vol 19, ASM International, Materials Park, Ohio, 1996.
6. Suresh S. *Fatigue of materials.* Cambridge Univesity Press, Cambridge, 1991.
7. ETBX Engineers Toolbox. [online] [cited 2011/04/07] [http://www.fea-optimization.com/ETBX/stresslife_help .html.]
8. MSCsoftware.[Online][cited 2011/08/08] [http://www.efunda.com/formulae/solid_mechanics/fatigue/fatigue_highcycle.cfm]
9. Juvinall R. C. and Marshek K.M. *Fundamentals of Machine Component Design*. (4th Ed.) John Wiley & Sons, Hoboken, NJ, 2006.
10. ASM International. Boyer H. E., editor. *Atlas of Fatigue Curves*. ASM International, Materials Park, Ohio, 1986.
11. Radonovich D. C. *Methods of extrapolating low cycle fatigue data to high stress amplitudes.* MSc thesis, University of Central Florida, Florida, USA, 2007.
12. ASM International. *Titanium - A Technical Guide.* (2nd Ed.) ASM International, Materials Park, Ohio, 2000.

13. Custompsrtnet. Custompsrtnet. [Online].; 2009 [cited 2011/07/15. Available from: http://www.custompartnet.com/wu/sheet-metal-forming.
14. Muncheryan H. M. *Principles & Practices of Laser Technology.* TAB books, Blue Ridge Summit, 1983
15. Luxon J. T. and Parker D. E. *Industrial Lasers and Their Applications.* Englewood Cliffs, Prentice-Hall, Englewood Cliffs, NJ, 1985.
16. Namba Y. *Laser Forming of Metals and Alloys.* In Proceedings of LAMP '87, Osaka, Japan, pp. 601-603, May, 1987.
17. E Edwardson. Laser Forming. [Online]. [cited 2011/07/18. Available from: http://www.liv.ac.uk/~me0u5040/forming1.html.
18. Burger H. P. and Theron M. *Laser Beam Characterization.* Progress Report, CSIR, National Laser Centre, Pretoria, 2011.
19. Lawrence J., Pou J., Low D. K. and Toyserkani E. *Advances in Laser Materials Processing Technology, Research and Applications.* (1st Ed.) CRC Press and Woodhead Publishing Ltd, Cambridge, UK, 2010.
20. Marya M. and Edwards G. R. *The Laser Forming of Titanium Alloys*. In Proceedings of Trends in Welding Research, Pine Mountain, GA, USA, pp. 982-987, June 1998.
21. Marya M. and Edwards G. R. *An analytical model for the optimization of the laser bending of titanium Ti-6Al-2Sn-4Zr-2Mo.* Journal of Materials Processing Technology, 124(3), pp. 337-344, 2001.
22. Sumitomo Metals. [Online]. [cited 2011/08/17. Available from: http://www.sumitomometals.co.jp/e/titanium/alloy.html.
23. Almen J. O. and Black P. H. *Residual stresses and fatigue in metals.* McGraw-Hill Book Company, New York, 1963.
24. www.asminter.com. [Online].; 2006 [cited 2011/07/19. Available from: http://www.google.co.za/imgres?q=residual+stress&hl=en&safe=off&gbv=2&biw=1280&bih=857&tbm=isch&tbnid=_ECML0RMWPBt0M:&imgrefurl=http://www.asminternational.org/emails/etsspraytips/090809/tssenews090809.html&docid=iNkKQKrhtvCfiM&imgurl=http://www.asminter.
25. Hughes C. J. *Fatigue Behaviour of Laser-Formed High-Stength Low-Alloy*

(HSLA) Sheet material. MTech thesis, Tshwane University of Technology, Pretoria, South Africa, 2004.

26. McGrath P.J. and Els-Botes A. *Characterising the bending behaviour of 2D laser*. In Proceedings of Light Metals, Johannesburg, South Africa, pp. 446-457, October 2010.
27. ASTM International. *Standard Test Methods for Notched Bar Impact Testing of Metallic Materials.* E 23-02$^{\varepsilon 1}$, West Conshohocken, PA, US, 2002.
28. ASTM International. *Standard Test Method for Microindentation Hardness of Materials.* E 384-99$^{\varepsilon 1}$, West Conshohocken, PA, US, 2002.
29. ASTM International. *Standard Test Method for Vickers Hardness of Metallic Materials.* E 92-82$^{\varepsilon 1}$, West Conshohocken, PA, US, 2002.
30. ASTM International. *Standard Test Methords for Tension Testing of Metallic Materials*. E 8-01$^{\varepsilon 1}$, West Conshohocken, PA, US, 2002.
31. ASTM International. *Standard Test Method for Determining Residual Stresses by the Hole-Drilling Strain-Gage Method*. E 837-01$^{\varepsilon 1}$, West Conshohocken, PA, US, 2002.
32. ASTM International. *Standard Practice for Conducting Force Controlled Constant Amplitude Axial Fatigue Tests of Metallic Materials.* E 466-96$^{\varepsilon 1}$, West Conshohocken, PA, US, 2002.
33. Micro-Measurements. *Measurement of Residual Stresses by the Hole-Drilling* Strain Gage Method.* Tech note TN-503, Vishay Precision Group.
34. Churchill SW and Usagi R. *A general expression for the correlation of rates of transfer and other phenomena*. The American Institute of Chemical Engineers,18(6), pp 1121-1128, 1972.
35. Korkmaz S. *Extension of the Uniform Material Law for High Strength Steels*. MEng thesis, Bauhaus University, Germany, 2008.
36. BenPAllen. Wikipidia. [Online].; 2006 [cited 2010/07/21. Available from: http://en.wikipedia.org/wiki/File:BrittleAluminium320MPA_S-N_Curve.jpg.
37. Edwardson S. University of Liverpool. [Online]. [cited 2011/08/08. Available from: www.liv.ac.uk.

38. ASTM International. *Standard Test Methods for Notched Bar Impact Testing of Metallic Materials.* E 23-02$^{\varepsilon 1}$, West Conshohocken, PA, US, 2002.

Appendix A

Gosmeta EP-25 mechanical press setup procedures

Pre-setup inspection

- Always ensure that the correct safety gear is worn before any work procedure may begin e.g. cloves, safety goggles, closed shoes and long pants.
- Ensure that the main power supply is switched to the off position at the orange isolator which is fixed at the side of the torsion measuring machine.
- Check that the area on and around the mechanical press is clean and free of any debris.

Setup procedures

- Ensure that the correct tool and die set are fitted to the mechanical press.
- Move the jig against the backing plate to check that the alignment of the tool and die is correct. This is done without a sample being fitted to the jig.
- Rotate the orange flywheel slowly by hand, while a second person depresses the foot pedal. Now the ram will move in a downward or upward position. This is done to check the spacing between the tool and die.

- **<u>IMPORTANT:</u> Never let the tool bottom out on the die, as this can cause severe damage to the machine.**
- The correct travelling distance can either be set by means of the top toothed set screw, which works in increments of 6 mm, or by the fine tuning screw which is located on the main shaft.
- After any adjustments have been made, make sure that all locking screws are tightened correctly.

Bending Procedures

- After the machine has been set up correctly, a plate specimen can be fitted to the jig. Make sure that the cap screws, which hold the shoes down, are tightened to the correct torque setting.
- The jig can now be moved into position under the tool.
- Before power can be switched on, make sure the tool is in its top dead centre rest position.
- The main power supply isolator can now be switched on.
- Before pressing the on button, which is located on the left hand side of the machine, can be pressed, make sure that all users stand at a safe distance from the machine.
- When the operator feels that all conditions are safe, the on button can be pressed.
- The flywheel will start to rotate and when it has reached its operating speed the foot pedal may be depressed.
- **<u>IMPORTANT:</u> Make sure that the foot pedal is only depressed and released for a brief moment, as keeping the foot pedal**

depressed will cause the machine to continuously press the specimen.

- When the tool has reached its top dead centre rest position, the machine must be switched off. Now the jig may be moved away from under the tool and the plate specimen can be removed.

Shut down

- When all work has been completed move the jig from under the tool to make sure that the tool will not collide with any part of the jig if the pedal is accidentally depressed.
- The main power supply can now be switched to the off position on the orange isolator which is fixed at the side of the torsion measuring machine.

Appendix B

Below is the test report supplied by the manufacturer of the CP Ti grade 2.

TEST REPORT

CustomerName	Our Reference No	Date	Customer Order No
C S I R NATIONAL LASER CENTRE PO BOX 395 PRETORIA 0001	20080201	30-Sep-08	180246

Material Description	No PCS.	Length / Weight	HeatNo
TITANIUM PLATE 3.00MM THK X 1000MM X 2000MM	1		152531

Specification	ASME SB 265-06 GR. 2 SECT. II PART B ADD.06

Chemical Analysis

N	C	H	Fe	O2	Al	V	Sn	Pd	Mo	Zr	Ni
0.009	0.005	0.0030	0.04	0.155							
RESIDUALS EACH	RESIDUALS TOT. L	Ti	Cr	Ta	Cb	Y1	O and Fe	Mn	Si	Mg	Ca
<0.070	0.250	BAL									
Cu	W	NB	Co	P	S	Hf	FeCr	ZrHf			

Mechanical Properties

TENSILE STRENGTH KSI	L	459	L		HARDNESS
	T	444	T		
YIELD STRENGTH KSi (0.2%) OFFSET	L	329	L		
	T	346	T		
% ELONGATION (INCHES)	L	28	L		GRAIN SIZE
	T	28	T		
% REDUCTION IN AREA	L		L		
	T		T		

BEND TEST	OK	OTHER DATA
STATIC NOTCH STRESS RUPTURE		TEST TEMPERATURE: T-20 deg C. / L-20 deg C. MATERIAL IDENTIFICATION No: 028201 04 01 TEST No: A 8599 ANNEALED AND PICKLED. THE MATERIAL SUPPLIED IS IN COMPLIANCE WITH THE REQUIREMENTS OF THE ORDER. INSPECTION CERTIFICATION No: 2008-2167
ULTRASONIC TEST		
FLARE TEST		
IMPACT TEST		
FLATTENING TEST		
HYDROSTATIC TEST		
EDDY CURRENT TEST		
PNEUMATIC TEST		
REVERSE FLATTENING TEST		
DYE PENETRANT		
RADIOGRAPHIC (X-RAY) TEST		
MICROSTRUCTURE PERFORMED		
MICROSTRUCTURE COMPLIANCE		
MACROSTRUCTURE PERFORMED		
MACROSTRUCTURE COMPLIANCE		

CUSTOMER COPY

THIS IS TO CERTIFY THAT THE ABOVE TEST RESULTS ARE CORRECT AS CONTAINED IN THE RECORDS OF THE COMPANY

DATE 2008/09/30

SIGNED

Appendix C

This sheet gives the dimensions of the sub-standard specimen used to correlate the tensile data supplied by the manufacturer of the CP Ti grade 2 sheet.

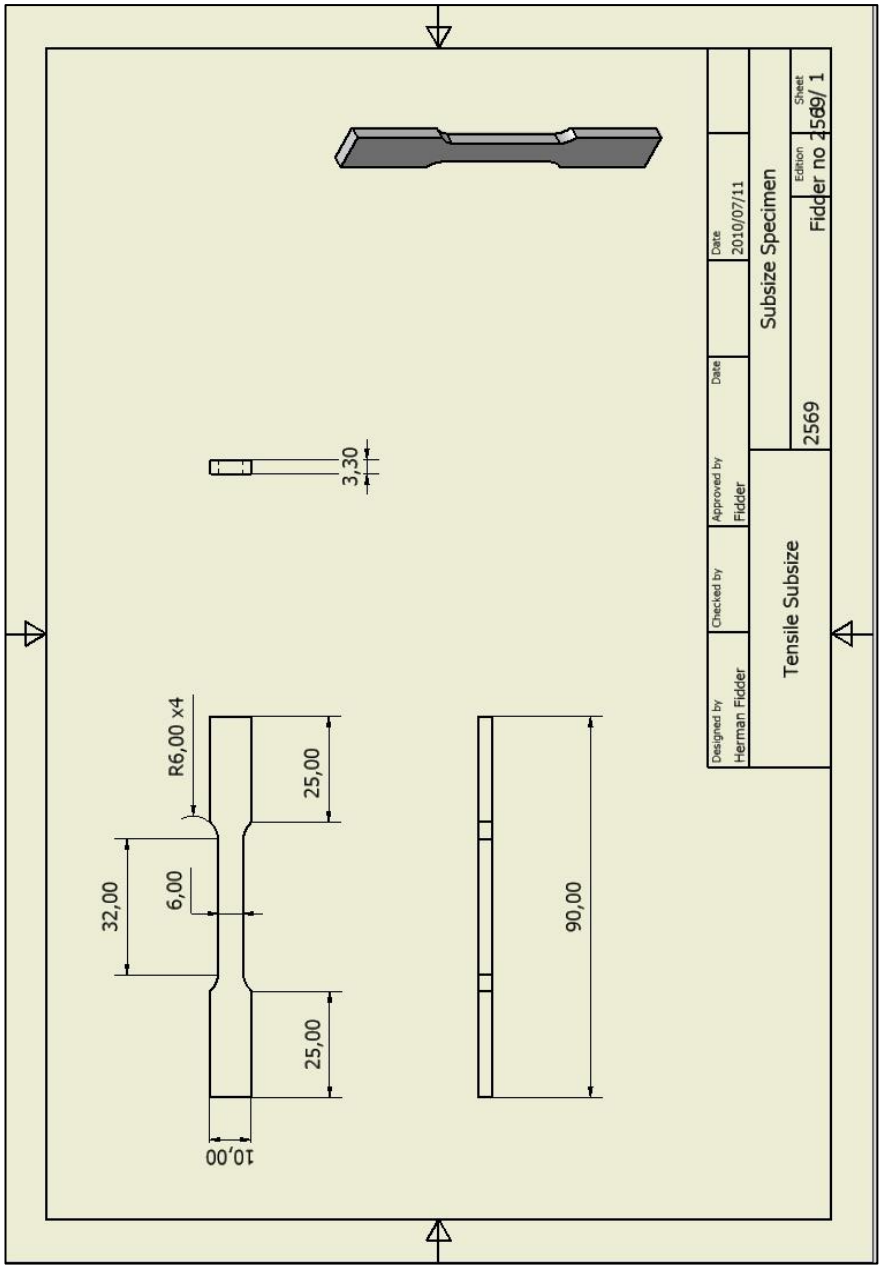

Appendix D

The sheets given below indicate the major fatigue components and assemblies used to fatigue test the specimens. They were designed and implemented by the author of this thesis to ensure that the fatigue specimens coincide with the rotating axis.

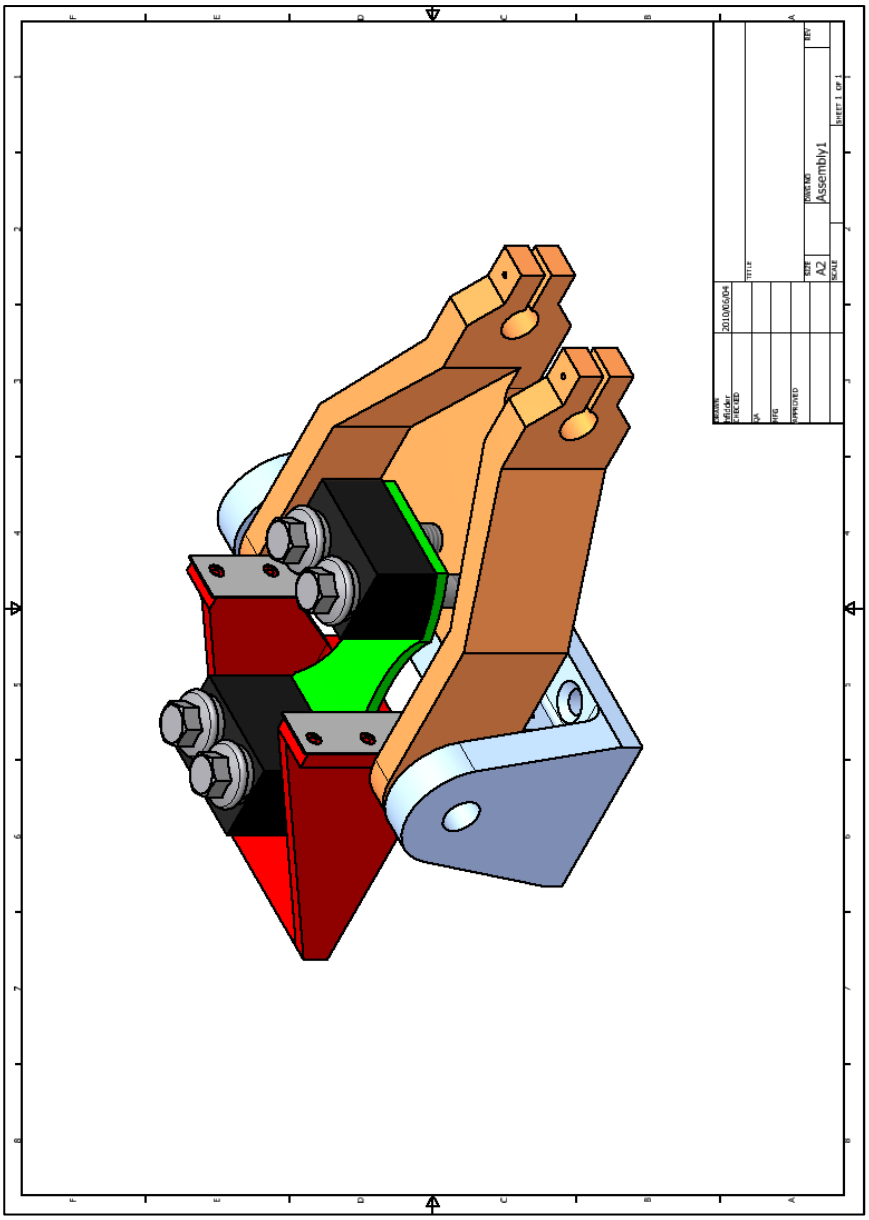

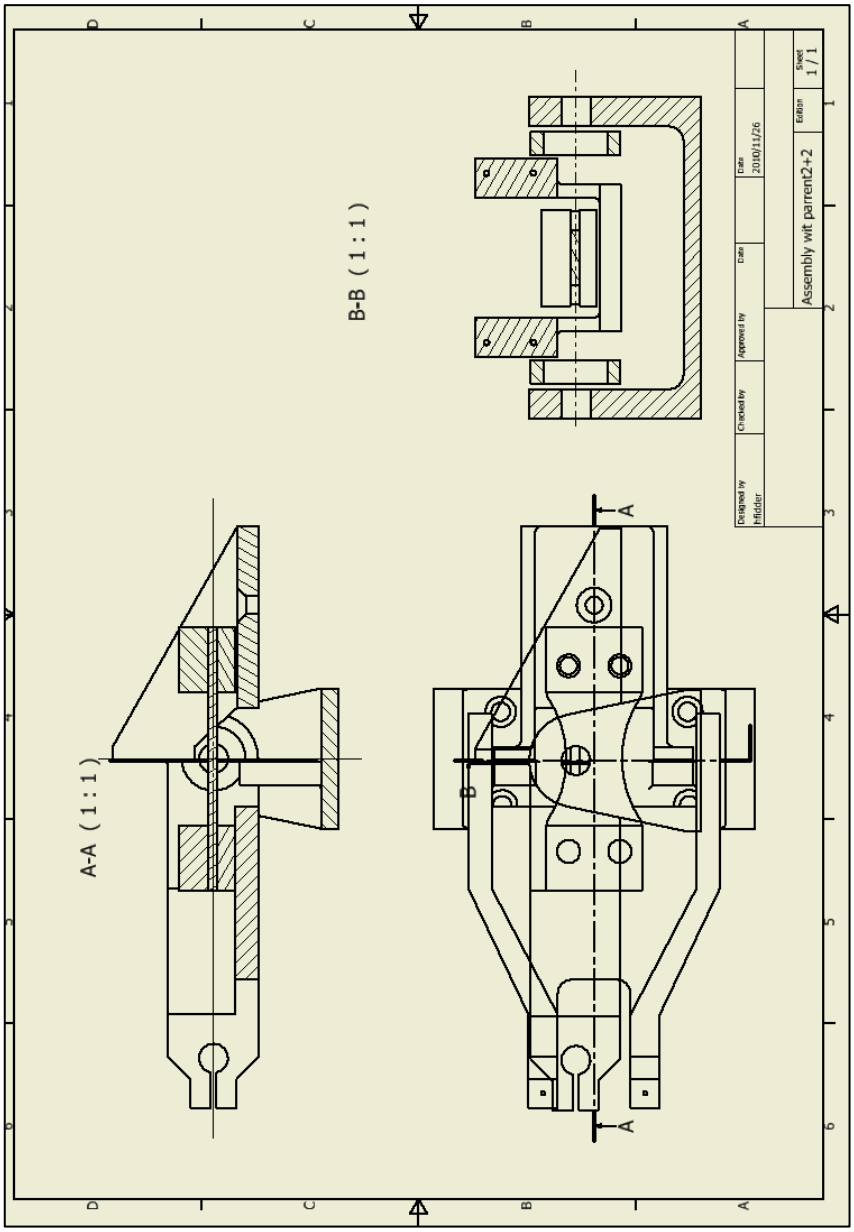
B-B (1 : 1)
A-A (1 : 1)
A
B
A
Assembly wit parrent2+2
Date
2010/11/26
Sheet
1 / 1
Designed by
hfidder

The sheet given below indicates the electrical wire diagram which was designed and installed by the author of this thesis.

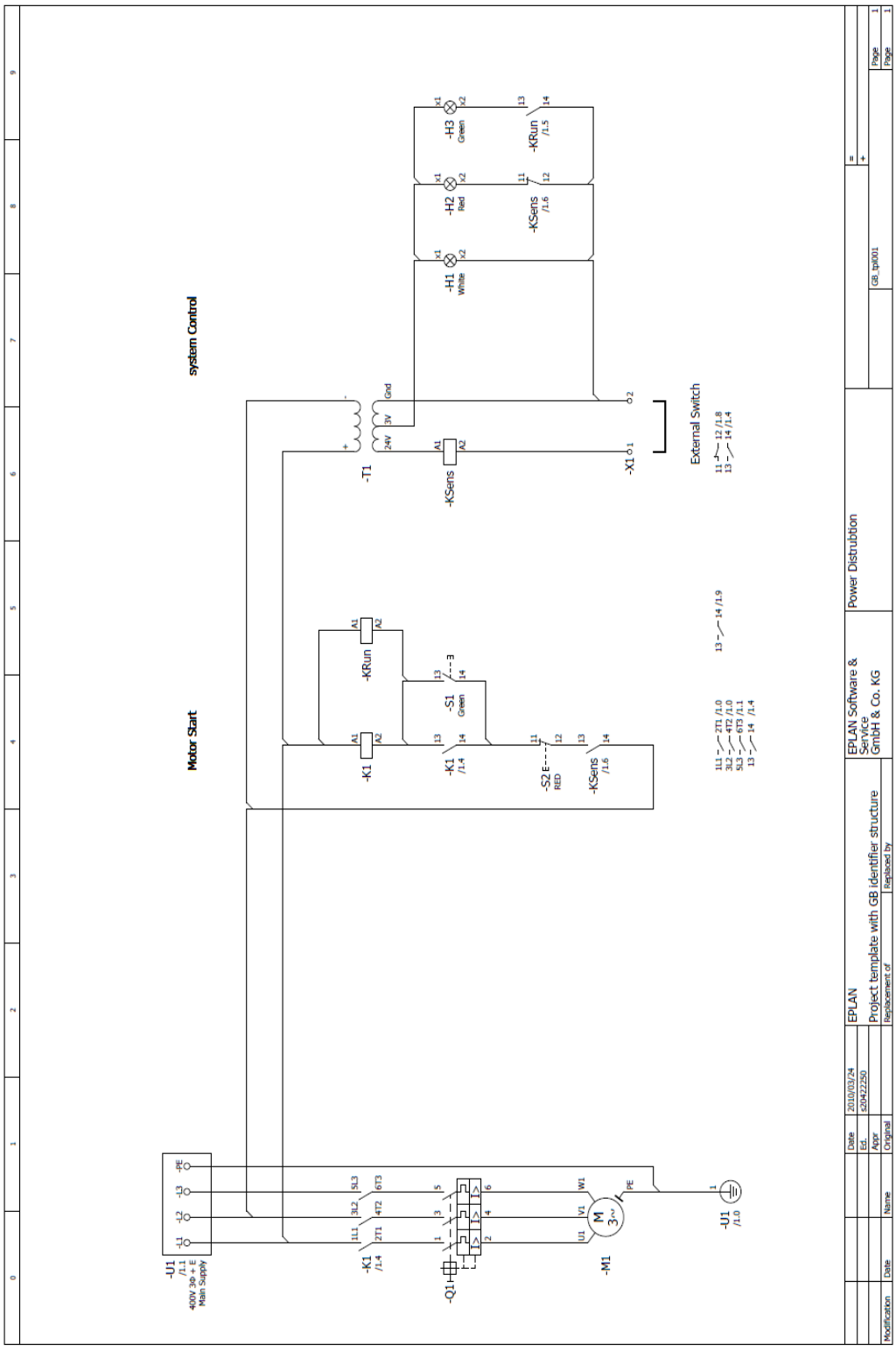

Appendix E

In this appendix the procedure to install a specimen in the fatigue machine is discussed.

- Before installing the master specimen in the fatigue machine, the eccentric wheel must be set to zero and tightened.
- The grab screws at the back (x2) should be loosened and the machine must be adjusted (up or down) so that the base is level on both sides. Tighten the grab screws in such a way that the machine can be adjusted (up or down) under tension.
- Before installing the master specimen, the strain gauge lead should be connected to the strain gauge amplifier and calibrated.
- Install the master specimen and only fasten it finger-tight.
- After inspection torque all four M8 cap screws in a crisscross pattern to a value of 40 Nm [25].
- Rotating the wheel and examining the values obtained on the strain gauge amplifier, the machine can be fine-tuned to display a near zero value. This can be done by slightly adjusting the machine up or down and moving the eccentric wheel.
- If the desired value is obtained, clap down all screws.

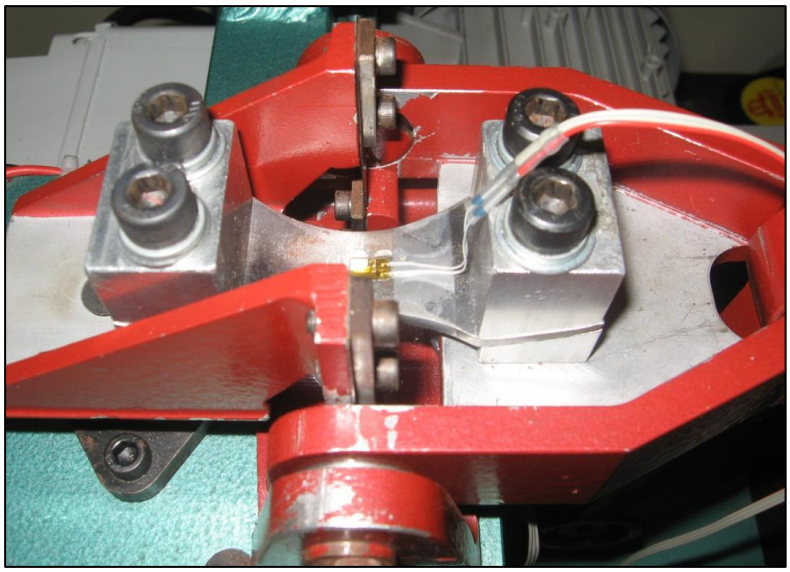

Figure E1 : Master specimen inserted in fatigue machine

Adjustment for the required load on the fatigue machine can only be done via the eccentric wheel. Therefore the following steps should also be considered:

- Set the eccentric wheel to a load that displays the required value. Tighten the eccentric wheel to approximately 40 Nm.
- Rotate the wheel and verify that the two strain gauges display approximately the same value. If not, loosen the grab screws slightly and adjust the machine up or down and then tighten it. Rotate the wheel again and verify the values of the strain gauges. This might take a reasonable amount of time but the calibration can be well within a 5% difference. The calibration setup is shown in Figures E2 and E3 (p 160).

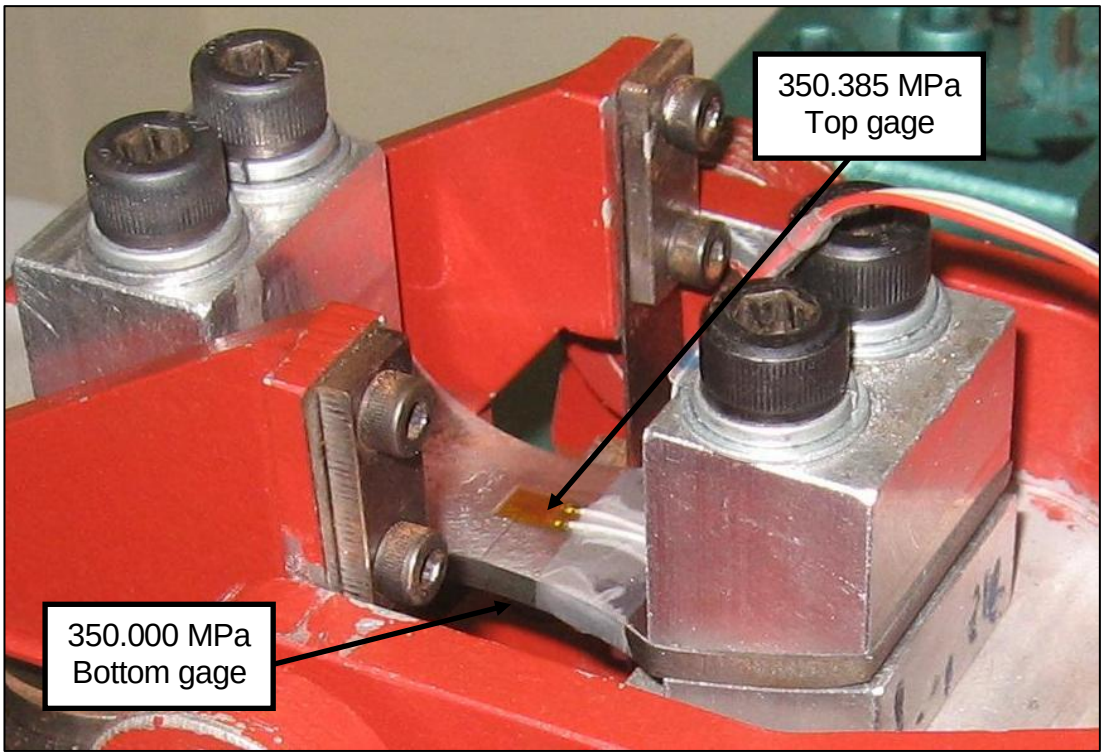

Figure E2 : Master specimen reading during setup

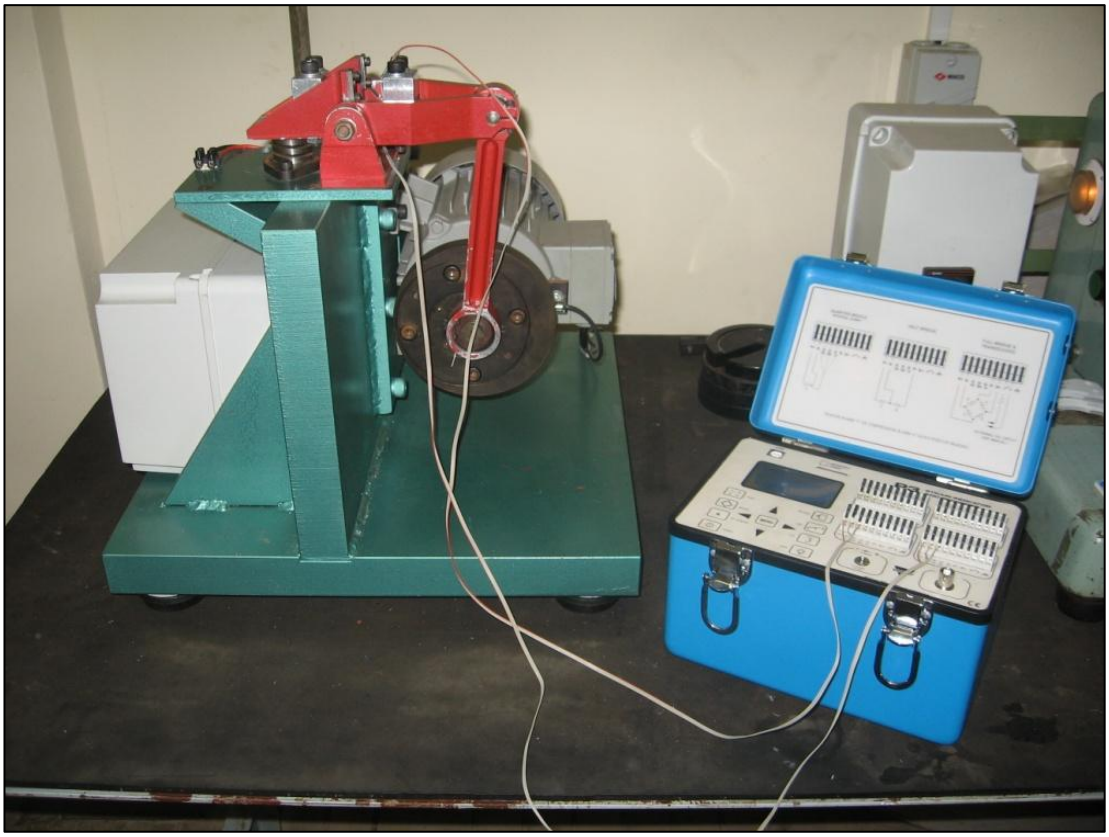

Figure E3 : Master specimen still attached after calibration

Appendix F

This appendix contains tables with the raw data obtained from the residual stress experiments for the parent plate and the three bending processes.

Parent plate					
Depth (mm)	e1x10-6	e2x10-6	e3x10-6	σ(min) MPa	σ(max) MPa
0	0	0	0	0	0
0.1	-1.03E-05	-8.71E-06	-1.51E-05	6.79665676	9.54525501
0.2	-1.83E-05	-1.34E-05	-2.21E-05	10.6513782	15.3020225
0.3	-2.43E-05	-1.68E-05	-2.94E-05	13.820659	20.7534219
0.4	-3.27E-05	-2.17E-05	-4.44E-05	18.9931091	30.5872218
0.5	-4.02E-05	-2.70E-05	-5.92E-05	24.1528579	39.8089987
0.6	-4.27E-05	-2.89E-05	-6.27E-05	25.7070635	42.1150873
0.7	-4.15E-05	-2.89E-05	-6.30E-05	25.5667655	41.6518926
0.8	-4.51E-05	-3.31E-05	-7.09E-05	28.733769	45.8889332
0.9	-4.53E-05	-3.18E-05	-7.19E-05	28.4577746	46.9369865
1	-4.67E-05	-3.45E-05	-7.73E-05	30.4001263	49.3400391
1.1	-4.69E-05	-3.52E-05	-8.02E-05	31.1166019	50.6129018
1.2	-4.83E-05	-3.93E-05	-8.79E-05	33.8998245	53.7192013
1.3	-5.12E-05	-4.40E-05	-9.64E-05	37.2312052	57.7024345
1.4	-4.70E-05	-4.48E-05	-9.57E-05	36.7779995	55.0674049
1.5	-4.78E-05	-4.67E-05	-9.81E-05	37.9161881	55.9777457
1.6	-4.86E-05	-4.75E-05	-1.00E-04	38.6262814	57.2280385
1.7	-5.06E-05	-5.00E-05	-1.03E-04	40.2693099	58.8707637
1.8	-5.19E-05	-5.13E-05	-1.05E-04	41.1598496	59.9200218
1.9	-5.11E-05	-5.16E-05	-1.06E-04	41.212357	59.7291871
2	-5.22E-05	-5.26E-05	-1.07E-04	41.9124736	60.5139969

Laser Outer curve					
Depth (mm)	e1x10-6	e2x10-6	e3x10-6	σ(min) MPa	σ(max) MPa
0	0	0	0	0	0
0.1	-4.00E-06	-4.00E-06	-6.00E-06	1.80641141	2.25705609
0.2	-2.10E-05	-1.40E-05	-2.00E-05	6.86551597	9.79470075
0.3	-3.90E-05	-2.50E-05	-3.00E-05	11.8783958	16.1595299
0.4	-5.40E-05	-3.30E-05	-4.20E-05	16.1247994	22.8844885
0.5	-6.60E-05	-4.10E-05	-4.30E-05	19.1039927	25.1878029
0.6	-8.30E-05	-5.10E-05	-5.40E-05	23.8915245	31.7779801
0.7	-9.60E-05	-6.10E-05	-6.10E-05	27.9549488	35.8414909
0.8	-1.12E-04	-6.90E-05	-7.10E-05	32.1107957	42.2506594
0.9	-1.23E-04	-7.70E-05	-7.80E-05	35.5425558	46.1331408
1	-1.32E-04	-8.30E-05	-8.40E-05	38.2521421	49.5187557
1.1	-1.39E-04	-8.90E-05	-8.80E-05	40.5996767	51.6410353
1.2	-1.44E-04	-9.40E-05	-9.10E-05	42.4503622	53.0411239
1.3	-1.48E-04	-9.70E-05	-9.20E-05	43.5788532	53.9443666
1.4	-1.49E-04	-9.90E-05	-9.20E-05	44.0294969	53.4937229
1.5	-1.50E-04	-1.00E-04	-9.20E-05	44.3453185	53.584248
1.6	-1.50E-04	-1.00E-04	-9.30E-05	44.5263434	54.2159167
1.7	-1.50E-04	-9.90E-05	-9.20E-05	44.2104961	54.1254172
1.8	-1.50E-04	-9.90E-05	-9.10E-05	44.1199705	53.8095961
1.9	-1.49E-04	-9.90E-05	-8.90E-05	43.9389186	53.1779545
2	-1.48E-04	-9.80E-05	-8.80E-05	43.5325719	52.7716077

Laser Inner curve					
Depth (mm)	e1x10-6	e2x10-6	e3x10-6	σ(min) MPa	σ(max) MPa
0	0	0	0	0	0
0.1	-4.76E-05	-6.68E-05	-1.28E-04	35.4093545	46.3531842
0.2	-6.84E-05	-9.23E-05	-1.76E-04	49.0651509	64.4829915
0.3	-8.27E-05	-1.13E-04	-2.11E-04	59.5522451	76.7661759
0.4	-9.52E-05	-1.38E-04	-2.45E-04	70.7041045	87.2621494
0.5	-1.03E-04	-1.55E-04	-2.67E-04	78.0417679	93.6780463
0.6	-1.09E-04	-1.68E-04	-2.85E-04	83.9709216	99.1800072
0.7	-1.15E-04	-1.78E-04	-2.97E-04	88.5140025	103.188784
0.8	-1.19E-04	-1.86E-04	-3.07E-04	91.8394549	105.972
0.9	-1.21E-04	-1.94E-04	-3.15E-04	94.9310856	107.245695
1	-1.24E-04	-2.00E-04	-3.19E-04	97.218986	108.258259
1.1	-1.24E-04	-2.04E-04	-3.22E-04	98.6357058	108.577916
1.2	-1.26E-04	-2.07E-04	-3.24E-04	99.8309487	108.954655
1.3	-1.26E-04	-2.08E-04	-3.26E-04	100.386035	109.349723
1.4	-1.26E-04	-2.09E-04	-3.26E-04	100.65246	109.318747
1.5	-1.25E-04	-2.09E-04	-3.26E-04	100.560622	108.910431
1.6	-1.25E-04	-2.10E-04	-3.25E-04	100.587534	108.576553
1.7	-1.25E-04	-2.10E-04	-3.25E-04	100.586295	108.234602
1.8	-1.24E-04	-2.09E-04	-3.24E-04	100.309957	107.9467
1.9	-1.24E-04	-2.10E-04	-3.24E-04	100.379764	107.834167
2	-1.24E-04	-2.10E-04	-3.24E-04	100.401989	107.947546

Laser-mechanical outer curve					
Depth (mm)	e1x10-6	e2x10-6	e3x10-6	σ min) MPa	σ(max) MPa
0	0	0	0	0	0
0.1	8.00E-06	7.00E-06	-9.00E-06	-1.7665626	2.25137193
0.2	2.50E-05	1.80E-05	-1.50E-05	-5.9064037	1.0583106
0.3	4.40E-05	2.60E-05	-2.60E-05	-8.9175115	0.1909439
0.4	6.10E-05	3.00E-05	-3.20E-05	-11.182679	-2.8767909
0.5	7.20E-05	3.40E-05	-4.30E-05	-12.25472	-1.8047495
0.6	8.10E-05	2.70E-05	-5.30E-05	-10.271878	-3.3027826
0.7	8.30E-05	2.80E-05	-6.30E-05	-9.6723765	-0.0238097
0.8	7.70E-05	1.90E-05	-7.40E-05	-5.4177677	3.96333974
0.9	6.80E-05	1.50E-05	-8.30E-05	-2.3937696	9.66590923
1	5.80E-05	8.00E-06	-8.40E-05	0.67482047	11.9302215
1.1	4.70E-05	4.00E-06	-8.80E-05	3.37364997	16.5035317
1.2	3.80E-05	0.00E+00	-8.60E-05	5.20479269	18.0660541
1.3	3.40E-05	-2.00E-06	-8.10E-05	5.63231897	17.1537185
1.4	2.30E-05	-6.00E-06	-8.30E-05	6.92063756	16.8350185
1.5	2.10E-05	-6.00E-06	-8.20E-05	8.00575518	20.597994
1.6	1.90E-05	-6.00E-06	-8.20E-05	8.22276306	21.3506048
1.7	1.70E-05	-7.00E-06	-8.40E-05	8.92452453	22.5880805
1.8	1.70E-05	-9.00E-06	-8.50E-05	9.78569452	23.1813384
1.9	1.70E-05	-1.00E-05	-8.70E-05	10.2704486	23.6662029
2	1.40E-05	-1.30E-05	-9.00E-05	11.3993635	23.991716

Laser-mechanical Inner curve					
Depth (mm)	e1x10-6	e2x10-6	e3x10-6	σ(min) MPa	σ(max) MPa
0	0	0	0	0	0
0.1	-2.00E-05	-1.70E-05	-1.50E-05	8.35023098	8.61809482
0.2	-5.00E-05	-3.60E-05	-4.20E-05	19.6226482	24.9798082
0.3	-7.30E-05	-5.20E-05	-6.00E-05	28.3558678	36.1237702
0.4	-1.05E-04	-7.40E-05	-8.10E-05	39.9979028	50.1766285
0.5	-1.28E-04	-9.00E-05	-9.60E-05	48.4056482	60.1916368
0.6	-1.50E-04	-1.06E-04	-1.11E-04	56.704911	69.8303184
0.7	-1.66E-04	-1.18E-04	-1.24E-04	63.0649706	77.5297288
0.8	-1.73E-04	-1.26E-04	-1.32E-04	66.8349801	81.0318589
0.9	-1.78E-04	-1.30E-04	-1.39E-04	69.2081431	84.4764076
1	-1.78E-04	-1.35E-04	-1.45E-04	71.1983432	85.3950634
1.1	-1.76E-04	-1.36E-04	-1.54E-04	72.2256139	87.7614578
1.2	-1.71E-04	-1.38E-04	-1.60E-04	72.8698529	87.6020282
1.3	-1.64E-04	-1.38E-04	-1.66E-04	72.7613925	87.2256793
1.4	-1.57E-04	-1.38E-04	-1.72E-04	72.6528868	86.8493756
1.5	-1.54E-04	-1.39E-04	-1.77E-04	73.1376554	87.3342257
1.6	-1.51E-04	-1.40E-04	-1.79E-04	73.2970023	86.6900694
1.7	-1.50E-04	-1.40E-04	-1.81E-04	73.4054547	87.0664264
1.8	-1.50E-04	-1.41E-04	-1.82E-04	73.7817795	87.1749109
1.9	-1.50E-04	-1.39E-04	-1.81E-04	73.1375975	87.3342835
2	-1.50E-04	-1.38E-04	-1.81E-04	72.8697404	87.6021407

Mechanical outer curve					
Depth (mm)	e1x10-6	e2x10-6	e3x10-6	σ(min) MPa	σ(max) MPa
0	0	0	0	0	0
0.1	-1.90E-05	-1.00E-05	1.00E-06	3.68329201	4.17925895
0.2	-2.90E-05	-1.20E-05	5.00E-06	5.24155733	5.24184395
0.3	-3.30E-05	-1.10E-05	6.00E-06	5.27688996	6.51693649
0.4	-4.00E-05	-8.00E-06	1.10E-05	4.72182892	7.94561429
0.5	-4.50E-05	-9.00E-06	1.60E-05	4.96962396	7.69781925
0.6	-4.50E-05	-8.00E-06	2.30E-05	4.06051738	5.54926713
0.7	-4.60E-05	-1.00E-05	2.50E-05	4.4618962	4.71107992
0.8	-5.00E-05	-9.00E-06	2.60E-05	4.49718295	5.98621833
0.9	-5.40E-05	-5.00E-06	2.80E-05	3.6942044	7.66281366
1	-6.10E-05	-6.00E-06	3.00E-05	4.41413152	9.12692847
1.1	-5.70E-05	-9.00E-06	3.20E-05	4.5913543	6.32885537
1.2	-5.90E-05	-9.00E-06	3.30E-05	4.68572423	6.67129382
1.3	-6.40E-05	-6.00E-06	3.20E-05	4.50845287	9.46941551
1.4	-6.30E-05	-7.00E-06	3.40E-05	4.56746415	8.53678745
1.5	-6.30E-05	-6.00E-06	3.60E-05	4.03619409	7.75763235
1.6	-6.50E-05	-5.00E-06	3.60E-05	3.7882602	8.00556624
1.7	-6.50E-05	-6.00E-06	3.50E-05	4.31948117	8.78477043
1.8	-6.70E-05	-6.00E-06	3.50E-05	4.31948117	8.78477043
1.9	-6.70E-05	-7.00E-06	3.60E-05	4.66177681	8.87928318
2	-6.70E-05	-7.00E-06	3.50E-05	4.75623948	9.2216289

Mechanical Inner curve					
Depth (mm)	e1x10-6	e2x10-6	e3x10-6	σ(min) MPa	σ(max) MPa
0	0	0	0	0	0
0.1	-2.10E-05	-1.00E-05	-1.30E-05	6.09215349	9.69732019
0.2	-5.60E-05	-3.00E-05	-2.20E-05	15.7937097	20.4292005
0.3	-9.60E-05	-4.90E-05	-3.50E-05	26.1685505	34.6673628
0.4	-1.31E-04	-7.00E-05	-4.40E-05	36.1272626	45.1420872
0.5	-1.70E-04	-8.60E-05	-5.40E-05	45.3153724	58.7093954
0.6	-1.97E-04	-9.70E-05	-5.30E-05	50.8365653	65.2625059
0.7	-2.16E-04	-1.05E-04	-4.90E-05	54.4473718	68.6176437
0.8	-2.34E-04	-1.09E-04	-4.60E-05	57.0280965	73.0028632
0.9	-2.46E-04	-1.13E-04	-4.30E-05	58.9883693	75.222157
1	-2.55E-04	-1.13E-04	-3.80E-05	59.4013833	76.6667281
1.1	-2.58E-04	-1.13E-04	-3.60E-05	59.5045435	77.0279643
1.2	-2.62E-04	-1.12E-04	-3.50E-05	59.557072	78.3686246
1.3	-2.64E-04	-1.10E-04	-4.00E-05	59.7663242	81.4101464
1.4	-2.63E-04	-1.08E-04	-4.20E-05	59.3549174	82.2859494
1.5	-2.63E-04	-1.08E-04	-4.40E-05	59.5619163	83.0077432
1.6	-2.62E-04	-1.08E-04	-4.50E-05	59.5620286	83.0076309
1.7	-2.61E-04	-1.08E-04	-5.30E-05	60.2866205	85.5338129
1.8	-2.61E-04	-1.09E-04	-5.70E-05	60.9581145	86.7199041
1.9	-2.61E-04	-1.09E-04	-5.90E-05	61.1651046	87.4417065
2	-2.59E-04	-1.09E-04	-5.50E-05	60.5443434	85.27609

Appendix G

This appendix contains the paper presented by the author of this thesis at the ZrTa2011 New Metals Development Network Conference at Mount Grace Country House & Spa, Magaliesburg, 12-14 October 2011.

STRESS-LIFE RESPONSE OF COMMERCIALLY PURE TITANIUM COMPONENTS SHAPED BY VARIOUS FORMING PROCESSES

H Fidder, A Els-Botes, P J McGrath
Department of Mechanical Engineering, Nelson Mandela Metropolitan University, South Africa

Abstract

The Advanced Metals Initiative (AMI) was established in 2003 with the aim to research, develop and innovate across the advanced metals value chain. Advanced metals are defined as all metals which can be used for producing new products and/or having advanced properties through the utilization of new technologies. The Light Metals Development Network (LMDN) is one of the focus areas which fall under the AMI with a research focus primarily on light metals such Titanium and Aluminium alloys. The two most beneficial properties of Titanium are its corrosion resistance and high strength-to-weight ratio. Laser forming (LF) is a sheet metal shaping process that results in deformation by introducing thermal stresses into the surface of a metal component with a laser beam to induce plastic strains that result in local elastic-plastic behaviour. The overall aim of conducting research studies in the field of LF is to develop the process as a flexible fabrication technique for three dimensional components without mechanical contact and hence avoiding expensive hard tooling. Technology development in the field of

laser forming of titanium directly links with the aims of the Titanium Center of Competence (TiCoC) as the role of TiCoC is to integrate and coordinate research and development and commercialisation across the value chain.

Commercially pure (CP) titanium grade 2 shows low ductility at room temperature and therefore springback is a concern during cold forming of high precision components for industrial applications. In this paper CP titanium has been deformed employing three different processes i.e. (i) mechanical forming (tool & die), (ii) laser forming and (iii) a combination of mechanical–laser forming. Samples were evaluated in order to compare the effect that the various forming processes have on the fatigue life and micro-hardness of the resultant components. The experimental results indicate that CP titanium grade 2 laser formed fatigue specimens showed an increase in life (at higher stress amplitudes) compared to the mechanically formed and combined formed specimens. The results obtained from Vickers micro-hardness testing revealed no significant change in hardness due to the various forming processes. From this study it is envisaged that laser forming can be a beneficial forming process for CP titanium when high precision and extended fatigue life is required.

1. Introduction

Commercially pure titanium (CP Ti) is a potential material for structural components due to its high specific strength and excellent corrosion properties [10]. Press forming is the general standard manufacturing process for CP Ti due to the process having high productive performance [2]. Difficulty in forming titanium is due to the following material characteristics: notch sensitivity, galling, relatively poor ability to shrink, potential embrittlement from heating and

absorption of gasses, limited workability and higher spring-back compared with ferrous alloys [10, 5]. The hexagonal close-packed (HCP) structure of CP Ti exhibits limited ductility at room temperature when using a tool and die method of forming and therefore elastic recovery i.e. spring-back is a great concern when precision components are required [4]. The laser forming (LF) process has become of great interest to industrial sectors like aviation, automotive and ship building due to its process agility and automation capabilities [1]. Most published literature of CP Ti is focused on micro-structural changes, whereas literature regarding formability of CP Ti is relatively scarce. Materials subjected to fluctuating stresses and strains may fail after a sufficient number of fluctuations at stresses below the yield of the material [7, 8]. This failure is referred to as fatigue failure. In the present study, the formability of CP Ti was investigated by subjecting the material to three different forming processes i.e. (i) mechanical forming (tool & die), (ii) laser forming and (iii) a combination of mechanical–laser forming. Setting for the three forming processes were such as to result in an approximate radius of curvature of 120mm. The fatigue life of samples produced by forming processes, at different stress amplitudes, were obtained by experimental testing. In addition, micro-hardness plotting was recorded along the length and thickness of the various microstructure zones.

2. Experimental approach and method

2.1 Material

The material utilized for this experiment was commercially pure titanium grade 2. In industry this material is most widely used due to its corrosion properties and ease of fabrication. The material displays two crystallographic forms depending

on temperature. It has a hexagonal close-packed structure below 883ºC and a body centred cubic structure above 883ºC. Creep resistance of CP titanium grade 2 is considered better compared to beta alloys [10]. Formability of CP Ti is limited at room temperature and can be improved by elevating the forming temperature [3]. Due to the fact that the material is an alpha alloy it cannot be hardened by heat treating [1]. The parent material exhibits an equiaxed grain structure and has an average hardness of 176HV0.3. Tensile testing revealed the material has a yield strength of 352MPa and a tensile strength of 450MPa.Test specimen dimension were 200 x 50 x 3.2 mm.

2.2 Fatigue setup

Dog-bone shaped fatigue specimens were machined from (i) parent plate, (ii) mechanical formed (tool & die), (iii) laser formed and (iv) combination of mechanical–laser formed test specimens given in ASTM E468-82 as shown in Figure 1. To accurately determine the stress–strain characteristics of the material, $R = -1$ strain control testing was employed for the generation of open hysteresis loops. An approximate R ratio of −1 was employed to allow for fully reversed stress conditions. Testing was done at room temperature and the fatigue samples were coated with a base paint to prevent electrical contact between the sample and silver paint crack detection circuit. An Avery Dynamic Fatigue Testing machine was utilized for the testing, operating at approximately 24Hz. The typical sample appearance used for setup (Master sample) is shown in Figure 2.

Figure 1: Master sample used for strain controlled loading.

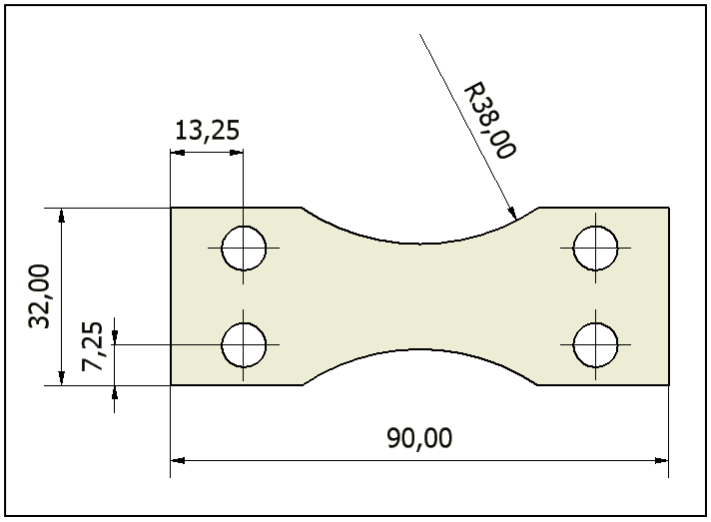

Figure 2: ASTM E468-82 fatigue dag-bone specimen.

2.3 Evaluation procedures

Vickers micro-hardness was done according to ASTM E384-99 with a 15 second dwell time and a weight of 300 grams. Since the material was supplied in the annealed condition an average hardness value was determined with measurements taken along the length as well as through the thickness of the sample.

Prediction of material behaviour requires a thorough understanding of the stress – strain conditions that occur during fatigue loading. As displayed in Figure 2 a master sample was manufactured using strain gauges which allowed for recording of stress-strain values under strain control loading. The Juvinall & Marshek model [9] was used to predict the fatigue behaviour of specimens under fully reversed loading conditions. High cycle fatigue [11] testing was conducted and the parameters were chosen to result in lives comparing to $100x10^3$, $60x10^3$, 10 $x10^3$ cycles, therefore loads corresponding to 99.4%, 68.6% and 65.5% of yield (parent material) were determined.

3. Results and Discussion

3.1 Fatigue analysis

Results from fatigue testing of CP Ti grade 2 are given in Table 1 and graphically displayed in Figure 3.

	Parent Plate	Mechanical	Laser	Combined
Load 1 (99.4%)	45420	11281	14242	13382
Load 2 (68.6%)	66457	46649	36526	42600
Load 3 (65.5%)	88115	64504	40801	55998

Table 1: Average N_f at the various load settings

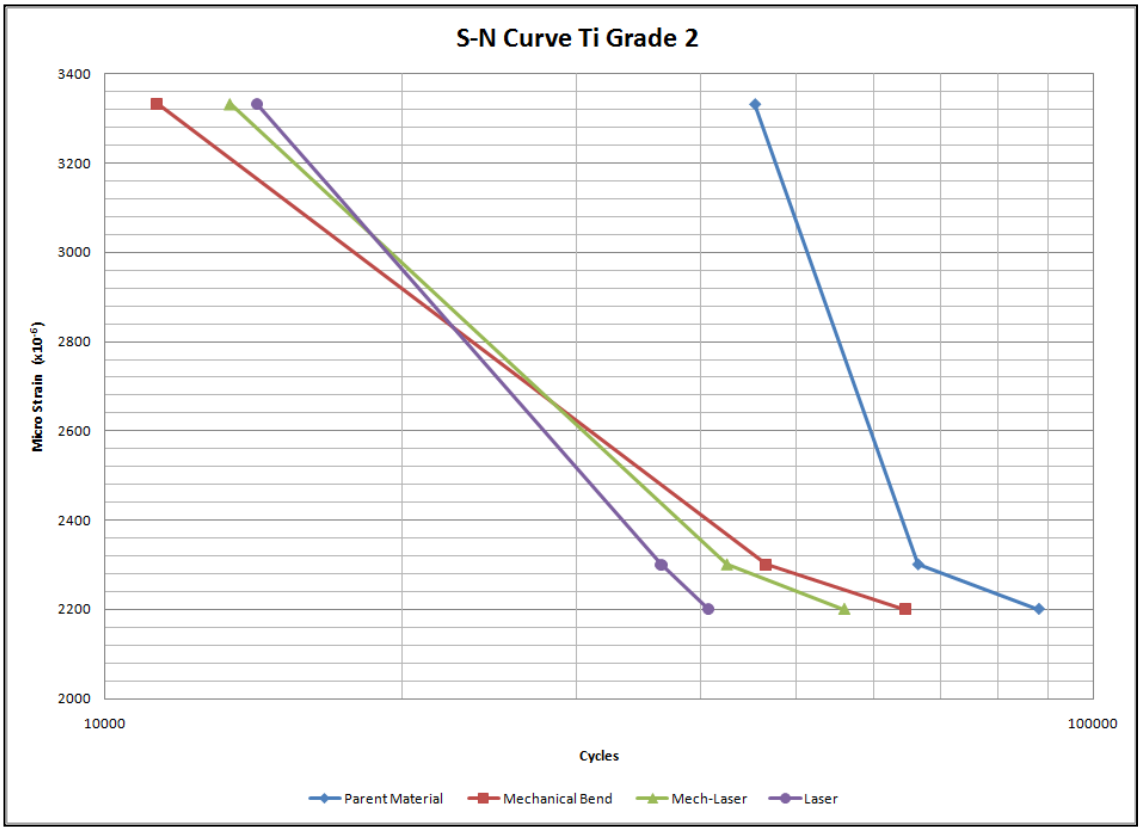

Figure 3: Fatigue curves of various forming possesses at three different loading amplitudes at room temperature and R=-1 conditions.

Figure 3 illustrates that the parent plate show a far superior fatigue life compared to the three bending processes.

Table 2 illustrates the percentage of cycles when compared to the parent plate. The highest percentage difference can be seen at load 1 where mechanical formed samples achieved 75.2% of parent plate cycles. At 26.8% the mechanical formed samples performed the best when compared to parent plate.

Table 2: Percentage difference in life cycles compared to parent plate

	Parent Plate	Mechanical	Laser	Combined
Load 1 (99.4%)	100%	75.2%	68.7%	70.5%
Load 2 (68.6%)	100%	29.8%	45%	36%
Load 3 (65.5%)	100%	26.8%	53.7%	36.5%

3.2 Vickers micro hardness

Vickers micro-hardness profiles are recorded for all three bending methods along the length and through the cross section of the samples. Figure 4 illustrates an average through thickness hardness profile of the three bending processes. Measurements started at a depth of 0.14 mm below the irradiated surface up to a depth of 3mm with intervals of 0.2mm between indentations. The laser bent samples displayed an average hardness of 173HV0.3 whereas the average laser-mechanical hardness obtained was 169HV0.3. The highest average hardness value was recorded for the mechanical formed samples, i.e. 177HV0.3. It can be noted that the maximum average difference between the forming processes is 8HV and can be considered as negligible as the Vickers micro-hardness test equipment has a deviation of 30HV units.

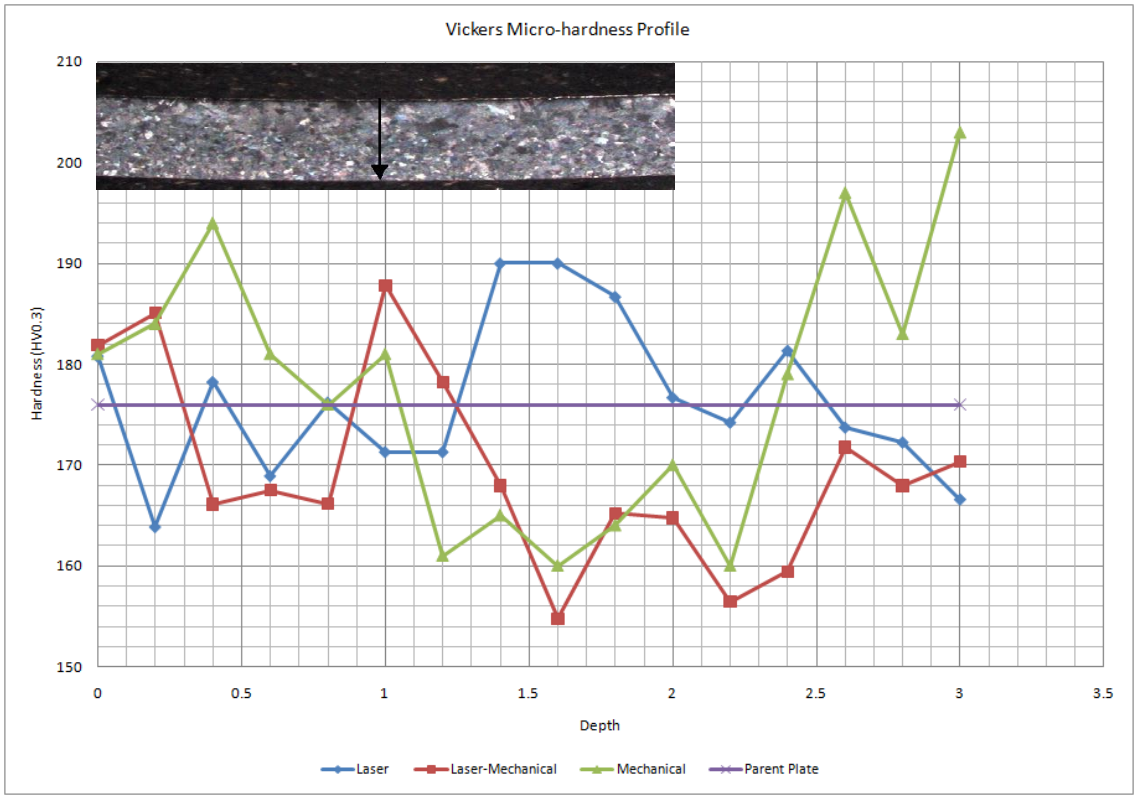

Figure 4: Micro hardness profile of (i) mechanical forming (tool & die), (ii) laser forming, (iii) a combination of mechanical–laser forming and (iv) parent plate.

4. Conclusions

- At the higher strain amplitudes the laser formed samples performed better than the mechanical formed samples. However at the lower strain amplitude the opposite trend occurs.
- No significant difference in hardness was obtained between the laser, laser-mechanical, mechanical and parent plate. Maximum difference in micro-hardness between the forming processes is 8HV.

5. Acknowledgements

This work would have not been possible without the assistance of:

- Mr. Glynne Erasmus for assistance with hardness testing.
- NRF for project funding
- NMMU for financial assistance

6. References

1 McGrath PJ, Els-Botes A. *Characterizing the bending behaviour of 2D laser formed titanium sheet material.* Light Metal Conference 2010:1-8 (446 – 454)

2 Chen K, Chiu K. *Stamping formability of pure titanium sheets*. Journal of Materials Processing Technology 170 (2005): 181 – 186

3 Chun XU, Wen-feng ZHU. *Transformation mechanism and mechanical properties of commercially pure titanium.* Trans. Nonferous Met. Soc. China 20 (2010): 2162-2167

4 De-hue HE, Dong-sheng LI, Xiao-qiang LI, Chao-hai JIN. *Optimization on springback reduction in cold stretch forming of titanium-alloy aircraft skin.* Trans. Nonferous Met. Soc. China 20 (2010): 2350-2357

5 Jeswiet J, Geiger M, Engel U, Kleiner M, Schikorra M, Duflou J, Neugebauer R, Bariani P, Bruschi S. *Metal forming progress since 2000.* Journal of Manufacturing Science and Technology. 1 (2008): 2-17

6 Santos EC, Osakada K, Shiomi M, Abe F. *Microstructure and Mechanical properties of pure titanium models fabricated by selected laser melting.* Journal of Mechanical Egineering Science (2004): 711-719.

7 Whittaker MT, Harrison W, Hurley PJ, Williams S. *Modelling the behavouir of titanium allys at high temperature for gas turbine applications.* Materials Sience and Engineering. Issues 16-17 (2010): 4365-4372

8 Boehlert CJ, Cowen CJ, Quast JP, Akahori T, Niinomi M. *Fatigue and wear evaluation to TI-Al-Nb alloys for biomedical applications.* Materials Science and Engineering. Issue 3 (2008): 323-330

9 Juvinall R C, Marshek K M. Fundamentals of machine component design.4th ed. Asia: John Wiley & sons, inc; 2006

10 ASM International, Materials Properties Handbook: Titanium Alloys.4th ed. USA: Materials Park; 2007

11 Pook L. Metal Fatigue. The Netherlands: Dordrecht; 2007

Appendix H

Characterization of microstructure and fatigue life of CP titanium grade 2 specimens subject to various bending processes

H. Fidder[1], A. Botes[1], S. Woudberg[2] & P. J. McGrath[1]
[1]*Department of Mechanical Engineering, Nelson Mandela Metropolitan University, Port Elizabeth, South Africa*
[2]*Applied Mathematics Division, Department of Mathematical Sciences, Stellenbosch University, Stellenbosch, South Africa*

Abstract

This study focussed on an investigation into the fatigue behaviour of commercially pure (CP) titanium (Ti) grade 2 specimens produced by various bending (deformation) processes, i.e. mechanical bending, laser bending and laser-mechanical bending. Although published literature on the fatigue behaviour of components produced by laser forming is relatively limited, it was found that laser bending could improve the mechanical behaviour of such components. At high fatigue load settings the microstructure was the dominant contributor to crack initiation and crack growth. After the specimens were bent, residual stress analysis as well as a characterization of the microstructure was performed on the three bent samples as well as the parent plate. Mathematical equations were formulated and presented for the laser forming process for predicting the fatigue life of CP Ti grade 2. This study revealed that the laser forming process can be successfully used as a manufacturing method in the forming of CP Ti grade 2.

Keywords: Laser forming, fatigue testing, residual stress, commercially pure titanium, microstructure

Introduction

When a material is subjected to cyclic loading, progressive and localised damage occurs in the material with time. These loading cycles, measured in stress values, are lower than the (ultimate) tensile strength and often below the tensile yield strength of the material. Cyclic loading can be described as repeated loading and unloading of a component and could lead to microscopic cracks developing on the surface. When these cracks develop to a critical size through the load bearing cross-section, sudden failure of a structure can occur. A significant influence on fatigue life is the shape of the component which can amplify concentrated stress levels (ASM International [1, 2]).

This study was aimed at describing the fatigue behaviour of CP Ti grade 2 specimens (3.2mm thick) produced by three different forming methods. The three processes investigated were: a) mechanical bending; b) laser bending and; c) laser-mechanical bending. Few literary sources exist describing the fatigue behaviour of components produced by laser forming and the possibility

exists that this forming method could lead to an improvement in the fatigue behaviour of components.

From literature it has been identified that the grain size of unalloyed titanium has a significant effect on the number of cycles to failure [2]. The crack initiation and crack growth mechanism as well as the surface residual stress magnitudes are additional factors that significantly influence the fatigue life of CP Ti grade 2. This experimental study was performed to measure the residual stress magnitudes of the various formed samples together with microstructure evaluation in order to determine their influence on the resultant fatigue life of samples produced by the different forming processes.

Experimental Setup

Forming processes

All specimens were deformed to a radius of curvature of approximately 120 mm. Mechanical forming was performed on a Rejva\Gosmeta mechanical bending press capable of a maximum force of 25 tons. Laser forming was done using a continuous wave 5kW CO_2 Trumpf laser system with a doughnut shaped laser beam. Because of the laser system's long wavelength (10.6µm) the sample surfaces were coated with a matt black spray to ensure maximum laser beam absorptivity. Although burn-off was evident after the first scan the irradiated surfaces remained sufficiently dark to prevent reflection of the laser beam. The specific laser settings used to produce the laser formed samples was a 1.4kW laser power; 12mm laser beam diameter; 1.2m/min scanning velocity. The number of scans per line was six with a 6mm interval spacing between consecutive line scans i.e. a 50% overlap between lines.

Laser-mechanical formed samples were produced by first laser forming to an average radius of curvature of 240 mm after which it was mechanically formed to an average radius of 120 mm. Plate samples of size 200 x 50 x 3mm were prepared for laser and mechanical forming.

Fatigue

The dimensions of the fatigue specimens were based on details given in ASTM E466-96 [3]. After cleaning the samples with a deburring tool and acetone, the specimens were coated with a non-conductive primer where after conductive paint was used to replicate a circuit on the specimen to ensure that the machine switches off once crack initiation commences.

Residual stress

Residual stress measurements were performed using the hole drilling method. An EA-06-062RE-120 strain gauge was used and the principal stresses were calculated using ASTM E837-01 [4]. The drilling depth was set to 2 mm. Residual stress measurements were recorded for the inner and outer radius of the specimens.

Microstructure

Sections for microstructure evaluation were removed from the cross-section of the formed sample at a position that corresponds to the center of the fatigue specimens. The samples were prepared by following standard metallographic procedures and etched in Kroll's reagent to reveal the microstructure.

Results and discussion

Residual stress

The stress relaxation curves as a function of drilled hole depth for measurements taken at the inner radius of curvature, is shown in fig. 1.

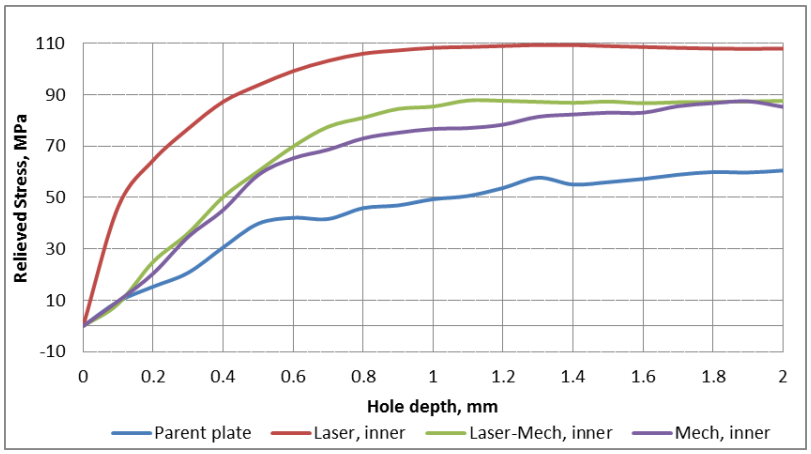

Figure 1: Relieved residual stress of parent plate and formed samples (inner radius of curvature).

The parent plate sample's curve is given as a reference to indicate the material's residual stress state in the as-received condition. From fig. 1 it can be observed that the laser formed specimen has the highest relieved stress values at all depths compared to the other forming processes. Because the laser forming process takes place with the aid of thermal stresses, a higher residual stress value can be expected. However, when considering the outer radius of curvature, the laser formed specimens yielded similar relieved stress values than the parent plate. The average value was significantly less than what was obtained on the inner radius of curvature, but still higher than the average values obtained for the mechanical and laser-mechanical forming processes. The relieved residual stress values obtained at the inner radius of curvature is thus regarded as the "worst case scenario" and therefore Table 1 only gives the residual stress data measured at the inner radius of curvature for the three forming processes. It is evident from table 1 that the laser forming specimens yielded the highest maximum residual stress value when compared to the other

two forming processes. In general all the forming processes lead to an increase in maximum residual stress value as compared to the as-received parent plate.

Table 1: Maximum relieved residual stress values (measured at the inner radius of curvature).

Specimen	Maximum Relieved Stress (MPa)
Parent Plate	69.15
Laser Formed	108.25
Mechanical Formed	87.44
Laser-Mechanical Formed	87.86

Fatigue

According to literature (ASM International [5]), the S-N (i.e. stress vs. number of cycles) curve for CP Ti grade 2 exhibits a distinctive levelling at approximately 10^5 cycles. Therefore, a steeper decrease in fatigue life is observed between 10^4 and 10^5 cycles as opposed to the range of 10^5 to 10^7 cycles. Radonovich [6] also encountered this phenomenon, whereby the transition from high cycle fatigue to low cycle fatigue differs in gradient. Table 2 gives the number of cycles to failure at high, medium and low fatigue load settings for the parent plate and the three forming processes.

Table 2: Results of fatigue testing.

Load (MPa)	Parent Plate	Laser Formed	Mech. Formed	Laser-Mech. Formed
350.0 (High)	45 420	13 896	11 657	13 382
241.5 (Med.)	66 457	36 526	48 772	42 600
231.0 (Low)	88 115	38 506	63 434	55 998

Considering all the forming processes, the laser formed specimens performed slightly better (3.8% better than Laser-Mech. Formed specimens) at the highest load setting but it performed the worst at the medium and low load settings.

Microstructure

The original microstructure of CP Ti grade 2 as-received plate is shown in fig. 2A. The microstructure consists of equiaxed alpha grains with an average grain diameter of 83.4µm. Fig. 2B shows the microstructure of the laser formed specimens which exhibited a Widmanstätten-like structure throughout the thickness of the specimens. This microstructure for pure titanium is associated with fast cooling rates typically between 800˚C to 25˚C via quenching [2]. The microstructure at higher magnification near the laser irradiated surface is shown

in fig. 3C. It is evident that small precipitated particles are present in the microstructure.

The cooling rate associated with the laser forming of these specimens was recorded using an infrared thermal camera and the highest cooling rate was obtained during the first line scan corresponding to a cooling rate of 2320.5°C/s whereas the cooling rate for subsequent scan lines were less severe and corresponded to a value of approximately 110°C/s between subsequent scan lines [7].

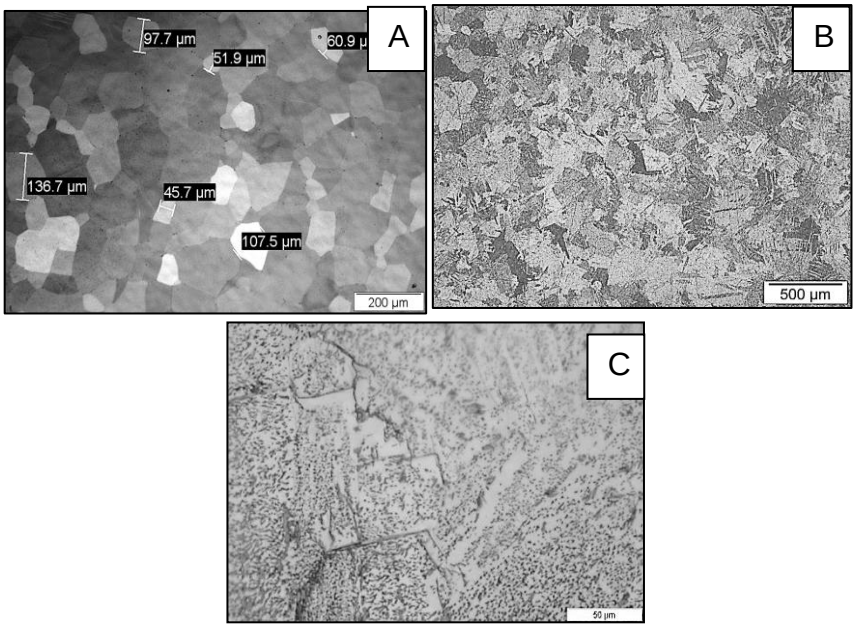

Figure 2: A, original microstructure; B, microstructure of laser formed specimens; and C, near surface microstructure of laser formed CP Ti grade 2 specimen.

Fig. 3A shows the microstructure of the mechanical formed specimens which shows clear evidence of twinning at both the inner and outer surface of the radius of curvature. Twinning was observed up to a depth of approximately 257.5µm from the outer radius surface and to a depth of 502.7µm from the inner radius surface. Fig. 3B shows the near surface microstructure of the combined laser-mechanical process (laser irradiated side i.e. inner radius of curvature). The Widmanstätten-like structure was observed up to a depth of approximately 312.5µm at the irradiated side while twinning was found to a depth of approximately 261.6µm below the outer radius of curvature surface.

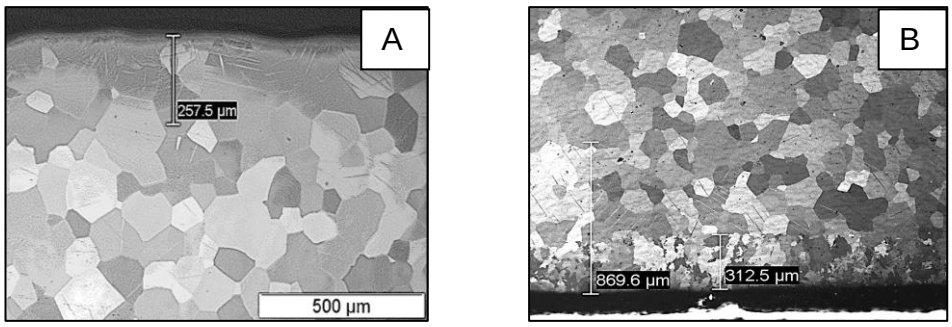

Figure 3: A, microstructure of mechanically formed CP Ti grade 2, and B, microstructure of laser-mechanical formed CP Ti grade 2.

Fatigue models

In order to obtain a mathematical model that can predict the dependence of the fatigue life on the number of cycles to failure, as obtained experimentally for CP Ti grade 2, the power addition technique of Churchill & Usagi [8] is used. The Gerber model (Bannantine, Comer & Handrock [9]) is used as an upper limit and the Goodman model (Bannantine, Comer & Handrock [9]) as a lower limit. Regression curves for the Gerber, Goodman and the actual data were obtained and the residual stress values were incorporated into these models. The power addition technique was first applied to the Gerber model and the curve representing the actual data. The resulting equation was then used together with the Goodman model in the power addition technique, yielding:

$$\boldsymbol{y} = \left[\left([(\boldsymbol{y_{Gerber}})^{\boldsymbol{s}} + (\boldsymbol{y_{actual}})^{\boldsymbol{s}}]^{\boldsymbol{1/s}}\right)^{\boldsymbol{-t}} + (\boldsymbol{y_{Goodman}})^{\boldsymbol{-t}}\right]^{\boldsymbol{-1/t}} \quad (1)$$

The shifting exponents $\boldsymbol{s}$ and $\boldsymbol{t}$ determines the rate at which the cross-over takes place between the two asymptotic limits. The higher the value of the shifting parameters, the closer the resulting curve approaches the point of intersection of the two limits. The value of $\boldsymbol{s}$ and $\boldsymbol{t}$ that provided sufficient correspondence with the experimental data was 50. The resulting prototype predictive equation for the fatigue life of CP Ti grade 2, subject to laser forming, is given by:

$$\boldsymbol{y} = \left[\left(\left[(\boldsymbol{-0.00075x + 352})^{\boldsymbol{50}} + \left(\boldsymbol{440e^{-1.6\times10^{-5}x}}\right)^{\boldsymbol{50}}\right]^{\boldsymbol{1/50}}\right)^{\boldsymbol{-50}} + (\boldsymbol{-0.0009x259.74})^{\boldsymbol{-50}}\right]^{\boldsymbol{-1/50}} \quad (2)$$

Eqn (2) as well as the Gerber and Goodman models are represented graphically in fig. 3. In eqn 2, $\boldsymbol{y}$ denotes the fatigue life and $\boldsymbol{x}$ the number of cycles to failure. By following the same procedure as above, similar eqns can be obtained for the parent plate, mechanical- and laser-mechanical forming processes. Since a primary focus of this study is laser forming, the predictive fatigue life equations and corresponding figures for the parent plate and the mechanical and laser-mechanical bending processes are omitted.

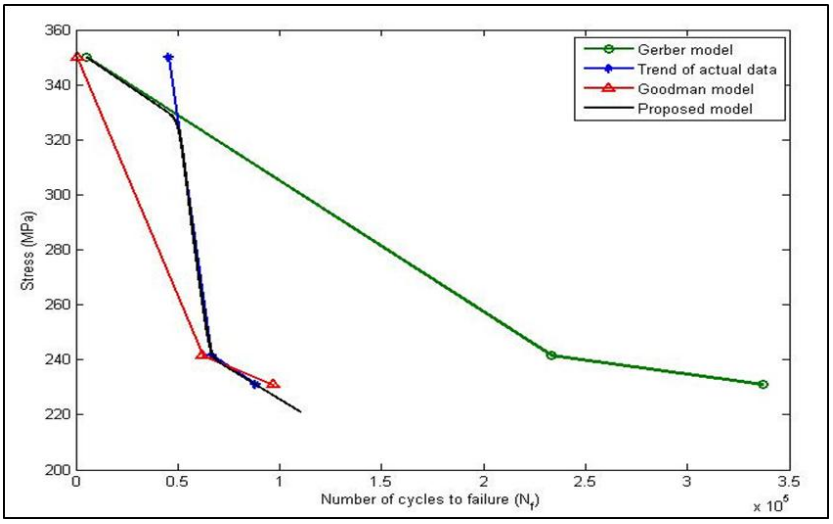

Figure 4: Prototype prediction curve for laser forming.

Conclusions

It was found that the primary factor influencing the fatigue life of CP Ti grade 2 specimens was the microstructure with the secondary factor being the residual stress, especially at medium to low fatigue load settings. Laser forming resulted in microstructural changes from equiaxed grains to a Widmanstätten structure due to the fast cooling rates experienced during the forming process.

Laser formed samples also revealed the highest values in relieved residual stress whereas the other two processes, i.e. mechanical and laser-mechanical forming, exhibited an increase midway between the parent plate and laser formed samples.

Fatigue testing revealed that samples produced by laser forming performed the best at the high fatigue load setting even though it performed only marginally (3.8%) better than the Laser-Mechanical formed specimens. This slight improvement in life cycles at high load settings can be due to the fact that no twinning was observed after forming; therefore crack initiation was slower to develop.

When considering the low fatigue load setting, it can be observed that crack propagation develops relatively quickly within the Widmanstätten structure (at the surface). This phenomenon was also observed by other researchers ((Matthew and Donachie – ASM International [2]) where the equiaxed microstructure achieved more cycles before failure than that of the lamellar microstructure. However, it should be noted that the samples were laser formed without any deliberate protective gas shielding. The possibility therefore exists that oxygen and hydrogen diffused into the metal surfaces due to their high solubility in CP Ti. At elevated temperatures hydrides form as hydrogen diffuses into the material during exposure with either gaseous or cathodic hydrogen. Hydrides cause a loss in ductility and reduce the intensity threshold for crack propagation [2].

The proposed mathematical model for predicting the fatigue life of CP Ti grade 2 subject to laser forming incorporates existing fatigue models as well as the measured experimental data which can be used for further analysis in understanding the behaviour of this material.

Acknowledgements

This work would not have been achieved without the assistance of the personnel at the National Laser Centre facility at the CSIR and Mr G Erasmus from the Department of Mechanical Engineering at the Nelson Mandela Metropolitan University for laboratory and technical assistance.

This material is based upon work supported financially by the National Research Foundation. Any opinion, findings and conclusions or recommendations expressed in this material are those of the authors and therefore the NRF does not accept any liability in regard thereto.

References

[1] ASM International. Eds. R. Boyer, G. Welsch & E. W. Collings, *Materials Properties Handbook: Titanium Alloys.* ASM International, Materials Park, Ohio, 1994.

[2] ASM International. *Titanium - A Technical Guide.* (2nd Ed.) ASM International, Materials Park, Ohio, 2000.

[3] ASTM International. *Standard Test Method for determining Residual Stresses by the Hole-Drilling Strain-Gage Method*. E837-01^{e1}, West Conshohocken, PA, USA, 2002.

[4] ASTM International. *Standard Practice for Conducting Force Controlled Constant Amplitude Axial Fatigue Tests of Metallic Materials.* E466-96^{e1}, West Conshohocken, PA, USA, 2002.

[5] ASM International. Boyer H. E., editor. *Atlas of Fatigue Curves*. ASM International, Materials Park, Ohio, 1986.

[6] Radonovich, D.C., Methods of extrapolating low cycle fatigue data to high stress amplitudes*. MSc thesis*, University of Central Florida, Florida, USA, 2007.

[7] McGrath, P.J. & Els-Botes, A, *Characterising the bending behaviour of 2D laser formed Titanium (Grade 2) sheet material*. Proceedings of the Light Metals Conference – Advance Metals Initiative, Johannesburg, South Africa, 2010.

[8] Churchill, S.W. & Usagi, R., *A general expression for the correlation of rates of transfer and other phenomena*. The American Institute of Chemical Engineers, **18(6)**, pp. 1121-1128, 1972.

[9] Bannantine, J.A., Comer, J.J. & Handrock, J.L., *Fundamentals of metal fatigue analysis.* Prentice-Hall: New Jersey, 1990.